

ABSTRACT

Title of Document: INTERANNUAL VARIABILITY OF SEA SURFACE TEMPERATURE IN THE EASTERN TROPICAL PACIFIC OCEAN AND CENTRAL AMERICAN RAINFALL

Kristopher B. Karnauskas, Ph.D., 2007

Directed By: Professor Antonio J. Busalacchi
Department of Atmospheric and Oceanic Science

Sea surface temperature (SST) in the east Pacific warm pool (EPWP) plays a potentially important role in Central American rainfall, tropical cyclogenesis, ocean biology, large-scale tropical heating, and the El Niño-Southern Oscillation (ENSO). The first part of this dissertation is aimed at understanding what processes govern the interannual variability of SST in the EPWP. Interannual wind stress, shortwave radiation, and precipitation were used as forcing to an ocean general circulation model. Shortwave heating was identified as the primary driver of the interannual SST tendency in the EPWP. The high correlation between the EPWP and the equatorial Pacific Ocean is explained by the fact that equatorial SST anomalies modify the distribution of atmospheric vertical motions and therefore cloud cover and shortwave heating. In a parallel set of experiments, the low-frequency variability of the Tehuantepec gap winds was also shown to have a considerable effect on that of SST in the EPWP.

Motivated by the results of the first part of this dissertation, the second part offers significant improvements to the mean state of the equatorial Pacific Ocean in a climatology ocean model experiment by including the Galápagos Islands in the model topography. In this context, the equatorial cold bias is reduced. Furthermore, when the ocean model is coupled to

the atmosphere through zonal wind stress, the problem of an excessively regular and biennial ENSO is also reduced. The change in ENSO timescale is a result of the same dynamics operating on a different mean state.

The third part of this dissertation is aimed at understanding the role of the interannual variability of SST in the EPWP in that of Central American rainfall. An anomalously warm EPWP can trigger a rapid enhancement of the east Pacific intertropical convergence zone (ITCZ) in rainy seasons following peak ENSO events, which leads to a rainfall anomaly over Central America. Moreover, the timing and amplitude of the SST-enhanced ITCZ depends on the persistence of the ENSO event. The longer the equatorial SST anomaly persists, the longer the EPWP is subject to anomalous shortwave heating and thus the greater the subsequent SST enhancement of the ITCZ.

INTERANNUAL VARIABILITY OF SEA SURFACE TEMPERATURE IN
THE EASTERN TROPICAL PACIFIC OCEAN AND
CENTRAL AMERICAN RAINFALL

By

Kristopher B. Karnauskas

Dissertation submitted to the Faculty of the Graduate School of the
University of Maryland, College Park, in partial fulfillment
of the requirements for the degree of
Doctor of Philosophy
2007

Advisory Committee:
Professor Antonio J. Busalacchi, Chair
Professor Raghu Murtugudde
Professor Sumant Nigam
Professor Ernesto Hugo Berbery
Dr. Wayne Higgins

© Copyright by
Kristopher B. Karnauskas
2007

Preface

This dissertation adopts a modified version of the standard five-chapter layout. There are three major body chapters which include original research results: Chapter 2: Interannual variability of SST in the east Pacific warm pool, Chapter 3: On the interannual variability of SST in the equatorial Pacific Ocean, and Chapter 4: The role of SST in the eastern tropical Pacific Ocean in the interannual variability of Central American rainfall. In the interest of the future usability and readability of this dissertation, each of the major body chapters includes its own introductory remarks, literature survey, data and methodology descriptions, and a short summary which serves to segue into the next major body chapter. Where aspects of methodology are common to multiple chapters, however, they are not repeated. Thematically binding the three major body chapters are a comprehensive introduction (Chapter 1) and summary with concluding remarks (Chapter 5).

In total, this dissertation has been arranged into sections that represent separate submissions as six journal articles. Sections 2.1–2.4 will be submitted to *J. Phys. Oceanogr.*, Sections 2.5.1–2.5.2 are in revisions at *J. Climate*, Section 2.5.3 will be submitted to *J. Climate* (Note), Section 3.3 is published in *J. Phys. Oceanogr.*, Section 3.4 is in revisions at *J. Phys. Oceanogr.*, and Chapter 4 will be submitted to *J. Climate*. Full citations may be found in the CV included in the back matter.

Foreword

The primary motivation for this Ph.D. thesis by Kristopher Karnauskas was the need for a fundamental understanding of the mechanisms that determine the existence and variability of the east Pacific warm pool (EPWP) and potential influence on regional hydroclimate. During the decade, 1985-1994, of the Tropical Ocean Global Atmosphere Program, the Coupled Ocean-Atmosphere Response Experiment was organized to understand the air-sea interaction processes at work in the west Pacific warm pool. Yet to this day, on the eastern side of the tropical Pacific, relatively little is known about the smaller, but similarly warm, east Pacific warm pool. Tightly against Central America, beneath the eastern terminus of the Intertropical Convergence Zone (ITCZ), rich in marine life, and close to the maximum interannual variability of sea surface temperature in the equatorial Pacific, the east Pacific warm pool has remained an enigma.

Here it is demonstrated that the interannual variability of sea surface temperature (SST) within the EPWP is not a result of oceanic processes, but rather a regional atmospheric teleconnection in which solar insolation anomalies stemming from ENSO-related translations in the ITCZ govern interannual fluctuations SST. The lead time enabled by such forcing is demonstrated to have important implications for the predictability of precipitation over Central America. During the course of this dissertation, related avenues of investigation were pursued. Additional work detailed here led to an improved understanding of decadal controls on the gap winds across Central America and subsequent forcing of the EPWP and Costa Rica Dome. Another important finding illustrated the ramifications of neglecting the presence of the Galápagos Islands in most ocean general circulation models with implications for ameliorating the well known equatorial cold tongue bias and changes to ENSO behavior in coupled models. When considered in total, this thesis represents a significant advance in our understanding of

the eastern tropical Pacific Ocean, related air-sea interactions, and subsequent predictability of the regional hydroclimate.

Antonio J. Busalacchi

Antonio J. Busalacchi

Professor and Director

Earth System Science Interdisciplinary Center

Dedication

I dedicate this dissertation to my family. To my beautiful wife Alexis who has remained a constant and patient source of encouragement. To my loving parents: my mother Vicki whose courage is an inspiration, and my father Frank whose strong commitment to family makes it easy to forget his tireless enthusiasm in his own work. To my parents-in-law Susan and Richard Johnson, and sister-in-law Claire Johnson, who have graciously provided a local base of family and camaraderie, which helped ease my transition to a new place. Finally, to my loving Grandparents, Aunts, Uncles, and Cousins who have always believed in me.

Acknowledgements

First and foremost, I thank my advisor Professor Tony Busalacchi for his generosity with his time and resources to support my graduate studies. This dissertation would not have been possible without his guidance ranging from in-depth discussions of results to the broader vision of my work. I also cannot thank enough Professor Raghu Murtugudde, especially for always reminding me to “have fun.” I owe a great deal of gratitude also to the remainder of my committee, Professors Sumant Nigam and Hugo Berbery, and Dr. Wayne Higgins, each of whom have invested significant amounts of time on my behalf.

There are several members of the ESSIC research staff who frequently provided assistance with the technical side of things, especially Eric Hackert, Jim Beauchamp, Rong-Hua Zhang, and Mark Baith. I also thank Professor Rachel Pinker for providing her shortwave radiation dataset which was essential to Chapter 2. Finally, I thank my fellow students in the AOSC department.

Table of Contents

Preface	ii
Foreword	iii
Dedication	v
Acknowledgements	vi
Table of Contents	vii
1. Introduction	1
1.1. Statement of the problem	1
1.2. Importance of the problem	3
1.3. Scope of the problem	8
2. Interannual Variability of SST in the East Pacific Warm Pool	10
2.1. Introduction and prior work	10
2.2. Data and methodology	24
2.3. Observed and simulated interannual variability of SST in the EPWP	40
2.4. Mechanisms governing the interannual variability of EPWP SST	47
2.5. Gap winds and their role in the interannual variability of SST in the EPWP	83
2.6. Summary and discussion of the role of local versus remote forcing of the EPWP	128
3. On the Interannual Variability of SST in the Equatorial Pacific Ocean	130
3.1. Introduction and prior work	130
3.2. Data and methodology	134
3.3. On the mean state of the equatorial Pacific Ocean	140
3.4. Improvements to the simulation of ENSO in forced and hybrid coupled models	166
3.5. Summary	201
4. The Role of SST in the Eastern Tropical Pacific Ocean in the Interannual Variability of Central American Rainfall	206
4.1. Introduction and prior work	206
4.2. Observed scales of interannual variability of Central American rainfall	211
4.3. Observed covariability with SST in the eastern tropical Pacific Ocean	228
4.4. On the relationship between SST in the eastern tropical Pacific Ocean and Central American rainfall	240
4.5. Summary and implications for predictability	252
5. Summary and concluding remarks	260
Appendices	265
List of References	276
Curriculum Vitae	

Chapter 1: Introduction

1.1. Statement of the problem

In terms of sea surface temperature (SST), there are three major large-scale features of the tropical Pacific Ocean (Figure 1.1). Covering most of the western tropical Pacific is the massive west Pacific warm pool (WPWP). The WPWP is also considered to be a part of an even larger Indo-Pacific warm pool. In the eastern tropical Pacific, the SST field is dominated by a meridional gradient between the equatorial Pacific cold tongue (CT) and the east Pacific warm pool (EPWP). The CT is the site of very large interannual variations of SST due to the El Niño-Southern Oscillation (ENSO). For the purposes of this dissertation, the eastern tropical Pacific Ocean is inclusive of the EPWP and the CT.

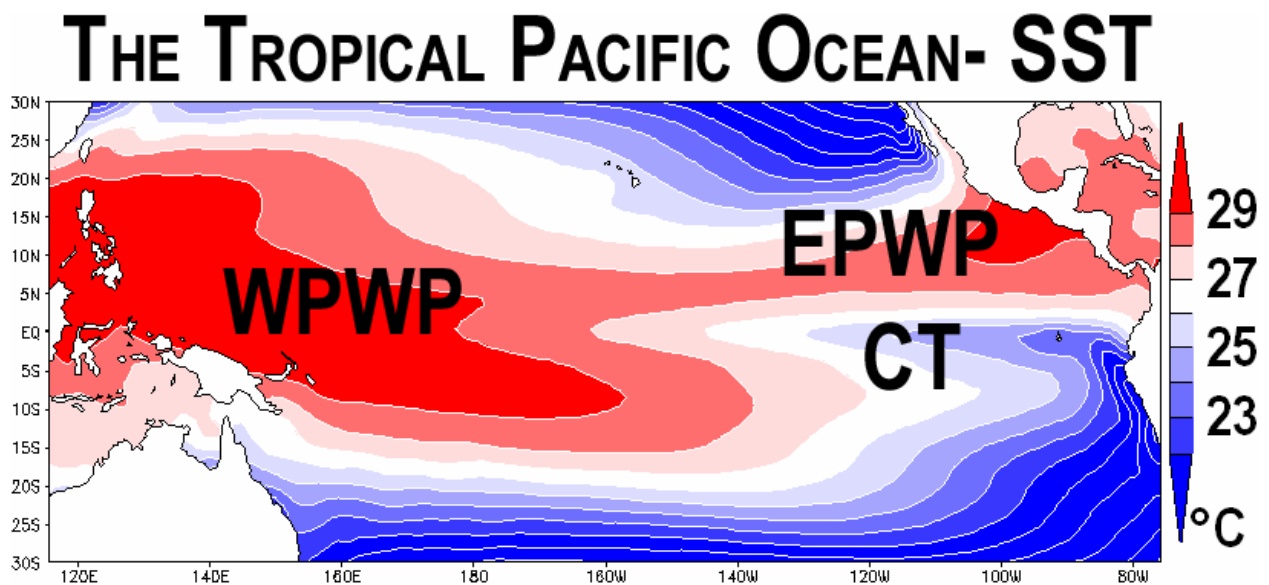


Figure 1.1. Climatological mean May-July SST in the tropical Pacific Ocean (1982-2006; Reynolds OI v.2 SST).

The ocean thermocline is the boundary between warm near-surface water and cold deep water. One general assumption about the thermocline is that its depth influences what physical processes can affect changes in SST at the surface. For example, various dynamical processes

can cause vertical displacements of the thermocline. Being associated with a sharp vertical gradient of temperature, then, it follows that the closer the thermocline is to the surface, the more effectively a thermocline displacement of a given vertical scale can affect changes in SST. The thermocline in the tropical Pacific slopes upward (shoals) from west to east. That is, the WPWP is associated with a very deep thermocline (~150 m), while the CT and EPWP are situated within a relatively shallow background thermocline (meters to tens of meters in the CT, and ~75 m in the EPWP).

As one would expect based on the above description of the mean subsurface thermal structure of the tropical Pacific Ocean, the mean balance and temporal variations of SST in the WPWP are essentially a one-dimensional radiative equilibrium, meaning the ocean mixed layer heat balance is largely between incoming surface shortwave radiation and outgoing longwave radiation. In contrast, one would expect a somewhat different picture in the eastern tropical Pacific Ocean, where dynamical processes regulating the depth of the thermocline and mixing across the base of the mixed layer could potentially have a more substantial impact on SST. As will be discussed in the literature review in Chapter 2, this is known to be the case in the CT. However, where does the EPWP lie within this dichotomy?

Although the size of the EPWP does not compare to the WPWP, the magnitude of the SST within it, and potential climatic consequences, do compare. In terms of interannual variability, even if SST in the EPWP has smaller variability than that in, say, the CT, it is operating at a higher mean temperature where even small changes thereof have significant effects on tropical convection (Zhang 1993, Wang and Enfield 2001). The following subsection outlines major reasons why a better understanding of the interannual variability of SST in the EPWP is important. The major goals of this dissertation are to (1) understand what physical processes within the coupled climate system govern the interannual variability of SST in the EPWP, (2) understand the role of that variability in the hydroclimate of Central America—particularly interannual variations of rainfall, and (3) advance, if possible, the present

capabilities of coupled models to simulate whatever processes are found to be important through inquiries (1) and (2).

1.2. Importance of the problem

There are five major reasons why a better understanding of the interannual variability of SST in the EPWP is important. They are enumerated and discussed below.

1. SST in the EPWP plays a potentially important role in the interannual variability of regional rainfall over Central America.

Throughout this dissertation, the name “Central America” will be inclusive of geopolitical Central America (i.e., Belize, Guatemala, El Salvador, Honduras, Nicaragua, Costa Rica, and Panama), as well as southern Mexico (all Mexican states east of Oaxaca). Approximately 50 million people live in narrow, mountainous Central America, snug between the warm waters of the EPWP and Caribbean Sea. Central America is also in very close proximity to a major center of precipitation. The intertropical convergence zone (ITCZ) over the EPWP is in boreal summer the rainiest place on Earth. On average, up to 50 cm of rain falls on the EPWP between May and July, which rivals the Indo-Pacific warm pool and Indian monsoon. In terms of a first order spatial scale, the ITCZ over the EPWP is part of a tropics-wide belt of heavy precipitation, and therefore rainfall over Central America must be considered in that context.

An improved understanding of the factors relevant to the year-to-year variations in rainfall over Central America, and especially our ability to predict those variations, would be potentially useful in agricultural, land-use, and disaster management sectors. For example, recent studies by Hong, Adler, and Huffman (2006, 2007a, 2007b) and Nadim et al. (2006) have focused on identifying regions particularly susceptible to rain-induced landslides. Such landslide “hotspots” are identified primarily on the basis of land surface characteristics (e.g.,

elevation slope and soil type), and rainfall statistics. The Pacific side of Central America has been identified by both groups as one of the major global landslide hotspots (Figure 1.2).



Figure 1.2. Landslide hazard zonation in Central America and northwestern South America. Figure adapted from Nadim et al. (2006).

At present, the EPWP/Central America region is also home to one of the largest rainfall biases in global coupled models. One example of such a bias, in the Community Climate Model version 3 (CCM3), is shown in Figure 1.3. Collier et al. (2004) identified the EPWP/Central America region as one of two major rainfall biases in boreal summer. The other is located over the central Indian Ocean. The magnitude of the bias is nearly 10 mm day^{-1} (equivalent to 30 cm month^{-1}).

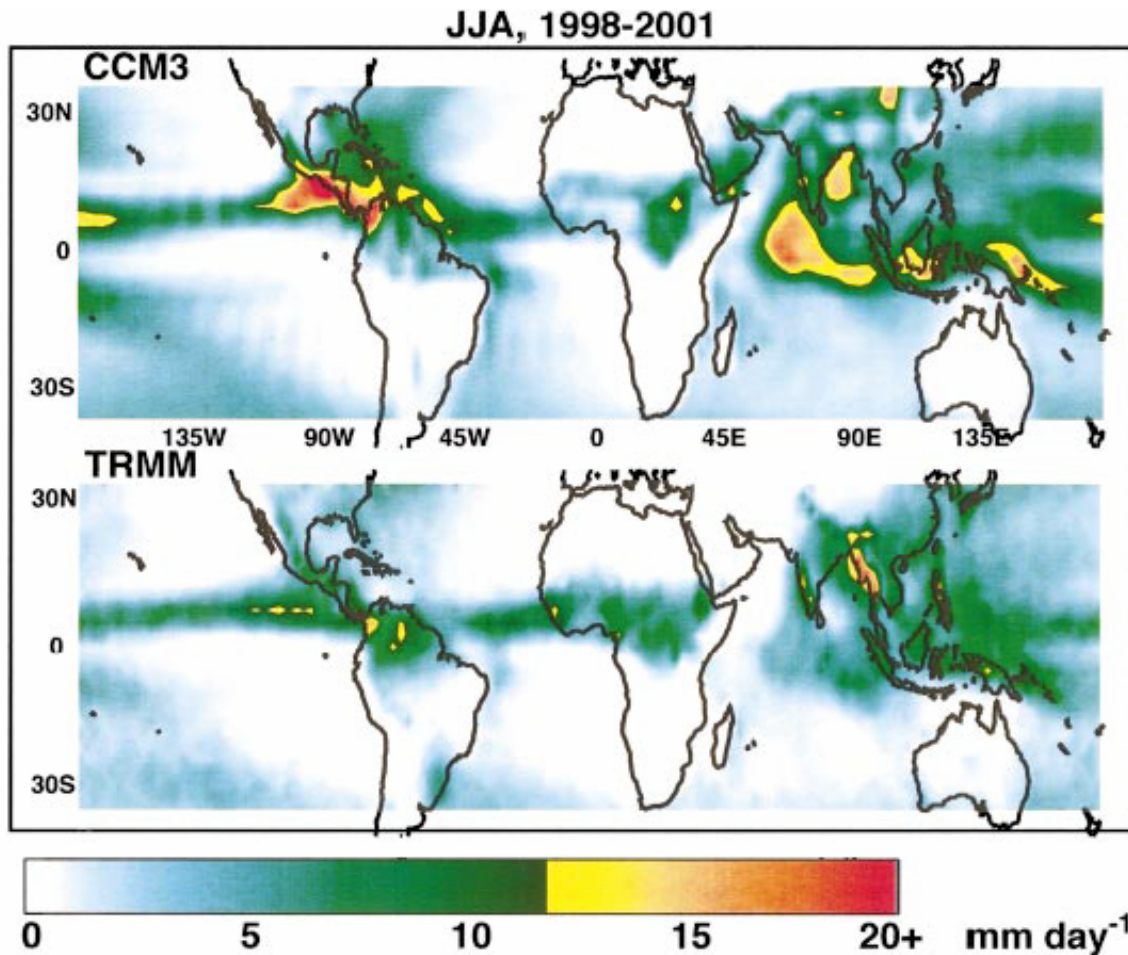


Figure 1.3. Mean June-August precipitation (1998-2001) over the global tropics from ensemble-averaged CCM3 output and TRMM satellite observations. Figure adapted from Collier et al. (2004).

2. The EPWP is the primary genesis region for eastern Pacific tropical cyclones.

Tropical cyclones are explicitly beyond the scope of this dissertation, but it is worthwhile to mention here that the EPWP is the primary region in which eastern Pacific tropical cyclones form. Shown in Figure 1.4 is a depiction of the EPWP (the boundary of the 28.5°C SST isotherm) and the tracks of all named tropical cyclones and hurricanes in the 2005 eastern Pacific hurricane season.

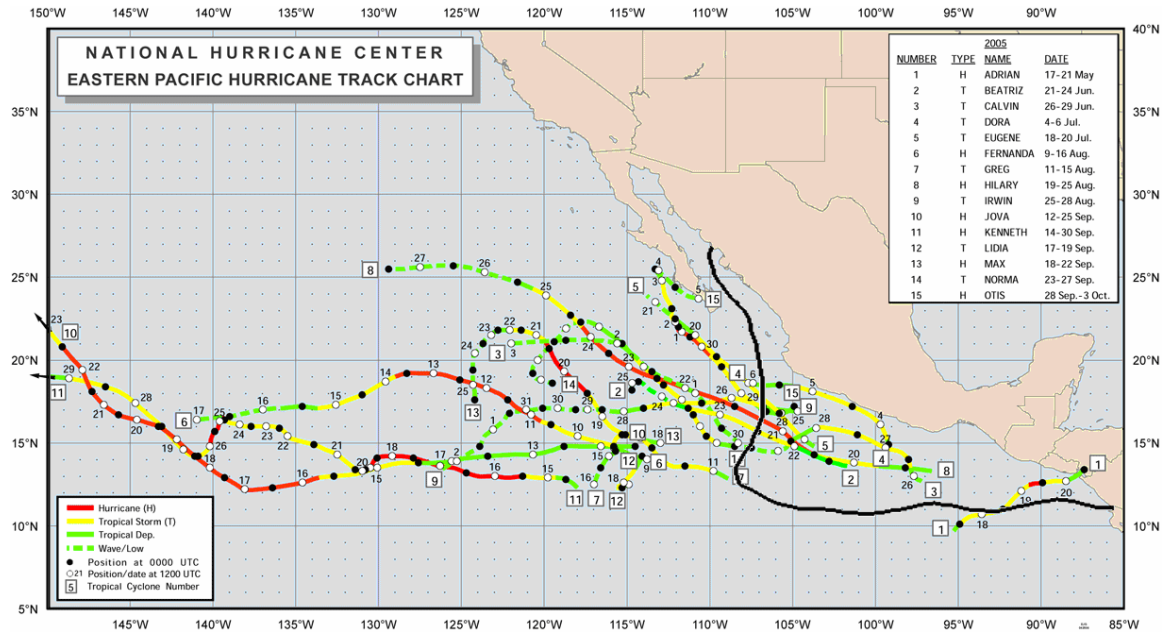


Figure 1.4. Tracks of all named tropical cyclones and hurricanes in the eastern Pacific basin during the 2005 hurricane season (map courtesy NOAA National Hurricane Center) and the mean 28.5°C SST isotherm averaged over the 2005 hurricane season.

From the EPWP, most tropical cyclones propagate northwestward where they eventually decay. Those who study tropical cyclones in the Atlantic basin often place great emphasis on a “main development region,” or MDR, and variables such as SST within the MDR (Goldenberg and Shapiro 1996). To the authors’ knowledge, the terminology “MDR” has not been applied to the eastern Pacific basin, but if it were it would surely include the EPWP. Since SST is an important boundary condition to transient tropical mesoscale phenomena such as tropical cyclones, an improved understanding of the interannual variability of SST in the EPWP would be synergistic with the study of eastern Pacific tropical cyclones.

3. The interannual variability of SST in the EPWP is linked to that of near-surface regional ocean biology from plankton to mammals.

Numerous studies have identified the EPWP as a “hotspot” for ocean biology. Fiedler (2002a) focused on the seasonal cycle of SST in the EPWP and implications for phytoplankton, whales and dolphins. Much of the seminal work of Klaus Wyrтки was done with tuna fisheries in mind (e.g., Wyrтки 1964a, 1964b). With modern technology including satellite observations of ocean color, we now know that the EPWP is also a region of maximum surface chlorophyll concentration, and large interannual variability thereof compared to the seasonal cycle (Karnauskas and Busalacchi 2006). Chlorophyll is a proxy for small biota such as phytoplankton, which serves as the important base of the marine food web. Given that processes governing SST also have the potential to regulate the availability of nutrients from below, and sunlight from above, understanding the interannual variability of SST in the EPWP is synergistic with understanding that of the marine food web.

4. The EPWP can be considered a part of a broader tropical warm pool (the western hemisphere warm pool), and therefore have important global teleconnections.

In this dissertation, the EPWP is examined as an independent warm pool located exclusively within the Pacific Ocean. However, several recent studies by colleagues at the NOAA Atlantic Oceanographic and Meteorological Laboratory (AOML) consider the EPWP a part of a much broader “Western Hemisphere warm pool” (WHWP) that also includes the Caribbean Sea, Gulf of Mexico, and in some cases, the tropical Atlantic Ocean. The rationale is that, taken together, the WHWP is a major tropical heating center interfacing with the atmosphere, much like the Indo-Pacific warm pool, with important influences and teleconnections around the globe. The present work is complementary to the recent work by David Enfield, Chunzai Wang, and Sang-Ki Lee, by examining in detail one of the components of the WHWP. This is also a very timely contribution as the upcoming CLIVAR-VAMOS Inter-Americas Study of Climate Processes (IASCLIP) program is presently in the planning phase. The relevant papers by the AOML group are reviewed in further detail in the following chapter.

5. *The EPWP could play an important role in the evolution of ENSO, including regional and global teleconnections associated with ENSO.*

ENSO is the dominant mode of interannual climate variability on Earth. The EPWP is situated within $\sim 10^\circ$ latitude of the eastern equatorial Pacific Ocean, where ENSO-related SST anomalies are most prominently manifested. Sun (2000) suggested that poleward heat transport by the ocean is considerable following El Niño events. Thus, a relevant question is what role does the EPWP play in the evolution (decay) of ENSO events? More specifically, what is the role of the EPWP in the teleconnections associated with ENSO? Does the EPWP play a role in any regional manifestations of ENSO teleconnections, such as with Central American rainfall? An improved understanding of the processes governing SST in the EPWP and the climatic consequences for nearby Central America would add to the knowledge base on ENSO and one of its potential teleconnections.

1.3. Scope of the problem

As discussed in the previous subsection, understanding the interannual variability of SST in the EPWP is important for several reasons, including applications to Central American rainfall, tropical cyclones, ocean biology, the WHWP, and ENSO. The scope of this dissertation beyond understanding what processes govern the interannual variability of SST in the EPWP, is limited to the application to Central American rainfall and, where called for, ENSO. Also, issues pertaining to long-term climate change such as global warming are beyond the scope of this dissertation entirely. However, given the relevance of this work to such societally relevant aspects as tropical cyclone intensity and Central American hydroclimate, considerations of the EPWP in a warming world will likely become a relevant topic for future research. Also, with respect to ocean biology, the observed and hypothetical effects of decadal and longer timescale

variability on ocean biology in the EPWP region are already beginning to be examined (e.g., Fiedler 2002b).

The remainder of this dissertation is organized as follows: Chapter 2 examines the interannual variability of SST in the EPWP, Chapter 3 attempts to contribute to the state-of-the-art of coupled modeling of ENSO, Chapter 4 examines the role of the EPWP in the interannual variability of Central American rainfall, and Chapter 5 summarizes the entire dissertation and provides concluding remarks.

Chapter 2: Interannual Variability of SST in the East Pacific Warm Pool

2.1. Introduction and prior work

In recent decades, a great deal of research has been invested in the coupled ocean-atmosphere system of the western and equatorial Pacific Ocean. The Tropical Ocean-Global Atmosphere (TOGA) program greatly advanced our understanding of the west Pacific warm pool (WPWP; McPhaden et al. 1998). One of the primary reasons for so much interest in the western Pacific is its critical role in atmospheric convection and the overlying Walker circulation. A major process study during the TOGA decade was focused on the WPWP. The TOGA Coupled Ocean Atmosphere Response Experiment (COARE) aimed to provide an understanding of the role of the warm pool regions of the tropics in the mean and transient state of the tropical ocean-atmosphere system (Webster and Lucas 1992). In comparison, relatively little is known about the eastern Pacific counterpart. Only recently has attention begun to shift to the east, including the Pan American Climate Studies program (PACS), the Eastern Pacific Investigation of Climate (EPIC; Raymond et al. 2004), the CLIVAR North American Monsoon Experiment (NAME), the Global Energy and Water Cycle Experiment (GEWEX), and the upcoming CLIVAR Inter-Americas Study of Climate Processes (IASCLIP). Although the scope of EPIC includes the equatorial Pacific, the only program with explicit plans to address the variability or climatic consequences of the east Pacific warm pool (EPWP) is the upcoming IASCLIP.

The TOGA research program, initiated in 1985 by the World Climate Research Program (WCRP), aimed to investigate the coupled ocean-atmosphere system as a time dependent system and its predictability, determine the extent to which the coupled ocean-atmosphere system could be modeled and predicted, and build a scientific knowledge base to support the design and implementation of an observing system for use in operational forecasting

(McPhaden et al. 1998). The atmospheric and oceanic communities worked toward these goals in five ways: building the TOGA observing system through a process study in the tropical Pacific Ocean (COARE), developing coupled ocean-atmosphere models, studying the predictability of the coupled ocean-atmosphere system, studying El Niño-Southern Oscillation (ENSO), and assessing the role of ENSO in governing the variability of the tropical Pacific region on various timescales (McPhaden et al. 1998).

Facilitated by the TOGA observing system, a considerable body of literature was generated on the coupled ocean-atmosphere system and, most notably, ENSO. Not only was our understanding of ENSO advanced by TOGA, its perceived importance and predictability was of substantial motivation to planning and implementing TOGA and its observing platforms. Further understanding of the WPWP, equatorial Kelvin waves, tropical instability waves, the relationship between surface winds and SST, ENSO-related signals in the atmosphere, and how deep tropospheric convection affects local ocean dynamics to sustain warm SSTs resulted. These are all problems of coupled nature, to which TOGA contributed. Stockdale et al. (1998) considers the inherent synergy between ocean modeling and TOGA. Ocean modeling during TOGA resulted in a better understanding of the coupled mode of interannual variability that is ENSO (McPhaden et al. 1998, Stockdale et al. 1998). As our understanding of ENSO advanced, the more accurate our vision of the observing systems required to effectively study ENSO became. In turn, observational platforms implemented by TOGA (e.g., the TAO array, drifting buoys, island tide gauges, volunteer observing ships) allowed for improved datasets used for model initialization, forcing and validation.

The spectrum of ocean modeling during the TOGA decade included a hierarchy of complexity and scale from simple to ocean general circulation models (OGCMs). In some cases, simple models were useful because they bypass numerous process and parameterization problems inherent in OGCMs, such as mixing and diffusion along the thermocline. In fact, some prior studies suggested that the dynamic response of the tropical ocean could be simulated with

a simple model (Busalacchi and O'Brien 1980 and 1981, Cane 1984, and Busalacchi and Picaut 1983, Gent et al. 1983). Intermediate models that introduce advection, surface heat fluxes, and entrainment into the ocean mixed layer are more apt to capture the variability of SST and other fields that simple models cannot fully represent (e.g., Zebiak and Cane 1987). On the complex side of ocean modeling lay OGCMs. Of notable success were the modeling and understanding of the tropical Pacific seasonal cycle (e.g., Chen et al. 1994) and interannual variability (e.g., Philander and Hurlin, 1988, Carton and Huang 1994).

While TOGA and COARE greatly advanced our understanding of the WPWP and equatorial processes, few studies have been conducted on the EPWP, and decades have passed since the seminal work on the Costa Rica Dome (e.g., Wyrtki 1964a). Both the WPWP and EPWP are similar in that they are potentially coupled with the atmosphere through warm SSTs, however, the applicability of the work on the WPWP to the eastern Pacific is limited by the fundamental difference between the two warm pools: the mean tropical thermocline in the western Pacific is quite deep (mean June-August 20°C isotherm depth along 8°N approximately 150 m at its deepest point), while the mean tropical thermocline in the east is relatively shallow (mean June-August 20°C isotherm depth along 8°N approximately 75 m at its deepest point) (Figure 2.1).

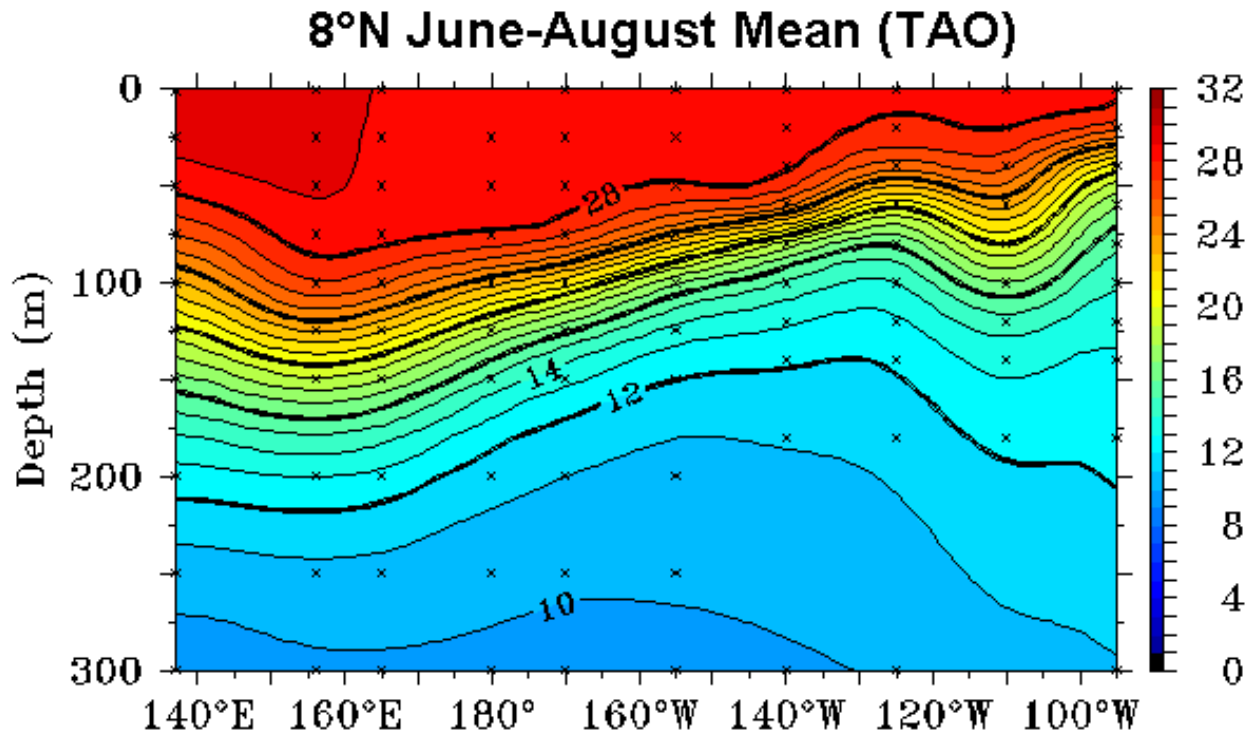


Figure 2.1. July-August mean TAO subsurface temperature (°C) across the Pacific Ocean at 8°N.

Several recent studies by a group at NOAA AOML have brought into focus a Western Hemisphere warm pool (WHWP): Wang and Enfield (2001, 2003), Lee et al. (2005), Enfield and Lee (2005), Wang et al. (2006), Enfield et al. (2006), and Lee et al. (2007). The AOML group defines the WHWP as the combined EPWP, Gulf of Mexico, Caribbean Sea and, in some cases, the tropical Atlantic Ocean. The choice to treat those regions as a single warm pool is based on the notion that the atmosphere responds to the combined WHWP as a monolithic boundary condition serving as a source of heat and moisture. However, it has been acknowledged by the authors that there could be fundamentally different oceanographic and/or atmospheric processes operating in the EPWP versus the rest of the WHWP. Also, the question of regional atmospheric responses to SST interannual variability cannot be answered without considering the subregions of the WHWP separately.

In a short paper by Wang and Enfield (2001), the WHWP was introduced and formally defined. Wang and Enfield (2001) analyzed observed surface fluxes (da Silva 1994) primarily to describe the first order balance and the annual cycle in the broadly defined WHWP region. A positive ocean-atmosphere feedback operating through longwave radiation was also suggested as a possible mechanism to explain the correlation between the WHWP and ENSO. Wang and Enfield (2003) followed up on the first order balance and seasonal evolution described in Wang and Enfield (2001), while noting that the (interannual) longwave feedback only applies to the non-Pacific part of the WHWP. As for the northeastern tropical Pacific, it was inferred that SST in that region is most likely “directly” controlled by the anomalous Pacific mixed layer associated with ENSO, although this was not supported by any analysis. Lee et al. (2005) returned to studying the annual cycle in the WHWP, by forcing an ocean model with eight different heat flux climatologies, and assessing the quality thereof based on their ability to result in good simulations of WHWP SST. Using the “best” heat flux climatology, the seasonal heat budget was recomputed, confirming their prior conclusions that, among other things, the annual cycle in the Pacific part of the WHWP is dominated by net surface flux. Still focusing on the annual cycle, Enfield and Lee (2005) again judged several heat flux climatologies by intercomparing “bubble” and “slab” style heat budget calculations.

Wang et al. (2006) marked the group’s first study aimed at assessing not what dominates the seasonal evolution of SST in the WHWP, but how the WHWP influences summer rainfall and Atlantic hurricanes. The Pacific part of the WHWP was left out of Wang et al. (2006) entirely, with the exception of a few remarks restating the assumption that the Pacific part of the WHWP must be dominated by ENSO by virtue of being in close proximity to the region of maximum ENSO-related SST variance. Enfield et al. (2006) focused on how ENSO events do (or do not, in some cases) force the non-Pacific part of the WHWP to be anomalously large and/or warm. The major conclusion of Enfield et al. (2006) is that an ENSO event alone is not sufficient to force an anomalous WHWP the following summer; it is the persistence of the ENSO

event that appears more critical than its amplitude. Finally, Lee et al. (2007) dropped the Atlantic part of the WHWP and used multiple modeling techniques to reassess the annual cycle of the WHWP. According to Lee et al. (2007), the WHWP “cannot be considered a monolithic whole with a single set of dominating processes that explains its behavior.” As for the Pacific part of the WHWP, the dominant role of shortwave heating was confirmed, while the importance of cloudiness later in the summer, as well as a year-round cooling contribution from the Costa Rica Dome, was emphasized. Clearly it is time for a study aimed specifically at the interannual variability of the Pacific part of the WHWP- that is, the EPWP.

Given the location of the EPWP, it would be expected that its interannual variability be directly influenced to a large degree by ENSO. Of course it has long been known that El Niño plays a vital role in the poleward transport of heat. Fluids have a strong tendency to redistribute energy, especially in the presence of such markedly uneven distributions of heat as those which occur during El Niño events. According to Sun (2000), the majority of heat exported from the equatorial Pacific during El Niño is done so through the ocean circulation of the eastern Pacific and not locally through the air-sea interface. Meinen (2005) used satellite altimetric observations of sea surface height anomalies (SSHA) to track warm water volumes northward and southward of the equator during the strong El Niño event of 1997-98. Meinen found that, while warm water volumes might be tracked as far south as 20°S, northward propagating volumes were only traceable to approximately 10°N. Meinen mainly focused on the east-central Pacific Ocean. In fact, studies isolating the effects of El Niño on the three-dimensional spatial and temporal characteristics of the EPWP are absent from the scientific literature.

Analysis of SST fields in the eastern tropical Pacific Ocean have revealed that the EPWP itself is more spatially complex than a uniform body of warm water and includes the well-known Costa Rica Dome, a permanent wind curl-induced upwelling maximum within a nominally shallow thermocline at 9°N, 90°W (Wyrtki 1964a). A recent contribution from Xie et al. (2005) describes the orographically-triggered air-sea interaction involving wintertime gap winds

through the Central American cordillera which produce patches of surface water to 3°C colder and stronger chlorophyll signatures than background. Xie et al. suggest that increased turbulent heat flux away from the ocean and enhanced mixing across the base of the mixed layer are responsible for communicating the effects of the winds to the ocean in producing such features. Model simulations targeting such processes would be helpful to confirm this explanation.

The Central American cordillera has three appreciable gaps through which wind jets may form, from north to south: Tehuantepec, Papagayo, and Panama. Using IR and high resolution microwave precipitation and SST products, Xie et al. further suggest that the cold patch of water under the Panama jet, the southernmost of the three gaps, reduces convection enough to produce a noticeable hole in the winter ITCZ and reduce local precipitation by 50%. Furthermore, a 500-km hole in the summertime ITCZ was found over the CRD. Elaborating upon conventional wisdom that the generation of the CRD is seasonal and the result of cyclonic wind stress curl from the mean wind stress field (e.g., Wyrтки 1964a, Hoffman et al. 1981), Xie et al. suggest that the CRD is produced by cyclonic wind stress curl imparted *uniquely* by the Papagayo jet. This is in contrast with the work of Umatani and Yamagata (1991), which, by diagnosing the seasonal cycle of the CRD with a fine-resolution regional ocean circulation model, found that the CRD is *not* a linear response to the mean wind stress curl, but a planetary nonlinear mode. Xie et al. is a compelling discussion of the atmospheric mechanisms leading to some of the finer spatial variability in the EPWP and the effects of the cold patches within the EPWP on convection directly above those cold patches. However, the processes governing the interannual variability of the EPWP and the climatic consequences thereof, both locally and remotely, remain unknown.

In a recent review of the atmospheric fields relevant to the oceanography of the eastern Pacific, Amador et al. (2006) offer a picture of the mean fields and annual cycles of radiation, atmospheric pressure, wind stress curl, temperature, and precipitation. While Amador et al. is largely a presentation of valuable analyses of updated atmospheric and oceanic datasets, it is

mentioned in the present literature review for two reasons. First, the descriptions of the atmospheric phenomena relevant to oceanography are relevant to the present study. Secondly, and most importantly, Amador et al. (2006) includes a statement of general agreement that SST in the EPWP has considerable variability, and its role as a potential source of moisture in the hydroclimate of the Americas is far from understood.

Central in determining what processes govern the interannual variability of the EPWP are the details of the ocean mixed layer heat budget. With the exception of seasonal perspectives from the AOML group, and a very short timescale (single cruise) perspective from Wijesekera (2005), a complete interannual heat budget analysis of the EPWP has not been performed to date. However, a number of prior heat budget studies of the Pacific Ocean have provided an abundance of methodologies and results for nearby regions. Following the work of Charney (1959), Haney (1971) addressed how best to perform large-scale thermal coupling of the ocean and atmosphere. Instead of prescribing SST as a thermal boundary condition to the atmosphere and relying on a vertical eddy diffusion coefficient, Haney formulated a flux-type boundary condition for net downward heat flux across the ocean surface: $Q_{NET} = Q_2 (T_A^* - T_S)$ where Q_2 is a latitudinally dependant coupling coefficient determined from zonally and time averaged data, T_A^* is an apparent atmospheric equilibrium temperature, and T_S is sea surface temperature. Haney shows that a heat budget analysis of this formulation for Q_{NET} yields similar results to that obtained from an analysis of the traditional equation for net downward heat flux across the ocean surface: $Q_{NET} = Q_{SW} - (Q_{LW} + Q_{SH} + Q_{LH})$. Haney does not consider the effects of horizontal and vertical temperature advection or mixing across the base of the ocean mixed layer on SST. Haney states that understanding the long-term interaction between the ocean and the atmosphere requires proper coupling between ocean and atmospheric models. Thus, all processes that affect the evolution of the thermal boundary condition to the atmosphere (SST) must be considered.

Applying a similar approach to the SST variations and heat budget in the eastern equatorial Pacific Ocean, i.e., the cold tongue, Wyrski (1981) evaluated a rather complete heat budget, including both surface fluxes and ocean dynamics, for a 50-m deep “box” from 170°E-100°W by 5°S-5°N. Wyrski (1981) considered three separate processes involved in the heat budget: net surface flux, horizontal advection and vertical advection. Diffusion was neglected in Wyrski’s calculations. Wyrski concluded that net surface flux was approximately balanced by horizontal advection with contribution from upwelling.

Using a linear dynamical model of the Pacific Ocean, Pares-Sierra et al. (1985) estimated the horizontal oceanic heat transport in the tropical Pacific Ocean in which adiabatic advection of heat by the wind driven circulation was the only heat transport mechanism allowed. Since the results were in agreement with estimates based on other complex models that include full thermodynamics, Pares-Sierra et al. concluded that adiabatic advection of heat by the wind driven circulation plays a dominant role in the heat budget of the tropical Pacific Ocean. Pares-Sierra et al. then performed a heat budget analysis on the zonally integrated Pacific Ocean. They used a heat budget formulation for oceanic heat storage $HS = Q_{SFC} + Q_W + Q_T$ where Q_{SFC} is the net downward heat flux across the ocean surface, Q_W is the horizontal advection of heat by the wind-driven circulation, and Q_T is the horizontal advection of heat by the thermohaline circulation. By assuming that changes in oceanic heat content are negligible, the radiative input (Q_{SFC}) must be balanced by poleward heat transports, or $(Q_W + Q_T) < 0$ wherein Q_W is the dominant form of advection. While this points to the importance of ocean dynamics, which are in part the result of wind forcing, Pares-Sierra et al. stress that their formulation of the heat budget only includes two terms and that the use of a complete thermodynamical framework should be used to fully assess the heat budget of the tropical Pacific Ocean. It is also noted that regions that have large seasonal variability coincide with regions of large interannual variability. The mean annual cycle as well as the effects of El Niño on the interannual variability of the complete heat budget would seem an appropriate follow-up.

Seager et al. (1988) used a dynamical ocean model to construct the mean SST field in the tropical Pacific without prescribing near surface air temperature. This was an important step because the near surface air temperature is itself strongly influenced by SST. In the case of the EPWP region, Seager et al. found that the warm SSTs are explained both by ocean dynamics and a local minimum in wind speed. The details of such dynamics and their relative importance compared to radiative fluxes remain elusive. Also, Seager et al. cite the EPWP as one of two major discrepancies in their simulation of the mean SST field of the tropical Pacific Ocean. By claiming that ocean dynamics play only a moderate role in the evolution of SST in the eastern tropical Pacific, Seager et al. attribute their overestimate of SST in the EPWP to errors in the net surface heat flux.

Philander et al. (1988) also pointed to the need to examine all terms, especially those related to diabatic processes, in the heat budget and understand their seasonal and interannual variations. Philander et al. state that enormous value can be derived from a more accurate understanding of the heat budget of the tropical Pacific. It seems this would be particularly true in the east where El Niño events have strong implications for diabatic processes and overall ocean-atmosphere coupling.

Chen et al. (1994) investigated the various processes that control the seasonal variability of SST in the equatorial Pacific Ocean from 5°S to 5°N. Chen et al. used the formulation $\partial T/\partial t = Q_S + Q_D + Q_U + Q_W$ where Q_S is the net surface heat flux divided by the mixed layer depth (heat loss from the mixed layer due to penetrative radiation is removed from this term), Q_D is the sum of the vertical mixing and horizontal diffusion, Q_U is zonal advection, and Q_W is the sum of the vertical and meridional advection. The authors' analysis of the seasonal variability of the heat budget for the eastern equatorial Pacific (110°W-80°W) resulted in the important conclusion that vertical mixing plays a large role in defining the seasonal evolution of SST. Especially important in the eastern equatorial Pacific is the influence of vertical mixing on SST by way of changing the depth of the mixed layer. While the conclusions of Chen et al. do highlight the

importance of vertical mixing, they do not isolate every term in the mixed layer heat budget for direct comparison (e.g., comparisons such as vertical mixing versus meridional advection cannot be made). Due to a lack of sufficient wind forcing data, Chen et al. postponed consideration of the interannual variability of the mixed layer heat budget. It is likely that the heat budget results of Chen et al. for the eastern equatorial Pacific would differ from those for the EPWP, which is effectively north of the equatorial domain.

For a region similar to the eastern equatorial Pacific domain in the heat budget part of Chen et al. Swenson and Hansen (1999) evaluated the annual cycle of the oceanic processes that are thought to control the seasonal evolution of SST based on data from satellite-tracked drifting buoys, volunteer observing ships (VOS) and expendable bathythermographs (XBT). Swenson and Hansen found that the most important contributions to the mean annual heat export from the cold tongue region between 1979 and 1995 were meridional advection and entrainment. However, coincident radiative fluxes are not analyzed for comparison to the horizontal and vertical advective processes. As in Chen et al., interannual variability is not discussed, and important differences between the heat budgets for the cold tongue and the EPWP may exist.

A recent study of the heat budget of the EPWP based on in situ observations from a 2001 ship survey by Wijesekera et al. (2005) suggested that important components of the heat budget were heat storage, advection, turbulent transport, and penetrative radiation. As Wijesekera et al. focused on in situ measurements of both air-sea fluxes and ocean currents, the constraints of *in situ* sampling prevent interpretation within the context of interannual variability of the mixed layer heat budget of the EPWP.

While many previous studies involving heat flux and budget calculations provide useful methodologies and comparisons, the time has come for a comprehensive investigation into the mechanisms governing the interannual variability of SST in the east Pacific warm pool.

The monsoon system of the eastern Pacific directly affects the socioeconomic well-being of vast numbers of people through such pathways as agriculture, human and ecosystem health,

floods and droughts, land use and quality, and hydropower generation. The EPWP, being a nearby body of warm water, has the potential to induce land-sea temperature contrasts critical to a monsoon circulation and potentially serve as a reservoir for heat and moisture to be released into the hydrologic cycle of the region. Studies by Webster et al. (1998) and Magaña et al. (1999) have shown that the climatology of precipitation over Central America and Mexico is governed by the ITCZ. Just as in the western Pacific, the ITCZ in the east is critically linked to the underlying SST field. Various studies have also hinted at the role of SSTs in the interannual variability of the monsoon circulation over the Americas (e.g., Mitchell and Brown 1996, Higgins et al. 1998 and 1999, Magaña et al. 1999). Each of these studies explicitly state that further understanding of the interannual variability of precipitation depends on an improved understanding of what controls the SST variability in the eastern Pacific Ocean. The essence of this problem was summarized in the *PACS Scientific Prospectus and Implementation Plan*, that:

“For climate prediction of a season or more in advance, it is necessary to take into account the evolution of the boundary forcing of the atmosphere. Sea surface temperature anomalies in the tropical Atlantic and Pacific ... are known to influence climate variability over parts of the Americas.”

The seasonal cycle of precipitation over Central America and southern Mexico is marked by a reduction in precipitation in the midst of the rainy season known as the midsummer drought (MSD). As early as 1966, the idea was put forth that ocean conditions partially control the geographic and temporal distribution of the MSD (Mosiño and García 1966). As Magaña et al. (1999) pointed out, precipitation over southern Mexico and Central America exhibits maxima during June and September-October with a relative minimum during July-August. While precipitation and other variables are often influenced by the twice-annual crossing of the ITCZ,

Magaña et al. suggests that the region's bimodal seasonal cycle of precipitation is attributable to *fluctuations* in the intensity and location of the ITCZ in the eastern Pacific. Since a bimodal seasonal cycle of precipitation is observed as far north as 20°N where the ITCZ does not cross twice, the mean meridional propagation of the ITCZ cannot fully account for the MSD.

Using microwave precipitation data (Spencer 1993) and the NCEP-NCAR reanalysis (Kalnay et al. 1996), Magaña et al. provide evidence that the MSD is related to the divergence of the low level trade winds. At the onset of the MSD, the low level trade winds over the region wherein the MSD is observed change from convergent to divergent, thereby reducing convection in the ITCZ and precipitation. At the end of the MSD, the low level trade winds change from divergent to convergent, thereby restoring deep convection to the ITCZ. Drawing upon the important recognition by Lindzen and Nigam (1987) that tropical SSTs and SST gradients are a strong determinant of low-level divergence, Magaña et al. explore the prospect that SSTs in the EPWP may cause the seasonal fluctuations in the strength of the ITCZ necessary to produce the observed bimodal seasonal cycle of precipitation. The authors conclude that the problem is full of nonlinear relationships; the troposphere responds to warm SSTs with convection, which by mass continuity causes a convergent low-level wind field; SSTs respond indirectly to convection both by cooling in response to reduced incoming solar radiation and warming in response to reduced loss of longwave radiation; finally, low-level winds (including transient gap wind events) influence SSTs by way of latent heat flux, turbulent mixing, and Ekman pumping.

With regard to the North American monsoon system (NAMS), Higgins et al. (1999) characterized and diagnosed the general features and interannual variability of the warm season monsoon over the southern U.S., Mexico, and northern Central America. Using the U.S.-Mexico merged analysis of precipitation (refer to Higgins et al. 1999), Higgins et al. found that the maximum warm season (July-September) precipitation occurs over southern Mexico, while the region wherein warm season precipitation constitutes the greatest percentage of the annual total was west-central and northwest Mexico. Turning to interannual variability, Higgins et al. also

noted that wetter than average monsoon years were associated with large positive Southern Oscillation Index (SOI), or La Niña events, and drier monsoon years were associated with large negative SOI, or El Niño events. Given the high level of confidence in this finding, it is suggestive that the role that the interannual variability of SST in the eastern equatorial Pacific plays in determining the ocean-land temperature contrast is critical in determining the interannual variations in warm season precipitation over the NAMS region. Given that the EPWP is in closer in proximity to Mexico and the southwestern U.S. than the equatorial Pacific where ENSO events most strongly manifest themselves in SST, and the EPWP is a permanent oceanographic feature with appreciable interannual variability, a similar investigation into the role that the EPWP plays in the monsoon system is timely and relevant.

An additional study addressing the impact of the interannual variability of SST on the North American monsoon system (NAMS) is worth mentioning here. Farrara et al. (2003) performed a series of ensemble atmospheric general circulation model (AGCM) experiments with the UCLA AGCM with and without interannual variations of SST in the lower boundary conditions. The authors used composite SSTA fields for anomalously wet and dry monsoon years from a Reynolds SST product. Strictly limiting their analysis of the impact of SST on atmospheric circulation to the extratropics (northern Mexico and northward), the authors found that interannual SST anomalies had no systematic impact on the atmospheric circulation over North America during summer. Although Farrara et al. note that their results are not statistically significant, they corroborate this finding by noting that similar work by Koster et al. (2000) also determined that chaotic atmospheric dynamics contribute the most to precipitation variance in the extratropics. However, Koster et al. (2000) also determined that in the *tropics*, SSTs in fact contribute the *most* to precipitation variance.

Given the valued understanding of the WPWP generated during the TOGA decade, numerous studies have been aimed toward exploiting the promise of similar consequence in the eastern Pacific region. The foci of such studies include the observed variability of the broader

body of water surrounding Central America (i.e., the WHWP), the interactions between gap winds and the mesoscale spatial variability in the EPWP, parts of the heat budget of the nearby equatorial Pacific, and the seasonal to interannual variability of precipitation over the southwest U.S., Mexico and Central America. However, two outstanding questions remain that constitute a critical gap in our present understanding of the climate system of the Inter-Americas region: (1) explicitly what processes govern the interannual variability of SST in the EPWP, and (2) what impact does that variability have on the hydroclimate of Central America.

2.2. Data and methodology

In striving to understand what physical processes in the coupled ocean-atmosphere system govern the interannual variability of SST in the EPWP, Chapter 2 makes use of output from carefully designed ocean general circulation model (OGCM) experiments, satellite observations, and other atmospheric and oceanic datasets. The present section describes the details of the OGCM, the experimental design, and other major datasets used.

2.2.1. Description of ocean model and control experiment

The ocean model used in the present study is the Gent and Cane (1989) reduced gravity, primitive equation, sigma coordinate OGCM of the tropical oceans. In a reduced gravity model, the Boussinesq approximation is applied to the primitive equations; variations in density are neglected except where they affect buoyancy. This leads to a few assumptions about the deep ocean (below the active upper layer): it is at rest, has a constant density (and temperature, in this model) and is infinitely deep. This also implies that there cannot be any vertical variation of topography. The reduced gravity formulation is quite popular because it nicely captures the first baroclinic mode, the structure of the main thermocline/pycnocline, and the time evolution of the free surface elevation. In a sigma coordinate model, the depth of each model layer (except for the mixed layer) is determined by a prescribed ratio of the depth of each layer to the total

depth (not including the mixed layer). This is a common alternative to a z-coordinate model, in which the depth of each layer (except for the mixed layer, in some cases) is a fixed, true depth.

The version of the Gent-Cane OGCM used in the present study also includes the hybrid vertical mixing scheme of Chen et al. (1994), and is coupled to the atmospheric mixed layer model of Seager et al. (1995). There are three primary mechanisms for ocean turbulent mixing: entrainment-detrainment, shear flow instability, and convection in the thermocline. The Chen et al. (1994) hybrid scheme combines the classic mixed layer physics of Kraus and Turner (1967) with the Price et al. (1986) dynamic instability model to simulate each of the three mechanisms for ocean mixing. The Chen et al. (1994) hybrid mixed layer is far more realistic than a constant-depth mixed layer or one with highly simplified physics.

Murtugudde et al. (1996) coupled the atmospheric mixed layer (AML) model of Seager et al. (1995) to the Gent-Cane OGCM. The Seager et al. (1995) AML simulates the atmospheric advection of air temperature and humidity, after which heat fluxes are computed. Air temperature and humidity are determined by a balance between surface heat fluxes, horizontal advection by prescribed winds, entrainment from above the AML, horizontal diffusion, and radiative cooling. Such a coupling allows a realistic representation of the feedbacks between SST and surface heat fluxes (Murtugudde et al. 1996). Compared with other common approaches in ocean modeling pertaining to surface heat fluxes, such as relaxing SST to observations (e.g., Haney 1971), specifying observed surface heat fluxes, or even specifying observed air temperature and humidity, this approach is far more realistic and “honest,” especially if it is the variability of SST itself that is of primary interest (Seager et al. 1995). The OGCM-AML coupling by Murtugudde et al. (1996) should not be confused with a fully coupled ocean-atmosphere GCM, in which winds respond to SST, cloud cover responds to winds, etc.; the Seager et al. (1995) AML cannot change the prescribed dynamical wind stress or shortwave forcing.

The horizontal resolution of all OGCM experiments analyzed in Chapter 2 is uniform $1/3^\circ$ zonal and meridional. The meridional boundaries of the model grid are 30°N to 10°S , along which a sponge layer is used at the meridional open boundaries (see Chen et al. 1994). Zonal boundaries are represented by the approximate coastlines of Asia, Indonesia, and Australia in the western Pacific (Indonesian throughflow is closed off) and the Americas in the eastern Pacific. There are 20 layers: the mixed layer plus 19 subsurface layers. Finally, in the experiments analyzed in Chapter 2, a reduced-order Shapiro filter of order 8 is used, applied once every 4 timesteps (2 hours, in this case). A Shapiro (1970) filter is a horizontal smoothing scheme required to maintain computational stability. It is applied at the end of a timestep to velocity and tracer fields to remove small scale grid noise, presumably without affecting the physical structure of the field. Compared to other schemes (Laplacian, biharmonic, etc.), the Shapiro filter damps fields less and is computationally efficient on stretched grids. A higher order filter means less smoothing. “Reduced-order” means that, along the boundaries, the Shapiro filter starts at order 2 (strongly smoothed), and doubles at each gridpoint away from the boundary until reaching the full order (in this case, 2, 4, then 8).

A control and several process-oriented experiments were performed. The *control* experiment was integrated using interannually varying wind stress, surface shortwave radiation, and precipitation forcing. The integration spans 1988–2004, using a 30 minute model timestep, saving weekly averages. Interannual wind stress forcing was derived from a wind stress dataset merging Special Sensor Microwave Imager (SSM/I) ocean surface winds and SeaWinds wind vectors. The SSM/I instrument is a passive sensor flown aboard Defense Meteorological Satellite Program (DMSP) satellites, and the SeaWinds instrument aboard the National Aeronautics and Space Administration (NASA) Quick Scatterometer (QuickSCAT) satellite. Both instruments have a nominal spatial resolution of 25 km. The merged wind stress dataset includes SSM/I using the variational analysis of Atlas et al. (1997) from 1988-1999 (v. 10) and QuickSCAT from 1999-2004, with a smooth conversion from SSM/I to QuickSCAT

between July-September 1999. The QuickSCAT dataset was produced using the optimal interpolation method of Bourassa et al. (1999). The SSM/I-QuickSCAT wind stress were regridded to a 1° by 1° horizontal grid with weekly temporal resolution.

Interannual surface downward shortwave radiation forcing was derived from a product developed in conjunction with the Global Energy and Water Cycle Experiment (GEWEX) Surface Radiation Budget (SRB) project. The dataset combines satellite observations of top-of-atmosphere fluxes with a radiative transfer model to infer the downward flux of shortwave radiation at the surface of the Earth. Complete details of the surface downward shortwave radiation data used can be found in Pinker and Laszlo (1992). Finally, interannual freshwater forcing was derived from Xie et al. (2003) precipitation.

Prior to integrating the *control* experiment from 1988-2004, it was necessary to ensure a smooth transition of the ocean from a climatological state resulting from the initial 60-year spinup beginning with Levitus and Boyer (1994) initial conditions to the true, “interannual” ocean state beginning in 1988. To achieve this, the model was spun up for an additional 20 years using as forcing the climatology of the interannual forcing to be used in the *control* and process experiments. Then, the model was further integrated by repeating the 1988 forcing for 5 years before initiating the full interannual integration which spans 1988-2004. This rather lengthy process was necessary to minimize the model “shock” when transitioning from the spinup or climatological forcing to the full interannual forcing.

Examining the results of the spinup of the OGCM using the climatology of the interannual forcing, however, revealed that biases in the wind stress and shortwave forcing resulted in a surface ocean that was too warm with an exaggerated zonal gradient of thermocline depth and SST. Therefore, bias corrections to the wind stress and shortwave forcing were necessary prior to further integration. In terms of climate experiments, our group’s version of the Gent-Cane OGCM has been used most successfully with wind stress from ECMWF (Bengtsson et al. 1982) and shortwave radiation from the Earth Radiation Budget Experiment

(ERBE; Barkstrom 1984). Therefore, an attempt has been made to scale biases from the QuickSCAT-SSM/I wind stress and SRB shortwave radiation according to ECMWF and ERBE, respectively, while being mindful of observations from *in situ* observations from TAO moorings. After careful analysis and trail-and-error procedures, the most appropriate bias corrections were a 20.8% reduction of the QuickSCAT-SSM/I zonal wind stress, and a uniform 30 $W m^{-2}$ reduction of SRB surface downward shortwave radiation. Shown in Figure 2.2 are comparisons of the mean seasonal cycles of the original and modified wind stress and shortwave radiation, along with additional analyses (e.g., TAO).

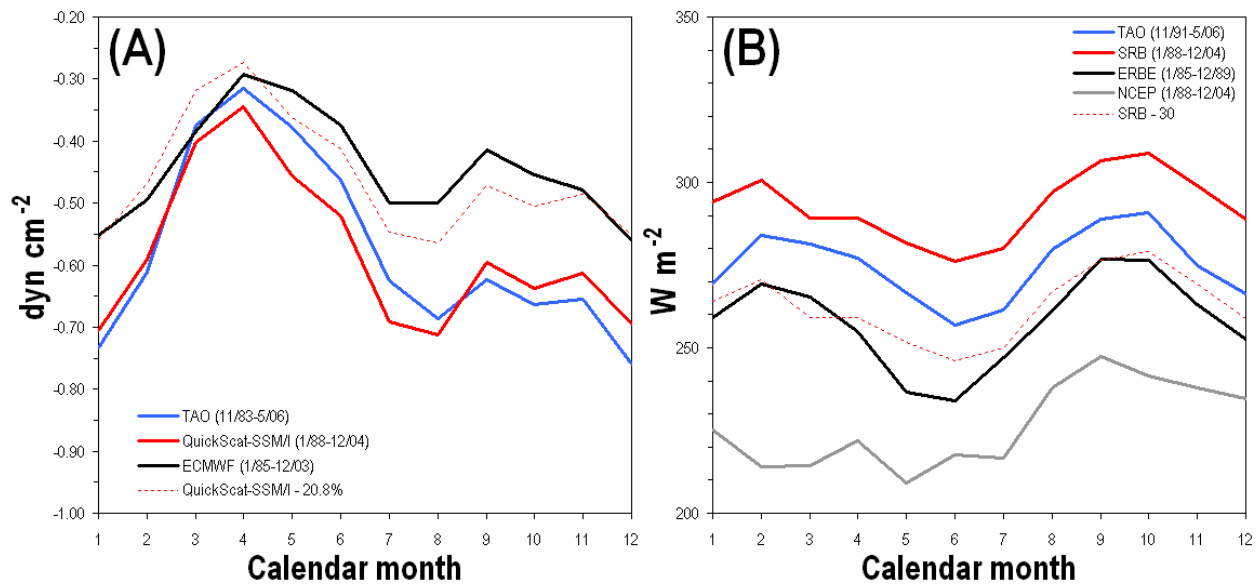


Figure 2.2. (A) Mean seasonal cycle of zonal wind stress ($dyn cm^{-2}$; $1 dyn cm^{-2} = 0.1 N m^{-2}$) at the equator, $140^{\circ}W$ from TAO (blue), QuickSCAT-SSM/I (red), ECMWF (black), and the modified QuickSCAT-SSM/I (red dashed). (B) Mean seasonal cycle of surface downward shortwave radiation ($W m^{-2}$) at the equator, $140^{\circ}W$ from TAO (blue), SRB (red), ERBE (black), NCEP Reanalysis (gray), and the modified SRB (red dashed).

Once the aforementioned bias corrections were applied to the interannual wind stress and shortwave radiation forcing data, the spinup procedure was repeated beginning with the 20-year transition spinup. Then, finally, the interannual *control* experiment was integrated from

1988-2004. A validation of the model climatology and mean seasonal heat budget is provided in the following subsection.

2.2.2. Validation of model climatology and heat budget

The specific focus of Chapter 2 is the interannual variability of SST in the EPWP, that is, the year-to-year departures from the mean seasonal cycle. However, it is necessary to first examine the model's ability to represent the climatology of SST and the seasonal ocean mixed layer heat budget with respect to observations. Shown in Figure 2.3 is the climatological mean SST field in the northeastern tropical Pacific Ocean from the *control* experiment and Reynolds OI v.2, stratified by season. To ensure a fair comparison, the periods over which the climatology from the model and observations were computed are identical: 1988-2004. Qualitatively, the model represents the annual mean SST field in the northeastern tropical Pacific Ocean to a reasonable degree of fidelity. The warmest SSTs are found in boreal spring, summer, and fall, exceeding 28.5°C near the coast. During boreal winter, SSTs within the EPWP drop below 26.5°C. Toward late boreal summer and fall, the model captures the evolution of the shape of the EPWP as being more elongated and confined to the coast of Central America. During boreal winter, the model reveals small-scale cold patches in the Tehuantepec and Papagayo influence regions. It should be noted that there is considerable difference between the resolution of the model and observations in this case; both the zonal and meridional resolution of the model is three times finer (uniform 1/3°) than the Reynolds OI v.2 SST dataset (uniform 1°).

Two apparent discrepancies stand out in the climatological mean SST fields: an underestimate of SST to the north in March-May, and an underestimate of SST in boreal winter to the south (between the Papagayo and Panama gap winds). Reasons for these deficiencies are unclear. In March-May, the area enclosed by the sea surface warmer than 28.5°C is smaller in the model, but at least that is when the EPWP is largest in the model, which does agree with the observations. In December-February, the discrepancy between the model and observations to

the south is again relative; there is a region which does not appear warm enough, but at the very least the region is a relative maximum as in observations.

The primary focus of this chapter is interannual variability. It is suggested that the model's simulation of the mean and seasonality of SST in the EPWP is sufficiently accurate to allow meaningful analysis of its interannual variability. Overall, for an OGCM which was designed to simulate equatorial processes and spatial variability presumably larger than the finer details of the EPWP, the Gent-Cane OGCM with the prescribed forcing in this setup is quite good.

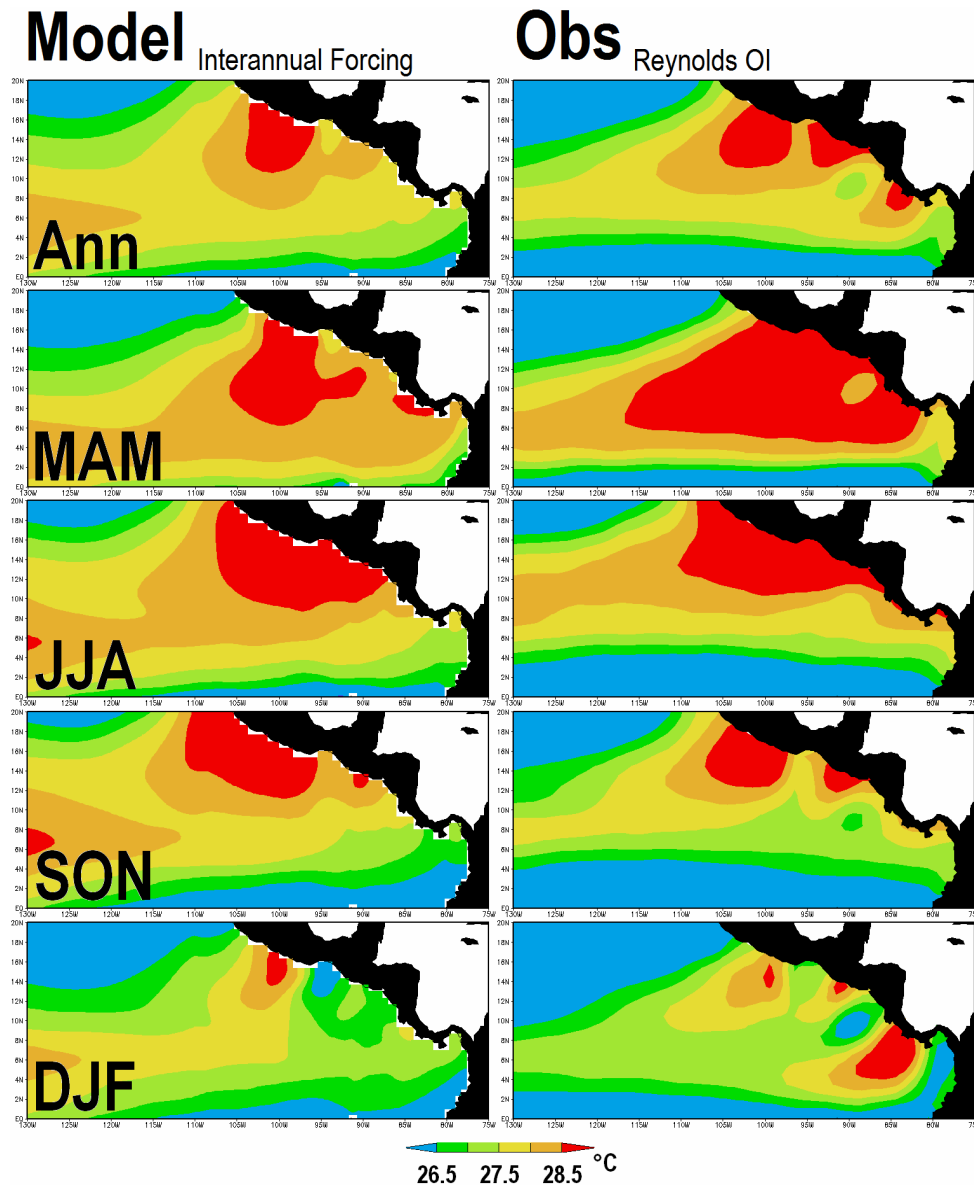
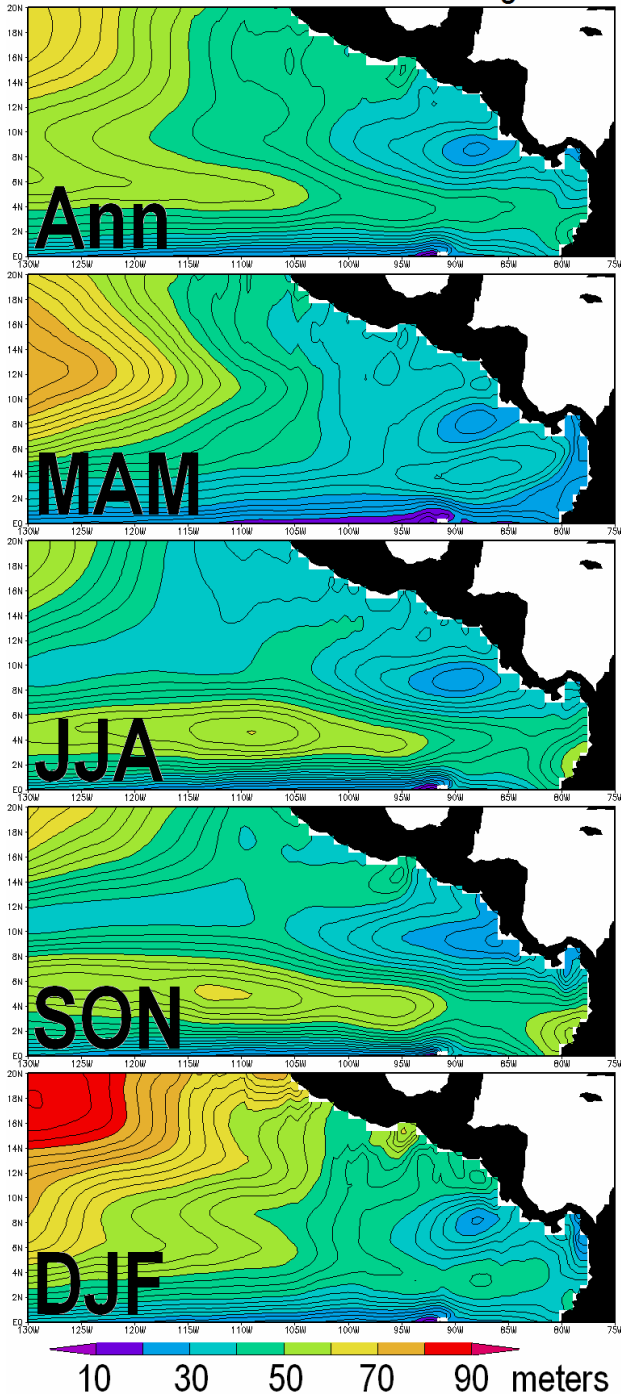


Figure 2.3. Mean (1988-2004) annual, March-May, June-August, September-November, and December-February SST ($^{\circ}\text{C}$) in the northeastern tropical Pacific Ocean from the *control* experiment (left column) and Reynolds OI v.2 SST (right column).

Shown in Figure 2.4 is the climatological mean mixed layer depth (MLD) in the northeastern tropical Pacific Ocean from the *control* experiment. MLD ranges from 25 m in the Costa Rica Dome to 95m toward the north central Pacific Ocean. Comparing the annual mean MLD in the *control* experiment with a similar depiction (of thermocline depth) from observational data compiled by Fiedler (2002a), there is remarkable qualitative similarity. Fiedler defines the thermocline depth as the depth of the 20°C isotherm; his meridional temperature section (not shown) confirms that is a good approximation, i.e., the 20°C isotherm coincides with the maximum vertical temperature gradient. In the *control* experiment, the thermocline and 20°C isotherm do not quite coincide. However, the maximum vertical temperature gradient in the *control* experiment is found at 37 m. Thus, the annual mean thermocline depth in the *control* experiment is within 2 m of Fiedler's. The larger-scale features of the subsurface structure are also similar, including the existence of the countercurrent thermocline ridge, the equatorial thermocline ridge, and an elongated thermocline trough wedged in between along $4-5^{\circ}\text{N}$. The seasonal evolution of the Costa Rica Dome, and associated biological activity, were the main foci of Fiedler (2002a). In the *control* experiment, the Costa Rica Dome does exhibit marked seasonality in its shape and perceived genesis mechanisms, which is highly consistent with Fiedler's description.

Model Interannual Forcing



Obs Fiedler (2002)

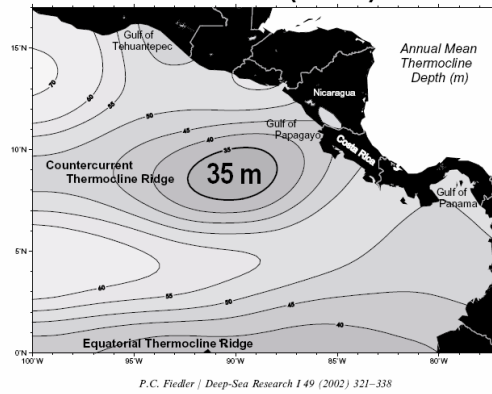


Figure 2.4. Mean (1988-2004) annual, March-May, June-August, September-November, and December-February mixed layer depth (m) in the northeastern tropical Pacific Ocean from the *control* experiment (left column). Shown to the right is the depiction of the subsurface thermal structure (thermocline depth; m) from Fiedler (2002a).

Finally, we examine the scales and relative importance of the major terms in the ocean mixed layer heat budget. Reliable observed estimates of heat budget terms in the northeastern tropical Pacific Ocean are a rare commodity. To produce a fair comparison between the *control* experiment and *in situ* observations from TAO moorings, we examine the *total* heat budget terms for the years for which necessary TAO estimates are available. This method avoids problems inherent to calculating climatologies and anomalies over short periods of time. The TAO moorings within the EPWP are stationed at 8°N, 10°N, and 12°N latitude along 95°W longitude. For those moorings, reliable data are available from 2000 to 2003. Therefore, heat budget terms from those three TAO moorings were averaged together, and heat budget terms from the *control* experiment at gridpoints corresponding with the locations of those three TAO moorings were averaged together. The result, shown in Figure 2.5, is a depiction of the mixed layer heat budget from TAO estimates and the *control* experiment, representing a meridionally-oriented line through the EPWP. For calculating turbulent heat flux estimates (sensible and latent) from TAO data, the same coefficients were used as those specified in the model code. An overview of all heat budget equations, including parameters and coefficients, used for observed estimates and model calculations is provided in Appendix A.

As evident in both the TAO estimates and calculations from the *control* experiment (Figure 2.5), the first order balance of mixed layer temperature in the EPWP is between the atmosphere-ocean heat flux by shortwave radiation ($\sim 225 \text{ W m}^{-2}$), and ocean-atmosphere latent heat flux ($\sim 100 \text{ W m}^{-2}$) and longwave radiation ($\sim 60 \text{ W m}^{-2}$). The seasonal cycle of SST tendency in the EPWP (Figure 2.5, heavy black line) is largely dominated by that of shortwave radiation (the amplitude of the seasonal cycle is $\sim 100 \text{ W m}^{-2}$). The sum of the advective heat fluxes (zonal advection, meridional advection, and vertical entrainment-mixing) is also shown in Figure 2.5 (right panel). The advective heat fluxes are generally very small and negative, approximately of the same order of magnitude as sensible heat fluxes ($\sim 10 \text{ W m}^{-2}$).

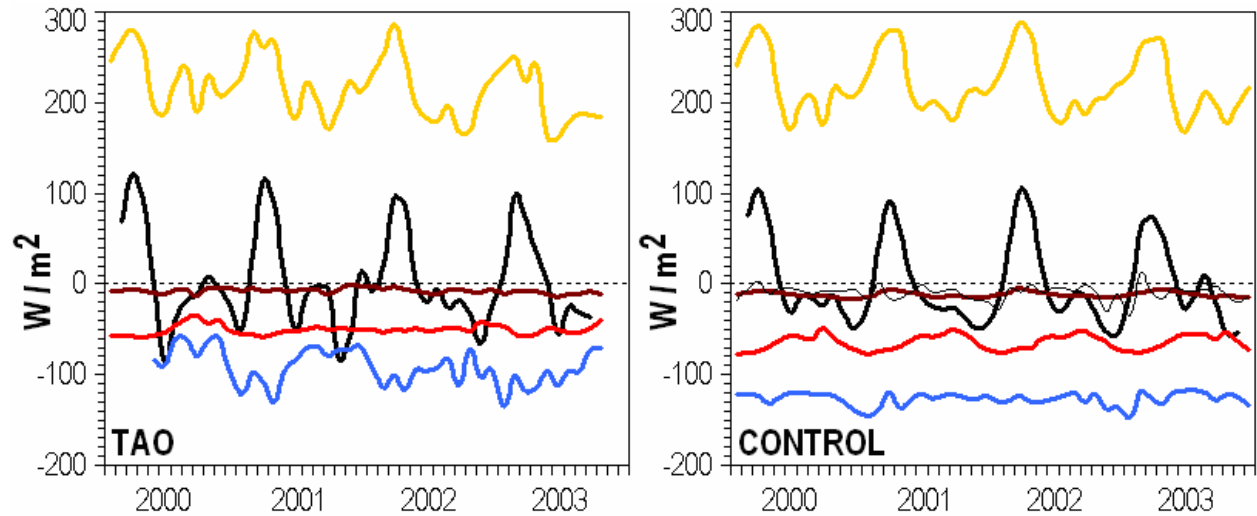


Figure 2.5. Monthly mixed layer heat budget at 95°W , $8\text{-}12^{\circ}\text{N}$ from 2000 through 2003 as estimated from TAO observations (left) and the *control* experiment (right). Q_{SW} in orange, $\partial T/\partial t$ in heavy black, Q_{SH} in brown, Q_{LW} in red, Q_{LH} in blue, and sum of Q_{ZA} , Q_{MA} , and Q_{EMX} in thin black (right panel only). All heat fluxes are in units W m^{-2} except SST tendency, which is $^{\circ}\text{C month}^{-1}$ multiplied by a factor of 100 for clarity.

Overall, the comparison between the TAO fluxes and those computed from the *control* experiment is in good agreement. The only major disagreement is in latent heat flux (Q_{LH}), in which the model appears to have a high mean bias and muted variability. However, extensive diagnostic effort has confirmed that this is due to a necessary model parameter that limits the minimum wind speed to 5 m s^{-1} . That the first-order balance is between shortwave radiation versus latent and longwave heat flux, and that the large seasonal amplitude is dominated by shortwave radiation, is indicative that the model-simulated mixed layer is consistent with first physical principles. Together with the validation of SST and MLD shown above, it is clear that the *control* experiment is potentially useful for understanding the interannual variability of SST in the EPWP.

2.2.3. Process experiments

2.2.3.1. Large-scale forcing

To isolate the relative roles of momentum, heat, and freshwater flux forcing on the interannual variability of SST in the EPWP, three process experiments related to the interannually varying forcing were performed. In this very simple experimental setup, one type of forcing was held to climatology while the rest were interannually varying as in the *control* experiment. The experiment *clim-winds* is the same as *control* except wind stress forcing was held to climatology. The experiment *clim-solar* is the same as *control* except surface downward shortwave radiation was held to climatology. The experiment *clim-rain* is the same as *control* except precipitation was held to climatology. In this manner, differences between *control* and *clim-“forcing X”* can be interpreted as the effect of the interannual variability of “forcing X” on the ocean, plus nonlinear effects. Integration of each process experiment began with the same initial conditions as *control*.

2.2.3.2. Gap winds

The objective of Section 2.5.3 is to quantify and understand what effect the Tehuantepec and Papagayo gap winds have on the interannual variability of sea surface temperature. In addition to the *control* experiment described in previous subsections, we conduct three additional experiments, nearly identical to *control*, except that we first remove from the wind stress the Tehuantepec gap winds (*smooth-teh*), the Papagayo gap winds (*smooth-pap*), and both the Tehuantepec and Papagayo gap winds (*smooth-gaps*). The objective is to remove primarily the interannual variability of the gap winds while leaving the larger-scale atmospheric flow unchanged.

The following explanation of the technique used to remove the gap winds from the wind stress forcing refers to Figure 2.6. For Tehuantepec, the algorithm is as follows:

- If τ_y at any point in box T1 $< -0.66 \text{ dyn cm}^{-2}$ ($1 \text{ dyn cm}^{-2} = 0.1 \text{ N m}^{-2}$), then change τ_x and τ_y in box T1 to climatology.
- If τ_y at the black dot in box T2 < 0 , then reduce τ_x and τ_y in T2 by half.

- Taper linearly around the edges of the boxes for smooth continuity with surrounding wind stress values.

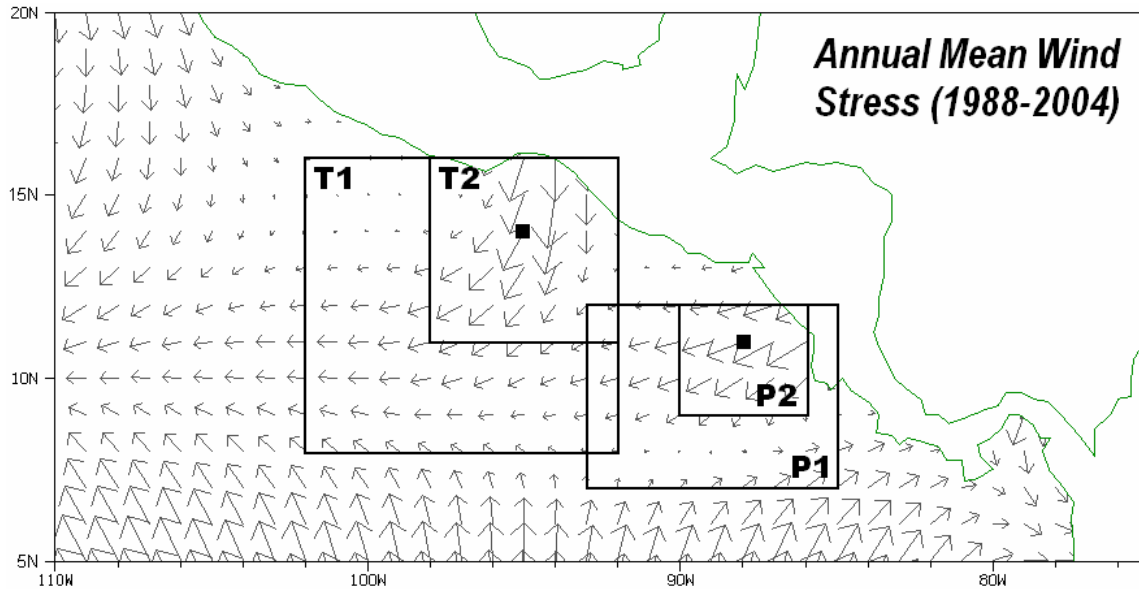


Figure 2.6. Annual mean SSM/I-QuickSCAT wind stress for the period 1988-2004 in the east Pacific warm pool region. Boxes and black dots are referred to in the discussion of the algorithms for removal of the Tehuantepec and Papagayo gap winds.

The algorithm for removal of the Papagayo gap winds from the wind stress forcing is similar, but requires use of wind stress magnitude, since the Papagayo gap winds usually have equally strong zonal and meridional components:

- If the magnitude of τ at any point in box P2 $> 0.60 \text{ dyn cm}^{-2}$, and the direction of τ at the dot in box P2 is northeasterly, then change τ_x and τ_y in box P1 to climatology.
- If the direction of τ at the dot in P2 is northeasterly, then reduce τ_x and τ_y in P2 by half.
- Taper linearly around the edges of the boxes for smooth continuity with surrounding wind stress values.

The first EOF of total wind stress in a domain restricted to the northeastern tropical Pacific ($105\text{-}82^\circ\text{W}$ by $8\text{-}17^\circ\text{N}$) were computed to show the change in the structure and variability of the wind stress field due to the gap winds removal. Shown in Figure 2.7 are the differences in

wind stress vector EOF between *control* minus *smooth-teh* (left) and *control* minus *smooth-pap* (right). Thus, the vectors effectively show what was removed from the *control* experiment.

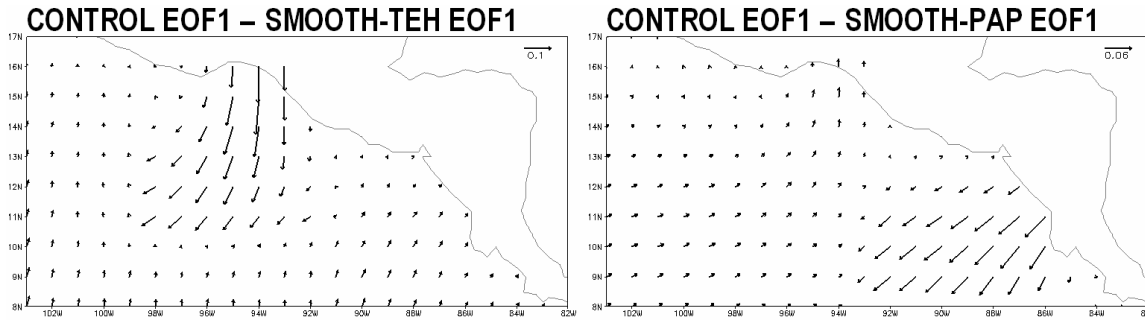


Figure 2.7. Difference of the leading pattern of weekly wind stress (total) in the east Pacific warm pool region (EOF analysis performed on domain shown) between *control* minus *smooth-teh* (left), and that between *control* minus *smooth-pap* (right).

When compared with the known structure of the gap winds (e.g., Figure 2.6), it is clear from Figure 2.7 that the gap winds removal algorithm was effective. Similarly, it is desirable to know the change in the variability of the wind stress field due to the gap winds removal. To do so, we compute the weekly τ_x and τ_y anomalies, from which we compute the standard deviation. Shown in Figure 2.8 are the differences between the standard deviation of τ_x and τ_y for *control* minus *smooth-teh* and *control* minus *smooth-pap*. The x-component of the vectors represent the difference in τ_x standard deviation, and the y-component of the vectors represent the difference in τ_y standard deviation. Again, by this sense, the vectors show how much variability, and where, was removed from the *control* experiment. It is clear that the gap winds removal technique was effective at removing the interannual variability of the gap winds, without serious contamination of wind stress outside the general region of the individual gap winds.

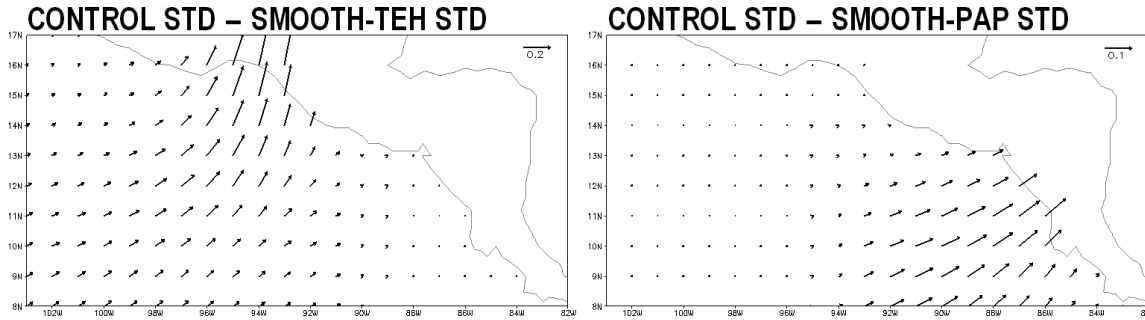


Figure 2.8 Difference in the standard deviation of weekly zonal and meridional wind stress anomalies in the east Pacific warm pool region between *control* minus *smooth-teh* (left) and *control* minus *smooth-pap* (right). The x-component of the vectors indicate the difference in STD of zonal wind stress, and the y-component of the vectors indicate the difference in the STD of meridional wind stress.

A final necessary check on the methodology used to remove the gap winds is to ensure that the modified wind stress fields do not artificially modify important derivative fields in areas that the gap winds in reality do not influence (e.g., the perimeter of the “boxes” within which wind stress was changed as described in the gap winds removal algorithms). This would result in differences in the ocean model experiments that could not realistically be due to the gap winds. Wind stress curl imparts an important influence on the sea surface that modifies the three-dimensional circulation and, consequently, the spatial distribution of heat on scales large and small. Shown in Figure 2.9, are the annual mean (1988-2004) wind stress curl in the northeastern tropical Pacific region for experiments *control*, *smooth-teh*, and *smooth-pap*. The distribution of curl in the *control* experiment is as would be expected in the presence of two strong wind jets- positive-negative couplets straddling the major axes of the Tehuantepec and Papagayo gap wind jets. The curl associated with the Panama gap wind jet is also evident in Figure 2.9 (not discussed further).

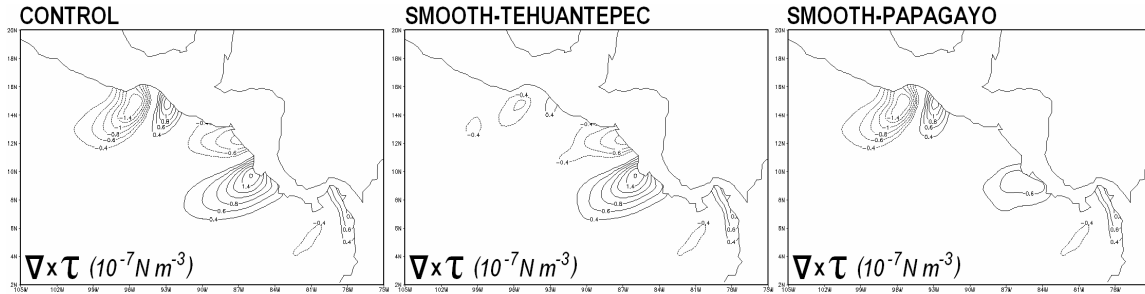


Figure 2.9. Annual mean wind stress curl (10^{-7} N m^{-3}) in the east Pacific warm pool region for experiments *control* (left), *smooth-teh* (center), and *smooth-pap* (right). Contour interval is $0.2 \cdot 10^{-7} \text{ N m}^{-3}$ beginning with $\pm 0.4 \cdot 10^{-7} \text{ N m}^{-3}$.

In the map of wind stress curl for *smooth-teh* (Figure 2.9, center), very little curl remains in the vicinity of the Tehuantepec gap wind region, while the Papagayo region is unchanged. In the *smooth-pap* map (Figure 2.9, right), the Tehuantepec region is unchanged, however, there remains a patch of positive wind stress curl that was not removed. This is an important point—that not *all* of the wind stress curl in the *control* experiment (Figure 2.9, left) was due to the Papagayo gap winds. Examining the annual mean wind stress map (Figure 2.6), there are also strong southwesterly winds flowing from the equatorial Pacific, which diminish rather abruptly near 7°N . This feature of the larger scale flow imparts a patch of positive wind stress curl apparently very similar in structure to that imparted by the Papagayo gap winds, which is not removed by the gap winds removal algorithm. This is a desirable result, and is useful to the discussion of the Costa Rica Dome (to follow).

2.2.4. Other major datasets

To complement the analysis of the aforementioned ocean model experiments, numerous observation-based and reanalysis datasets are utilized. Oceanographic datasets used include SST from the NOAA-Reynolds Optimal Interpolation version 2 (OI v.2; Reynolds et al. 2002) and the TRMM Microwave Imager (TMI; Kummerow et al. 2000), surface ocean Chlorophyll-*a*

concentration from the Sea-viewing Wide Field-of-view Sensor (SeaWiFS; McClain et al. 1998), surface and subsurface data from Tropical Atmosphere Ocean (TAO) moorings (Hayes et al. 1991) and the Simple Ocean Data Analysis (SODA; Carton et al. 2000), and sea level measurements from the TOPEX altimeter (Fu et al. 1994).

Atmospheric datasets used in Chapter 2 include the NCEP global reanalysis (Kalnay et al. 1996), the North American Regional Reanalysis (NARR; Messinger et al. 2006), CPC Merged Analysis of Precipitation (CMAP; Xie and Arkin 1997), and NOAA interpolated outgoing longwave radiation (OLR; Liebmann and Smith 1996).

2.3. Observed and Simulated Interannual Variability of SST in the East Pacific Warm Pool

The purpose of Chapter 2 is to understand what governs the interannual variability of SST in the eastern tropical Pacific Ocean. The present and following sections of Chapter 2 are dedicated to understanding what processes govern the interannual variability of SST in the east Pacific warm pool. Being in very close proximity to the eastern equatorial Pacific- the primary center of action for ENSO, the interannual variability of the east Pacific warm pool cannot easily be separated from the tremendous influence of ENSO. Thus, to truly trace the roots of interannual variability in the east Pacific warm pool, one must understand the factors that influence ENSO. However, it is not the objective of this dissertation to “explain” ENSO. The topic of ENSO dynamics is extremely vast, as evidenced by the body of literature on the topic; at times it seems it is hard to say that any one theory is right, yet none are wrong. Rather, Chapter 2 is organized to address the following questions: (1) How does one describe the interannual variability of SST in the EPWP, including the interrelationship with ENSO? (2) What are the mechanisms giving rise to the interannual variability of SST in the east Pacific warm pool? If it is being driven “remotely” by ENSO, how is such variability in the surface ocean *communicated* between the equatorial system and the east Pacific warm pool? (3) What is the role of the low-

level wind jets flowing through neighboring Central America and Mexico (i.e., the infamous Tehuantepec and Papagayo gap winds)? Is that a line of communication between the equatorial Pacific Ocean and the east Pacific warm pool (or, more generally, what are the remote forcing mechanisms for the low-frequency variability of the gap winds- a high-frequency phenomenon by nature)?

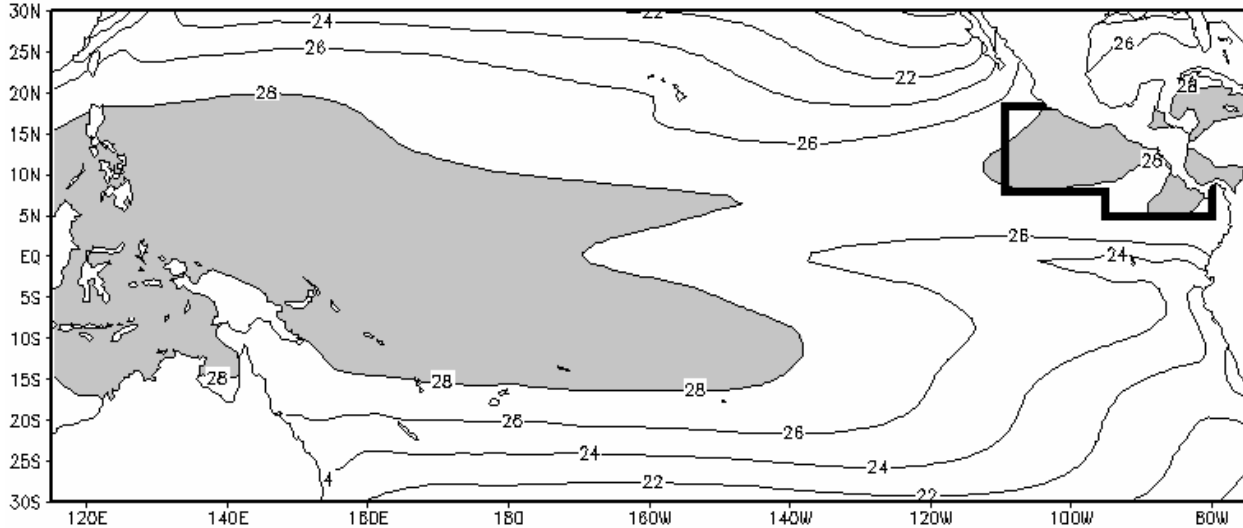


Figure 2.10. Map of annual mean SST in the tropical Pacific ($^{\circ}\text{C}$) for the period 1982-2006 (Reynolds OI v.2). The box represents the region used for constructing an index of area-averaged SST anomaly in the east Pacific warm pool (“EPWP”). The box is bounded to the west at 110°W , to the east at 80°W and the coast of Mexico-Central America, to the north at 18°N and the coast of Mexico-Central America, and to the south at 8°N west of 95°W and 5°N east of 95°W .

The primary objective of the present section is to characterize the interannual variability of SST in the east Pacific warm pool, mainly for the purposes of quantifying, in terms of SST covariability, the interrelationship between the east Pacific warm pool and ENSO, and to make an assessment of the model control simulation of the east Pacific warm pool. Similar to previous chapters, we define an index of area-averaged SST anomaly that corresponds to the annual mean position of the east Pacific warm pool (informally defined by the 28°C SST isotherm). Shown in Figure 2.10 is a map of annual mean SST in the tropical Pacific Ocean (Reynolds OI

v.2), with a box outlining the region used for constructing an index of area-averaged SST anomaly in the east Pacific warm pool. The index is hereafter referred to as EPWP.

Shown in Figure 2.11 (top panel) is the time evolution of SST anomaly in the EPWP and NINO3 from geostationary satellite observations. After a subtle smoothing (3-months) is applied, the interannual variability of SST in the EPWP and NINO3 are a close match; the correlation is 0.79. There are three large (high amplitude) ENSO events in the period shown (1982-83, 1987, and 1997-98), as manifested in SSTA in the NINO3 region. In each of those three cases, the SST anomaly in the EPWP corresponded very closely to that of the equatorial Pacific, if not lagging by a month or so. The early-mid 1990's and the 2000's were relatively devoid of notable ENSO events, yet the SST anomaly time series shown in Figure 2.11 still show many similarities during those inactive periods.

The cross-correlation of the unsmoothed indices is shown in Figure 2.12 (left panel). The maximum correlation is found when the EPWP lags NINO3 by 1 ($r_t = 0.76$) and 2 ($r_t = 0.75$) months. Also shown in Figure 2.12 are the autocorrelations of the indices themselves; NINO3 decorrelates by 6-7 months, while the NINO3-EPWP cross-correlation remains higher than e^{-1} until 9 months. The EPWP index itself decorrelates faster than does NINO3 in the first few months, but does not decay beyond e^{-1} until 7 months, similar to NINO3. Furthermore, there is a full four-month period where the EPWP remains positively correlated with NINO3 but NINO3 itself has become anticorrelated (lag months 10-13, inclusive). This is evident in the right panel of Figure 2.12, which indicates that the EPWP is more highly correlated with the NINO3 index than the NINO3 index is with itself for a full 16 month period beginning 4 months following a peak NINO3 anomaly. With the understanding that NINO3 variance tends to peak in December, this period would tend to begin with the calendar month of April. This raises an intriguing question: if ENSO is correlated with precipitation or tropospheric circulation over neighboring Central America, especially with a lag of one season, how much of a role does the EPWP play in that connection? This observation of delayed retention of SST anomaly by the

EPWP is very important, and will be revisited in the context of Central American-Southern Mexican hydroclimate in Chapter 4.

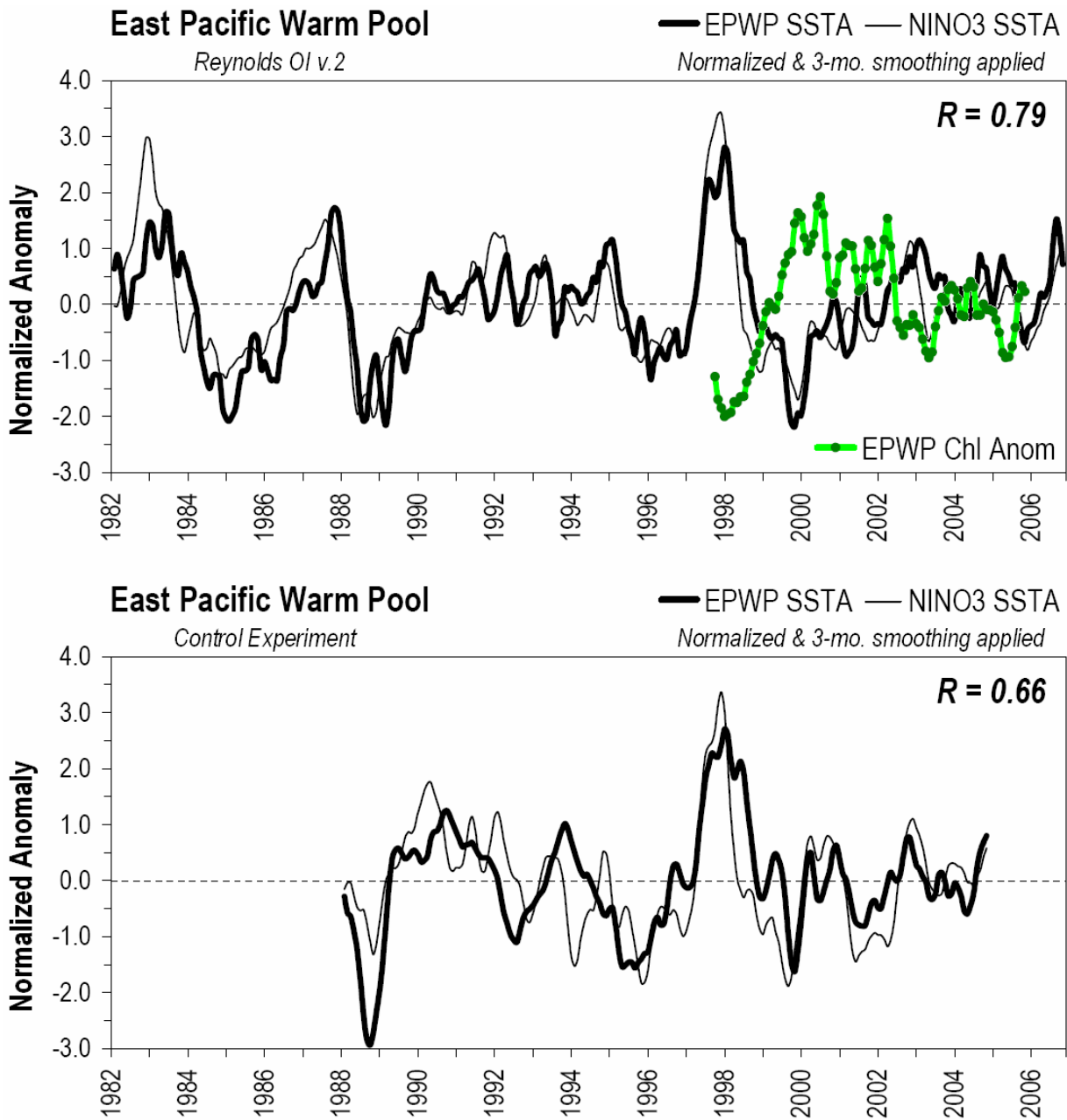


Figure 2.11. Top: Observed (Reynolds OI v.2) monthly mean SST anomaly in the EPWP (heavy black line) and the NINO3 region (thin black line), and the monthly mean Chlorophyll-*a* concentration anomaly in the EPWP. Bottom: Simulated (control experiment) monthly mean SST anomaly in the EPWP (heavy black line) and NINO3 (thin black line). All time series normalized and smoothed with a 3-month centered moving mean.

Also shown in Figure 2.11 (top panel) is the coincident time series of surface Chlorophyll-*a* anomalies in the EPWP. Although the satellite record of high-resolution ocean color is relatively short compared to, e.g., Reynolds OI v.2 SST, it is clear that whatever processes are responsible for interannual variations in SST in the EPWP are the same or related to those responsible for interannual variations in surface Chlorophyll concentration. The amount of small biota in the surface ocean, as manifest in Chlorophyll concentration, is of great importance to regional and global ecosystem productivity because it comprises the base of the food chain. Regionally, this is particularly important in the EPWP as the Costa Rica Dome (part of the EPWP) has long been a biological hotspot for ocean life (e.g., Fiedler 1994).

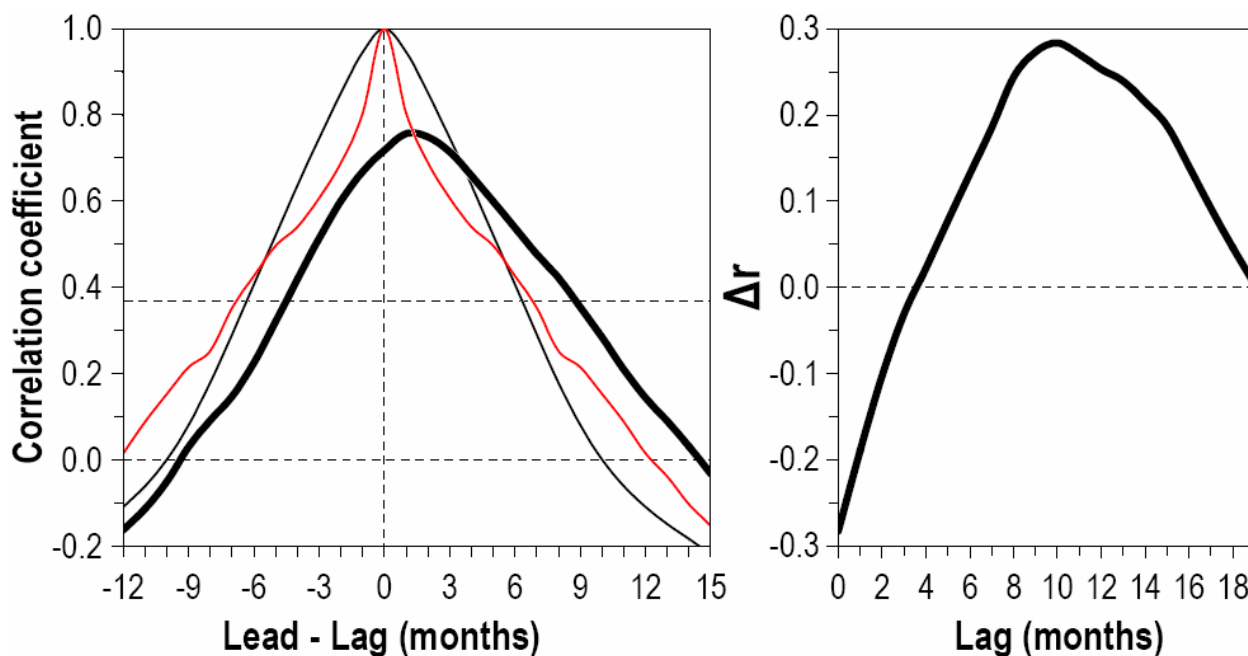


Figure 2.12. Left: Observed (Reynolds OI v.2) autocorrelation functions of the monthly unsmoothed NINO3 (thin solid black line) and EPWP (thin solid red line) indices, and cross-correlation between the monthly unsmoothed NINO3 and EPWP indices (heavy solid black line) from the period 1982-2006. Positive values on the x-axis are for the EPWP lagging NINO3. Right: Difference between the NINO3-EPWP cross-correlation and the NINO3 autocorrelation. Dashed lines mark zero months, zero correlation, and correlation = 0.367 (e^{-1} ; the e-folding decorrelation timescale).

Shown on the bottom panel of Figure 2.11 is the representation of SST in the EPWP and NINO3 region as in the top panel, but for the ocean model control simulation. Once again, there is a high correspondence between ENSO and SST in the east Pacific warm pool (correlation 0.66). Furthermore, by comparing the top and bottom panels of Figure 2.11, the simulated SST interannual variability is reasonably accurate (NINO3 correlation 0.72, EPWP correlation 0.64). Since all time series shown in Figure 2.11 are normalized, shown in Table 2.1 are the standard deviations by which they were normalized.

	$\sigma(\text{EPWP})$	$\sigma(\text{NINO3})$	$\sigma(\text{EPWP}) / \sigma(\text{NINO3})$
Reynolds OI v.2	0.33°C	0.94°C	0.35
<i>Control</i> experiment	0.25°C	0.48°C	0.52

Table 2.1. Comparison of the standard deviations (°C) of 3-month smoothed SSTA in the EPWP and NINO3 regions between observations (Reynolds OI v.2) and the *control* experiment (1988-2004).

The following section is dedicated to understanding, from a mechanistic point of view, what controls the interannual variability of SST in the EPWP. The comparison provided in Figure 2.11 instills some confidence that the mechanisms diagnosed with model results likely have strong rooting in nature. A final validation of SST anomaly from the control experiment is illustrated in Figure 2.13. Using the same reference period for climatology (1998-2004), there is strong similarity of the evolution of SST in the EPWP between the ocean model and the high-resolution satellite observations of TMI. There will inevitably be differences between models and observations, in this case possibly due to differences in spatial resolution, and an observational source that is limited by rain contamination. Heavy rain contamination can be especially troublesome in a region like the eastern tropical Pacific, as the boreal summertime ITCZ is roughly collocated with the EPWP, and stratus decks are prevalent in other seasons.

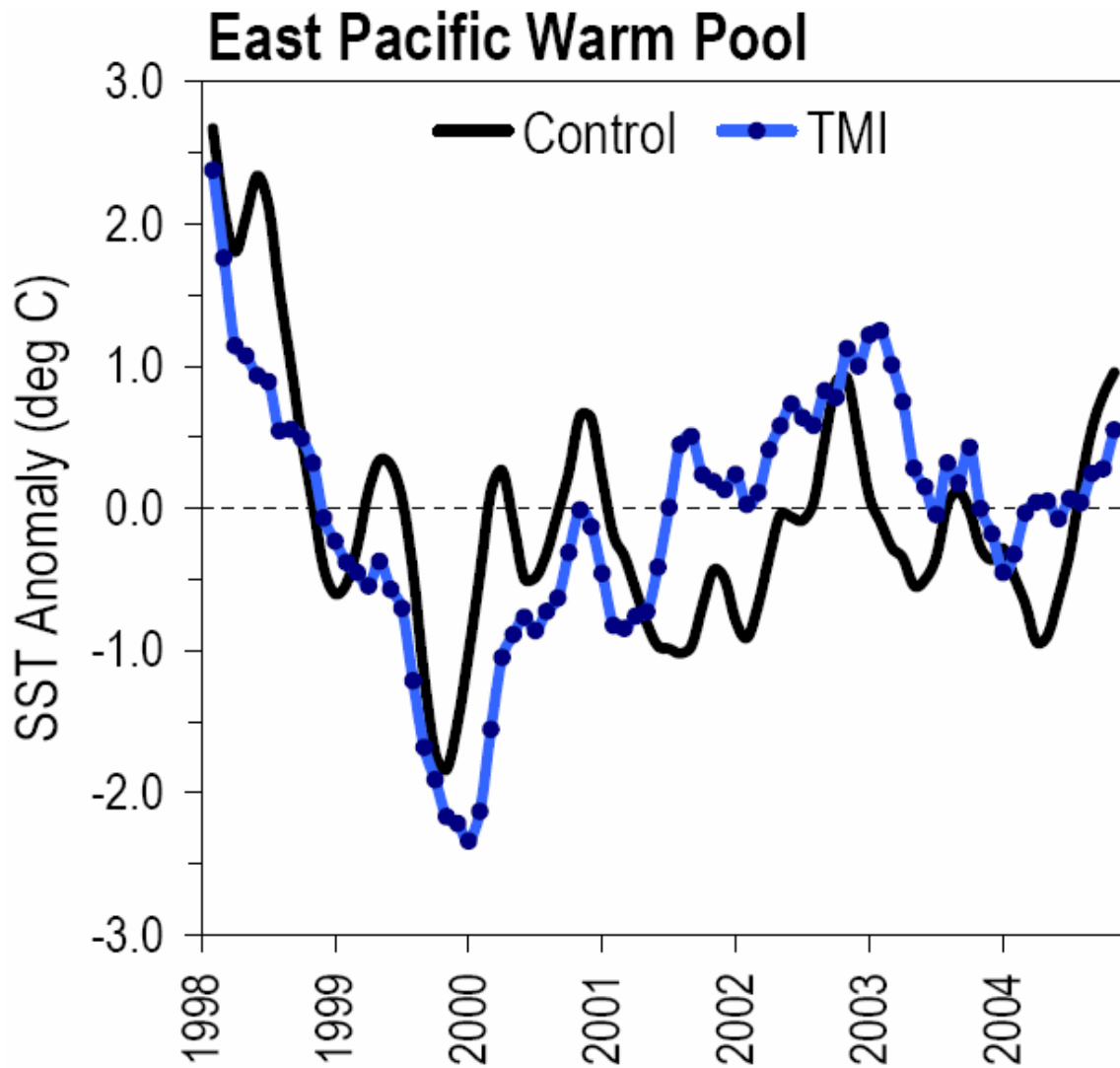


Figure 2.13. Monthly mean SST anomaly ($^{\circ}\text{C}$) in the EPWP from the ocean model control experiment (black line) and TMI observations (blue line). The same reference period for climatology was used in the calculation of anomalies for both time series. All time series normalized and smoothed with a 3-month centered moving mean.

Finally, interannual comparisons with *in situ* SST observations cannot be made due to the extremely short records from the 95°W TAO line (Figure 2.14), and the fact that the next closest TAO mooring is located at $8^{\circ}\text{N}, 120^{\circ}\text{W}$, i.e., the southwestern limit of the EPWP domain as defined above.

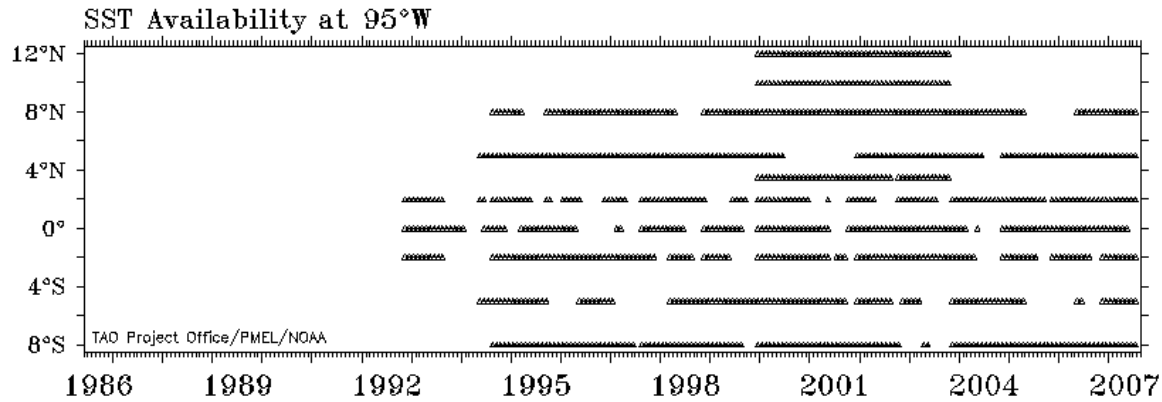


Figure 2.14. Time profile of data sampling from all moorings on the 95°W TAO line. The only two moorings that would be helpful in interannual analyses of the EPWP are 10°N and 12°N, which have only collected < 4 years of observations.

2.4. Mechanisms governing the interannual variability of SST in the east Pacific warm pool

2.4.1. The role of momentum, heat, and freshwater fluxes in SST interannual variability

The purpose of section 2.4 is to diagnose and discuss the mechanisms for the interannual variability of sea surface temperatures in the EPWP. The previous section characterized the interannual variability of SST in the east Pacific warm pool from the perspective of observations and model simulations. From both perspectives, and to a large extent, the interannual variability of SST in the EPWP follows closely that of the eastern equatorial Pacific Ocean. This leads to the inference that much of the interannual variability of the EPWP is driven by ENSO. Therefore, the present discussion of mechanisms for interannual variability of EPWP SST is necessarily focused on the mechanisms for ENSO influencing the EPWP. If ENSO forces the EPWP, what is the method by which the ENSO signal is communicated to SST in the EPWP? As noted in the introductory chapters, the EPWP is a warm pool situated within a relatively shallow background thermocline (the eastern tropical Pacific Ocean). The eastern tropical Pacific Ocean, including to the north and south of the equator, is also a region where strong ocean-

atmosphere coupling has been noted (Xie et al. 2005), and where coupled models show serious deficiencies (Mechoso et al. 1995, Collier et al. 2004). It is not clear whether the line of communication between the equator (ENSO) and the EPWP would be provided by ocean dynamics operating *between* the equator and the EPWP, such as equatorially forced waves propagating through the EPWP region, ENSO's modulation of the broader eastern equatorial thermocline (i.e., the canonical ENSO pattern) being broad enough to physically encompass the EPWP, poleward ocean heat transport, or by coupled ocean-atmosphere processes. The variability, remote forcing, and role of local effects on the EPWP, such as the gap wind jets flowing through neighboring Mexico and Central America, are discussed in Section 2.5.

To gain a first-order understanding of the role of the major types of forcing to the ocean (momentum, heat, and freshwater fluxes) on the interannual variability of the EPWP, four experiments were conducted, which were described in the methodology section of the present chapter. Figure 2.15 is meant to illustrate the amount of SST variability, basinwide, which is directly due to the interannual variability of each type of forcing, shown as differences of standard deviation between *control* minus *clim-flux*."

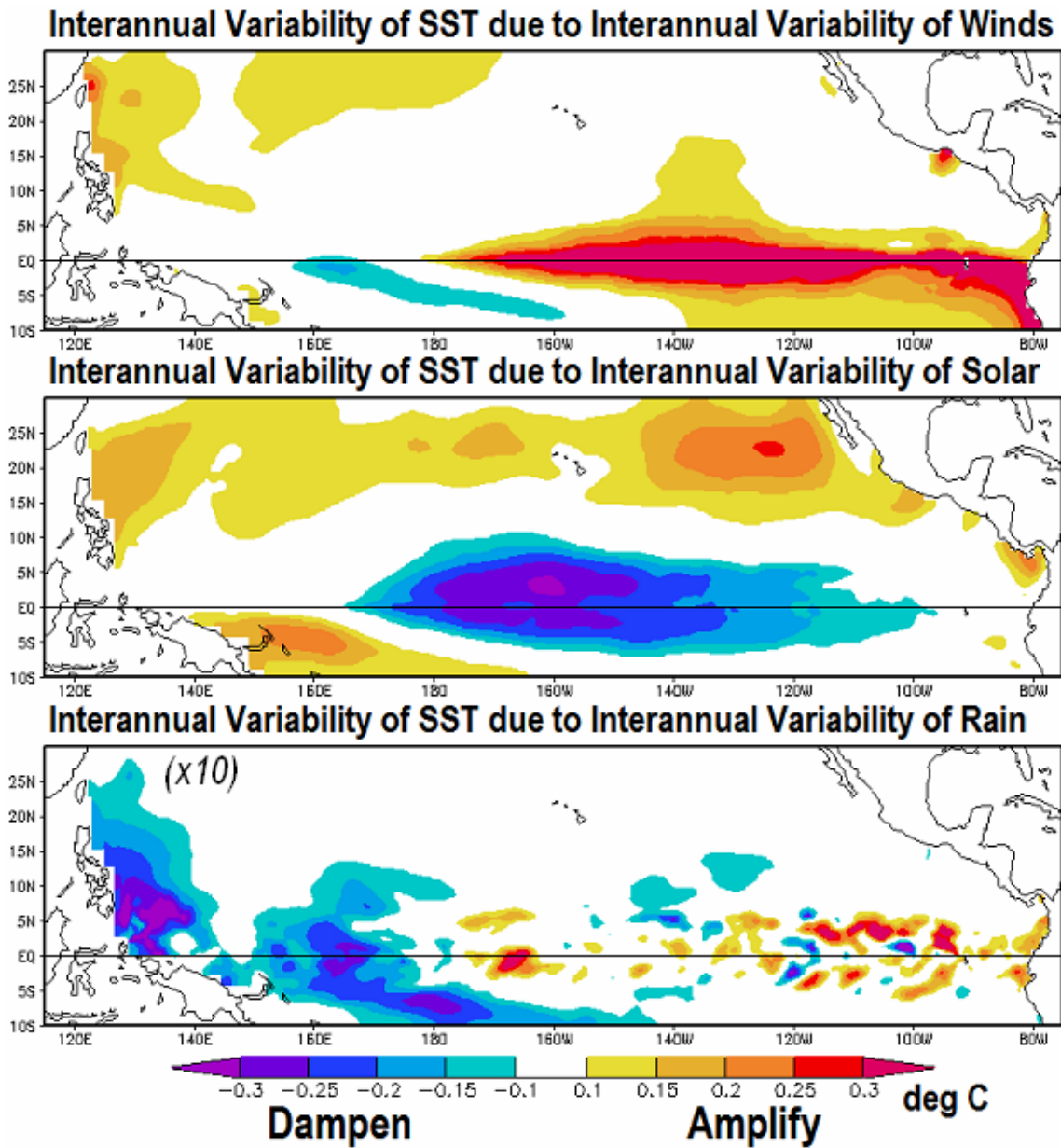


Figure 2.15. Difference in standard deviation of SST anomaly ($^{\circ}\text{C}$) between experiments *control* minus *clim-winds* (top), *control* minus *clim-solar* (middle), and *control* minus *clim-rain* (bottom). Values in the bottom panel are magnified by a factor of 10.

As expected, the result of the interannually varying wind forcing is high SST variability along the equator from the dateline to the coast of South America (Figure 2.15, top). This is the signal of the ocean response to ENSO, implying the winds are driving ENSO in our forced ocean model.

The equator responds with values of SST standard deviation up to 0.5°C . The SST variability amplification signal extends to the southern hemisphere (as far as can be determined by the model domain used), which is not apparent to the north of the equator, and the EPWP region. This is consistent with the well-documented notion that poleward ocean heat transport involved in the recharge-discharge cycle of ENSO is primarily to the south, but not to the north (e.g., Meinen 2005). Between 130°W - 140°W there is some evidence of poleward heat transport convergence north of the equator, but the majority of the signal is found south of the equator, east of 140°W (Figure 2.15, top). The only apparent effect of the interannually varying momentum forcing on the EPWP is amplified SST variability near the Gulf of Tehuantepec. The Tehuantepec and Papagayo gap winds are discussed in detail in the following section.

Shown in the middle panel of Figure 2.15 is the amount of SST variability due to interannually varying solar radiation (or surface shortwave radiation). In the central Pacific Ocean, surface shortwave radiation acts to damp interannual variability by up to 0.3°C . This can easily be explained within the context of the evolution of the coupled ocean-atmosphere system in an El Niño event: SST in the central equatorial Pacific warms, resulting in an eastward shift in the convective center normally situated over the western Pacific, resulting in greater cloud cover and reduced shortwave radiation reaching the surface. The reduction in shortwave radiation counteracts the warming and is thus a negative feedback to the warm SST anomaly. Over the model integration, this translates into reduced interannual variability of SST in the central equatorial Pacific Ocean. In the EPWP region, surface shortwave radiation appears to amplify SST variability except in the gap wind-influence regions (i.e., near the Gulfs of Tehuantepec and Papagayo). This provides a clue that shortwave forcing may be an important component in the interannual variability of the mixed layer heat budget, which is analyzed in the following subsection. Finally, the bottom panel of Figure 2.15 indicates that the interannually varying precipitation had negligible impact on SST. The largest values were approximately a 0.03°C damping of SST variability in the west Pacific warm pool, and up to 0.03°C amplification

of SST variability in the east-central equatorial Pacific. For the remainder of this chapter, the role of freshwater flux is not discussed in the context of SST interannual variability.

Shown in Figure 2.16 is a comparison between ENSO and the EPWP for the forced ocean model experiments: *control*, *clim-winds*, and *clim-solar* (*clim-rain* omitted). Compared with *control*, where all forcing is interannual, the correspondence between ENSO and the EPWP is reduced (correlation 0.29) when the winds are held to climatology (Figure 2.16, center). A closer look at the time series in Figure 2.16 (center) suggests that the main reason the correlation is reduced is that the absence of the 1997-98 El Niño event from the wind forcing had very different outcomes at the equator and the EPWP. As shown in Figure 2.15, momentum forcing (wind stress variability) results in an amplification of SST variability along the equator (since it is what drives the ocean model to exhibit ENSO variations), while shortwave radiation serves as a damping effect at the equator. Thus, the solar forcing contained the El Niño event, which served to reduce the SST as it would in nature, but the SST was not anomalously warm to begin with because the winds were climatological and thus did not force an El Niño event. Therefore, NINO3 in 1997-98 in the *clim-winds* experiment is cold. In contrast, the EPWP, even in the absence of an El Niño event at the equator, still exhibited a warm SST anomaly timed with the 1997-98 El Niño event. The fact that wind stress variability was not necessary for the EPWP to become anomalously warm during 1997-98- that the interannually varying surface shortwave radiation was enough- is again pointing to the need to investigate specifically the role of shortwave radiation in communicating the ENSO signal to the EPWP.

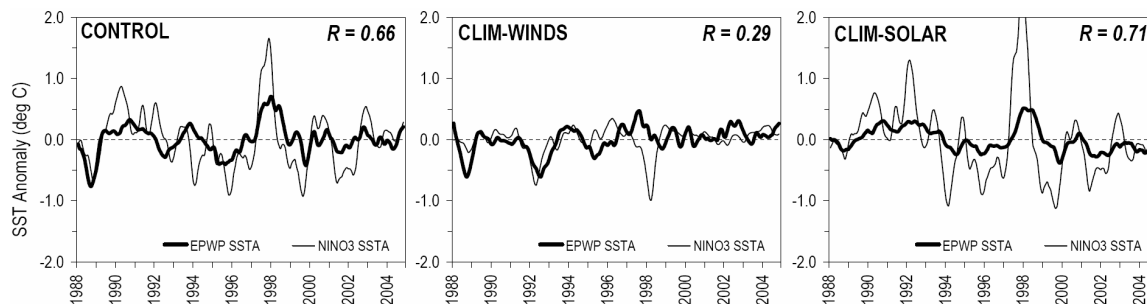


Figure 2.16. Time series of monthly SST anomaly (°C) at NINO3 (thin line) and the EPWP (bold line) in experiments *control* (left), *clim-winds* (center), and *clim-solar* (right). A 3-month smoothing was applied to all time series.

The right panel of Figure 2.16 indicates that the association between ENSO and the EPWP is actually strengthened when surface shortwave radiation is held to climatology. In the *absence* of the damping effect of shortwave radiation, ENSO's amplitude is allowed to grow unchecked and extend its reach northward into the EPWP using ocean phenomena alone. In the *clim-solar* experiment, ENSO, as driven by the winds, is played out unchecked by the damping effect of shortwave radiation. Thus, the ENSO variability is strongly amplified in *clim-solar* and the mechanism of communication for the ENSO signal to propagate to the EPWP can in fact be ocean dynamics, e.g., the canonical ENSO pattern, downwelling Kelvin waves, oceanic poleward heat transport, etc. Comparing the 1997-98 event in *control* to *clim-solar* (left and right panels of Figure 2.16), the warm anomaly in the EPWP shows slower growth and lags the equator in *clim-solar*, whereas in *control* the EPWP and NINO3 SSTA time series rise at the same time and grow at approximately the same rate. Put generally, in a world where shortwave radiation did not serve to damp equatorial SST anomalies, ocean dynamics alone may be enough to communicate the ENSO signal to the EPWP, but as will be shown in the heat budget calculations of the following subsection, this is not the case when all forcing is interannually varying.

Finally, to examine the overall effect of momentum versus solar forcing on the interannual variability of SST in the EPWP, Figure 2.17 shows the difference in SST anomaly between the *control* experiment and *clim-winds* (left) and *clim-solar* (right). By this sense, the value shown in the time series is the effect of that forcing. Again, the effect of the wind forcing is a lower frequency modulation of SSTA than that of surface shortwave radiation, which, as opposed to the equatorial Pacific, does not counteract one another. In the example of the 1997-98 El Niño event, the effect of the surface shortwave radiation is an earlier warming (the peak is

in mid-1997). The two EPWP time series displayed in Figure 2.17 represent the NW and SE halves of the EPWP index defined in the previous section (simply the previously defined EPWP index split along 95°W). The momentum and solar forcings affect both subregions similarly, which is interesting since the SE subregion is closer to the equator and the coast of South America; it would have not been surprising if the effect of the relative importance of momentum versus solar forcing was different than that of the NW subregion of the EPWP.

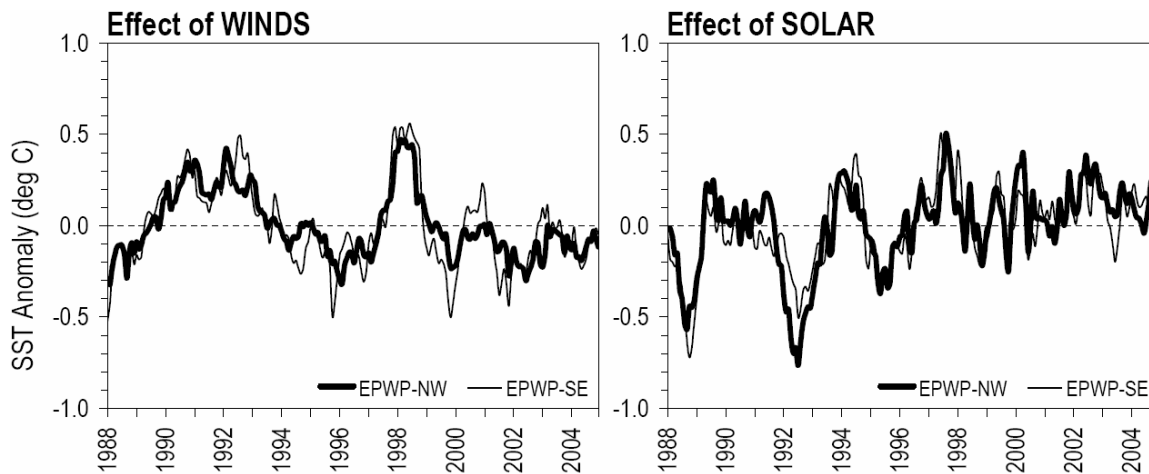


Figure 2.17. Difference in monthly unsmoothed SST anomaly ($^{\circ}\text{C}$) in the NW subregion of the EPWP (heavy line) and SE subregion of the EPWP (thin line) for experiments *control* minus *clim-winds* (left) and *control* minus *clim-solar* (right).

2.4.2. The role of advective versus surface fluxes from a complete interannual heat budget

The prior subsection discussed the overall effects of momentum, heat, and freshwater fluxes on SST. Such calculations were meant to provide a first-order impression of what processes might be important influences on the EPWP, and to help guide a more detailed heat budget calculation on the *control* experiment. The objective of this subsection is thus to present and discuss the results of calculations performed on the interannual variability of the mixed layer heat budget. As previously noted, the EPWP is unique in that it is situated within a relatively shallow background thermocline, as is a general characteristic of eastern portions of

ocean basins over which the tradewinds are generally easterly. As illustrated in Figure 2.18, the EPWP is actually dissimilar to its western Pacific counterpart, and more similar to the cold tongue, in terms of the importance of mixed layer processes on SST. In both the cold tongue and the EPWP, the mixed layer depth anomaly and SST anomaly is correlated ~ 0.5 or greater over the span of the *control* experiment. It should be noted that the spatial structure of the correlation appears strongly influenced by the existence of the Galápagos Islands on the equator. In the west Pacific warm pool, the surface mixed layer heat balance is generally thought to be dominated by surface heat flux, since the thermocline is so deep that subsurface processes are unlikely to make a difference in SST. Thus, mixed layer depth and SST anomaly show negligible correlation. In the cold tongue, where the thermocline is very shallow, it is almost entirely subsurface processes, including that imparted by equatorial waves, that govern SST variability. The key question surrounding the east Pacific warm pool is thus, in terms of SST interannual variability, is the EPWP analogous to the west Pacific warm pool, i.e., driven by surface fluxes, or the equatorial Pacific cold tongue, i.e., driven by the three-dimensional advective fluxes, especially vertical heat flux or entrainment-mixing?

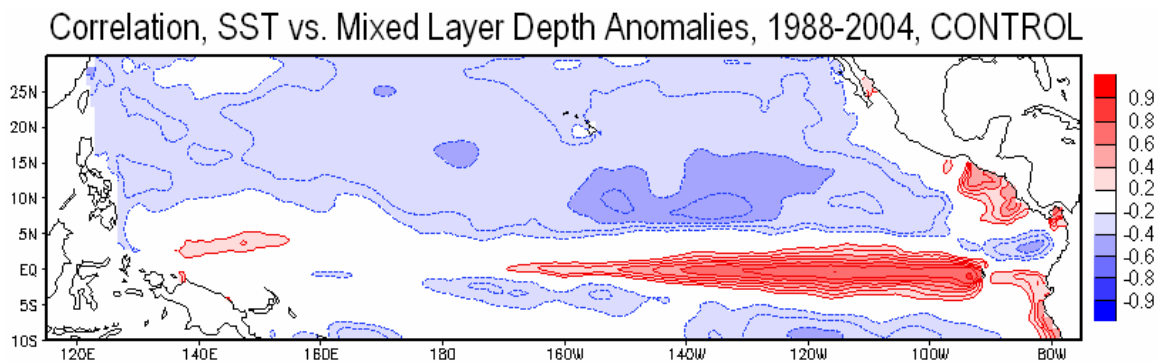


Figure 2.18. Linear correlation coefficient between weekly SST anomaly and mixed layer depth anomaly in the *control* experiment. Contour interval is 0.1, beginning with ± 0.2 . Color representation is indicated in the color bar to the right.

To simplify the portrayal of the heat budget terms, advective flux terms (i.e., zonal heat flux, meridional heat flux, and entrainment-mixing) have been combined to form the “advective sum,” and surface heat flux terms (i.e., shortwave radiation, longwave radiation, latent and sensible heat flux) were combined to form the “surface sum.” Thus, the surface sum includes both radiative and turbulent heat fluxes, which occur at the air-sea interface. The result of these calculations for the *control* forced ocean model experiment, as well as the equivalent heat flux $\partial T/\partial t$, is presented in Figure 2.19 (top). Our model results overwhelmingly suggest that the primary process by which surface ocean temperatures in the east Pacific warm pool change is through surface heat fluxes- not advective fluxes (which including entrainment-mixing). The correlation coefficient between the surface sum and $\partial T/\partial t$ time series is 0.88. The advective sum (anomaly) is in fact often of the opposite sign as $\partial T/\partial t$, meaning the surface heat fluxes are driving the SST anomaly, while the advective fluxes are at times slightly damping them. Discrepancies between $\partial T/\partial t$ and the surface sum are largely due to the advective sum.

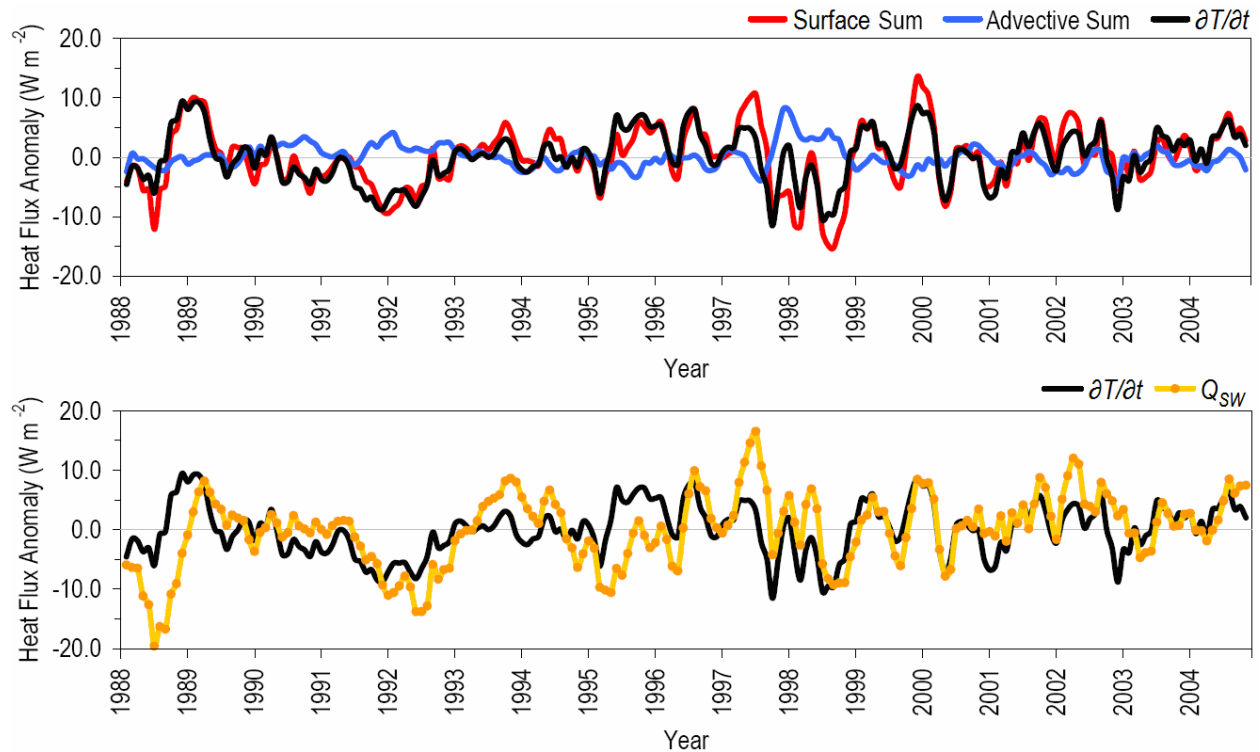


Figure 2.19. Top: time series of the sum of the surface heat fluxes (“Surface Sum,” W m^{-2} , red line; shortwave, longwave, latent, and sensible), the sum of the advective heat fluxes (“Advective Sum,” W m^{-2} , blue line; zonal heat flux, meridional heat flux, and entrainment-mixing), and $\partial T/\partial t$ (W m^{-2} , black line). Bottom: As in the top but for $\partial T/\partial t$ (black line) and the surface shortwave radiation heat flux term (“ Q_{SW} ,” W m^{-2} , orange line).

Of the terms grouped into the surface sum, the surface shortwave radiation has by far the largest amplitude and is the only one that displays correspondence with the $\partial T/\partial t$ time series (all other terms not shown). Shown in Figure 2.19 (bottom) is the evolution of the surface shortwave radiation Q_{SW} and $\partial T/\partial t$ indices for the EPWP over the *control* experiment. The correlation between the surface sum and the surface shortwave radiation time series is 0.70, and the correlation between the surface shortwave radiation and $\partial T/\partial t$ time series is 0.51. Of the dominant surface heat flux terms, shortwave radiation is the primary form of surface heat flux responsible for the evolution of the SST anomaly in the EPWP. This is in contrast to the equatorial region where shortwave radiation is a damping condition, or negative feedback, to SST anomalies.

The remaining surface heat flux terms (longwave and turbulent flux terms) tend to be of opposite sign and at times slightly offset the surface shortwave anomaly, with the exception that latent heat flux which, when high-frequency variability is filtered out, does appear to play a role in the mixed layer heat budget $\partial T/\partial t$. This is true in both the NW and SW subregions of the EPWP (Figure 2.20).

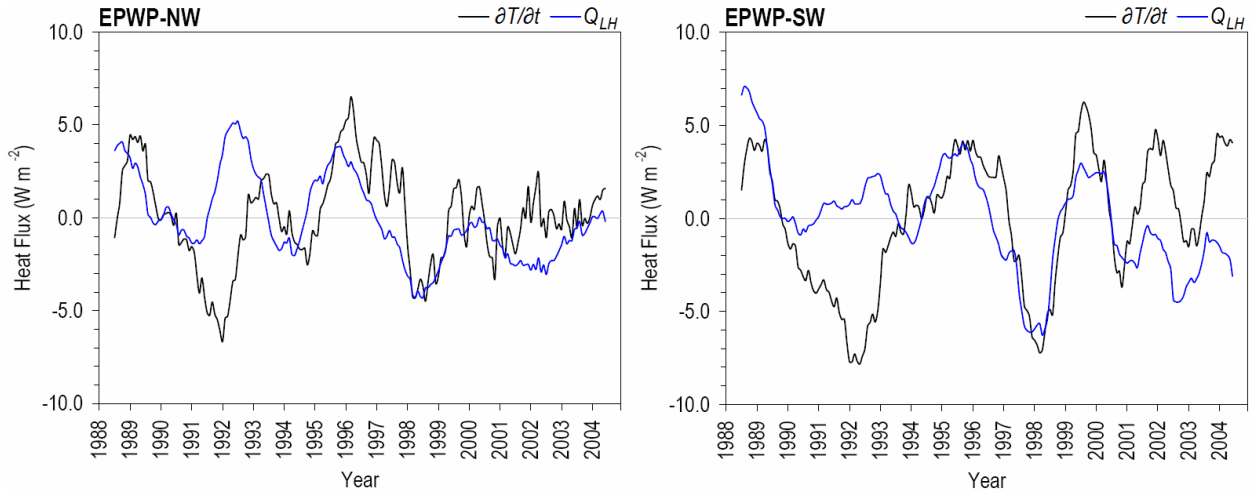


Figure 2.20. Time series of smoothed (12-month centered moving mean) $\partial T/\partial t$ anomaly (W m^{-2} , black line) and atmosphere-ocean Q_{LH} anomaly (W m^{-2} , blue line) for the NW (left) and SE (right) subregion of the EPWP.

The ocean-atmosphere latent heat flux (Q_{LH}) depends primarily on two factors: (1) wind speed (W) and (2) the moisture gradient at the air-sea interface (Δq). Q_{LH} increases with both (1) and (2). The magnitude of (2) depends on two factors: (2a) atmospheric specific humidity (q_a) and (2b) SST. Δq and thus Q_{LH} decreases with increasing q_a . By the Clausius-Clapeyron relation, the (saturation) specific humidity at the sea surface (q_s) increases with increasing SST, thus Δq increases with increasing q_s , and Q_{LH} increases with increasing SST. On the mean, Q_{LH} transfers energy from the ocean to the atmosphere everywhere over the global oceans. Only in very unusual cases is the transfer of energy via Q_{LH} from the atmosphere to the ocean. Ocean-atmosphere Q_{LH} is especially strong in the tropics, including the EPWP but excluding the equatorial Pacific cold tongue, where Q_{LH} is a relative minimum. According to TAO estimates, the annual mean ocean-atmosphere Q_{LH} over the EPWP is roughly 100 W m^{-2} .

Because of (2b) above, on short timescales, Q_{LH} acts as a negative feedback to SST and thus damps SST anomalies. However, as evident in Figure 2.20, on interannual and longer timescales, Q_{LH} contributes directly to SST variability in the EPWP. Q_{LH} in Figure 2.20 is shown

in terms of its heat flux contribution to the ocean mixed layer heat budget, thus positive anomalies indicate a positive *atmosphere-ocean* Q_{LH} anomaly (physically interpreted as a *reduced ocean-atmosphere* Q_{LH} anomaly). The fact that the Q_{LH} and $\partial T/\partial t$ time series are positively correlated indicates that the low-frequency Q_{LH} is not forced by the local SST (otherwise it would be anticorrelated as if trying to damp SST anomalies); rather, the low-frequency Q_{LH} is forcing a response in $\partial T/\partial t$. Therefore, the Q_{LH} variability must be due to variations in W and / or q_a .

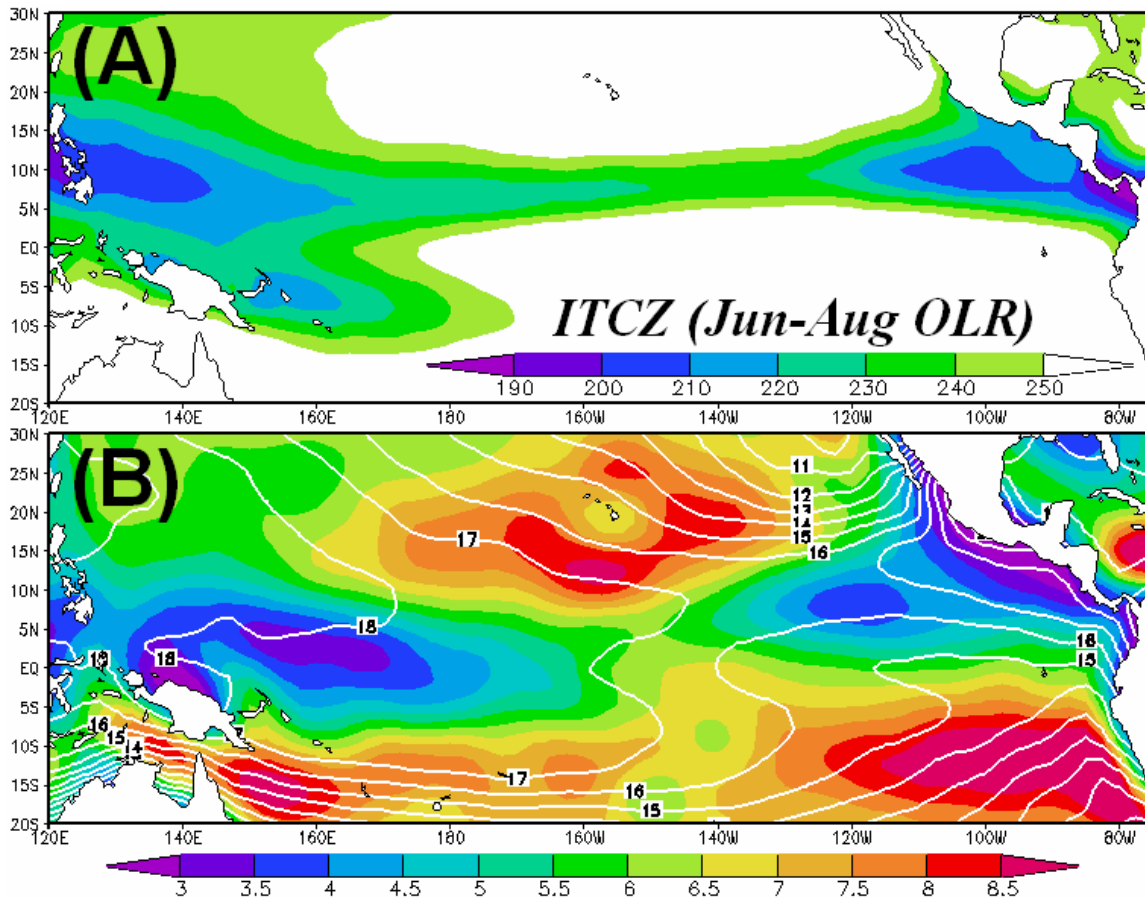


Figure 2.21. Top: Boreal summertime (June-August climatological mean) position of the ITCZ in terms of OLR ($W m^{-2}$). Bottom: 1000 hPa wind speed ($m s^{-1}$; shaded), and 1000 hPa specific humidity ($g kg^{-1}$; contoured). OLR from NOAA Interpolated OLR (AVHRR); W and q_a from NCEP-NCAR Reanalysis.

As previously noted, the EPWP lies directly beneath the ITCZ in the eastern tropical Pacific. This is because the ITCZ tends to situate itself directly over the warmest SSTs in the tropics, as they force large-scale ascent, convection, and provide a large supply of water vapor to the atmosphere (again, related to [2b] above). On the mean, the ITCZ is actually a region of minimum W and maximum q_a (Figure 2.21) which, based on 1 and 2a alone, is ideal for a *minimum* of ocean-atmosphere Q_{LH} . Low-frequency variations in the position of the ITCZ, along with its minimum W or maximum q_a , could thus modulate the Q_{LH} and drive a response in EPWP SST. Mechanisms for low-frequency modulation of the position of the ITCZ are revisited in Chapter 4 in the context of Central American rainfall variability. Another possible mechanism for low-frequency variability of Q_{LH} within the EPWP region is related to the Mexican-Central American gap winds. The fact that similar low-frequency Q_{LH} variability is seen in both the NW and SE subregions of the EPWP becomes relevant in section 2.5.3, where the impact of the Tehuantepec and Papagayo gap winds on various ocean mixed layer heat budget components are presented.

From the perspective of the mixed layer heat budget, it has been determined that the primary process governing the *interannual* variability of SST in the EPWP is surface shortwave radiation (Figure 2.19). However, as shown in the previous section, the time series of SST anomaly in the EPWP and NINO3 are a close match. Thus, one of two things must be true for the correlation to be physically-based: (a) the interannual variability of surface shortwave radiation over the EPWP is driving ENSO, thus SSTA in the EPWP and NINO3 are correlated, or (b) ENSO influences surface shortwave radiation by modifying the distribution of cloud cover over the EPWP. As is well known and described previously in this subsection, (a) cannot be true, as surface heat fluxes, including shortwave, act to damp the equatorial SST anomalies associated with ENSO. Shortwave radiation initially *responds* to ENSO forcing because ENSO changes the distribution of the warmest SSTs in the Pacific Ocean and thus the distribution of cloud cover. The remaining possibility (b) makes physical sense when considering *how* ENSO

modifies the distribution of cloud cover. During an El Niño event, for example, SST in the east-central equatorial Pacific become anomalously warm, which forces upward vertical motions and deep convection in the atmosphere (Zhang 1993), and compensating subsidence over the off-equatorial regions.

This simple mechanism can easily be corroborated with the NCEP Reanalysis (Kalnay et al. 1996). Shown in Figure 2.22 (left panel) is a vertical cross-section of annual mean omega (dp/dt) along 100°W from 20°S to 20°N averaged over the Reanalysis period (1948-2003).

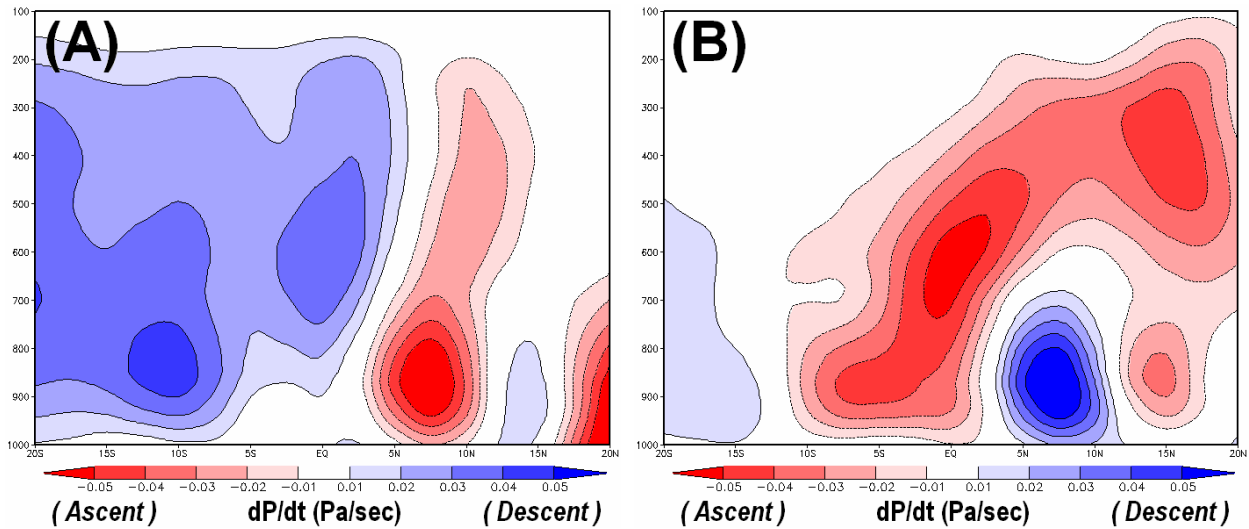


Figure 2.22. Vertical cross-section of annual mean (1948-2003) omega (dp/dt ; Pa s^{-1}) along 100°W (left) and the anomaly during November 1997 (right) from the NCEP Reanalysis.

On the annual mean, the general distribution of vertical motions is characterized by strong ascent (i.e., the ITCZ) centered over 7.5°N , with broad descent everywhere south of 5°N , and some weak descent immediately north of the ITCZ. The strong ascent is situated $5\text{-}10^\circ$ north of the equator because the warmest SSTs lie north of the equatorial cold tongue, and thus the thermal equator at 100°W is effectively at 7.5°N . It is thus no surprise that the EPWP is also a region of high precipitation. However, using November 1997 as an example (Figure 2.22, right panel), El Niño events result in strong ascent anomalies over the geographical equator, as well as strong compensating descent anomalies over a band of latitudes roughly $5\text{-}10^\circ\text{N}$, which

corresponds with the location of the EPWP. Thus, during an El Niño event, there would tend to be less clouds and precipitation over the EPWP and a greater abundance of surface shortwave radiation available to heat the ocean surface. To establish that this is a statistically robust tropospheric response to ENSO, including the signal over the EPWP, presented in Figure 2.23 is the correlation between the Oct-Dec mean omega anomaly and the NINO3 index (correlations significant at the 95% confidence level shaded). Negative correlations over the equatorial region (physically interpreted as ascent during warm ENSO phase) exceed -0.6 , and positive correlations over the EPWP (physically interpreted as descent during warm ENSO phase) exceed $+0.6$ over the 56 years of the NCEP Reanalysis. These are, in fact, the only statistically significant features in the cross-section.

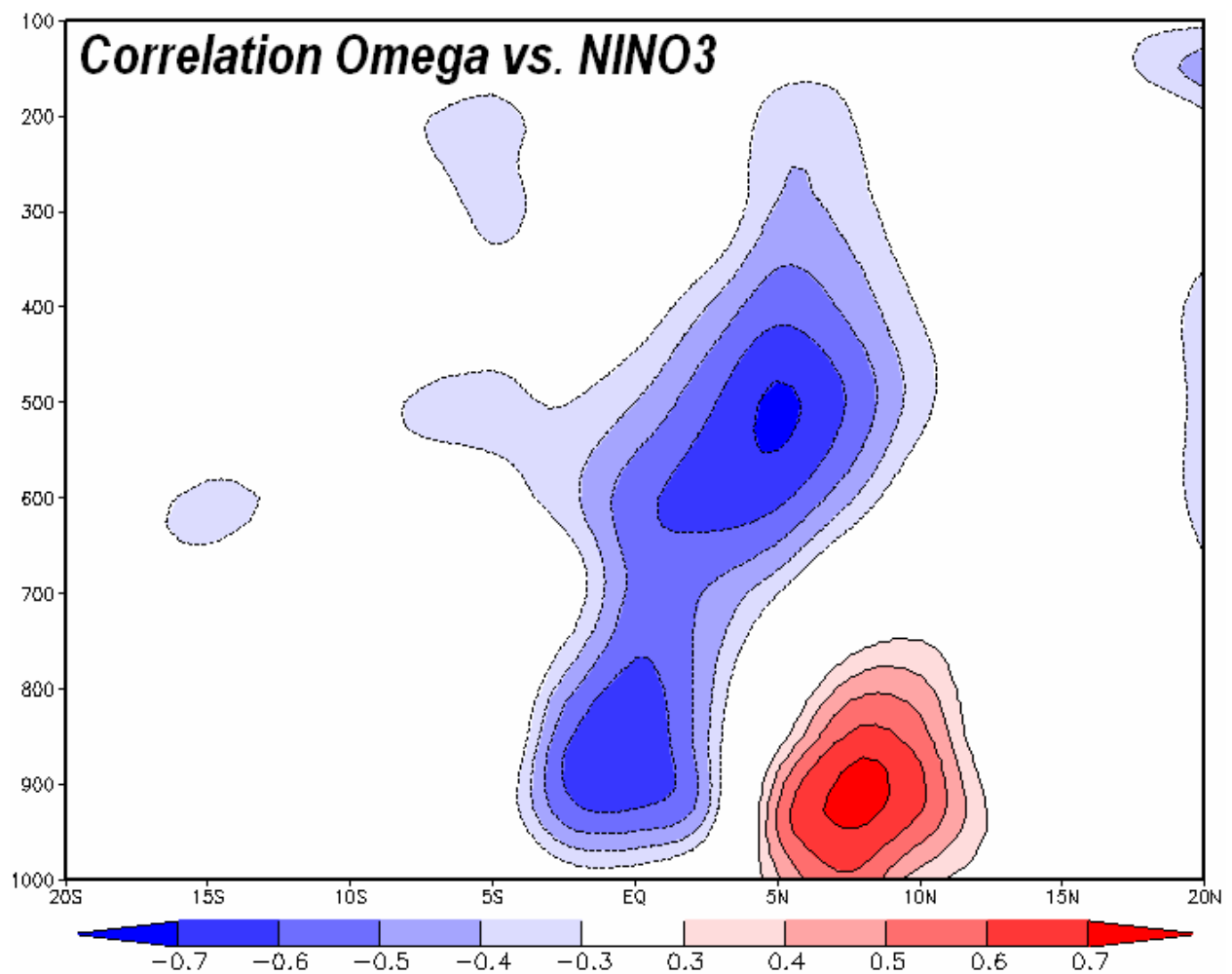


Figure 2.23. Vertical cross-section of the correlation between October-December mean omega anomaly and the NINO3 index along 100°W from the NCEP Reanalysis (Kalnay et al. 1996) over the full Reanalysis period (1948-2003).

To translate this response of the general circulation of the atmosphere into the heat flux forcing to the surface ocean, shown in Figure 2.24 (left panels) is the regression of surface shortwave radiation anomalies onto the index of SST anomaly in the EPWP. Since the SSTA in the EPWP and NINO3 regions are very similar, this can also be approximately interpreted as the regression onto a NINO3 time series. In either the regression using simulated or observed SST for the regression, there is reduced shortwave radiation along the equator extending eastward approximately to the Galápagos Islands, and enhanced shortwave radiation to the north of the equator as well as over the east Pacific warm pool. Such a configuration would be favorable for heating the ocean surface at the EPWP. Also shown in Figure 2.24 (right panels) is the regression of SRB surface downward shortwave radiation anomalies onto $\partial T/\partial t$ in the EPWP. These plots indicate how much shortwave radiation is required to drive roughly a standard deviation of SST increase. The values indicated by the regressions (6-9 W m⁻²) are well within the range of variability of the surface shortwave radiation (13-17 W m⁻² in the vicinity of the EPWP).

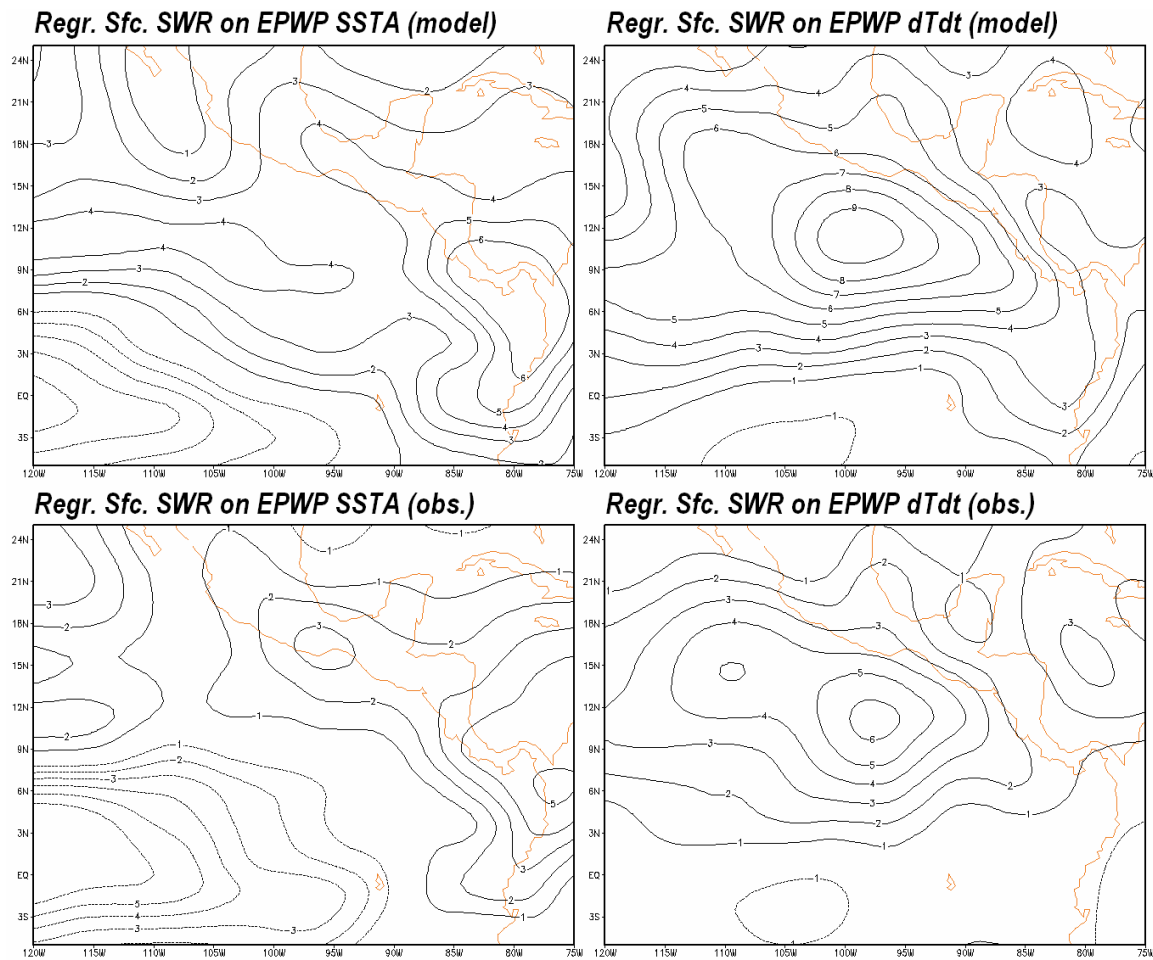


Figure 2.24. Regression of SRB surface downward shortwave radiation anomaly (W m^{-2} , contour interval 1 W m^{-2}) onto simulated (top) and observed (bottom) indices of EPWP SST anomaly (left) and time rate of change of EPWP SST anomaly ($\partial T/\partial t$, right).

The present subsection has been a discussion of the results of calculations of the interannual variability of the mixed layer heat budget in the EPWP. The objective was to determine what are the primary governing mechanisms for the interannual variability of SST in the EPWP, including why a strong association with ENSO is noted in observations and forced ocean model experiments. The following are the major conclusions and recommendations:

- ENSO drives the EPWP through surface heat fluxes (shortwave dominated), rather than advective heat fluxes (i.e., ocean dynamics). This suggests that the EPWP is dissimilar to the equatorial Pacific cold tongue in terms of mechanisms, even though the end result in terms of the evolving SST anomaly, and correlation with the mixed layer depth, is quite similar.
- The method for communication of the ENSO signal from the equator to the EPWP relies on an atmospheric link away from the equator. Warm ENSO events result in anomalous ascent in the lower troposphere over the anomalously warm eastern equatorial Pacific, equivalent to a southward-displaced ITCZ, which leads to anomalous descent and reduced cloud cover to the north of the equator and thus anomalously high surface shortwave radiation available to heat the EPWP. This serves as an example as to why accurately modeling tropical atmospheric circulation cells of only a few degrees in horizontal scale is important- especially for regional climate processes. The importance of regional atmospheric cells in the tropics will again come into focus in Chapter 4 with regard to the role of the EPWP in Central American rainfall.
- It is recommended that future coupled modeling studies and intercomparisons focus on improving the treatment of surface shortwave radiation, particularly the response to ENSO over nearby tropical and extratropical regions. Such an effort would share a common goal with ongoing observational and modeling efforts aimed at understanding problems with clouds in coupled models (e.g., CLIVAR VAMOS programs including upcoming IASCLIP).
- It is recommended that forced ocean models always take into account interannually varying shortwave forcing, and avoid “wind-forced with climatology-everything-else”

style experiments. In this light, it is necessary to improve and maintain existing shortwave radiation datasets and develop new, multi-decade-long surface downward shortwave radiation datasets. Securing high quality datasets suitable for forcing models of the global oceans remains a high priority for the ocean modeling community.

2.4.3. The role of ocean poleward heat transport

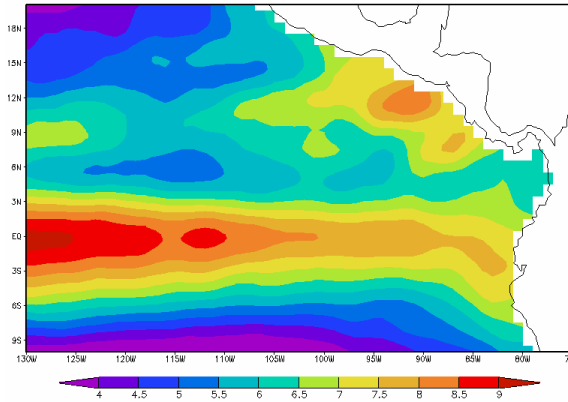
The concept of ENSO driving the interannual variability of SST in the EPWP primarily through surface fluxes would seem to require that there be some degree of disconnect in terms of ocean dynamics between the equatorial Pacific and the EPWP. Numerous prior studies on the general circulation of the ocean and atmosphere and the heat balance of the Earth suggest that the ocean plays a dominant role in the poleward transport of heat in the deep tropics (e.g., Vonder Haar and Oort 1973, Czaja and Marshall 2006). Furthermore, a leading theory for the cyclic nature of ENSO involves the recharge of heat in the equatorial Pacific during La Niña events, and a discharge of heat from the equatorial Pacific during El Niño events. This is known as the recharge-discharge theory of ENSO (Jin 1997). Given that the EPWP is in relatively close proximity to the equator, it is reasonable to ask what role the poleward heat transport away from the equator by the ocean plays in the interannual variations of SST in the EPWP (e.g., Sun 2000).

A useful way of tracking meridional movements of warm water (thus PHT) recently brought into popularity by Meinen and McPhaden (2000, 2001) and Meinen (2005) involves tracking warm water volume (WWV). This technique involves using the depth of the 20°C isotherm from in situ temperature observations (Meinen and McPhaden 2000, 2001), or spatially integrating satellite altimetry observations of sea surface height (Meinen 2005). In this subsection, we discuss in detail the results of Meinen and others, and finally, address the role of coastal Kelvin waves, in the sense that they are explicit agents of PHT. The mechanism proposed in the previous subsection for the interannual variability of SST in the EPWP (i.e.,

ENSO drives the interannual variability primarily through shortwave radiation, as ENSO modifies the three dimensional tropospheric circulation and thus cloud cover on and off the equator) requires, as a corollary, that there be a lack of connection from ocean dynamics and transports between the equatorial Pacific and EPWP SST variability. This “lack of an ocean connection” corollary is, as will be discussed here, also consistent with much recent work done the context of PHT, or meridional exchanges of warm water volume.

One of the ocean surface fields most strongly influenced by ocean dynamics (i.e., propagating waves, heat transports, thermocline depth variations, etc.) is sea level anomaly (SLA). Using the standard deviation of SLA as an indication of ocean dynamical activity, then, Figure 2.25 provides a general picture of where there is high and low amplitude of such activity. In the TOPEX observations and the *control* experiment, there is high SLA variability along the equator, which is primarily due to ENSO variability. There is also high SLA variability near the coast in the EPWP; coastally trapped Kelvin waves are a prominent feature of the northeastern tropical Pacific Ocean. By lead-lag correlation analysis, the TOPEX equatorial SLA signal (at 93°W, Eq.) explains at most 36% of the SLA variability within the coastal region of the EPWP (at 93°W, 11°N), with equatorial SLA leading by approximately 25 days. However, also in both TOPEX observations and the *control* experiment, there is a local minimum of SLA variability along 5°N in the TOPEX plot and 3°N in the *control* experiment plot (i.e., the local minimum lies between the equator and the EPWP). The apparent separation between the equator and the EPWP region is stronger in the TOPEX observations than in the *control* experiment, which may be due to model deficiencies, differing temporal periods over which the standard deviations were calculated, or altimeter deficiencies near the coast.

(a) TOPEX 1992-2005



(b) CONTROL 1988-2004

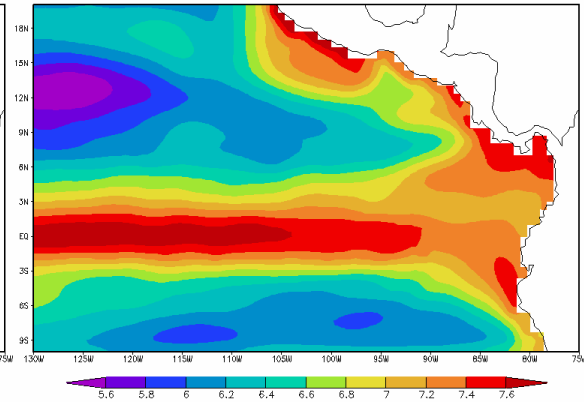


Figure 2.25. Weekly standard deviation of sea level anomaly (SLA; cm) in the eastern tropical Pacific Ocean from TOPEX satellite altimetry for the period 1992-2005 (left) and the *control* experiment for the period 1988-2004 (right).

The correlation between SSTA and SLA at each gridpoint in the eastern tropical Pacific is shown in Figure 2.26. As Figure 2.25 indicated a local reduction of sea level *amplitude* between the equator and the EPWP, Figure 2.26 confirms that this corresponds with a local reduction of SSTA-SLA correlation. Thus, the discontinuity in ocean dynamics between the equator and the EPWP leads to a discontinuity in the impact of ocean dynamics on SST variability.

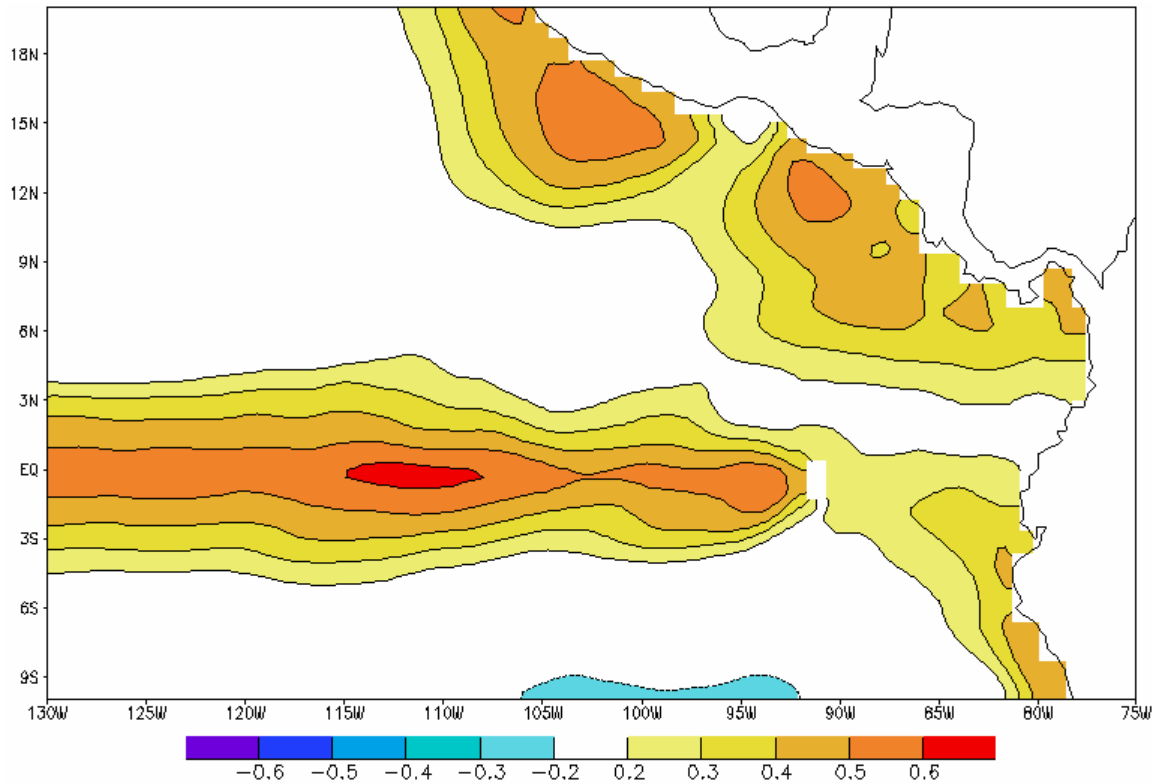


Figure 2.26. Correlation between weekly SSTA and SLA from the *control* experiment (1988-2004).

Shown in Figure 2.27 is a depiction of the 1997-98 El Niño event (Figure 2.27a) and the 1999-2000 La Niña event (Figure 2.27b) from the SODA Reanalysis (Carton et al. 2000). Clearly during the El Niño event, the equatorial SST is anomalously warm because the equatorial thermocline is ~100 m deeper than its climatological value of ~40m. From the SSTA time series discussed in section 2.3, SSTA in the EPWP closely follows that of the NINO3 region. However, during the 1997-98 El Niño event, the thermocline in the EPWP region is very close to its climatological value. Moreover, the subsurface temperature anomaly in the EPWP is up to *negative* 4°C. In the case of the 1999-2000 La Niña event (Figure 2.27b), the equatorial SSTA is negative, which would be the logical result of the thermocline displaced upward from its climatological value of ~40 m to only ~5 m beneath the surface. However, in the heart of the EPWP (10°N), the thermocline is very near climatology, and there is evidence of even slightly *positive* temperature anomalies at depth, rather than strongly negative like the equator.

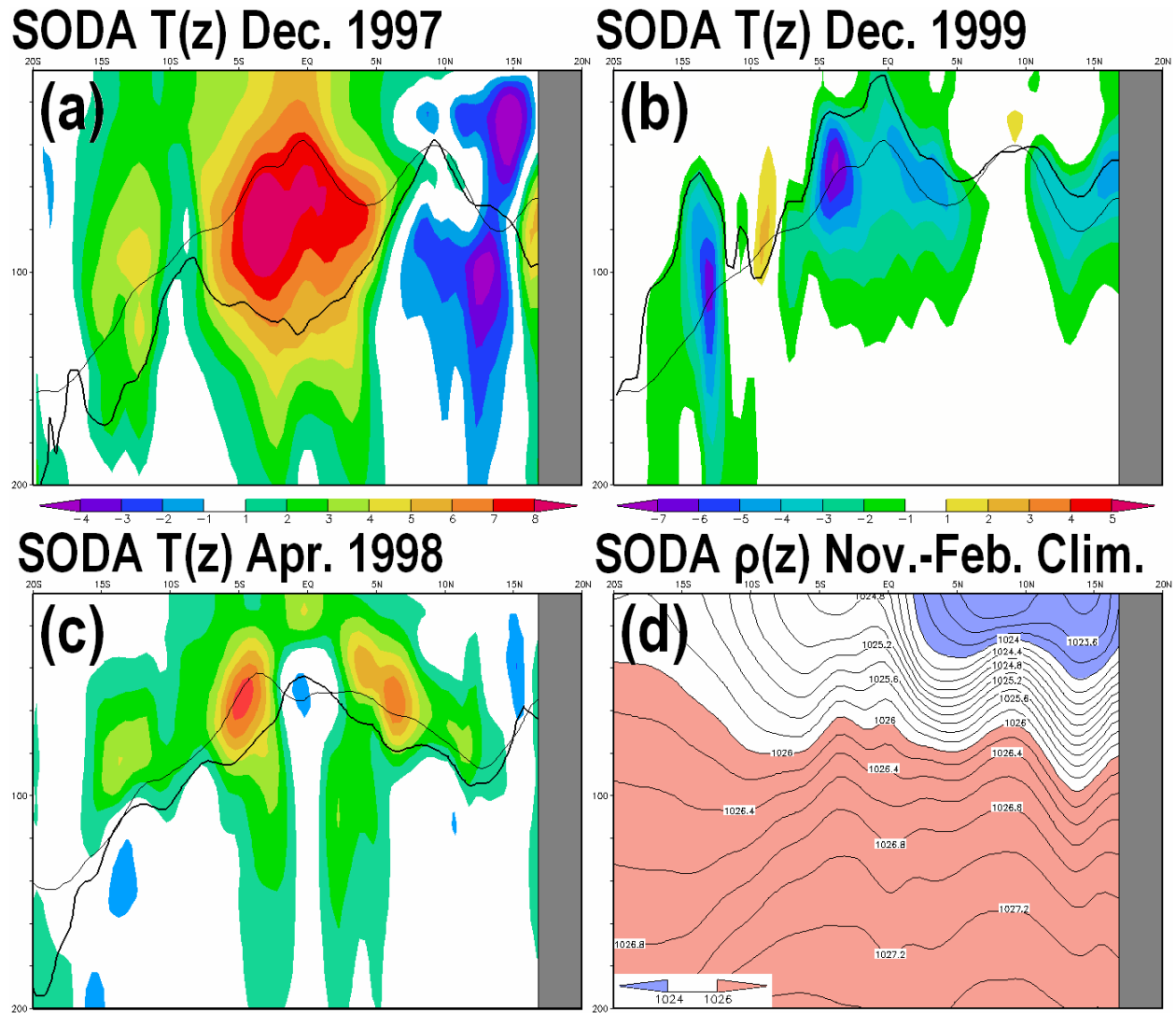


Figure 2.27. Panel (a): vertical cross-section of ocean temperature anomaly in the upper 200m along 100°W from 20°S to 20°N (shaded, °C), the depth of the 20°C isotherm (heavy black line, m), and the depth of the climatological 20°C isotherm for that month (thin black line, m) during December 1997. Panel (b): as in (a) but for December 1999. Panel (c): as in (a) but for April 1998. Panel (d): November-February climatological mean ocean density (kg m^{-3}) along the same section. All variables computed from the SODA Reanalysis (Carton et al. 2000). Gray shading indicates no data (the Pacific coast of Mexico).

Earlier cases were also analyzed in a similar fashion from the SODA reanalysis (1972-73, 1982-83, and 1986-87), and yielded very similar results as those discussed here. Progressing forward in time (i.e., January, February, March, etc.) from the case shown in Figure 2.27a indicates that

the positive temperature anomaly spreads poleward in both directions as a negative temperature anomaly begins to develop in its place. To the north, however, there is a strong horizontal density gradient separating the equatorial region from the EPWP (Figure 2.27d). In addition, there is a strong vertical density gradient beneath the EPWP. Such strong stratification both horizontally and vertically effectively serves to surround the EPWP with a barrier to mixing with neighboring regions. A nearly identical structure as that shown in Figure 2.27d can be found in TAO observations of potential density along 95°W (not shown). Since mixing and transport *across* isopycnals requires much greater energy than mixing and transport *along* isopycnals, the northward propagating temperature anomaly is confined to within or below the pycnocline. By April 1998 (Figure 2.27c), the difficulty with which the northward propagating temperature anomaly encounters to penetrate the stratification surrounding the EPWP is evident; the majority of the positive temperature anomaly is still equatorward of 8°N (the southern latitudinal boundary of the EPWP defined in Section 2.3) from the surface to a depth of ~40m. Clearly the preference is for propagation *along* the pycnocline, thus not greatly impacting the mixed layer heat budget of the EPWP. Figures 2.25-2.27 provide observational and experimental evidence of a disconnect in ocean dynamical processes between the equator and the EPWP, which is consistent with the notion that ENSO does not drive the interannual variability of SST in the EPWP through direct ocean dynamics and transport.

Meinen and McPhaden (2000) constructed a gridded dataset of subsurface temperature and identified two modes of thermocline depth variability: an east-west tilting mode and an equatorial recharge-discharge mode. The main objective of Meinen and McPhaden (2000) was to test the recharge-discharge theory of ENSO (Jin 1997) using observations. They found that the observations do support Jin's theory, although more relevant to the present discussion is the spatial structure of the recharge-discharge WWV pattern (Figure 2.28).

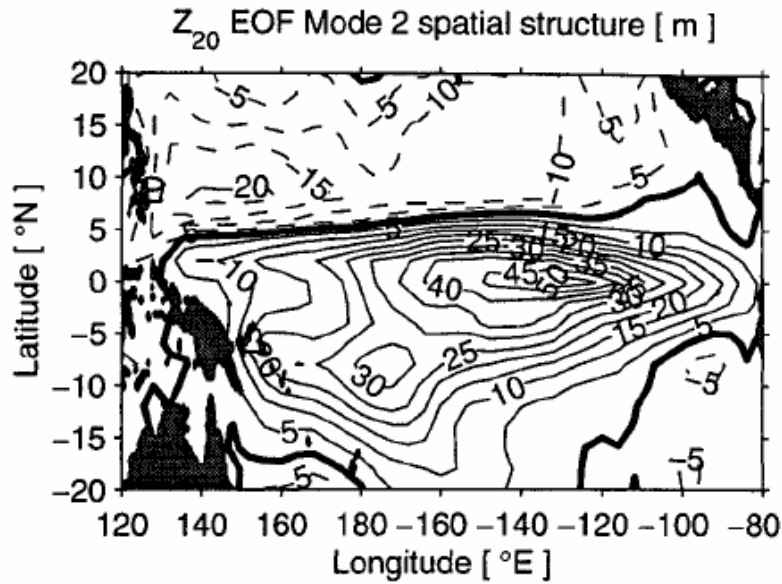


Figure 2.28. Part of Figure 3 from Meinen and McPhaden (2000), showing EOF2 of the depth of the 20°C isotherm (m) using observed subsurface temperature data.

There is virtually no involvement of the EPWP in this pattern, rather, there is a nodal line along approximately 5°N, and the Southern Hemisphere is most heavily involved, as well as the western boundary in the tropical north Pacific. Meinen and McPhaden (2001) focused on the WWV transport and mechanisms associated with the 1997-98 El Niño and subsequent La Niña event. One of the findings of that study was that there is only very weak anomalous WWV transport eastward across 95°W over the period 1993-1999.

Meinen (2005) utilized the aforementioned gridded dataset, along with satellite altimetry measurements of sea surface height anomaly (SSHA) and theoretical Sverdrup transport calculations from observed winds to analyze WWV and identify the pathways of exchange with subtropical latitudes, including the involvement of the Pacific Ocean subtropical cells (STCs). One of the novel aspects of this work is the use of SSHA as a proxy to WWV. However, one of the first observations in Meinen (2005) is that the integrated SSH (ISSH) did not validate well in a region which essentially outlines the EPWP (Figure 2.29). Although this

could hint to a problem with the in situ observations, it is speculated by Meinen that this could result from a real difference in ocean processes, e.g., local wind forcing and Ekman pumping affecting ISSH but *not* WWV. This phenomenon has also been observed for transition regions elsewhere. Mayer et al. (2001) investigated transition regions in the Atlantic Ocean between the tropics and the subtropics. Low and even negative correlations between altimetry and subsurface information were shown, and thought to be related to the subtropical sea level regions being dominated by surface buoyancy fluxes, versus the deep tropics being dominated by wind-driven thermocline variations. In the context of the EPWP, the result of Mayer et al. (2001) would seem to suggest that Meinen's ISSH vs. WWV correlations support the mechanism proposed in the previous subsection- that the EPWP, however close in proximity to the equatorial Pacific, is beyond a transition region where different physical processes dominate.

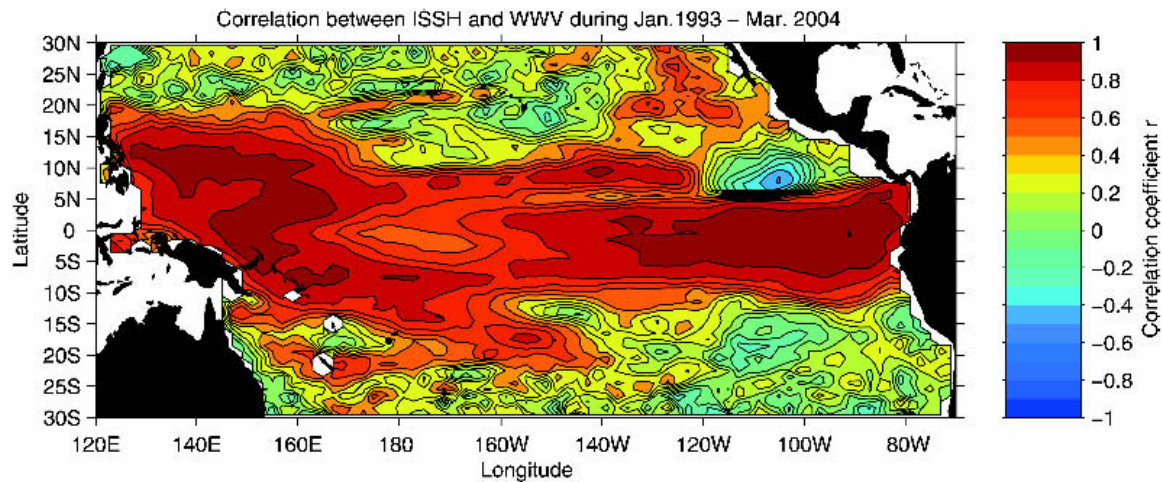


Figure 2.29. Figure 4 from Meinen (2005), showing the correlation between integrated SSH from satellite altimetry and WWV from observed subsurface temperature data.

With respect to the present discussion, Meinen (2005) makes two other very important observations about the zonal and meridional transports of WWV, both of which confirm that the connection between the equatorial Pacific and the EPWP is not provided by ocean dynamics and transport- so must rely on some other mechanism (which we argue is an atmospheric link).

First, and consistent with Meinen and McPhaden (2001), Meinen (2005) suggests that the strong WWV discharge associated with the 1997-98 El Niño event “does not result from a large eastward flow toward the coast of the Americas and then a divergence along the coast...” This is consistent with the aforementioned result of Kug et al. (2003), which was based on NCEP ocean data assimilation data.

Secondly, Meinen shows that the poleward flow of WWV in the northern hemisphere cannot be traced beyond 10°N, while in the Southern Hemisphere it can be traced to at least 20°S. This is evident in Figure 2.27a in the present section, where subsurface temperature anomalies are shown to spread southward, but not northward, from the equator during an ENSO event. A rectification of this can also be seen in Figure 2.15, where SST variability due to interannual wind stress forcing is much larger to the south of the main equatorial signal than to the north.¹ This result is also confirmed with Meinen’s use of theoretical Sverdrup transport calculations. Meinen points out that the latitude of 10°N, where the northward WWV transport seems to come to an abrupt stop, is also the mean latitude of the ITCZ, which is associated with large changes such as the wind stress curl. A prior study which utilized a modeling framework that does *not* include such a blocking mechanism (Zebiak 1989) indicated exchange well beyond 15°N.

Several previous studies have investigated flow in the opposite direction as that discussed here (i.e., equatorward flow of Northern Hemisphere subtropical water) was blocked by the strong upper ocean potential vorticity (PV) front located under the ITCZ. Examples of the PV front published in two separate studies are shown in Figure 2.30. The strong PV front is located along approximately 6°N in the eastern Pacific, which is effectively the southern limit of the EPWP as defined in this dissertation. Lu and McCreary (1995) showed that weakened negative Ekman pumping beneath the ITCZ creates a PV front which serves as a barrier that

¹ The exception to this is a localized northward extension of the pattern between 130-140°W, which appears prominently in Kug et al. (2003; see Figures 3a and 4a), and Meinen (2005; see Figure 4, here reproduced in Figure 2.29).

blocks North Pacific thermocline water moving toward the equator. By contrast, in the Southern Hemisphere, where there is no ITCZ except in the western Pacific, Lu and McCreary (1995) showed that as Ekman pumping velocity increases monotonically toward the equator, subtropical thermocline water was able to move directly to the equator. The PV front was also discussed in Johnson and McPhaden (1999) and McPhaden and Zhang (2002) as a feature which tends to block exchange between the equatorial band and the subtropics.

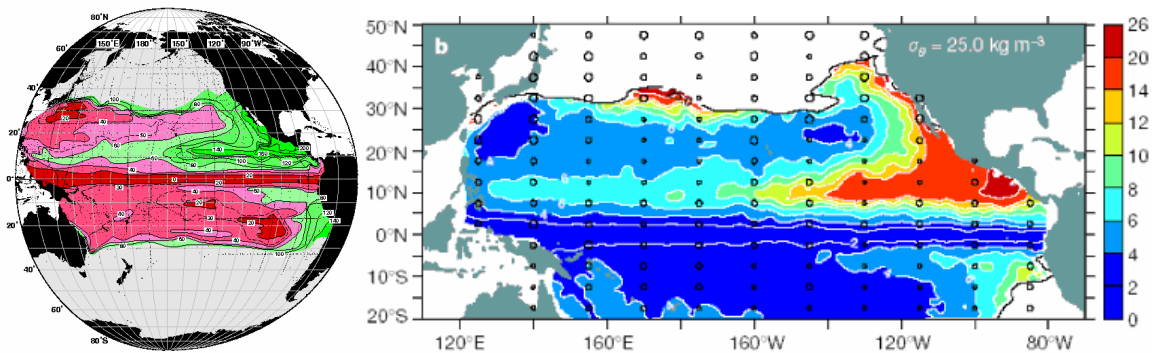


Figure 2.30. Left: Observations of the potential vorticity front (PV on the $\sigma_\theta = 25.2$ surface) from World Ocean Circulation Experiment (WOCE) observations (reproduced from Talley and McCarthy 1998). Right: Observations of the PV front (PV on the $\sigma_\theta = 25.0$ surface) from other hydrographic observations (part of Figure 1 from McPhaden and Zhang 2002).

With the exception of Kelvin waves, there is no reason why the PV-front mechanism cannot include blocking the exchange of warm water between the eastern equatorial Pacific and the EPWP. As a component of the meridional tropical cells in the Pacific Ocean, the ITCZ imparts negative wind stress curl and diapycnal downwelling (McCreary and Lu 1994, Johnson 2001, Sloyan et al. 2003). Thus at approximately 6°N , poleward flow downwells and converges back toward the EUC in the pycnocline (Figure 2.31). It is therefore necessary to invoke an atmospheric link to explain the observed correlation between NINO3 and EPWP SSTA, as presented and discussed in the previous subsection.

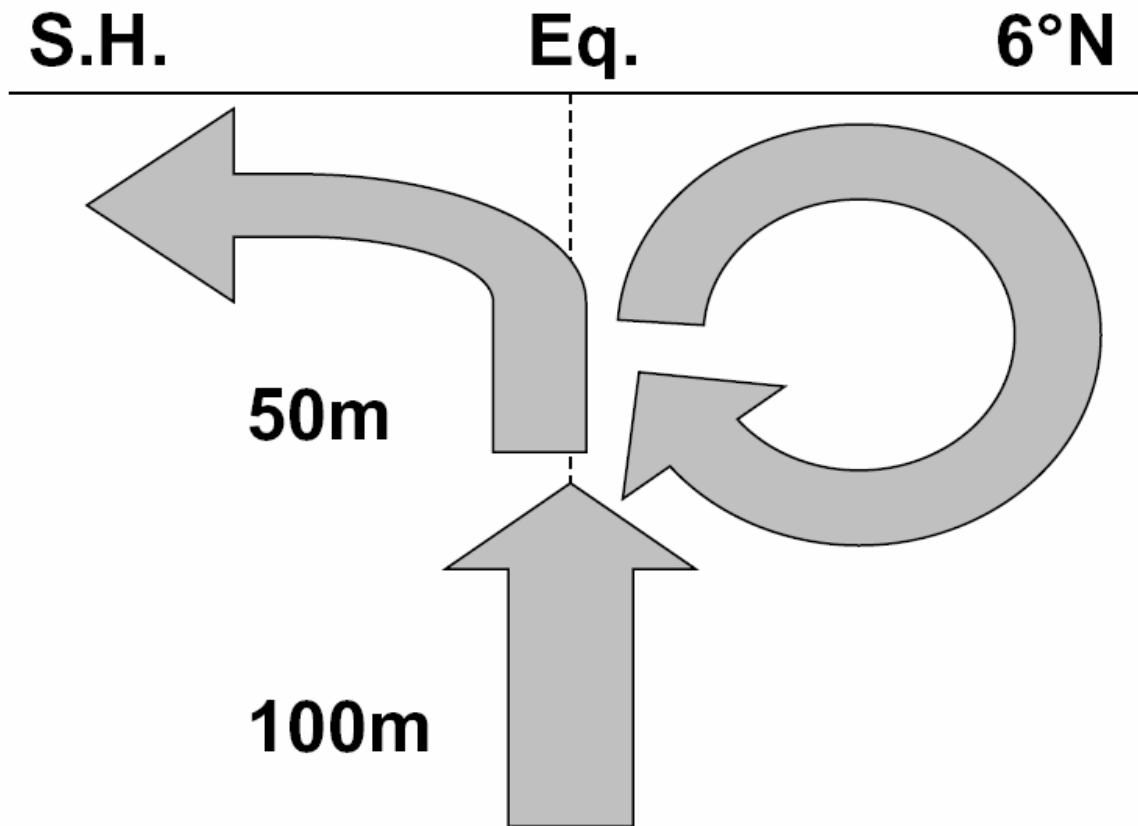


Figure 2.31. Schematic depiction of the meridional tropical cells in the Pacific Ocean.

The final task in this subsection is to address the role of coastally-trapped Kelvin waves (KWs), as explicit agents of poleward ocean heat transport, in the interannual variability of SST in the EPWP. Coastal KWs are an important feature of the circulation in the tropical Pacific Ocean, particularly the north eastern tropical Pacific (Kessler 2006) and thus the EPWP. As coastal KWs in this region can be equatorially forced, they could also provide an ocean connection between the equatorial Pacific and the EPWP, and thus a method of communication of the ENSO signal to the EPWP. The task is thus to determine the extent to which coastal KWs efficiently generate SST anomalies in the EPWP.

Shown in Figure 2.32a is a “boundary Hovmoeller” of SSTA for the *control* ocean model experiment. Time increases along the positive y-axis, and the x-axis represents distance,

following the coast, from the equator and 20°N. For convenience, latitude is also marked on the x-axis. Recall that the EPWP is generally within the latitude band from 5-15°N.

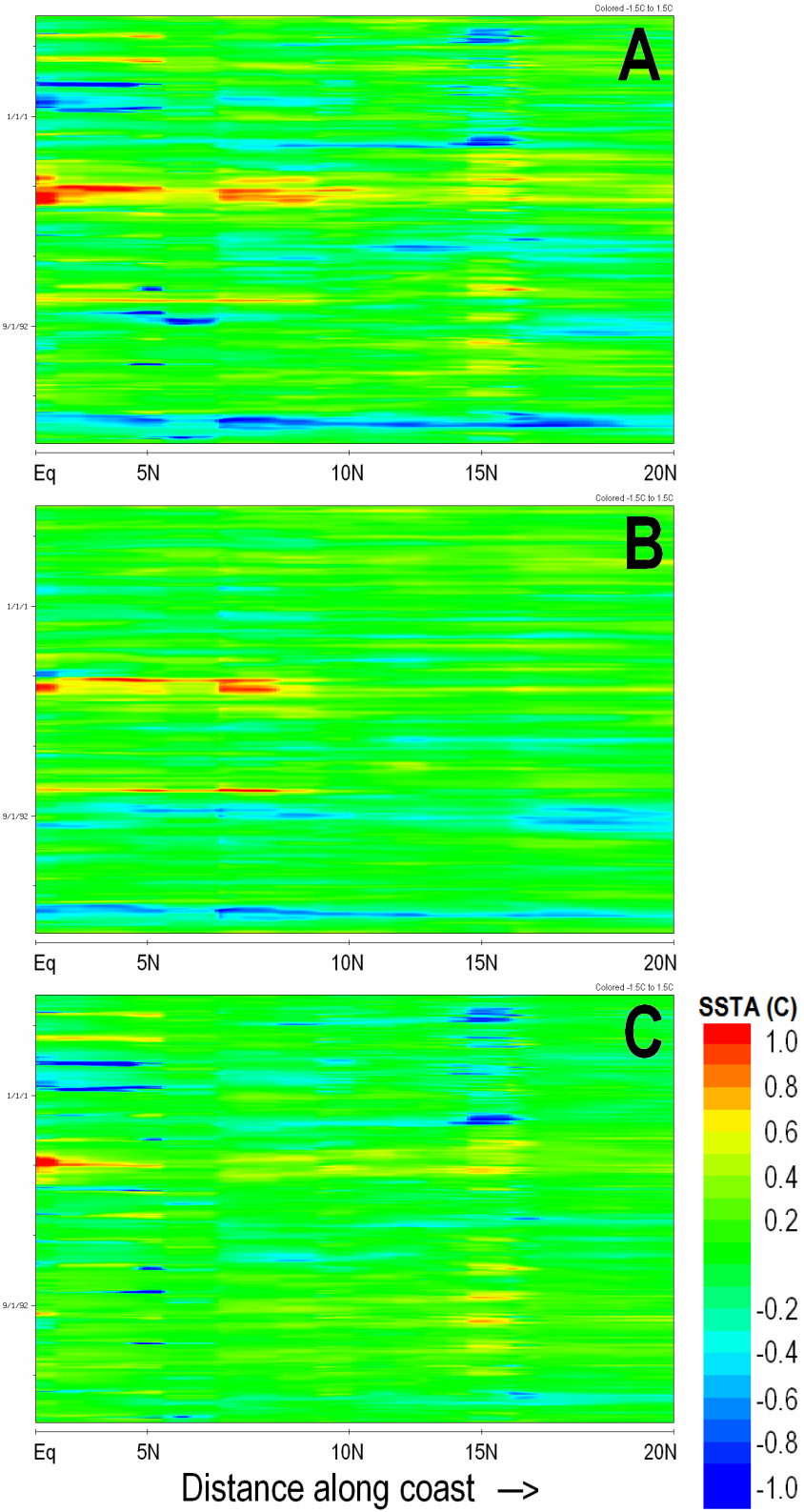


Figure 2.32. Boundary Hovmoeller diagrams of SSTA ($^{\circ}\text{C}$) along the Pacific coast of Central America and Mexico from the equator to 20°N in the *control* experiment (A), *clim-winds* experiment (B), and *clim-solar* experiment (C). Time increases along the positive y-axis from January 1988 through December 2004. The color legend shown in the lower right applies to all panels A-C.

Clearly evident in Figure 2.32a are significant variations in coastal SSTA near the equator (out to about 6°N), and between 8 - 15°N . Between 6 - 8°N , there is a subtle break in the northward propagating coastal signal. Also clearly evident are the SST anomalies associated with the Tehuantepec gap winds at 15°N , which will be discussed in the following section. As Figure 2.32a is for the *control* experiment, this includes contribution from interannual wind stress *and* surface shortwave radiation. Thus, from this depiction, it cannot be objectively determined what parts of, or how much of, the coastal SST anomalies are actually due to coastal KWs versus other processes. Shown in Figure 2.32b is the same boundary Hovmoeller of SSTA, but for the *clim-winds* ocean model experiment. In this experiment, there cannot be equatorially-forced coastal KWs, as shortwave radiation alone cannot initiate KWs. As a consistency check, it is noted that the SSTA variations in the Gulf of Tehuantepec are absent from Figure 2.32b. However, significant interannual SST variations *are* present near the equator and in the latitude band encompassing the EPWP. Although it may seem surprising that there could be a signal near the equator without the interannual wind stress forcing, this is actually feasible for two reasons: (1) as expected, the magnitude is smaller than that in the *control* experiment (i.e., Figure 2.32a), and (2) the shortwave regressions (Figure 2.24, left panels) show that the positive surface shortwave radiation anomaly pattern does extend along the coast as far south as the equator. Within the latitude band of the EPWP, the SST variations in the *clim-winds* experiment are nearly as large as those in the *control* experiment. To confirm that these SST variations are in fact related to variations in shortwave radiation, shown in Figure 2.32c is the corresponding boundary Hovmoeller diagram for SSTA in the *clim-solar* experiment. In this

case, one can still discern some of the SSTA signal propagating along the coast from the equator, but only to about 6°N (i.e., that which is certainly due to coastal KWs), beyond which SST anomalies are very weak until the Gulf of Tehuantepec. The implication is that surface shortwave radiation is responsible for some of the coastal SSTA signal that may otherwise appear to be due to coastal KWs, and is responsible for most of the coastal SSTA signal within the latitude band of the EPWP, which could also have been incorrectly ascribed to an extension of the KW signal originating at the equatorial coast.

To focus on the strong 1997-98 El Niño event, shown in Figures 2.33-2.35 are equatorial Hovmoeller diagrams connected to boundary Hovmoeller diagrams of SLA and SSTA restricted to the period January 1996 through August 1999, for experiments *control*, *clim-winds*, and *clim-solar*. This arrangement allows one to seamlessly follow the eastward propagation of equatorial KWs (in terms of SLA) and corresponding SSTA signals across the width of the basin, and subsequent propagation of coastal KWs up the coast of Central America and Mexico. In the *control* experiment (Figure 2.33), a series of strong equatorially-forced coastal KWs are evident. In terms of SSTA, the maximum SSTA along the equator is 3.4°C, along with relatively strong coastal SST anomalies. Other than the anomalies at the Isthmus of Tehuantepec (~15°N), it cannot be determined from Figure 2.33 how much of the coastal SSTA signal is actually forced by the propagating KWs. Certainly the analyses thus far in Chapter 2 would suggest other processes such as surface shortwave radiation could be important even along the coast.

Shown in Figure 2.34 is the same depiction as in Figure 2.33 but for the *clim-winds* experiment. Recall that the *clim-winds* experiment does not include interannual wind stress forcing, but *does* include interannual shortwave forcing. Thus, any SST anomalies along the equator or coast can *only* be attributable to surface shortwave radiation. Not surprisingly, there are no equatorial or coastal KWs present in the *clim-winds* experiment. Also not surprisingly, where there would otherwise be a positive SSTA propagating along the equator during 1997-98, there is instead a negative SSTA. This is because the shortwave forcing is trying to damp a

positive SST anomaly that does not exist in this experiment. However, what is notable and confirms the notion that shortwave radiation is important east of the Galápagos Islands and in the EPWP is the positive equatorial SST anomalies east of the Galápagos and coastal anomalies extending well into the EPWP.

A final affirmation of the previous statement, especially regarding the EPWP, is in comparing the *control* Hovmoeller depiction with that for *clim-solar* (Figure 2.35). The equatorial and coastal SLA Hovmoeller diagrams for *clim-solar* are nearly identical to those of *control*; the equatorial and equatorially-forced coastal KWs only depend on the wind forcing, which is the same in the two experiments. In terms of SST, the equatorial anomaly is larger in *clim-solar* than in *control* (4.9°C versus 3.4°C) because the shortwave forcing is not present to damp the SST anomaly. Along the coast, comparable (to *control*) SST anomalies are *only* present as far north as about 6°N, while the SST anomalies northward (into the EPWP) of 6°N are much reduced, suggesting the shortwave forcing is necessary to establish a correlation between the equatorial ENSO signal and SSTA in the EPWP, *including* the coastal areas of the EPWP, where equatorially-forced coastal KWs are prevalent. It is not clear whether the reduced, albeit positive, SST anomalies centered around 10°N are due to KWs or a southward extension of the Tehuantepec gap winds. Given the apparent phase lagging, it would appear to be due to KWs. This, however, may be an exaggerated effect because the amplitude of the ENSO event itself is higher due to the lack of the damping effect of shortwave radiation.

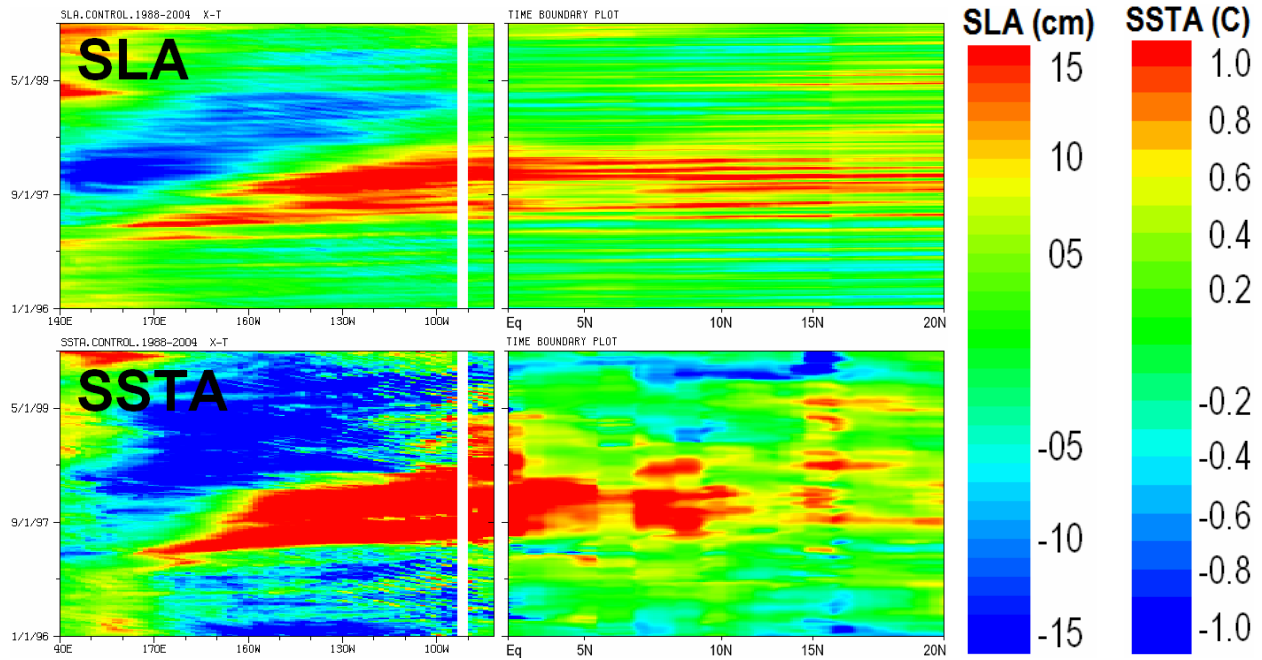


Figure 2.33. Top: Equatorial Hovmoeller diagram of SLA (cm) from 140°E-80°W connected to a boundary Hovmoeller diagram of SLA along the Americas from the equator to 20°N, from the *control* experiment between January 1996 through August 1999. Bottom: as in top by for SSTA (°C).

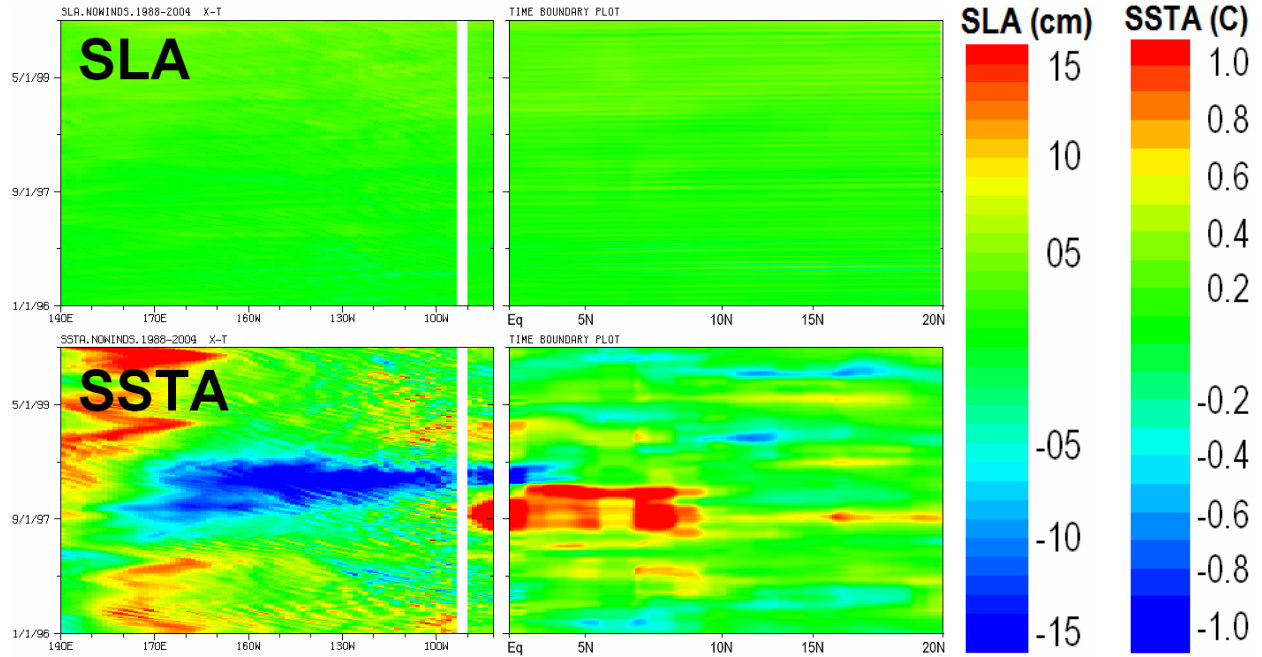


Figure 2.34. As in Figure 2.33 but for *clim-winds*.

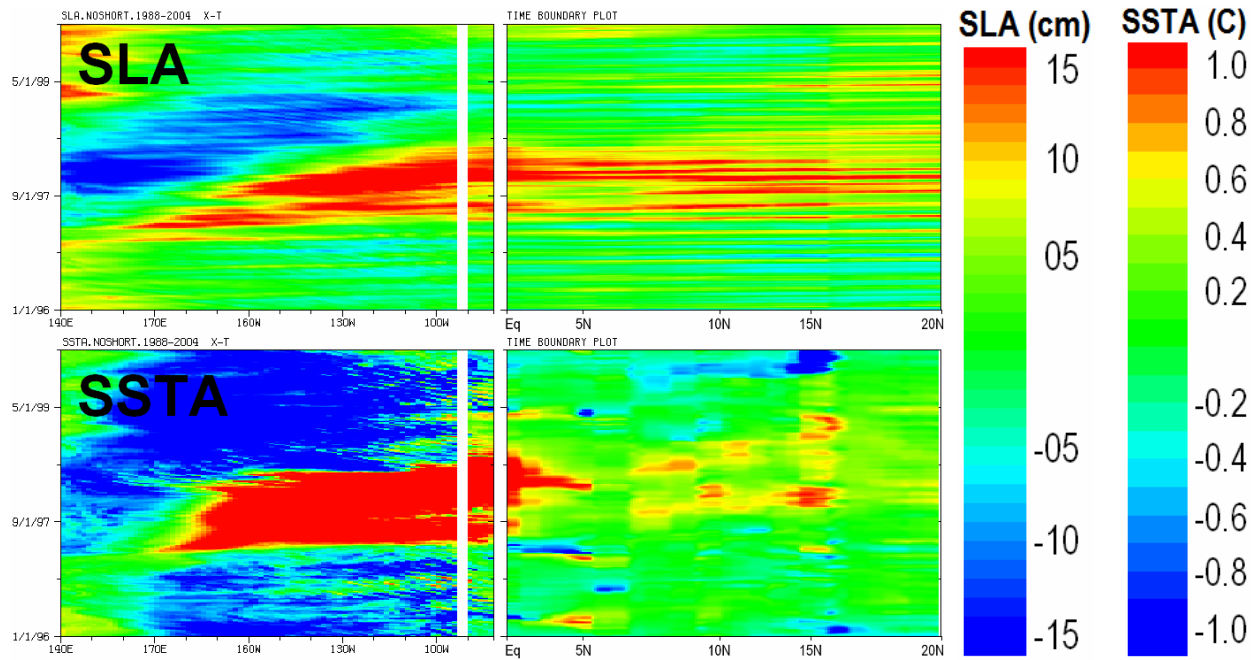


Figure 2.35. As in Figure 2.33 but for *clim-solar*.

As strong as the 1997-98 event was, and regardless of how freely the KWs propagate northward along the eastern boundary in terms of SLA, Figure 2.35 confirms that the northern reach of KWs, in terms of *continuous* SSTA response, is about 6°N, which is effectively the southern limit of the EPWP. This is highly consistent with Kessler (2006; see Figure 12 of that paper), although was interpreted differently. Enfield and Allen (1980, 1983) analyzed observations of sea level anomalies along the Pacific coast of the Americas, which could be observed as far north as mid-California. Spillane et al. (1987; with Enfield and Allen) determined that the main energy source for these oscillations was from remote processes in the equatorial waveguide. However, the results of Enfield and Allen (1980) also reveal that, within the latitude band of the EPWP, coastal SSTA exhibited relatively small variance compared with SLA (Figure 2.36). This is, in fact, where the smallest SSTA variance is found between 23°S (Antofagasta, Chile) and the northern reach of their study (59.5°N; Yakutat Alaska)! This curious feature was not discussed as it was not the focus of their paper. The results of Kessler (2006) and the seminal work of Enfield and Allen- that sea level anomalies do not generate

considerable SST anomalies within the latitude band of the EPWP- are internally consistent with the heat budget calculations discussed in the previous subsection; surface shortwave flux was the strongest contributor to $\partial T/\partial t$ in the EPWP.

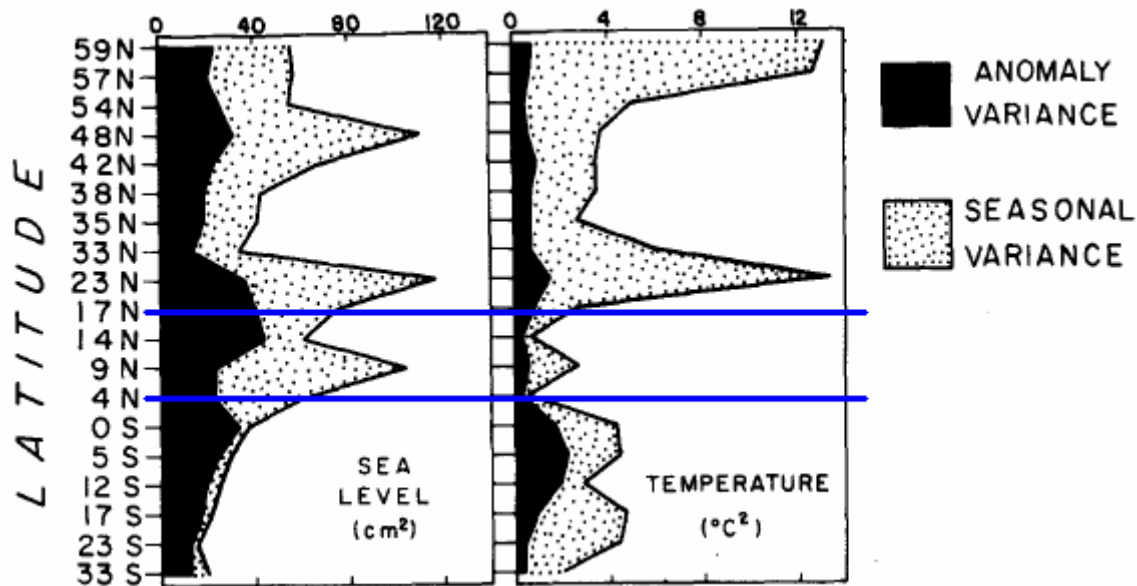


Figure 2.36. Latitudinal distribution of monthly sea level variance (cm^2 ; left) and SST variance ($^{\circ}\text{C}^2$; right) from sea level stations (adapted from Enfield and Allen 1980). Horizontal blue lines have been added to the original figure to indicate the approximate latitudinal band corresponding to the EPWP.

In the present subsection, the role of poleward heat transport in the interannual variability of SST in the EPWP was explored from the perspectives of simulated and observed PHT, the exchanges of warm water volume as previously studied by Meinen and others, and the contribution from Kelvin waves. A careful review of the work of Meinen and others suggests that it is feasible that ocean dynamics and warm water transports do not provide the primary link between the equatorial Pacific and the EPWP, necessitating the invocation of the atmospheric link/shortwave radiation mechanism discussed in the previous subsection to explain the high correlation between SST in the EPWP and eastern equatorial Pacific (i.e., NINO3). In particular, the strong PV front beneath the ITCZ in the north eastern tropical

Pacific is argued to be a key part of why warm water is not exchanged northward, while large discharges are made to the south. Finally, it was shown that Kelvin waves propagate quite freely along the Pacific coast of the Americas, yet there is very little SSTA response to such waves beyond 6°N. In Kessler's review (Kessler 2006), it is mentioned that many previous studies have identified examples of ocean responses as far north as Alaska to equatorially-forced coastal Kelvin waves associated with ENSO. However, and this is evident in Kessler's (2006) Figure 12 and Enfield and Allen's (1980) Figure 2, our model and heat budget calculations are not erroneous in their suggestion that the range of latitudes corresponding to the EPWP are not strongly subject to this influence. Rather, the results described herein strongly suggest that the EPWP is controlled by ENSO through its effect on the distribution of shortwave radiation.

2.5. Gap winds and their role in the interannual variability of SST in the east Pacific warm pool

2.5.1. Observed low-frequency variability of gap winds

Extending from Mt. McKinley in Alaska to Tierra del Fuego at the tip of South America is a series of mountain ranges collectively referred to as the American Cordillera. The important influence of the vast, continental mountain ranges such as the Rockies or the Andes on large-scale circulation and weather patterns is unquestioned, and has been the subject of a vast body of research (e.g., Broccoli and Manabe 1992, Nigam and DeWeaver 1998, Seager, et al. 2002). Through Mexico and Central America, the Sierra Madre Occidental and the Central American Cordillera link the North and South American continents. The coastal mountain ranges of southern Mexico and Central America have two appreciable gaps in which the surface elevation drops sharply to within a few meters of sea level: the Isthmus of Tehuantepec in Mexico, separating the Gulf of Mexico from the Pacific Ocean, and the Isthmus of Papagayo in Nicaragua and Costa Rica, separating the Caribbean Sea from the Pacific Ocean. The Central American mountains and their gaps have been shown responsible for key features of eastern tropical

Pacific climate, such as the boreal wintertime intertropical convergence zone (ITCZ) being displaced south of the sea surface temperature (SST) maximum associated with the east Pacific warm pool (Xu et al. 2005). Cold air masses and anticyclones moving southward from North America and Canada during boreal winter produce strong wintertime pressure gradients, and through orographic interaction with the Isthmuses of Tehuantepec and Papagayo, form intense low-level wind jets over the east Pacific warm pool (e.g., Hurd 1929, Clarke 1988, Schultz et al. 1997, 1998) (Figure 2.37).

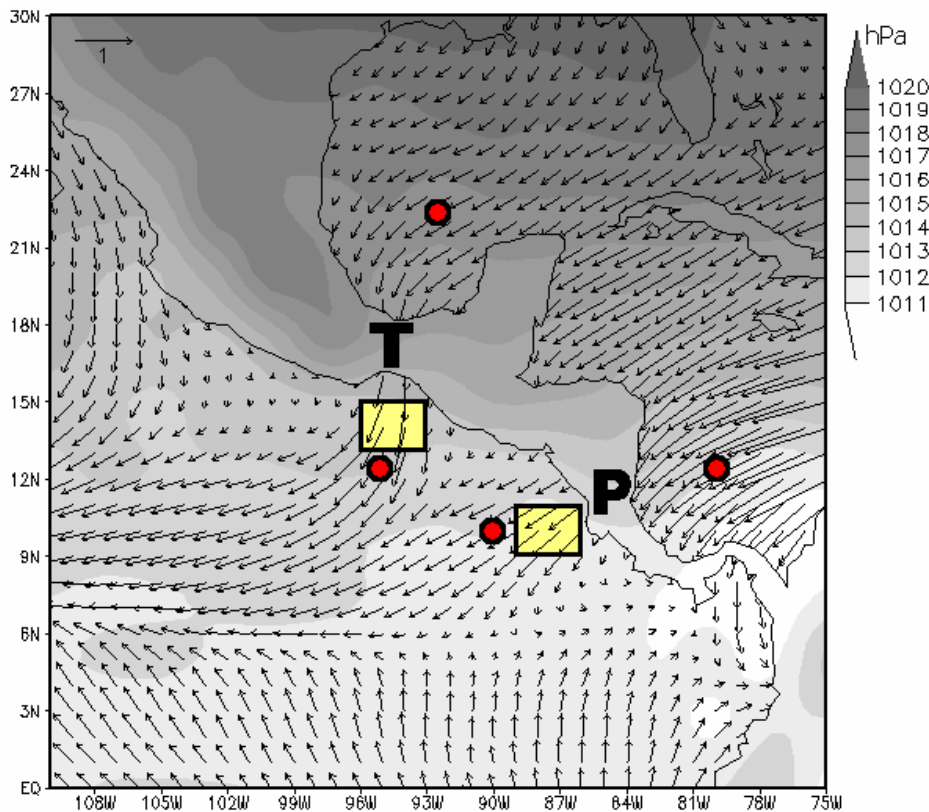


Figure 2.37. Climatology of 1° by 1° December-January SSM/I-QuickSCAT (1988-2004) wind stress (dyn cm^{-2}) and SLP (hPa) in the Inter-Americas region. Yellow boxes denote regions used for calculation of the area average wind stress time series, and red dots denote locations used for calculation of the cross-isthmus pressure differences at Tehuantepec (T) and Papagayo (P), as discussed in the main text.

These wind jets have long been known to the shipping and fishing industries, as well as recreational boaters, many of whom can recall encounters with “Tehuantepecers,” or gale-force

winds near the Gulf of Tehuantepec that seem to “come out of nowhere.” Tehuantepec gap wind events have been observed to carry sustained wind speeds of 50 m s^{-1} (Stumpf 1975), equivalent to a Category 3 hurricane on the Saffir-Simpson Hurricane Scale.

Earth-observing satellite remote sensing missions have provided the atmospheric-oceanic science community high spatial and temporal resolution observations of gap winds and the response of the underlying ocean surface. Although gap wind events are episodic, short-duration phenomena (order days; Chelton et al. 2000a), they have a strong effect on the surface ocean, which can easily be identified in long-term mean and derivative fields (Chelton et al. 2004). As illustrated in Figure 2.38, the Tehuantepec and Papagayo gap winds leave a rich, high-amplitude imprint on the interannual variability of sea surface temperature (SST) and surface chlorophyll concentration in the east Pacific warm pool. Easily identifiable are the Tehuantepec and Papagayo signals (and the Costa Rica Dome, which is not unrelated to the Papagayo gap winds [e.g., Fiedler 2002a, Xie et al. 2005]). The annual cycle and case studies of specific gap wind events have previously been addressed in detail (e.g., Chelton et al. 2000a and 2000b, Xie et al. 2005), as well as the local dynamical and biological consequences (e.g., Fiedler 1994 and 2002a, Farber-Lorda et al. 1994).

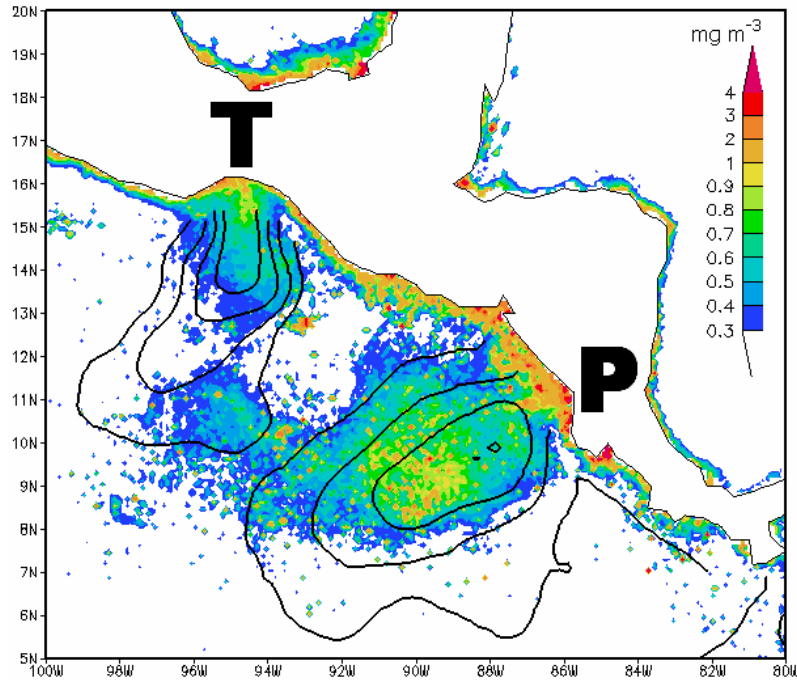


Figure 2.38. Map of standard deviation of monthly anomalies of $1/12^\circ$ by $1/12^\circ$ SeaWiFS (McClain et al. 2004) chlorophyll concentration (mg m^{-3}) (shades) and $1/4^\circ$ by $1/4^\circ$ TMI (Kummerow et al. 2000) SST (contours) (1998–2005). SST standard deviation contours are 0.6°C , 0.8°C , 1.0°C , and 1.2°C . The locations of the Tehuantepec (T) and Papagayo (P) mountain gaps are indicated for reference.

Some effort has also been directed toward understanding the large-scale forcing responsible for the interannual variability of the Tehuantepec and Papagayo gap winds. The temporal variability of Tehuantepec gap winds and its association with El Niño–Southern Oscillation (ENSO) was investigated by Romero-Centeno et al. (2003; hereafter RC-03). RC-03 used what sparse wind observations exist from the southern edge of the Isthmus of Tehuantepec to construct a statistical model for the relationship between the cross-isthmus pressure gradient and Tehuantepec gap wind speed. RC-03 then used the statistical model to reconstruct 31 years of Tehuantepec gap winds. Based on the statistically generated wind record, it was suggested that the monthly Tehuantepec gap winds were stronger during El Niño years and weaker during La Niña years compared with neutral years. However, as the authors note, the difference is only statistically significant for the “weaker gap winds during La Niña” association. Similarly,

Palacios and Bograd (2005) established that there was a higher occurrence of oceanic eddies in the east Pacific warm pool during El Niño years than during La Niña years, wherein it was implied *a priori* that the oceanic eddies were directly related to the gap winds. However, Zamudio et al. (2006) used the same satellite observations and a high-resolution regional ocean model to show that the higher occurrence of eddies in the Gulf of Tehuantepec during El Niño events was equatorially forced, i.e., by downwelling coastally trapped Kelvin waves, originating in the equatorial Pacific. Zamudio et al. (2006) also noted instances with high eddy activity, but calm Tehuantepec gap winds. This suggests that the association between ENSO and oceanic eddies in the east Pacific warm pool is not necessarily due to ENSO modulating the Tehuantepec gap winds, but directly forced by ENSO-related ocean waves.

The Isthmuses of Tehuantepec and Papagayo are only separated by approximately 1,200 km, and both are in close proximity to the eastern equatorial Pacific Ocean where ENSO is the overwhelmingly dominant driver of climate variability. There are, however, two fundamental differences between the two: the Tehuantepec gap is oriented meridionally and adjacent to the Gulf of Mexico, while the Papagayo gap is oriented zonally and adjacent to the Caribbean Sea. Xie et al. (2005) noted that these orientation differences have implications for the ability of each wind jet to influence oceanographic processes in the eastern Pacific Ocean. The fact that the two gaps are oriented along perpendicular axes should also have implications for their relationship with the large-scale flow, as the background mean pressure gradient is generally meridional. For example, Chelton et al. (2000a) concluded that Tehuantepec gap winds are probably forced solely by weather systems of midlatitude origin, while the Papagayo gap winds can exhibit, in some cases, synchrony with the western Caribbean region. The paradigm that ENSO controls the low-frequency variability (“low-frequency” here referring to interannual to decadal timescales) of *both* the Tehuantepec and Papagayo gap winds is the null hypothesis, which is investigated in this chapter within the context of current understanding of what processes are responsible for Central American gap winds.

Time indices of the cross-isthmus SLP difference at Tehuantepec (ΔP_T) and Papagayo (ΔP_P) were computed by taking the absolute magnitude of the difference of SLP between points on either side of each isthmus (illustrated as red dots in Figure 2.37), or:

$$(2.1) \quad \Delta P_T = | \text{SLP}(92.5^\circ\text{W}, 22.5^\circ\text{N}) - \text{SLP}(95^\circ\text{W}, 12.5^\circ\text{N}) | \text{ and}$$

$$(2.2) \quad \Delta P_P = | \text{SLP}(80^\circ\text{W}, 12.5^\circ\text{N}) - \text{SLP}(90^\circ\text{W}, 10^\circ\text{N}) |.$$

The above points were chosen based on the criteria that they are within a few degrees of the Isthmus, and correspond to NCEP-NCAR Reanalysis gridpoints.

The results of the weekly wind stress and cross-isthmus ΔP indices for Tehuantepec and Papagayo over the entire 17-year period 1988-2004 are shown in Figure 2.39. Recall that the background SLP gradient is generally meridional, thus the absolute magnitude of ΔP_T is always larger than ΔP_P . Annually, there is a strong correspondence between the Tehuantepec gap winds and ΔP_T , which simply is consistent with the notion that the strong wintertime cross-isthmus ΔP drives the gap winds and is responsible for their marked seasonality. Also evident in the gap winds indices is a decadal signal. The decadal signal is most robust in the Tehuantepec gap winds themselves, with an inflection point in the mid-1990s. The inflection point does not correspond to the merging of SSM/I and QuickSCAT wind stress data, which falls in July 1999. The 1997-98 and 2002-03 El Niño events are indistinguishable from neighboring years in the Tehuantepec gap winds due to the decadal signal, however, are clearly identifiable at Papagayo.

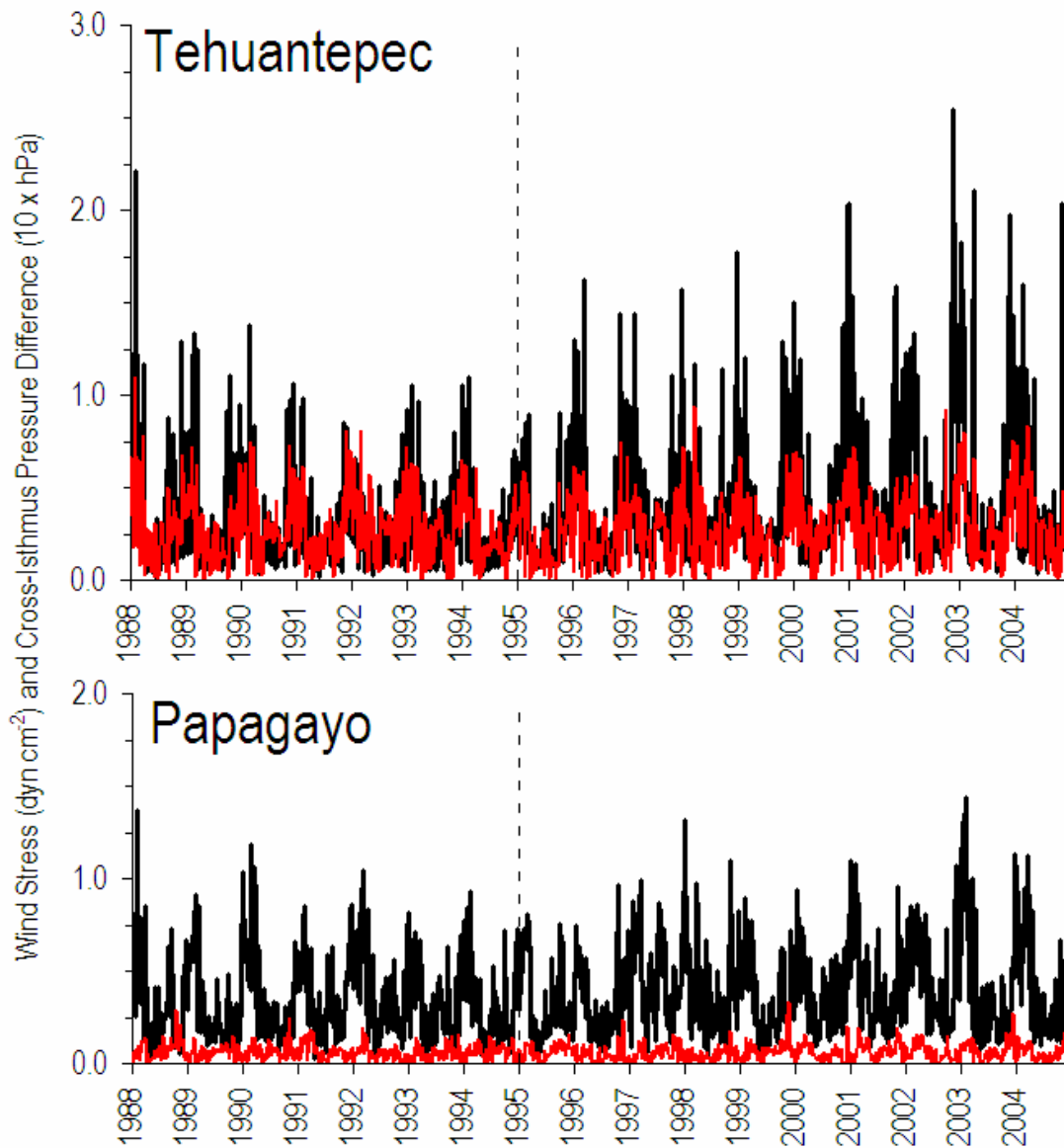


Figure 2.39. Time series of weekly SSM/I-QuickSCAT (1988-2004) wind stress magnitude (black; dyn cm^{-2}) and cross-isthmus pressure difference (red; $10 \times \text{hPa}$), in the Tehuantepec (top) and Papagayo (bottom) regions as denoted in Figure 2.37. The vertical dashed lines denote the boundary between periods discussed in the main text.

To cross-validate the decadal signal detected in the SSM/I-QuickSCAT wind stress, a comparison with the NARR wind speed squared and cross-isthmus ΔP is provided in Figure

2.40. In Figure 2.40, all values are monthly means and shown as standardized anomalies (anomalies divided by one standard deviation, with the mean climatology removed). Keeping in mind the natural differences between satellite observations and regional reanalyses (NARR is of coarser spatial resolution than SSM/I-QuickSCAT before regridding, the SSM/I-QuickSCAT and NARR indices are slightly displaced from one another, and NARR is still a model solution), the comparison is not expected to be a perfect match. Nevertheless, a decadal signal is identifiable in the Tehuantepec indices, as well as the concurrent ΔP_T time series. Additionally, as in Figure 2.39, the Papagayo gap winds appear to be dominated by variability on the interannual timescale. The exceptionally strong 1997-98 El Niño event did not coincide with a significant anomaly at Tehuantepec, but resulted in an anomaly in excess of three standard deviations at Papagayo, in both the SSM/I-QuickSCAT and NARR time series.

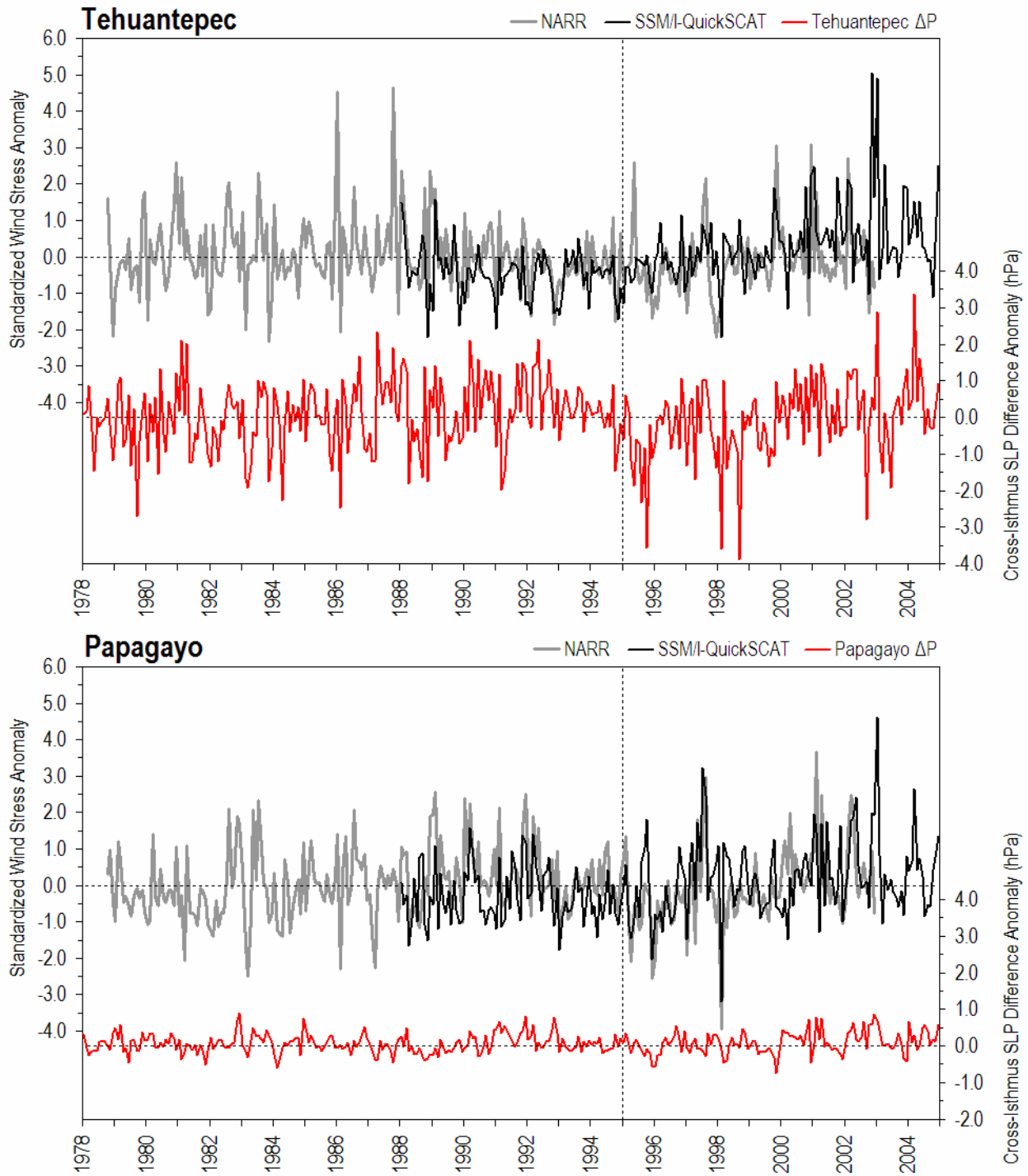


Figure 2.40. Time series of standardized monthly wind stress anomalies from SSM/I-QuickSCAT (1988-2004; black) and NARR (1978-2002; gray), and anomalous cross-isthmus pressure difference at Tehuantepec (1978-2004; red) (top), as in top but for Papagayo (bottom). The vertical dashed line denotes the boundary between periods discussed in the main text.

To summarize, the major differences between the low-frequency variability of the Tehuantepec and Papagayo gap winds are that the Tehuantepec gap winds appear to be dominated by a decadal signal with a lack of association with ENSO, and the Papagayo gap winds are dominated by variability on interannual timescales with a clear influence from ENSO. Diagnosing the low-frequency variability of the Tehuantepec and Papagayo gap winds and remote forcing mechanisms for decadal variability, therefore, are discussed in the following subsections.

2.5.2. Remote forcing of gap winds

In this subsection, a case is presented that the low-frequency variability of the Tehuantepec gap winds is related to a different remote forcing mechanism than that of the Papagayo gap winds. First, to gain a qualitative sense of what large-scale patterns of variability might be related to the Tehuantepec and Papagayo gap winds, linear regression analysis (least-squares method) was performed using global SST. Reynolds and Smith (2002) SST anomalies (mean climatology removed) were regressed onto the monthly SSM/I-QuickSCAT gap wind anomalies for both Tehuantepec and Papagayo. The results of the linear regression analysis for Tehuantepec (Papagayo) are shown in the top panel of Figure 2.41 (2.42). Also shown in the bottom panel of Figure 2.41 (2.42) is the regression of SST onto the Atlantic Tripole Pattern index (NINO3). NINO3 is defined as the area average SST anomaly from 5°S-5°N, 150°W-90°W. The Atlantic Tripole Pattern (ATP) is defined as the leading EOF of SST in the tropical North Atlantic Ocean (Deser and Timlin 1997). Observations by Deser and Blackmon (1993) show the ATP to vary with a period of 12-16 years. The ATP is also described by Chiang and Vimont (2004) as a meridional mode of coupled ocean-atmosphere variability between surface winds and the meridional SST gradient in the tropical Atlantic Ocean. The most surprising result of the linear regression analysis (Figure 2.41) is the lack of an ENSO signal in the

Tehuantepec winds. Rather, there is a high degree of similarity between the regression of SST onto the Tehuantepec gap winds and the regression of SST onto the ATP index; the spatial correlation over the domain shown is $r_s = 0.60$. The salient feature in the Atlantic basin is a positive SST anomaly across the tropical North Atlantic. Physical mechanisms for the ATP remotely forcing the Tehuantepec gap winds are discussed in the following subsection.

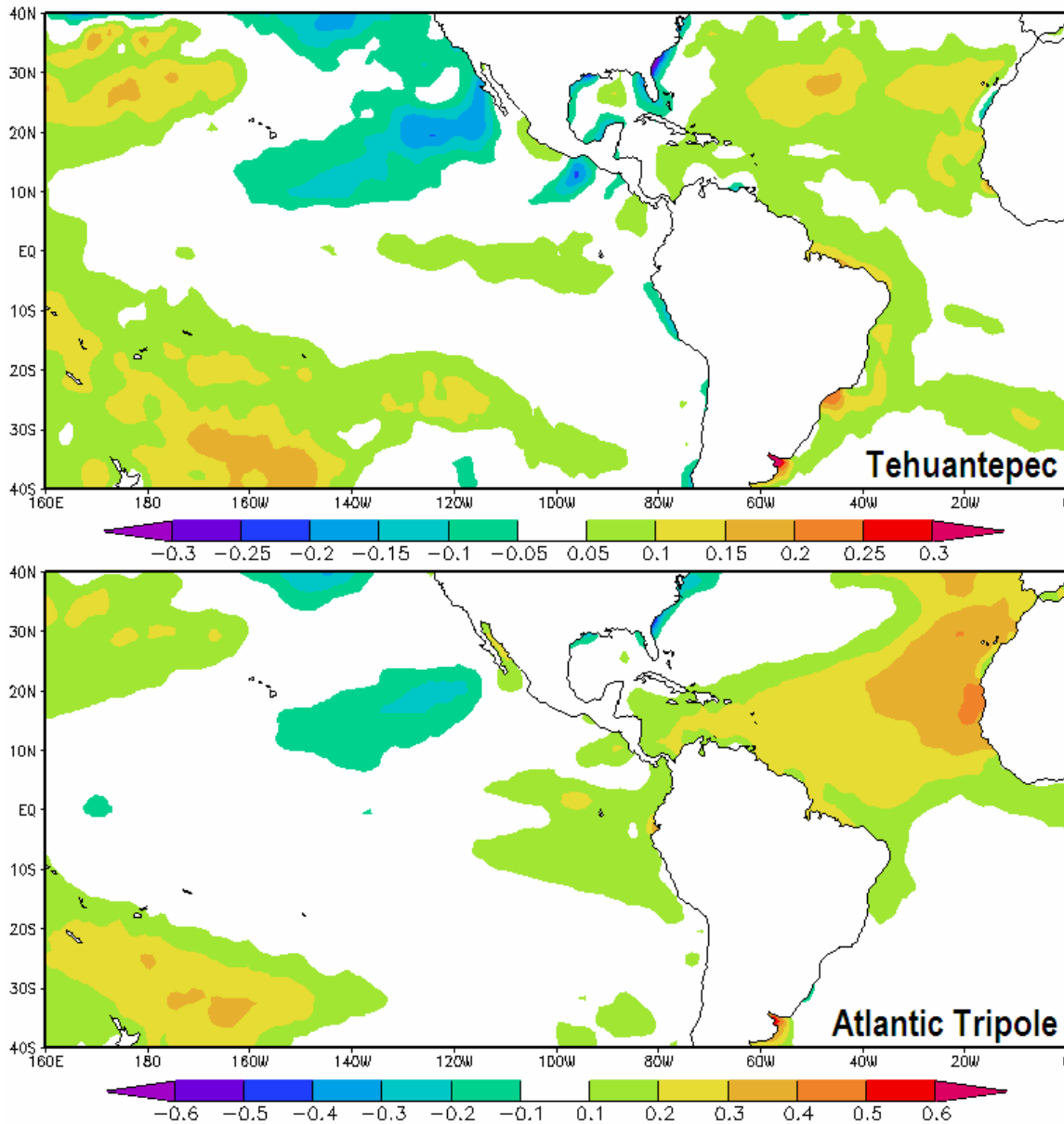


Figure 2.41. Reynolds SST anomalies (°C) regressed onto the SSM/I-QuickSCAT Tehuantepec (top), Atlantic Tripole (bottom) indices.

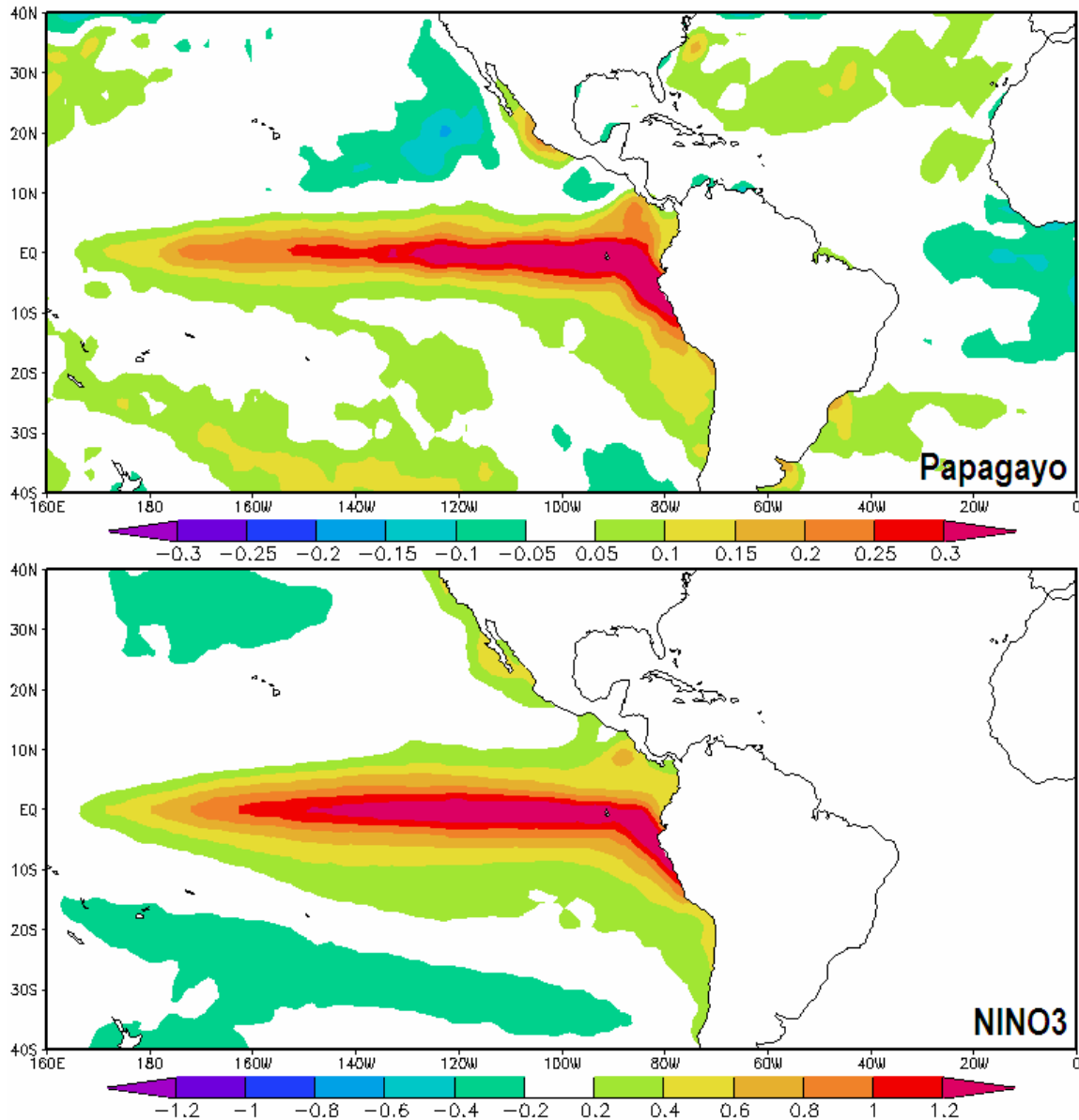


Figure 2.42. Reynolds SST anomalies ($^{\circ}\text{C}$) regressed onto the SSM/I-QuickSCAT Papagayo (top), and NINO3 (bottom) indices.

In contrast, the regression of SST onto the Papagayo gap winds (Figure 2.42) shows a clear ENSO signal. The spatial correlation between the regression of SST onto the Papagayo gap winds and the regression of SST onto NINO3 is $r_s = 0.72$ over the domain shown, which is consistent with the null hypothesis that ENSO governs the temporal variability of gap winds as it pertains to the Isthmus of Papagayo, but draws a sharp distinction with that of Tehuantepec.

The distinction is reconciled with the results of Zamudio et al. (2006) who established a mechanistic connection between ENSO and oceanic eddies in the Gulf of Tehuantepec, which was *not* ENSO modulating the Tehuantepec gap winds.

Appearing in the low-frequency evolution of the ATP time series (Figure 2.43) is a sharp transition between 1994 and 1995. After roughly a decade in the near-neutral phase of the ATP, came a shift into a full decade of positive ATP. The only exception is a brief (3 months) dip in early 2003. Similarly, as indicated by the dotted lines in all time series shown in this chapter, the shift in the ATP roughly corresponds to an inflection point in the decadal signal of the Tehuantepec gap winds. The wintertime (December-January) correlation of the Tehuantepec gap wind index and the ATP is $r_t = 0.49$ (significant at the 95% confidence level, based on a two-tailed Student's t-test).

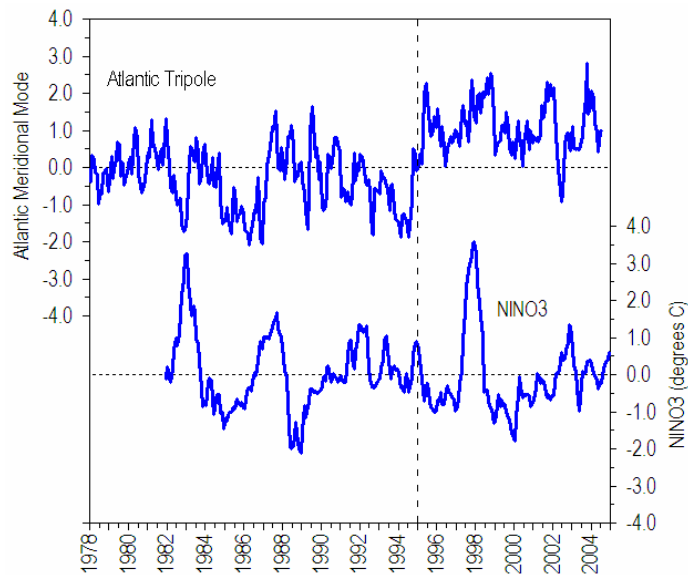


Figure 2.43. Monthly time series of Atlantic Tripole (January 1978-July 2004) and NINO3 (Reynolds and Smith [2002]; December 1981-2004) indices. The vertical dashed line denotes the boundary between periods discussed in the main text.

To contrast the large-scale flow features associated with the periods before and after the ATP shift, composite anomaly fields were constructed for wintertime 500-hPa geopotential height

and winds before and after the shift (Figure 2.44 top and middle panels). Also shown in Figure 2.44 (bottom panel) is the linear regression of wintertime 500-hPa geopotential height and wind anomalies onto the ATP index for the full NCEP-NCAR Reanalysis period (1949-2003). As previously discussed most prior work cites cold surges and anticyclones moving southward over North America and entering the Gulf of Mexico as one of the primary mechanisms for setting up a pressure gradient conducive to driving strong gap winds. Common to the post-shift and regressed large-scale flow fields is indeed a pattern favorable for steering such systems into the Gulf of Mexico. Furthermore, as the composites and regressions for pressure levels lower in the atmosphere look similar (not shown), it is possible that the large-scale flow contributes to the northerly momentum involved in the Tehuantepec gap winds themselves. Indeed, the strong anomalous northerly flow over the Gulf of Mexico toward the Isthmus of Tehuantepec associated with the post-shift pattern and the ATP regression (Figure 2.44, middle and bottom panels) is also clearly evident in a composite map of surface wind stress for strong Tehuantepec gap winds.

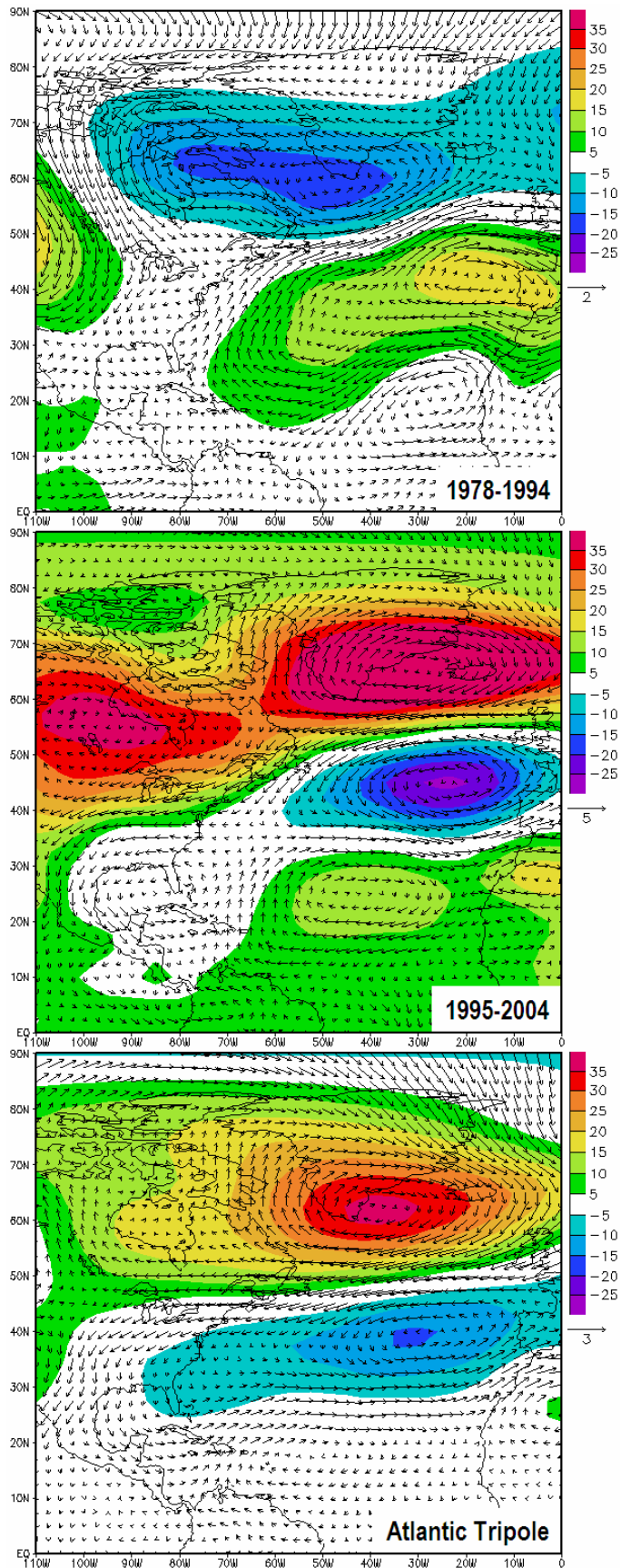


Figure 2.44. Composite December-January 500-hPa geopotential height (m) and wind (m s^{-1}) anomalies for 1978-1994 (top), 1995-2004 (middle), and the regression of December-January 500-hPa geopotential height and winds onto the December-January Atlantic Tripole Index from 1949-2003 (bottom).

After removing the weekly climatology, weeks during which the wind stress anomaly in the Tehuantepec index exceeded a value of 0.8 dyn cm^{-2} were included as members of the composite. The result is shown in Figure 2.45, and reveals anomalous northerly flow, which is consistent with the large-scale flow pattern indicated in the post-shift and ATP regression figures. The northerly flow effectively enters a topographic funnel, with broader Mexico to the west, the Yucatan Peninsula to the east, and the Isthmus of Tehuantepec being the primary, albeit narrow, outlet for the zonally-constricted northerly flow. In a composite map for strong Papagayo gap winds, the anomalous northerly flow over the Gulf of Mexico is not evident (not shown). In Figure 2.44, the pre-shift pattern is symmetric to the post-shift pattern; continental systems are drawn into the north Atlantic without the opportunity to interact with the Sierra Madre Occidental or the Central American Cordillera, and the background northerly flow is not present to contribute to the Tehuantepec gap winds.

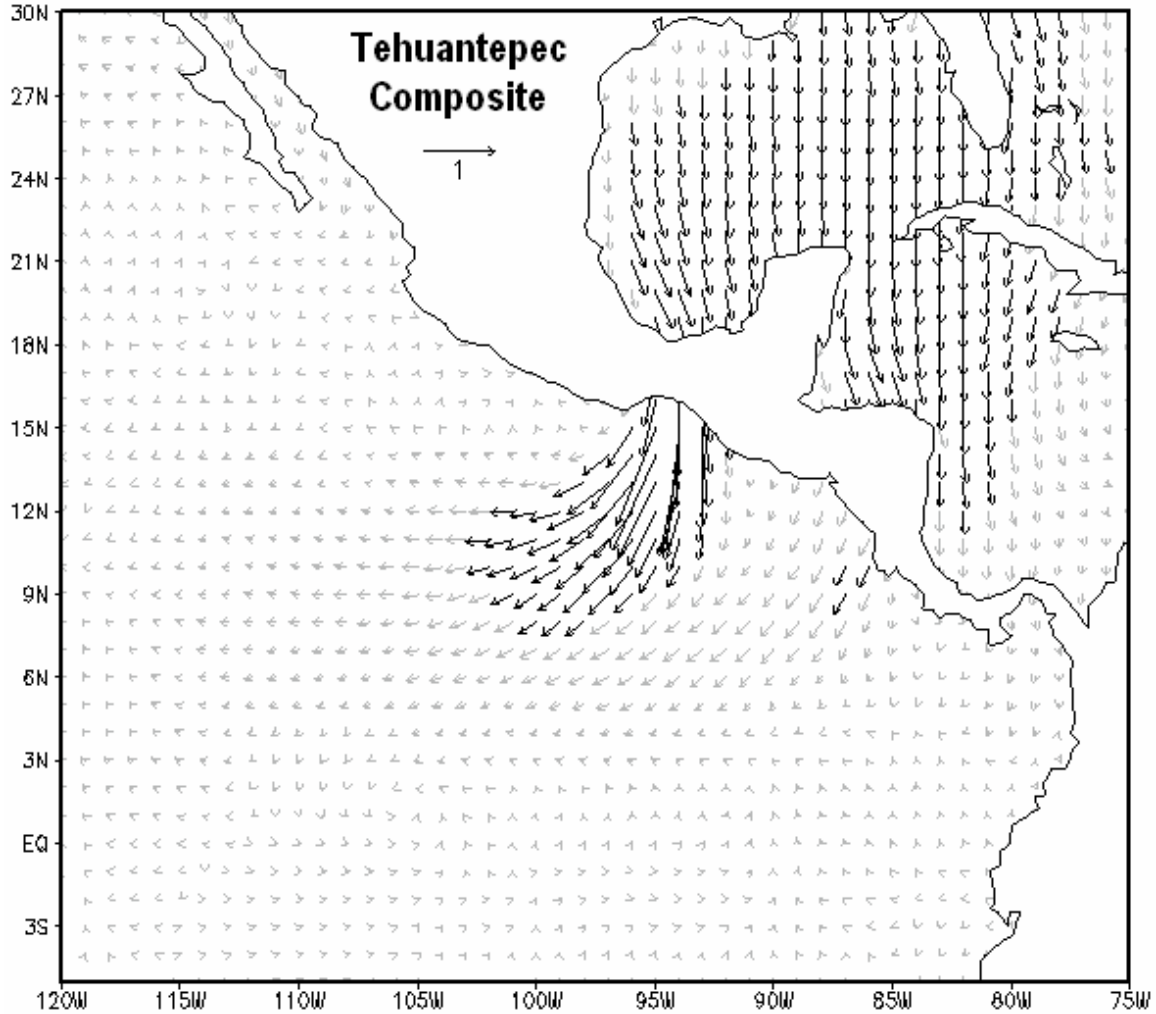


Figure 2.45. Composite weekly SSM/I-QuickSCAT surface wind stress anomalies (dyn cm^{-2}) for strong Tehuantepec gap winds. Values less than 0.3 dyn cm^{-2} are shaded gray.

While the Tehuantepec gap winds appear to be associated with the ATP, and the Papagayo gap winds associated with ENSO, interactions between the tropical north Atlantic Ocean and the extratropical atmospheric circulation, as well as interactions between the Pacific and Atlantic basins, complicate such generalizations. As the wintertime regression of 500-hPa flow onto the ATP (Figure 2.44, bottom) closely resembles the negative phase of the North Atlantic Oscillation (NAO), we consider the interaction between the extratropical Atlantic atmospheric circulation (i.e., the NAO), and SST in the tropical north Atlantic (i.e., the ATP).

The NAO can influence SST anomalies associated with the ATP by modulating the strength of the tropical Atlantic tradewinds and thus surface heat fluxes (e.g., Xie and Carton 2004). To illustrate the low-frequency variability of such interactions, the 6 year low-pass filter of Zhang et al. (1997) was applied to the ATP and NAO indices, and is provided in Figure 2.46. The low-pass-filtered ATP and NAO time series are correlated $r_t = 0.40$, although that correlation is not likely to be statistically significant due to the low number of degrees of freedom. Nevertheless, the NAO exhibits a shift in 1995 corresponding to the shift in the ATP that was described in the previous subsection. Given the spatial and temporal similarities, the ATP could in some sense be described as a low-frequency expression of the NAO, which would be consistent with the mechanism proposed in the previous subsection. The NAO forcing of tropical north Atlantic SST is strongest in boreal winter. Further details on the NAO and the low-frequency expressions thereof can be found in e.g., Curry and McCartney (2001), Eden and Jung (2001), or Czaja and Frankignoul (2002).

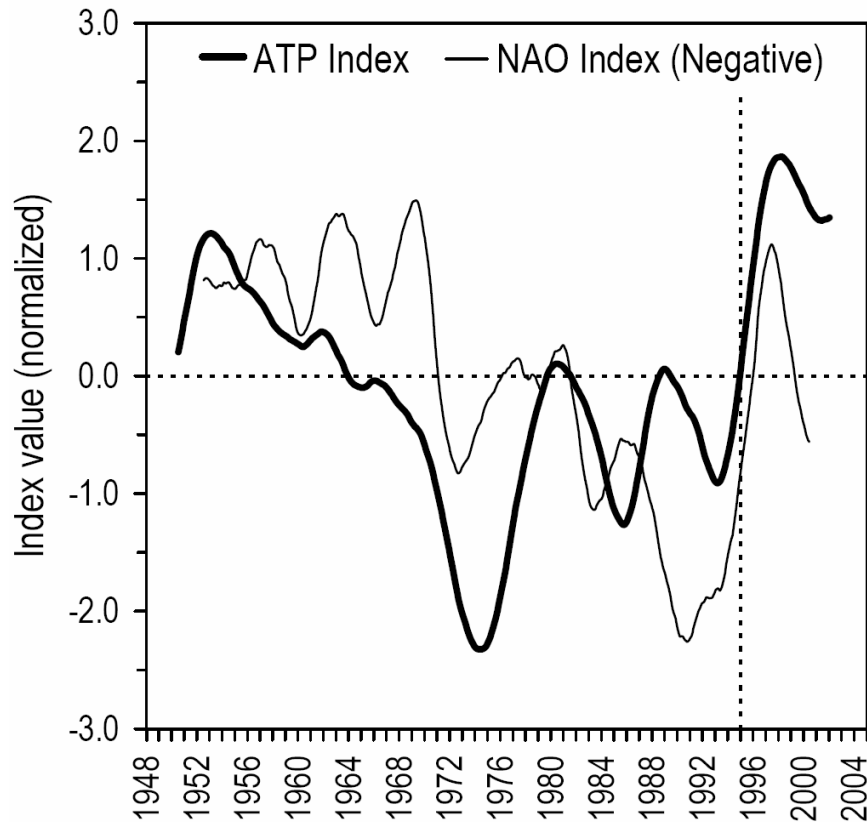


Figure 2.46. Six year low-pass filtered (Zhang et al. 1997) time series of Atlantic Tripole (heavy line) and North Atlantic Oscillation (negative; thin line) indices.

In addition to influences from the extratropical circulation, the ATP is also subject to the influence of interannual variability in the equatorial Pacific. It has been shown that the tropical north Atlantic responds to ENSO events by a reduction (in the case of El Niño) of the tradewinds over the tropical north Atlantic, leading to a delayed warming of SST through reduced evaporative heat flux (Enfield and Mayer 1997). Such response of the tropical north Atlantic to ENSO tends to manifest itself primarily in boreal spring. The GCM results of Saravanan and Chang (2000) further support this concept by showing that sensible heat fluxes also contribute to the tropical north Atlantic's warming response. Thus, there is the potential for ENSO to also influence Tehuantepec gap winds, by way of ENSO contributing to the ATP. Given the delayed response mechanism, this somewhat indirect remote forcing mechanism should be strongest in boreal spring, when the Tehuantepec gap winds are dying down from the active winter season. The relatively weak signal found in the eastern equatorial Pacific in the regressions of SST onto the Tehuantepec and ATP indices (Figure 2.41) could be a hint of this indirect and delayed role of ENSO in forcing Tehuantepec gap winds.¹ Alternatively, this could also be interpreted as consistent with the finding of Schultz et al. (1998) that, from 1900-1957, approximately twice as many cold surge events were observed in southern Mexico during cold seasons that correspond to El Niño years than those that correspond to La Niña years. Schultz et al. (1998) did not compare cold surge frequency with Atlantic modes of variability.

For completeness, the climate and cross-isthmus ΔP indices are shown in Figure 2.47 for the entire NCEP-NCAR Reanalysis period (1948-2004). With over five decades of data, the overall result is the same. Visually, the ΔP_T , ATP, and Tehuantepec gap wind time series (top)

¹ This is in contrast to the contribution of the NAO, which should be focused in the wintertime- concurrent with the season during which the gap winds are most active- when the NAO exerts greatest influence on the tropical north Atlantic SST and the steering of continental weather systems.

appear distinctly different than the ΔP_P , NINO3, and Papagayo gap wind time series (bottom) in their dominant timescales. To quantitatively confirm this visual impression, a discrete Fourier transform (DFT) was performed on the climate and cross-isthmus ΔP time series. Shown to the right of each time series comparison are the corresponding power spectra (in RMS as a function of period). In the power spectra comparison for the ΔP_T , there is a primary spectral peak at the decadal period, and a smaller peak at the ENSO period. This is consistent with the ATP power spectrum, which has a strong peak at the decadal (and one at a period of ~ 50 yr, which is caused by the singularly abrupt 1994-1995 shift).

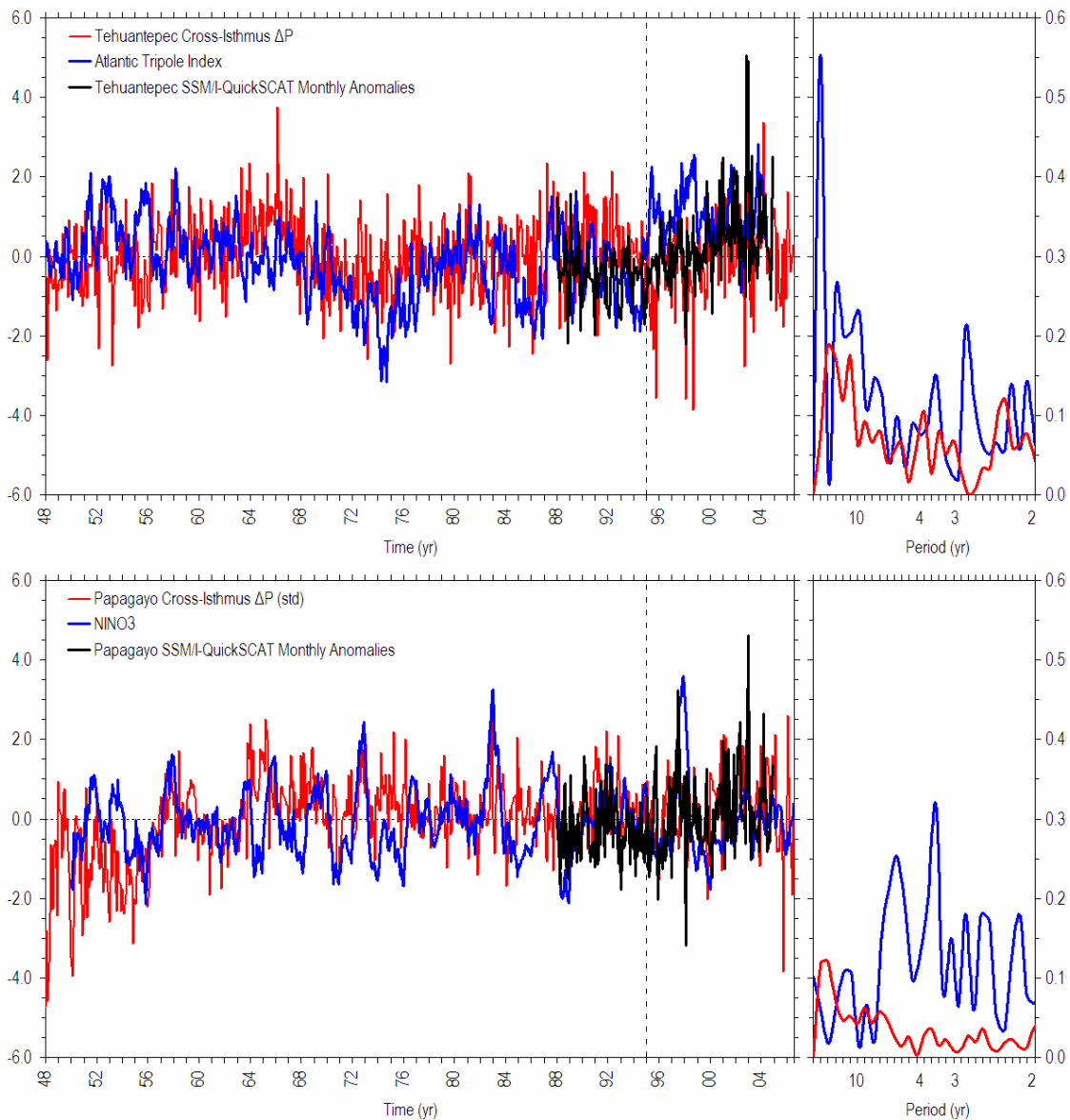


Figure 2.47. Top: Monthly time series of the Atlantic Tripole index, SSM/I-QuickSCAT wind stress anomalies, anomalous cross-isthmus pressure difference at Tehuantepec (left), and corresponding power spectra (RMS as a function of period computed using discrete Fourier transform) (right). Bottom: as in top, but for NINO3 and Papagayo.

An alternative technique for computing power spectra which readily lends itself to understanding the statistical significance of spectral peaks is the multi-taper method (available in UCLA SSA-MTM Toolkit for Spectral Analysis, useful mathematical discussion in Ghil et al. 2002). Based on the MTM method, decadal peaks in the ATP spectrum (8 and 11 yr) and ΔP_T spectrum (12 yr) are significant at the 99% confidence level. The ΔP_T spectrum also has a significant peak at an interannual (2.4 yr) period. In the NINO3 spectrum, interannual (2 and 5 yr) peaks are significant, while the interannual peak in the ATP spectrum is not. Our spectral analyses therefore support the idea put forth in the previous section: the low-frequency variability of the Tehuantepec gap winds is subject to considerable remote forcing from the ATP, while ENSO plays a more dominant role in the Papagayo gap winds.

RC-03 combined a relatively long, continuous record of observed cross-isthmus ΔP at the Isthmus of Tehuantepec with the shorter-duration intervals of wind observations that were available to construct a statistical model for the Tehuantepec gap winds. Here, we take a similar approach and attempt to reconstruct the Tehuantepec and Papagayo gap wind time series using multiple linear regression (least-squares method). In addition to cross-isthmus ΔP , we incorporate large-scale climate information into the statistical model by using the ATP and ENSO indices as additional predictors. It should also be noted that we are attempting to reconstruct the monthly anomalies, as the inputs to our regression model are themselves anomalies (mean seasonal cycle removed). The general equation for the multiple linear regression model is:

$$(2.3) \quad y = b_0 + b_1 x_1 + b_2 x_2 + \dots + b_k x_k$$

where y is the predictand, b_k is the k^{th} regression coefficient, and x_k is the k^{th} predictor. After solving for the regression coefficients, the regression model for the reconstructed Tehuantepec gap winds (V_T) using all three predictors is:

$$(2.4) \quad V_T = -0.028 + 0.064 \Delta P_T + 0.054 \text{ ATP} - 0.003 \text{ NINO3}$$

Furthermore, predictors can simply be removed from the regression process one-by-one to test the contribution of that information to the total reconstruction. In these cases, the regression model becomes:

$$(2.5) \quad V_T = -0.028 + 0.064 \Delta P_T + 0.054 \text{ ATP, and}$$

$$(2.6) \quad V_T = -0.002 + 0.053 \Delta P_T.$$

The results of this process are shown in Figure 2.48 (left column). The interannual and lower-frequency variability in the Tehuantepec gap wind time series is reproduced reasonably well when all three predictors are used: ΔP_T , ATP and ENSO (temporal correlation between the observed and reconstructed time series is $r_t = 0.46 / r_t = 0.59$ with 5-month centered moving mean). When ENSO is not included as a predictor in the regression process, the result is relatively unchanged ($r_t = 0.46 / 0.58$), confirming that ENSO plays a minor role in governing the low-frequency variability of the Tehuantepec gap winds. When ΔP_T is the only predictor (i.e., single linear regression), there is significant loss of fidelity of the time series, particularly in the interannual and lower-frequency variability ($r_t = 0.33 / 0.19$), suggesting that there is important information in the large-scale flow that is not transmitted directly through the SLP gradient. All of the aforementioned correlations between observed and reconstructed Tehuantepec gap wind time series are statistically significant at the 99.9% confidence level with the exception of the smoothed reconstruction using only ΔP_T .

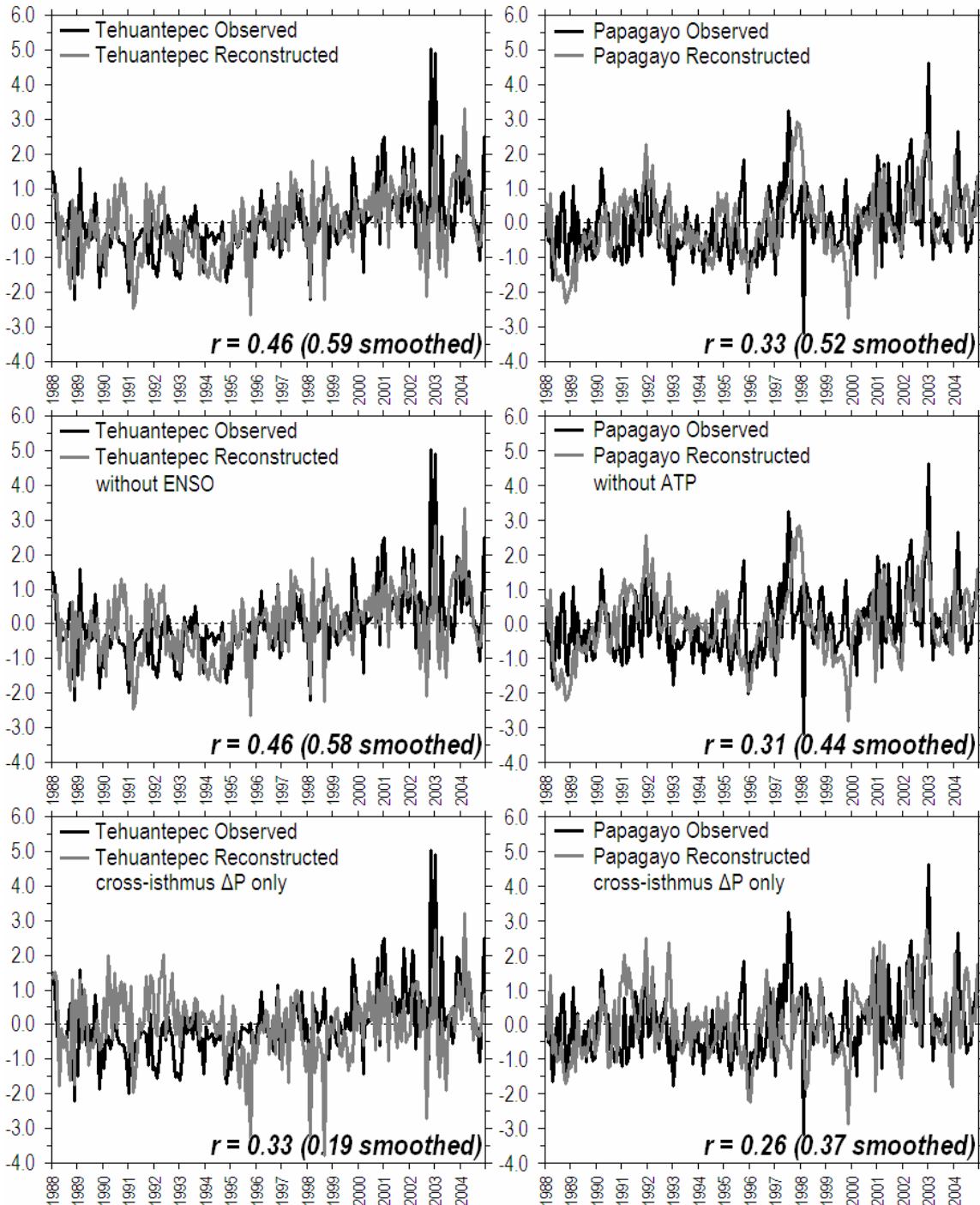


Figure 2.48. Left: Monthly time series of wind stress anomaly at Tehuantepec from SSM/I-QuickSCAT and that reconstructed via multiple linear regression using ΔP_T , ATP, and ENSO (top), as in top but without ENSO (center), as in top but using ΔP_T only (bottom). Right: monthly time series of wind stress anomaly at Papagayo from SSM/I-QuickSCAT and that reconstructed via multiple linear regression using ΔP_P , ENSO, and ATP (top), as in top but without ATP (center), as in top but using ΔP_P only (bottom).

Linear correlation coefficients are shown in lower-right corners; smoothed coefficients refer to observations and reconstructions to which a 5-month centered moving mean was applied as discussed in the main text. All time series shown are normalized.

The regression model with coefficients for the reconstruction of the Papagayo gap winds (V_P) are:

$$(2.7) \quad V_P = -0.011 + 0.088 \Delta P_P + 0.022 \text{ NINO3} + 0.011 \text{ ATP},$$

$$(2.8) \quad V_P = -0.005 + 0.085 \Delta P_P + 0.023 \text{ NINO3}, \text{ and}$$

$$(2.9) \quad V_P = -0.009 + 0.104 \Delta P_P.$$

The results of the Papagayo reconstruction are presented in Figure 2.48 (right column). As expected, the reconstructed Papagayo gap wind time series is optimal when ENSO is included as a predictor in the regression process ($r_t = 0.31 / 0.44$), with a minor improvement by including the ATP ($r_t = 0.33 / 0.52$), and the least fidelity when ΔP_P is the only predictor ($r_t = 0.26 / 0.37$).

As previously mentioned, the case studies of Chelton et al. (2000a) suggested that variability in the western Caribbean may, in some cases, be an important factor in driving Papagayo gap wind events. Rather than using the cross-isthmus SLP difference ΔP_P , we now consider the use of a sea level pressure gradient in the western Caribbean region. Shown in Figure 2.49 (top panel) is the result of a linear regression of SLP monthly anomalies onto zonal wind speed at a point near the western edge of the strong easterly tradewinds characteristic of the Caribbean region. From the sharp SLP gradient evident in the regression, we construct an index of a meridional pressure gradient across the Caribbean ΔP_{Carib} . The zonal wind speed at the chosen point is highly correlated with the ΔP_{Carib} index ($r_t = 0.92$). To obtain a regional picture of the influence of the meridional SLP gradient in the western Caribbean on the zonal wind field, we regress zonal wind on the ΔP_{Carib} index (Figure 2.49, middle). The analysis suggests that the meridional SLP gradient in the Caribbean can exert an influence not only on

the strength of the tradewinds in the western Caribbean, but its influence extends over the east Pacific warm pool with a relatively strong signal in the exit region of the Papagayo gap winds.

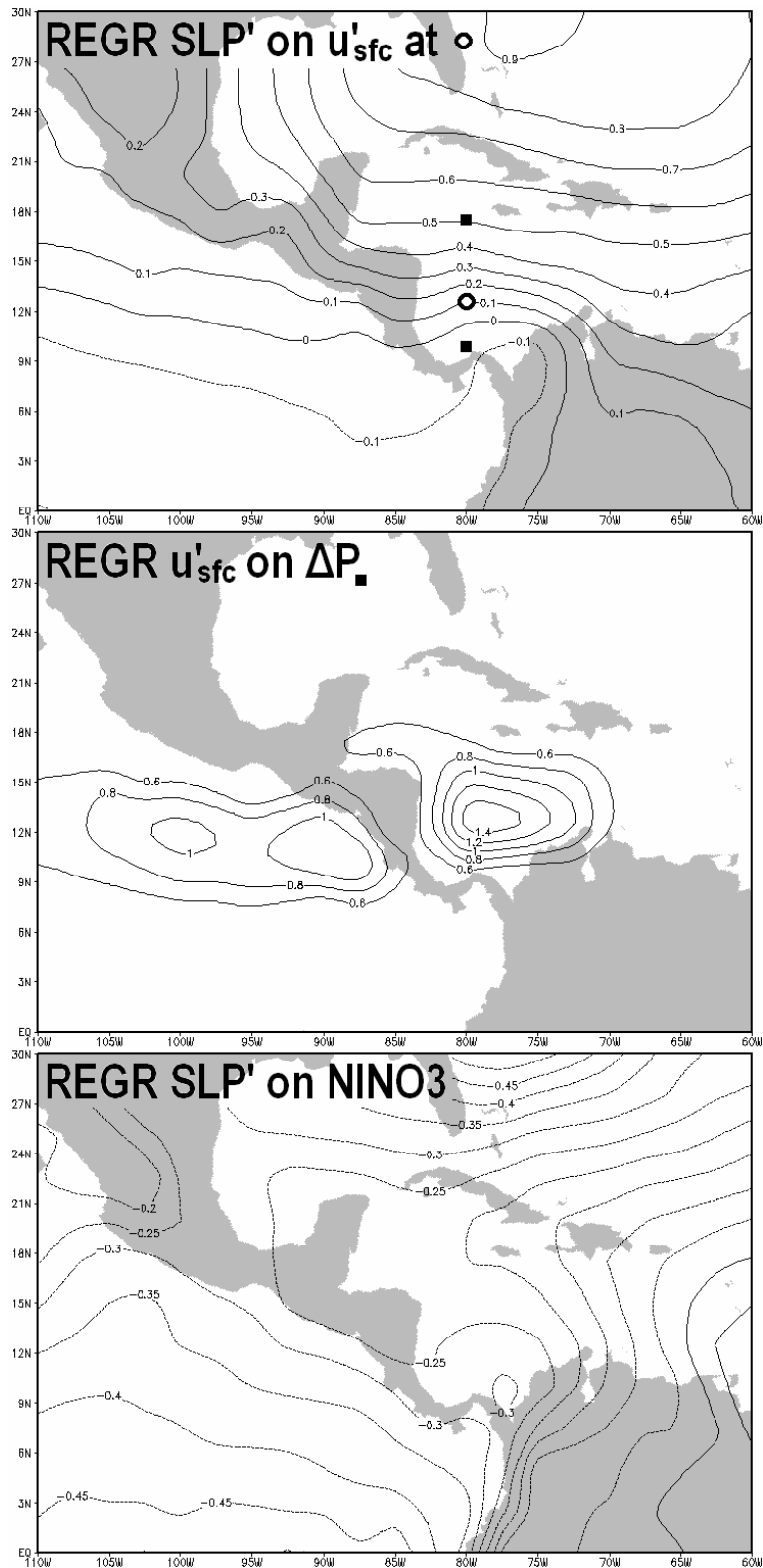


Figure 2.49. Linear regression of monthly SLP anomalies onto an index of easterly surface zonal wind speed anomalies at 80°W, 12.5°N (denoted by a circle) (contour interval 0.05 hPa) (top), linear regression of easterly zonal wind speed anomalies onto an index of the anomalous pressure difference between 80°W, 17.5°N and 80°W, 10°N (denoted by squares in top panel) (middle), and linear regression of SLP anomalies onto the NINO3 index (bottom), using monthly NCEP/NCAR Reanalysis data (Kalnay et al. 1996) for the period January 1988-December 2004.

This analysis is consistent with the notion that ENSO is a dominant control on the interannual variability of the Papagayo gap winds, since ENSO is capable of modifying the SLP field in such a way that the meridional SLP gradient in the western Caribbean would be affected. To illustrate this dependence, Figure 2.49 (bottom panel) shows the regression of monthly SLP anomalies onto the NINO3 index. During an El Niño, for example, anomalously warm SST in the eastern equatorial Pacific leads to lowered SLP as far east as the coast of South America, which is far enough to increase the meridional pressure gradient across the western Caribbean. In light of the fact that variability in the western Caribbean appears to be capable of contributing to the Papagayo gap winds, we repeat the time series reconstruction, but now incorporating ΔP_{Carib} as a predictor along with ΔP_P and NINO3. The multiple linear regression equation and coefficients thus become:

$$(2.10) \quad V_P = -0.002 + 0.050 \Delta P_P + 0.022 \text{NINO3} + 0.051 \Delta P_{\text{Carib}}.$$

The results of the reconstruction that includes the western Caribbean influence are provided in Figure 2.50, and are to be compared with the Figure 2.48 (right column, middle panel), which yielded a correlation coefficient of $r_t = 0.31 / 0.44$. The correlation coefficient when the ΔP_{Carib} predictor is included in the model is $r_t = 0.41 / 0.48$. This suggests that the improvement is more evident when the higher frequency variability is not smoothed out. Thus, we conclude that the Papagayo gap winds are still subject to ENSO as the dominant mode of interannual

variability, but a clear influence from the western Caribbean contributes to the overall variability- not to ignore that ENSO and ΔP_{Carib} are not independent of one another.

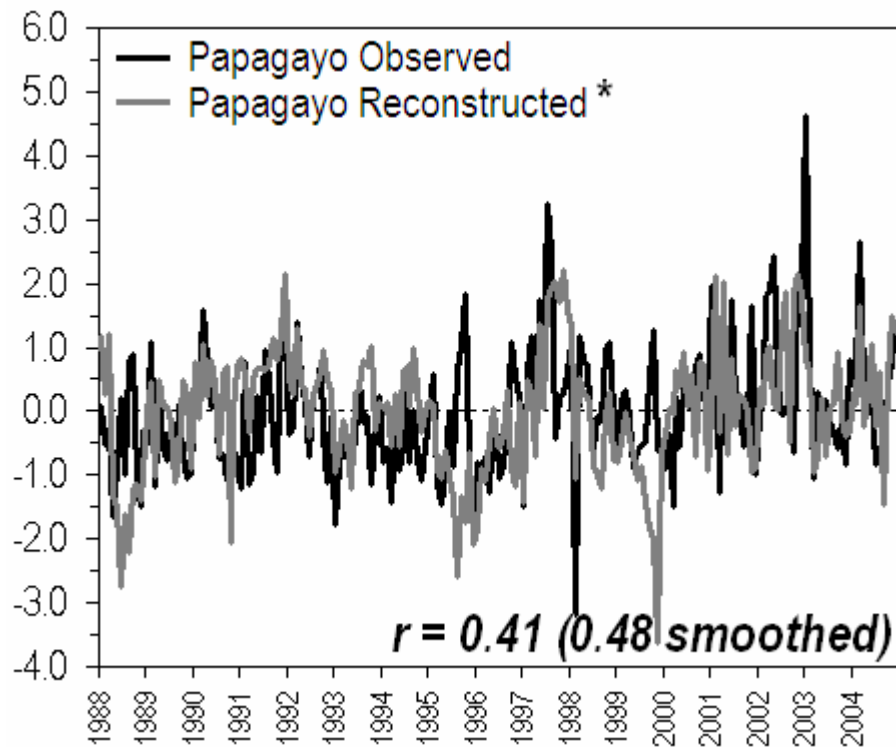


Figure 2.50. Monthly time series of wind stress anomaly at Papagayo from SSM/I-QuickSCAT and that reconstructed via multiple linear regression using ΔP_P , ENSO, and ΔP_{Carib} . Linear correlation coefficients are shown in lower-right corners; smoothed coefficients refer to observations and reconstructions to which a 5-month centered moving mean was applied as discussed in the main text. All time series shown are normalized.

The present chapter is aimed at describing the low-frequency variability of the Tehuantepec and Papagayo gap winds, and to examine the intuitive notion that ENSO would be the primary remote forcing mechanism for both phenomena. The Tehuantepec gap winds appear to be dominated by a decadal signal with a lack of association with ENSO, and the Papagayo gap winds are dominated by variability on interannual timescales with a clear influence from ENSO. The lack of an ENSO signal in the Tehuantepec winds is affirmed by regressing global SST onto the time series of Tehuantepec gap winds. Instead, there is a high

degree of similarity with the ATP. The regression of SST onto the Papagayo gap winds show a strong ENSO signal, which is consistent with the assumed relationship between ENSO and the temporal variability of gap winds as it pertains to the Isthmus of Papagayo. Common to the large-scale flow patterns after the 1994-1995 shift in the ATP as well as that regressed onto the ATP is a pattern favorable for steering midlatitude systems into the Gulf of Mexico. It is also possible that the large-scale flow contributes to the northerly momentum involved in the Tehuantepec gap winds themselves.

Given the observed effects of the Tehuantepec gap winds on variability in the tropical Pacific, this mechanism represents a direct pathway for Atlantic forcing of Pacific variability. It is also important to note that the Pacific and Atlantic basins are not completely independent from one another, and that the tropical Atlantic Ocean is also subject to remote forcing from the extratropical atmospheric circulation.

Through reconstruction of the Tehuantepec and Papagayo gap wind time series including large-scale climate information, the Tehuantepec gap wind time series is reproduced with higher fidelity when the cross-isthmus pressure difference, ATP and ENSO are included. When ENSO is not included, the result is relatively unchanged, confirming that ENSO plays a minor role in the Tehuantepec gap winds. However, there is significant loss of fidelity of the time series when the ATP is not included in the reconstruction process, suggesting there is important information in the large-scale flow that is not transmitted directly through the background SLP gradient. There is one dominant low-frequency forcing for the Tehuantepec gap winds: the ATP, and apparently multiple remote forcings for the Papagayo gap winds, with ENSO being the most important as it is of highest amplitude. The geostrophic modulation of the easterly trades in the western Caribbean can also act as a remote driver of the Papagayo gap winds, which is itself not fully independent from ENSO.

To the extent that ENSO and the ATP are predictable, these results suggest promise for the predictability of the interannual to decadal variability of the Tehuantepec and Papagayo gap

winds. For example, a simple analysis of the ATP-Tehuantepec gap winds paired data between 1988-2004 suggests that if the ATP is negative, there is a 78% probability that the monthly mean Tehuantepec gap wind stress magnitude will be less than normal (climatology). Further, if the ATP is negative by at least one standard deviation, it is nearly certain (100% probability) that the Tehuantepec gap winds will be weaker than normal. However very little predictability appears to be offered from the ATP when the ATP is positive. Conversely, the Papagayo gap winds are apparently more predictable from NINO3 when ENSO is in a warm phase. Again based on paired data from 1988-2004, there is a 76% probability that the Papagayo gap winds will be stronger than normal if NINO3 is positive by at least one standard deviation. Hence, to the extent that tropical north Atlantic SSTs and ENSO are predictable, some predictability of the Central American gap winds, accompanied by a measure of certainty which depends on the state of the predictor, can be offered.

2.5.3. The effects of gap winds on SST interannual variability in ocean model experiments

Thus far in the present section, we have discussed the observed low-frequency variability of the Tehuantepec and Papagayo gap winds. We have identified that the Tehuantepec gap winds, over the period 1988-2004, are dominated by a remote influence from the North Atlantic basin (the Atlantic Tripole Pattern), while the Papagayo gap winds are largely dominated by the influence of the equatorial Pacific (ENSO), including its modulation of the Caribbean trades. As discussed in the previous section, the Mexican-Central American gap winds have an observable effect on the sea surface in the northeastern tropical Pacific (e.g., Xie et al. 2005, Fiedler 1994). Without the aid of a wind-forced ocean model with reasonably high spatial and temporal resolution, it is difficult to quantitatively describe the unique impact of the gap winds on SST, MLD, as well as propagating features such as anticyclonic eddies evident in perturbations in the sea surface height (e.g., Palacios and Bograd 2005, Zamudio et al. 2006). This is a crucially

important part of understanding the full interannual variability of SST in the east Pacific warm pool, as it identifies a pathway by which the Atlantic basin can influence interannual variability in the tropical Pacific. Sun and Yu (2006) examined the impact of the Tehuantepec and Papagayo gap winds on the amplitude of the annual cycle of SST in the EPWP. Some of their results provide a point of comparison with ours, and are discussed where appropriate.

We begin by examining the effect of each gap wind, as well as the combined effect of both gap winds, on the mean MLD in the east Pacific warm pool. Given that we have shown in the preceding sections that there is significant decadal variability in the Tehuantepec gap winds, we also compute annual mean for the first and second half of the experimental period separately. This allows one to determine the effect of that low-frequency variability of the Tehuantepec gap winds on the subsequent variability of the sea surface of the east Pacific warm pool. Shown along the top row of Figure 2.51 are the differences in annual mean MLD uniquely due to the Tehuantepec gap winds (i.e., *control* minus *smooth-teh*). The Tehuantepec gap winds results in a deeper mixed layer in and just beyond the Gulf of Tehuantepec. Since this deeper mixed layer is directly beneath the wind jet, it is due to vigorous turbulent mixing of the upper ocean. Immediately to the east of the Gulf of Tehuantepec is a shallower mixed layer. This feature coincides with the positive wind stress curl associated with the Tehuantepec gap winds, and is thus not the result of turbulent mixing, but Ekman pumping. Both features of the MLD field due to the Tehuantepec are enhanced during the second half of the experiment, which is to be expected because the Tehuantepec gap winds themselves grow steadily stronger from 1995 onward.

Shown in similar fashion, Figure 2.51 (middle row) shows the effect of the Papagayo gap winds on the annual mean MLD. The primary effect the Papagayo gap winds have is on the production or enhancement of a thermocline dome known as the Costa Rica Dome. However, the MLD difference is only 3-4 m. A closer look at this feature is provided in the next paragraph. Finally, the combined effect of the Tehuantepec and Papagayo gap winds (i.e., experiments

control minus *smooth-gaps*) is shown in the bottom row of Figure 2.51. This appears similar to what would be the result of simply adding the top and middle rows of Figure 2.51, as apparently the two gap wind jets do not together produce an additional feature in the derivative fields that would lead to a unique MLD signal. However, the deeper mixed layer in the Gulf of Tehuantepec is enhanced by the Papagayo gap winds because it is on the northern side of the Papagayo wind jet- where the wind stress curl is anticyclonic and would thus drive the thermocline or mixed layer deeper.

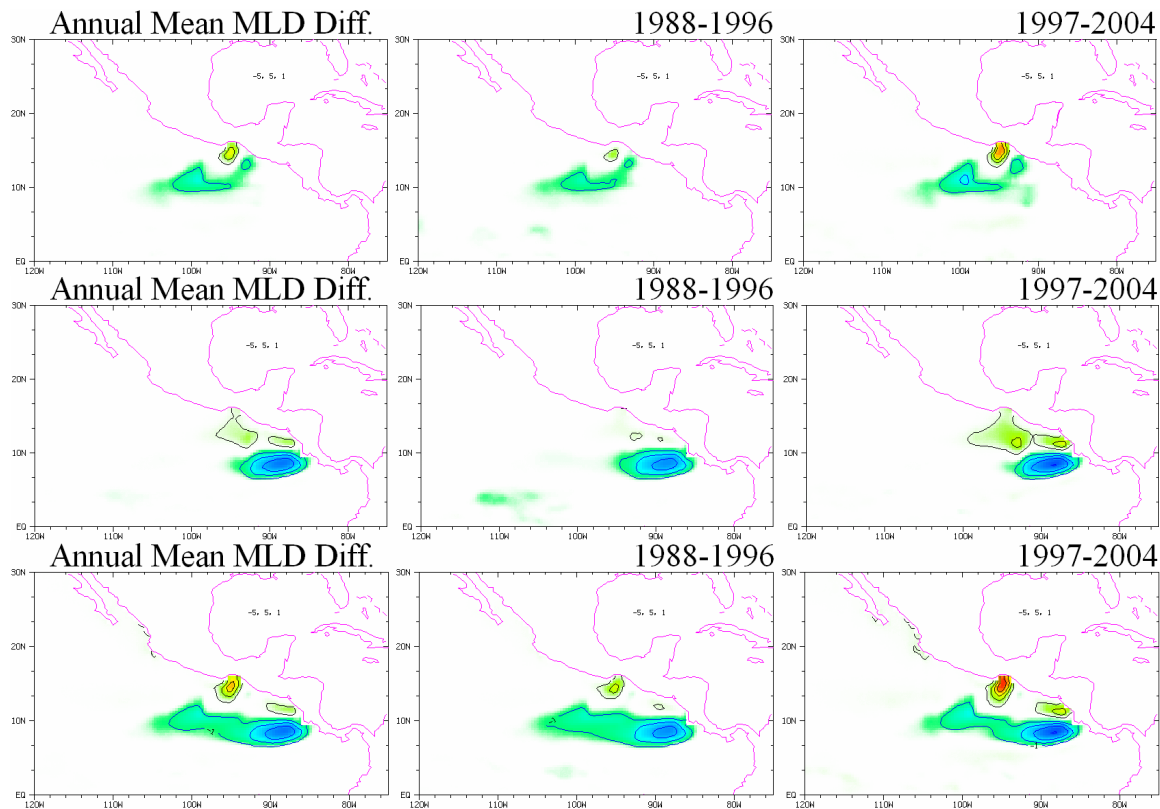


Figure 2.51. Annual mean difference in mixed layer depth (m) in the east Pacific warm pool region for experiments *control* minus *smooth-teh* (top row), *control* minus *smooth-pap* (middle row), and *control* minus *smooth-gaps* (bottom row). By this sense, the quantities shown are the effect of the gap winds. The MLD differences for the full period 1988-2004 are shown in the left column, while the differences during only the first half are in the center column and the second half in the right column. Contour interval 1 m and shading is from -5 m to 5 m.

A curiosity surrounding the east Pacific warm pool region that has long been discussed in the oceanographic literature is: why does the Costa Rica Dome exist? (e.g., Wyrski 1964a, Hoffman et al. 1981, Umatani and Yamagata 1991, Fiedler 1994, Xie et al. 2005). One popular explanation is that the Papagayo gap winds are at least partially responsible for the Costa Rica Dome. However, without an experimental setup that is able to explicitly test the sensitivity of the mixed layer to the Papagayo gap winds, such a hypothesis is difficult to test. Analysis of experiments described in this section, namely *control* and *smooth-pap*, offer an opportunity to test that hypothesis. Shown in Figure 2.52 is the annual mean MLD and wind stress in the vicinity of the Costa Rica Dome for experiments *control* and *smooth-pap*. Clearly the Papagayo gap winds are all but completely diminished in *smooth-pap*, yet there remains a dome-like feature in the same location as the Costa Rica Dome. Although the Costa Rica Dome is much sharper in the *control* experiment, the dome in *smooth-pap* is only ~4 m deeper than in *control*. These results offer to the debate that the Papagayo gap winds are not responsible for the existence of the Costa Rica Dome, but given its pre-existence as set up by the southerly equatorial winds, the Papagayo gap winds lead to further shoaling of the thermocline and sharpening of the gradient of mixed layer or thermocline depth (i.e., a general intensification of the Costa Rica Dome). From the distribution of wind stress overlaid on the MLD in Figure 2.52 (right), it is clear that the positive wind stress curl to the northwest of the southwesterly cross-equatorial flow is sufficient to explain the existence of the Costa Rica Dome, while the Papagayo gap winds locally enhance the dome. This is further corroborated by the fact that there is a similar thermocline dome in the southeastern tropical Atlantic Ocean, known as the Angola Dome (Mazeika 1967). The Angola Dome, although in the Southern Hemisphere, is similar in many ways to the Costa Rica Dome including being 10 degrees latitude from the equator, and shown to be the result of southeasterly tradewinds (Signorini et al. 1999). The nearby African coast, however, does not contain gap winds.

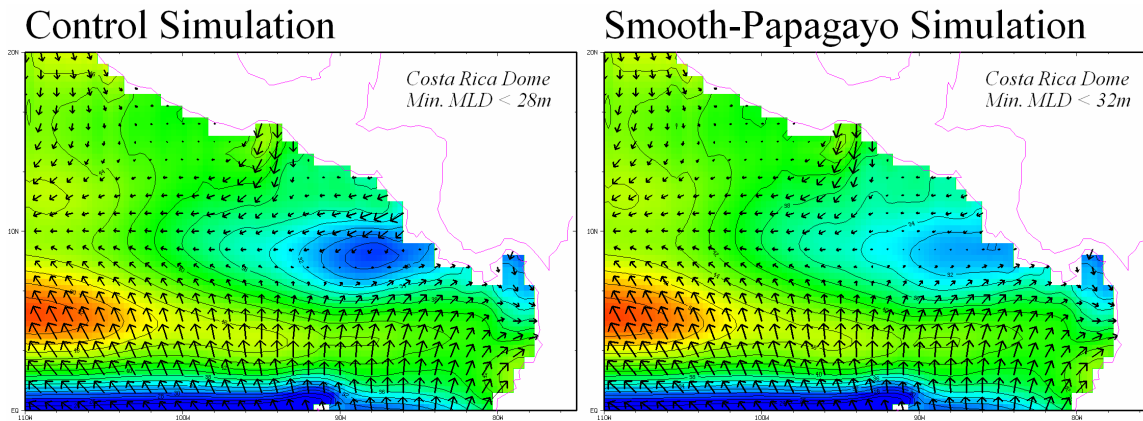


Figure 2.52. Annual mean mixed layer depth (m; contour interval 2 m) and wind stress in the east Pacific warm pool region for experiments *control* (left) and *smooth-pap* (right).

To quantify the contribution of the Tehuantepec and Papagayo gap winds to the interannual variability of MLD, shown in Figure 2.53 are the ratios of the standard deviation of the weekly MLD anomalies (same layout as Figure 2.51). Again, across the top row are STD ratios for *control* / *smooth-teh*, the middle row for *control* / *smooth-pap*, and the bottom row for *control* / *smooth-gaps*.

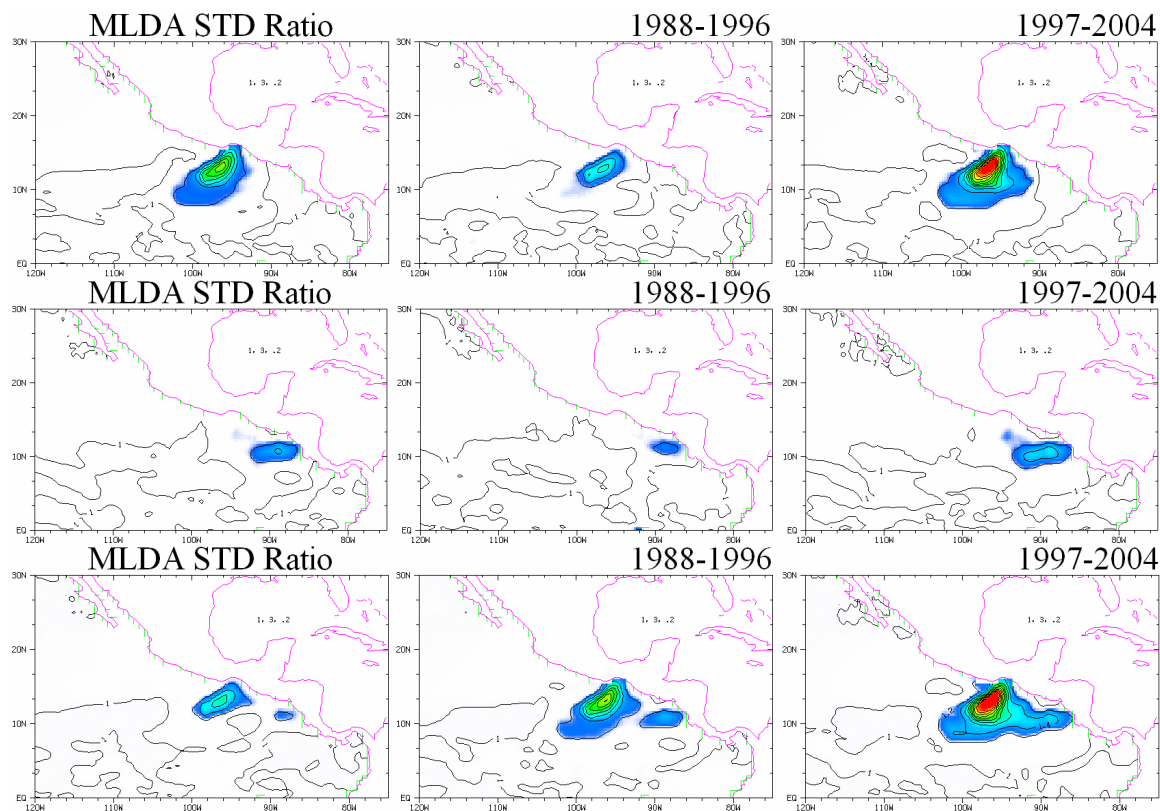


Figure 2.53. Ratio of the standard deviation of weekly mixed layer depth anomalies in the east Pacific warm pool region for experiments *control / smooth-teh* (top row), *control / smooth-pap* (middle row), and *control / smooth-gaps* (bottom row). By this sense, the quantities shown are the effect of the gap winds. The STD ratios for the full period 1988-2004 are shown in the left column, while the differences during only the first half are in the center column and the second half in the right column. Contour interval 0.2; shading from 1 to 3.

The Tehuantepec gap winds are responsible for interannual variability of MLD in the region beneath the gap wind signal up to double the standard deviation of MLD without the Tehuantepec gap winds. During the second half of the wind stress record, the effect is nearly tripling the standard deviation of the weekly MLD anomalies. In contrast, the MLD variability signal of the Papagayo gap winds is much smaller, only amplifying the interannual variability of MLD by 20-40%, and confined to a smaller area extending from the coast to the Costa Rica Dome (Figure 2.53, middle row).

We now examine the effect of the Tehuantepec and Papagayo gap winds on the mean and variability of SST in the east Pacific warm pool. Shown in Figure 2.54 are the differences in annual mean SST between experiments *control* minus *smooth-teh*, *control* minus *smooth-pap*, and *control* minus *smooth-gaps*. On the annual mean for the period 1988-2004, the Tehuantepec gap winds are responsible for a difference of up to -0.5°C . There is a large difference in the magnitude of this effect between the periods 1988-1996 (up to 0.2°C) and 1997-2004 (up to 0.8°C). By the mechanisms shown in the previous subsection, this is the manifestation of the Atlantic basin's influence on SST in the eastern tropical Pacific, i.e., the Atlantic basin drives the low-frequency variability of the Tehuantepec gap winds, while the strength of the Tehuantepec gap winds are related to the SST in the east Pacific warm pool. Not surprisingly, the Papagayo gap winds are responsible for a difference in the annual mean SST on the order of 0.25°C (Figure 2.54, middle row). The effect of both the Tehuantepec and Papagayo gap winds on annual mean SST are shown in the bottom row of Figure 2.54. Collectively, the effect of the gap winds is a cooler SST roughly the size of the east Pacific warm pool itself. That is to say that if the Tehuantepec and Papagayo gap winds did not exist, the east Pacific warm pool would be warmer throughout, but particularly in the northwest region near the Gulf of Tehuantepec, and the Costa Rica Dome.

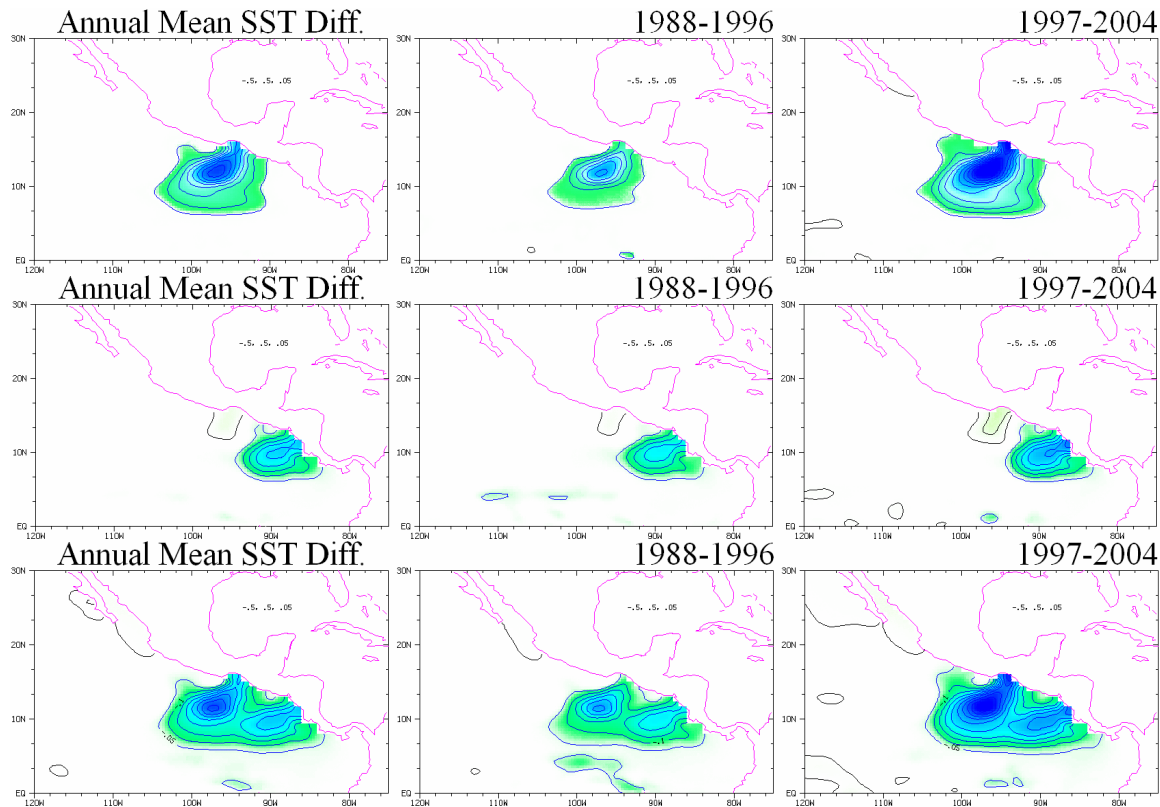


Figure 2.54. Annual mean difference in SST ($^{\circ}\text{C}$) in the east Pacific warm pool region for experiments *control* minus *smooth-teh* (top row), *control* minus *smooth-pap* (middle row), and *control* minus *smooth-gaps* (bottom row). By this sense, the quantities shown are the effect of the gap winds. The SST differences for the full period 1988-2004 are shown in the left column, while the differences during only the first half are in the center column and the second half in the right column. Contour interval 0.05°C ; shading from -0.5°C to 0.5°C .

Shown in Figure 2.55 is the ratio of the standard deviation of weekly SST anomalies, in similar fashion as that shown for MLD in Figure 2.53. The only major effect of the Tehuantepec or Papagayo gap winds on the interannual variability of SST in the east Pacific warm pool is the Tehuantepec gap winds amplifying the variability of SST in a region extending $\sim 5^{\circ}$ latitude south of the Gulf of Tehuantepec, with approximately 50% higher STD of weekly SST anomalies. The lack of amplification of SST variability at the Costa Rica Dome implies that, although the Papagayo gap winds contribute to the existence of the Costa Rica Dome, they do not contribute

to its variability. Likely mechanisms for Costa Rica Dome SST variability remain the interannual fluctuations in the depth of the broader eastern tropical Pacific thermocline, and fluctuations in the strength of the cross-equatorial flow to the southeast of the Costa Rica Dome and thus impart a positive wind stress curl over the Costa Rica Dome.

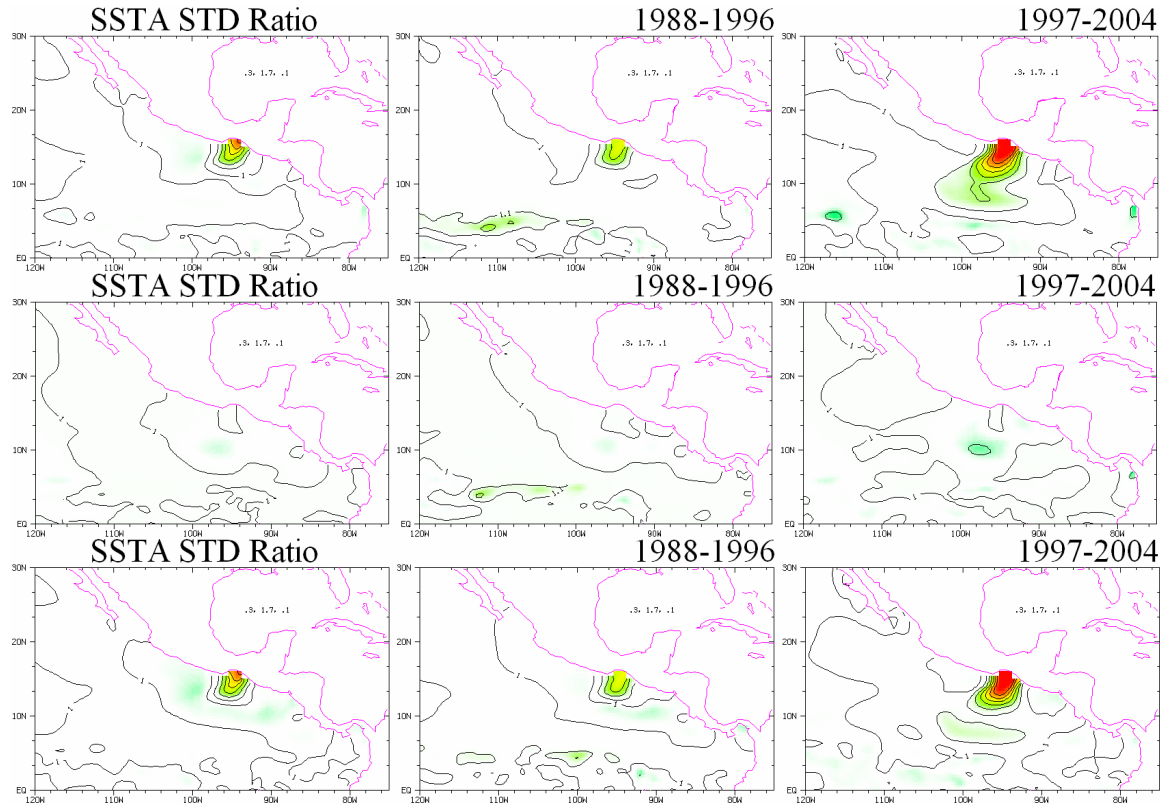


Figure 2.55. Ratio of the standard deviation of weekly SST anomalies in the east Pacific warm pool region for experiments *control / smooth-teh* (top row), *control / smooth-pap* (middle row), and *control / smooth-gaps* (bottom row). By this sense, the quantities shown are the effect of the gap winds. The STD ratios for the full period 1988-2004 are shown in the left column, while the differences during only the first half are in the center column and the second half in the right column. Contour interval 0.1; shading from 0.3 to 1.7.

Given the differences in the mean and variability of MLD and SST in the EPWP due to the Mexican-Central American gap winds, it is of interest to identify which physical processes are most sensitive to the gap winds. Calculations of the mixed layer heat budget were performed

on the *control* and *smooth-gaps* experiments. Weekly anomalies were computed, from which maps of STD ratio of each heat budget term were produced. The results for the advective heat flux terms (zonal heat flux, meridional heat flux, and entrainment-mixing) are shown in Figure 2.56. The STD ratios for surface radiative heat fluxes (net, longwave, latent, and sensible heat fluxes) are shown in Figure 2.57. Within the Tehuantepec influence region, the variability of *all* heat budget terms are amplified by 100-200%. In the Papagayo influence region including the Costa Rica Dome, the advective terms are also amplified by 100-200%, but the surface radiative terms are not greatly amplified except for latent heat flux, the variability of which is amplified by up to 100%. To summarize the heat budget calculations, for either the Tehuantepec or Papagayo region, the variability is amplified by the variability of the wind speed and thus evaporative cooling. Advective heat fluxes have higher variability in both regions, but particularly for the Tehuantepec gap winds region; the STD of entrainment-mixing in the *control* experiment, for example, is 4x that in the *smooth-gaps* experiment.

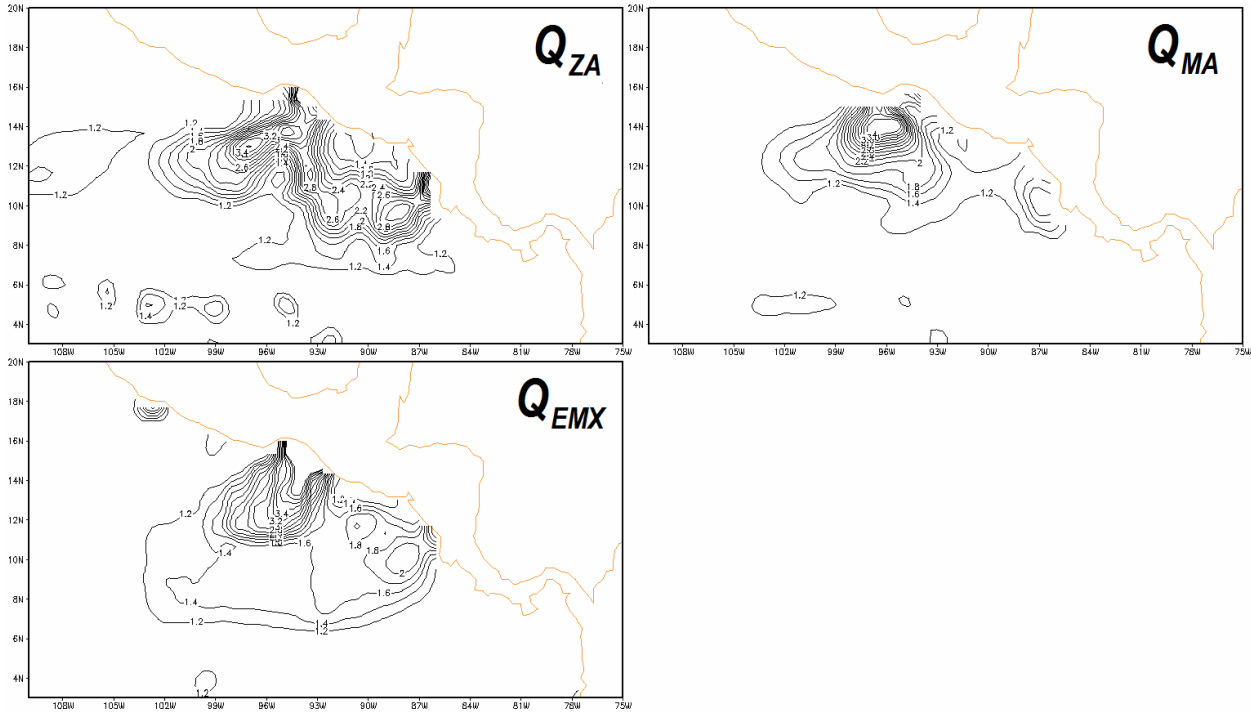


Figure 2.56. Ratio of the standard deviation of weekly *advective* mixed-layer heat budget terms in the east Pacific warm pool region for experiments *control* / *smooth-gaps*. Contour interval 0.2 W m^{-2} beginning with 1.2 W m^{-2} .

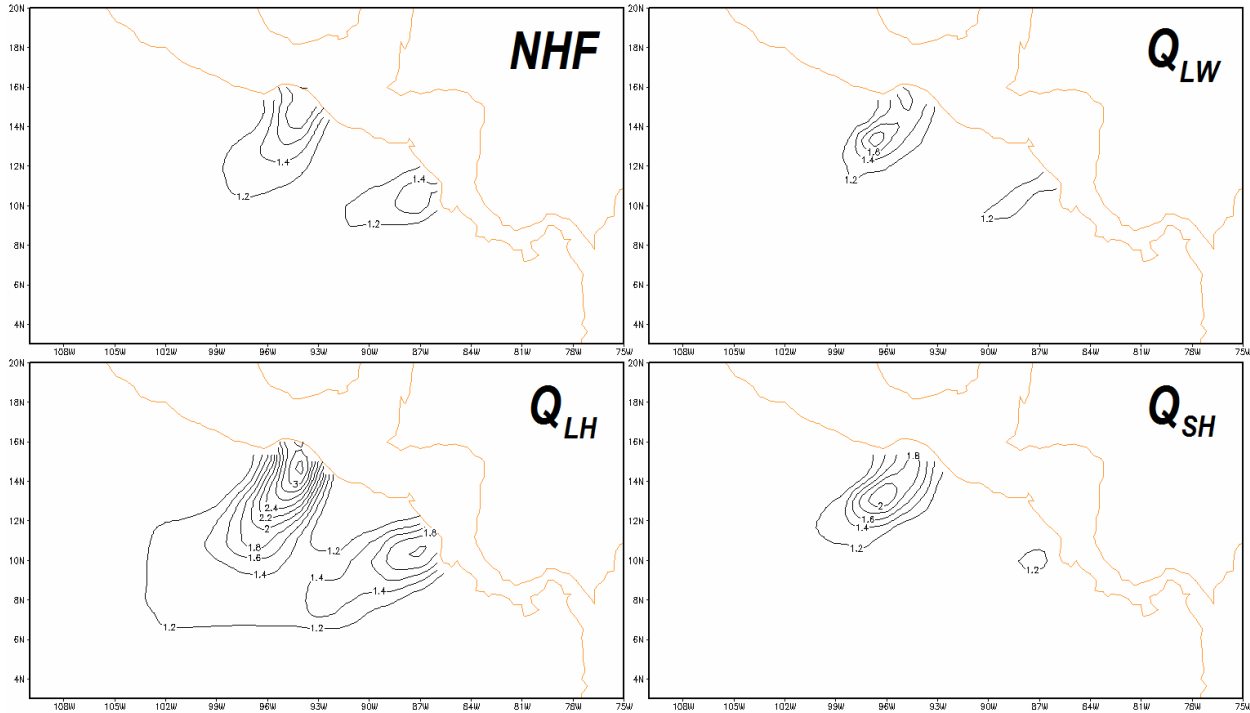


Figure 2.57. Ratio of the standard deviation of weekly *surface flux* mixed-layer heat budget terms in the east Pacific warm pool region for experiments *control* / *smooth-gaps*, including net heat flux (“NHF”). Contour interval 0.2 W m^{-2} beginning with 1.2 W m^{-2} .

To complement the above analyses of the effect of the Tehuantepec and Papagayo gap winds on the mean and general variability of MLD and SST in the east Pacific warm pool, we now consider the time-dependent effect of the gap winds on SST in the east Pacific warm pool. Before analyzing time series, Figure 2.58 shows the correlation of weekly SST anomalies between the *control* experiment and experiments *smooth-teh*, *smooth-pap*, and *smooth-gaps*. The correlation is reduced to 0.75 in the Gulf of Tehuantepec. The reduced correlation $\sim 2^\circ$ north of the equator is due to tropical instability waves and are not attributable to the gap winds.

TIWs are high-frequency phenomena and are likely to be different between experiments, regardless of how small the difference is in the forcing.

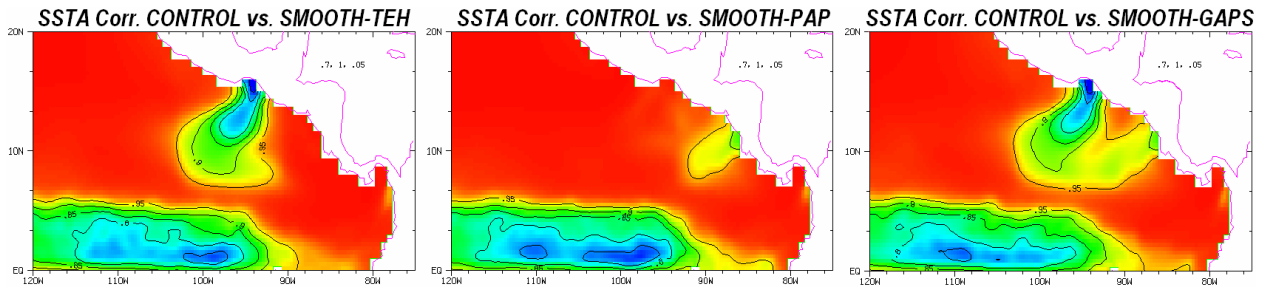


Figure 2.58. The correlation of weekly SST anomalies over the period 1988-2004 between experiments *control* vs. *smooth-teh* (left), *control* vs. *smooth-pap* (center), and *control* vs. *smooth-gaps* (right). Contour interval 0.05; beginning at 0.95, 0.90, ...

To quantify the time-dependent effect of the gap winds on SST in the east Pacific warm pool, we construct similar indices of SST anomaly for the east Pacific warm pool region, splitting it into the northwest and southeast subregions as in prior subsections (Figure 2.59). In both the NW and SE subregions, the effect of the gap winds is a low-frequency cooling of SST in the EPWP (Figure 2.60). In both subregions, the cooling is on the order of -0.2°C . The fact that the cooling is similar in both the NW and SE subregions implies that the gap winds have an effect on the time evolution of SST anomaly in the broader east Pacific warm pool rather than simply in the Gulfs of Tehuantepec and Papagayo as would be the direct result of e.g., evaporative cooling beneath a patch of strong surface winds. However, as indicated in Figure 2.61, the experiment without the Papagayo gap winds resulted in little difference in the time series of SST anomaly in the full EPWP (i.e., including NW and SE). It is apparently the Tehuantepec gap winds that are the most important factor in the interannual variability of SST in the east Pacific warm pool, and the Papagayo gap winds, although contributing to the existence of the Costa Rica Dome on the annual mean, has little effect on the interannual variability of SST in the east Pacific warm pool.

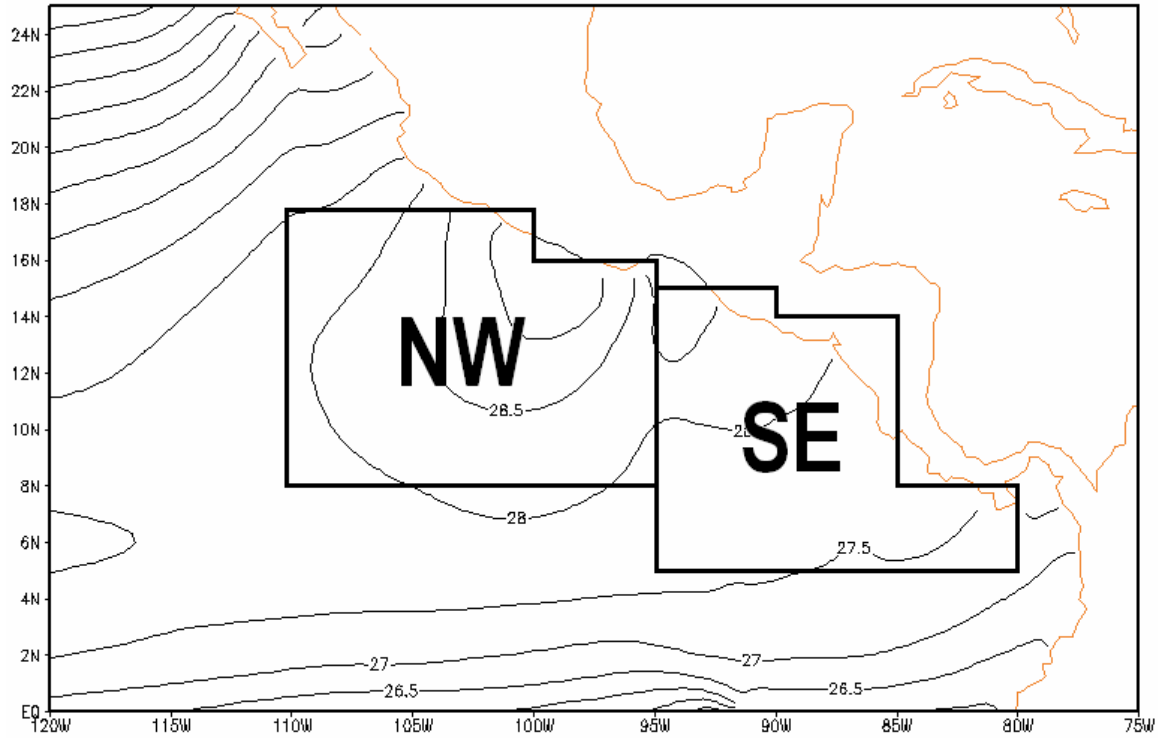


Figure 2.59. Map of the east Pacific warm pool index and its subregions, from which time series are calculated and displayed in subsequent figures.

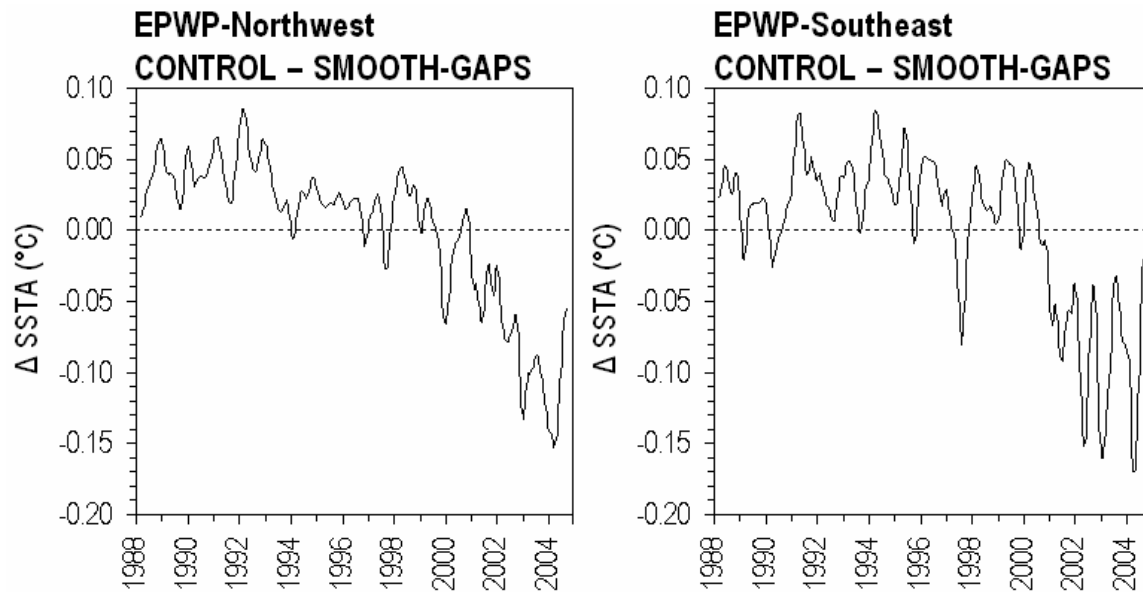


Figure 2.60. Time series differences of monthly SST anomalies between experiments *control* minus *smooth-gaps* in the NW (left) and SE (right) subregions of the east Pacific warm pool. By this sense, the quantities shown indicates the effect of the gap winds.

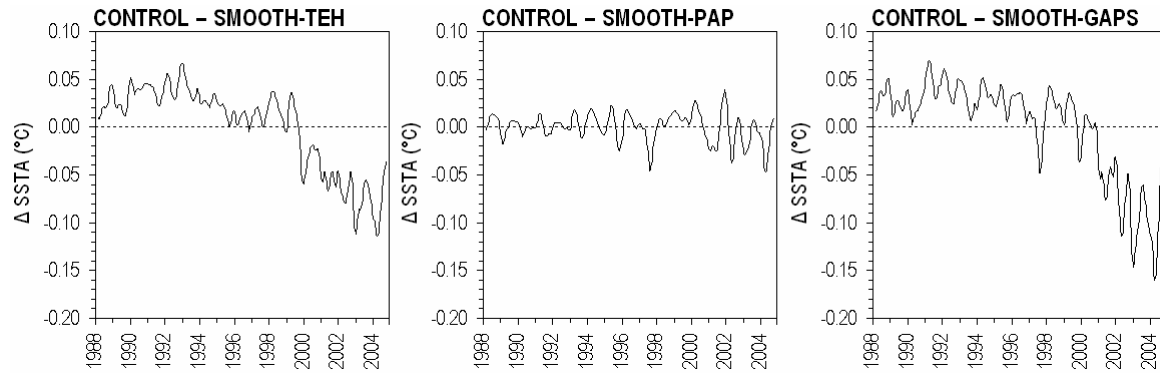


Figure 2.61. Time series differences of monthly SST anomalies in the full east Pacific warm pool region (combined area of NW and SE subregions shown in Figure 2.59) between experiments *control* minus *smooth-teh* (left), *control* minus *smooth-pap* (center), and *control* minus *smooth-gaps* (right). By this sense, the quantities shown indicates the effect of the gap winds.

As discussed in the previous section, some recent work has been aimed at understanding the role of the Tehuantepec gap winds in modulating the ocean eddy activity. One of the open questions, as evident by the conflicting outcomes of Palacios and Bograd (2005) and Zamudio et al. (2006), is whether ocean eddy activity is significantly higher due to the Tehuantepec gap winds or not. Until recently, the common wisdom was that the Tehuantepec gap winds forced an ocean response which was the primary mechanism for the genesis of long-lived anticyclonic eddies which begin in the Gulf of Tehuantepec and propagate westward (e.g., McCreary et al. 1989). This notion was recently supported by Palacios and Bograd (2005), who further showed that the Tehuantepec eddies are more prevalent during El Niño years (although statistical significance was only found for the “fewer during La Niña” association). On the other hand, Zamudio et al. (2006) used satellite observations of sea level anomaly and a regional ocean model to show that the primary mechanism for the genesis of Tehuantepec eddies is equatorially forced ocean waves, i.e., downwelling Kelvin waves propagating up the coast of Central America and being shed off the coast by the highly irregular coastline.

The experiments *control* and *smooth-teh* readily lend themselves to this debate because the equatorial forcing was identical between the experiments, i.e., ENSO and the associated equatorial waves should be exactly the same, thus any differences are due to the Tehuantepec gap winds. Shown in Figure 2.62 is the percent by which the variability of the weekly sea level anomalies is amplified as a direct result of the Tehuantepec gap winds. For the full period 1988-2004, the SLA variability is amplified in a very broad region beginning at the western edge of the Tehuantepec gap wind signal, extending as far west as the dateline and beyond. The amplification of the SLA signal is largely due to the second half of the wind stress record, 1997-2004, as the effect is very small during the first half 1988-1996. This suggests that the Tehuantepec gap winds do indeed generate strong eddy activity which propagates great distances to the west. This also highlights the importance of the low-frequency variability of the Tehuantepec gap winds, as discussed in the previous subsection, as having non-local implications in the tropical Pacific Ocean.

Amplification of Sea Level Variability by the Tehuantepec Gap Winds (STD Ratio %)

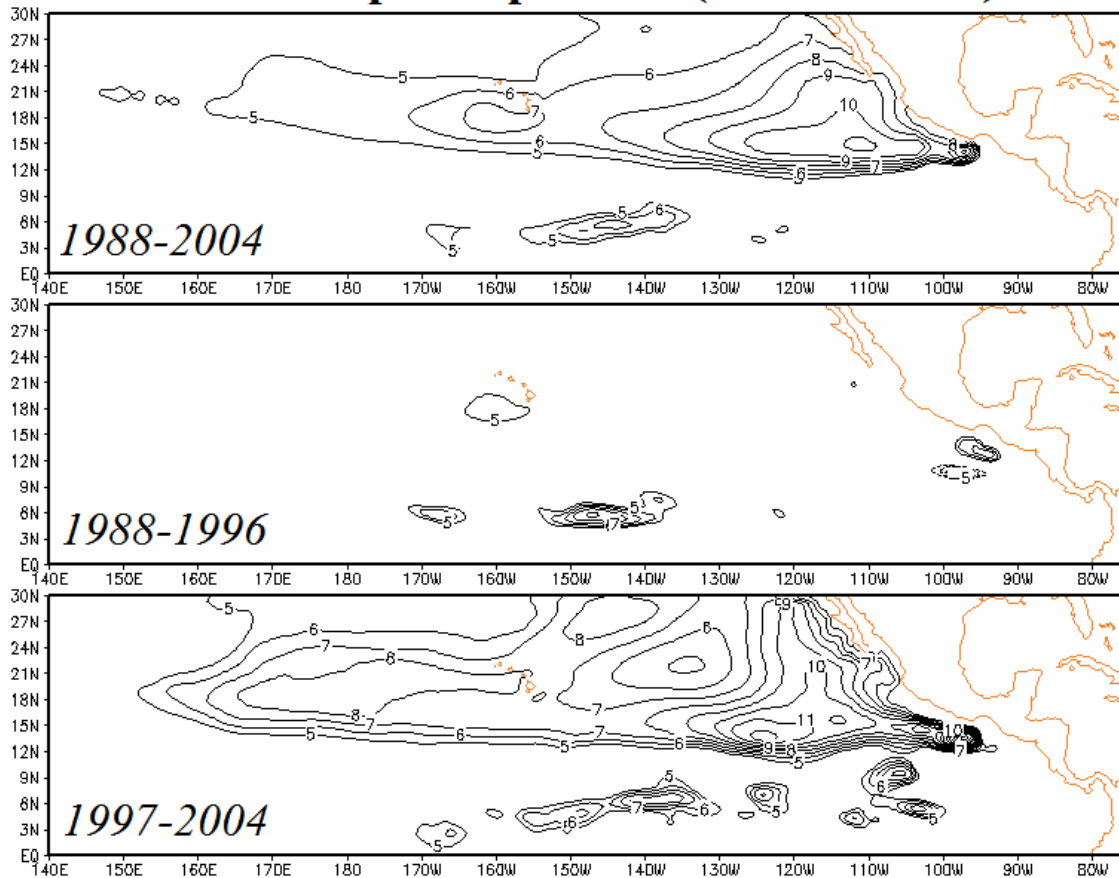


Figure 2.62. Ratio of standard deviation (expressed as percent increase) of weekly sea level anomalies in the north east-central tropical Pacific Ocean for experiments *control* / *smooth-teh* for the full period 1988-2004 (top), the first half (middle), and second half of the wind stress record (bottom). Contour interval 1% beginning with 5%.

To summarize the present subsection, we have conducted interannual experiments of the period 1988-2004 with an OGCM of the tropical Pacific to explicitly determine the effects of the Tehuantepec and Papagayo gap winds on SST in the east Pacific warm pool. Four experiments were conducted: a *control* simulation with the SSM/I-QuickSCAT wind forcing unchanged, a *smooth-teh* experiment where the Tehuantepec gap winds were removed, a *smooth-pap* experiment where the Papagayo gap winds were removed, and a *smooth-gaps* experiment where

both the Tehuantepec and Papagayo gap winds were removed. The response of the east Pacific warm pool to the gap winds differs between the two gap winds. The Tehuantepec gap winds lead to a deeper mixed layer in the Gulf of Tehuantepec, while the Papagayo gap winds lead to a shallower mixed layer within the existing Costa Rica Dome. This implies that, for the Tehuantepec gap winds, it is the entrainment-mixing that is of greatest importance, while for Papagayo, it is the associated wind stress curl that is of greatest importance. In terms of SST, both the Tehuantepec and Papagayo gap winds lead to a cooling of the sea surface on the annual mean, however, only the existence of the Tehuantepec gap winds amplifies the interannual variability of SST in its influence region. This result is consistent with Sun and Yu (2006), who also found that the Tehuantepec gap winds have a larger impact on the annual cycle of SST than the Papagayo gap winds. The interannual variability of *all* heat budget terms are amplified in the Tehuantepec influence region, particularly the advective heat fluxes. In the Papagayo influence region, there is similar amplification of the variability of advective and surface radiative heat fluxes, although most of the change in surface radiative heat fluxes comes from changes in latent heat flux.

All effects of the aforementioned Tehuantepec gap winds are more pronounced in the second half of the wind stress record, while the aforementioned effects of the Papagayo gap winds are relatively constant throughout the record. This observation, as discussed in the preceding subsection, is related to the fact that the low-frequency variability of the Tehuantepec gap winds is remotely forced by the Atlantic basin, while the Papagayo gap winds are strongly tied to ENSO. For this reason, and that the Papagayo gap winds have a smaller effect on the interannual variability of SST, the time series differences of SST in the east Pacific warm pool and its constituent subregions are largest for the *smooth-teh* experiment. There may also be some remote effects of the Tehuantepec gap winds by way of increasing the variability of sea level anomaly in a broader region to the west of the east Pacific warm pool. This notion is consistent with previous work (e.g., Palacios and Bograd 2005, Zamudio et al. 2006), although

such prior work was not be able to unambiguously confirm the farther-reaching effects of the Tehuantepec gap winds since the present work represents the first attempt at explicitly *removing* the gap winds while leaving the rest of the tropical Pacific unchanged.

2.6. Discussion of the role of local versus remote forcing of the east Pacific warm pool

The results described in Chapter 2 indicate that the interannual variability of SST in the EPWP is measurably subject to the influences of ENSO and the Tehuantepec gap winds. The mechanisms constituting the link between the equatorial Pacific (i.e., ENSO) and the EPWP are the focus of Section 2.4. Although the center of action of ENSO is a mere $\sim 10^\circ$ latitude south of the EPWP, ENSO is effectively a “remote” driver of the EPWP. ENSO modulates the distribution of shortwave radiation reaching the ocean surface through strong displacements of the ITCZ and subsequently the regions of descent adjacent to it. By the Clausius-Clapeyron relation, one expects an increase in SST to result in increased cloud cover and thus reduced surface shortwave radiation. Over the EPWP, however, this local air-sea process is apparently not strong enough to compete with the strong remotely-forced descent over the EPWP, which is compensating for the strong locally-forced ascent over the equator during an El Niño event.

Section 2.5 indicated that the Tehuantepec gap winds also impart an important influence on the interannual variability of SST in the EPWP. The Tehuantepec gap winds were shown to communicate a low-frequency (“decadal”) signal from the Atlantic to the Pacific. By comparing a control forced ocean model experiment to one where the Tehuantepec gap winds were removed, it was found that the EPWP, particularly in its northwest region, was up to 0.4°C colder when averaged over 1997-2004 than when averaged over 1988-1996. The standard deviation of weekly SST anomalies also increased more in the later period due to the Tehuantepec gap winds. This corresponds with an upswing in the strength of the Tehuantepec gap winds. Although gap winds flowing through a coastal mountain range adjacent to the EPWP

would seem to be a “local” influence, the analysis of the mechanisms behind the variability of the Tehuantepec gap winds presented indicates that the Tehuantepec gap winds are themselves strongly subject to remote forcing by the North Atlantic region.

In essence, remote forcing dominates the EPWP, with ENSO being the largest factor overall. As a corollary, the ability of coupled models to accurately depict the interannual variability of SST in the EPWP ultimately depends on their ability to simulate ENSO. Coupled modeling of ENSO is neither a small nor a new problem, but one specific aspect of ENSO that many current coupled models have difficulty in capturing is the observed frequency. This systematic deficiency would clearly have implications for the representation of the interannual variability in the EPWP. For example, if a model has an unrealistically biennial ENSO, then the EPWP should also exhibit primarily biennial variability in that model (especially if the gap winds are not properly resolved). The following chapter (Chapter 3) is focused on the nature of ENSO in idealized and simple coupled model experiments, with particular attention paid to any effect the Galápagos Islands have on the frequency of ENSO. Although advancing the state-of-the-art in numerical ENSO simulation is a broad and important problem applicable to many aspects of Earth system science, an improvement in the simulated frequency of ENSO would readily translate into a more realistic EPWP in coupled models.

Chapter 3: On the Interannual Variability of SST in the Equatorial Pacific Ocean

3.1. Introduction and prior work

The previous chapter revealed a strong mechanistic connection between SST variability in the eastern equatorial Pacific Ocean and the EPWP. Shortwave heating was identified as the primary driver of the interannual SST tendency in the EPWP. The high correlation between the EPWP and the eastern equatorial Pacific Ocean is explained by the fact that equatorial SST anomalies modify the distribution of atmospheric vertical motions and therefore cloud cover and shortwave heating. In this chapter we turn our focus to the equatorial Pacific itself. The salient feature in the eastern equatorial Pacific Ocean in terms of SST is the cold tongue (CT); a result of coastal upwelling along the west coast of South America caused by along-shore trade winds, and upwelling along the equator caused by Ekman divergence. Seasonally, the CT begins to intensify in boreal spring as coastal upwelling along the coast of Peru, prompting coupled-air sea interaction processes that effectively drive the CT westward along the equator (Mitchell and Wallace 1992, Nigam 1997). It would be difficult to overemphasize the importance of the CT in global hydrological and biogeochemical cycles, as it plays a key role in the formation of tropical cloud and precipitation patterns, the supply of nutrients for surface ocean biological productivity, and carbon cycling. The east-central tropical Pacific is the largest oceanic source of CO₂ to the atmosphere (e.g., Takahashi et al. 1999). Furthermore, large SST anomalies associated with El Niño and La Niña events are manifested as variations about the mean state of the CT.

In spite of the importance of the equatorial Pacific cold tongue in global hydrological and biogeochemical cycles, most ocean general circulation models (OGCMs) and coupled atmosphere-ocean general circulation models (CGCMs) produce a CT with a cold bias, including

an exaggerated westward extent (Stockdale et al. 1998, Harrison et al. 2002). The Modular Ocean Model version 3 (MOM v.3; Pacanowski and Griffies 1998), which is the core ocean model of the present National Oceanic and Atmospheric Administration Climate Forecast System (NOAA CFS; Saha et al. 2006), exhibits a cold bias in the east-central tropical Pacific up to 1°C on the annual mean (Vecchi et al. 2005). Such a cold bias presents serious obstacles to producing realistic tropical cloud and precipitation patterns in CGCMs, including a reasonable intertropical convergence zone (ITCZ) (Mehoso et al. 1995). Recent modeling studies have approached the tropical cold bias problem from diagnosing biases in the surface energy budget (Kiehl 1997), atmospheric feedbacks (Gordon et al. 2000, Sun et al. 2003), biological attenuation of shortwave radiation (Murtugudde et al. 2002, Marzeion et al. 2005), and coupled air-sea interactions (Luo et al. 2004). Despite advances in our understanding of the CT and the processes governing its mean and variability, the tropical cold bias problem remains the norm in OGCMs and CGCMs.

The existence of the Galápagos Archipelago on the equator near 90°W, made famous after the nineteenth century expeditions of British naturalist Charles Darwin, presents the potential for topographic interaction with the equatorial current system and other processes related to the CT. Current operational ocean analysis and prediction systems (e.g., the Global Ocean Data Assimilation System [GODAS], the oceanic component of the NOAA CFS) do not include the Galápagos Islands (David Behringer, personal communication). Early observational and theoretical studies examined the impact of the Galápagos Islands on the structure of the equatorial undercurrent (EUC) in the eastern Pacific (e.g., Stevenson and Taft 1971, Christensen 1971, White 1973, Lukas 1986). All observational analyses indicate that the core of the EUC east of the Galápagos Islands is at least reduced. Ship-based velocity measurements (e.g., World Ocean Circulation Experiment [WOCE] and N. B. Palmer sections) disagree on whether EUC remnants flow north or south of the islands (William S. Kessler, personal communication). Eden and Timmerman (2004) (hereafter ET-04) examined topographic effects on the EUC,

South Equatorial Current (SEC), and tropical instability waves (TIWs) by comparing output from an OGCM including the Galápagos Islands to that in which the islands' subsurface topography above 2,000 m depth was removed. The horizontal resolution of the ET-04 experiments was $\frac{1}{4}^\circ$ by $\frac{1}{4}^\circ$. Their analysis of SST focused on TIWs and changes in total eddy kinetic energy.

The El Niño-Southern Oscillation (ENSO) is among the most pervasive natural climate oscillations on Earth, affecting the web of life from plankton to people. During mature El Niño events, the temperature of the ocean surface in the eastern equatorial Pacific warms, leading to global-scale responses in the biosphere transmitted through modifications of large-scale atmospheric circulation. Likewise, during La Niña events, the eastern equatorial Pacific Ocean cools, and equally dramatic consequences ensue. The dynamics of- and global responses to ENSO have been studied for nearly eight decades (Walker and Bliss 1932, Ropelewski and Halpert 1989, Kiladis and Diaz 1989, Yulaeva and Wallace 1994), including its role in the genesis of North American drought (e.g., Schubert et al. 2004, Seager et al. 2005, Karnauskas et al. [accepted]). Cyclic patterns in climate events have also been connected to something resembling ENSO as early as the mid-nineteenth century. Reminiscing on his 1832 visit to Argentina during his expedition on the *H.M.S. Beagle*, British naturalist Charles Darwin notes “These droughts to a certain degree seem to be almost periodical; I was told the dates of several others, and the intervals were about fifteen years” (Darwin 1839). Nearly sixty years later, Darwin enters into his journal “...variations in climate sometimes appear to be the effect of the operation of some very general cause” (Darwin 1897). Some believe this “very general cause” was actually an early piecing-together of ENSO and its now-notorious impact on extreme weather events in South America (Cerveny 2005). It is only a coincidence that Charles Darwin may have been among the first to point out the cyclic nature of ENSO, and the focus of this chapter is the association between ENSO and the Galápagos Islands, which owe their fame to Darwin.

Two fundamental characteristics of any ENSO event are amplitude, or the magnitude of the peak SST anomaly in the eastern equatorial Pacific, and period, or the timescale of the oscillation itself. These are also common metrics for evaluating the realism of interannual variability in coupled climate models (e.g., Collins 2000, Collins et al. 2006, Wittenberg et al. 2006). In principle, the atmospheric response to an ENSO event should be, to some extent, dependent on its amplitude. History remembers the 1982-83 El Niño and the 1988 La Niña because they were strong, and impacts were felt as such around the globe. One feature of the equatorial circulation that has not been considered with respect to ENSO amplitude and period are the Galápagos Islands. The Galápagos Archipelago is a group of 19 islands roughly 1,000 km off the Ecuadorian coast of South America. Most of the islands comprising the Archipelago are miniscule, except for the largest, Isla Isabela, which accounts for 73% of the total land area of the Galápagos. Amounting to 5,825 km², Isla Isabela is larger than the U.S. state of Delaware. Given its prime location in the eastern equatorial Pacific Ocean, the Galápagos is a popular location for the paleoclimate community to extract time information on climate signals, including ENSO, from archives such as tropical corals. Here we consider whether the Galápagos Islands themselves are an important factor in the very makeup of the observed ENSO signal. The concept of the Galápagos affecting ENSO seems somewhat paradoxical and, admittedly, far-fetched before further consideration of its location. A vertical cross-section of Galápagos topography is presented in Figure 3.1. The cross-section cuts across the longest possible north-south section through Isla Isabela, which is what is relevant to the primarily zonal subsurface equatorial circulation. Isla Isabela covers the first degree south of the equator, and crosses well into the first degree north of the equator. Yet, the Galápagos are usually ignored in ocean and climate models.

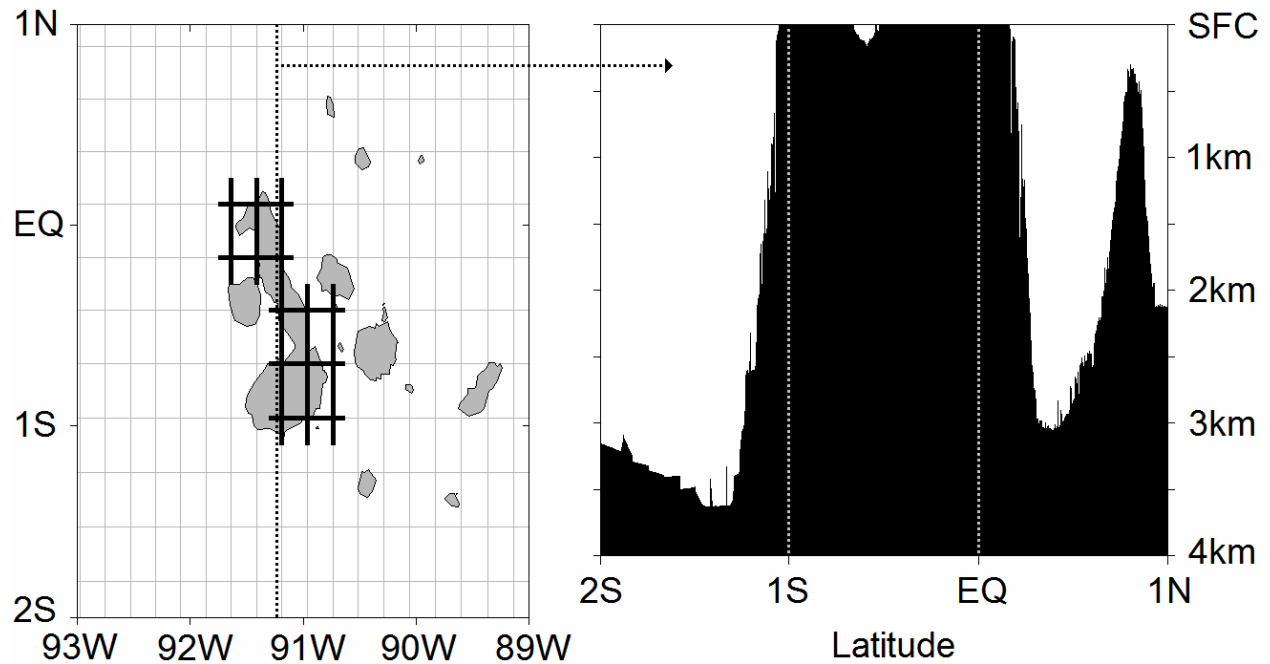


Figure 3.1. Left: 1-km resolution map of the Galápagos region, model gridlines (thin gray lines), and gridpoints used to represent the Galápagos Islands in the model (heavy black lines). Right: Vertical section of subsurface topography across Isla Isabela, constructed from multiple sources of bathymetric measurements along 91.25°W (black dashed line in left panel).

3.2. Data and methodology

The objective of Section 3.3 is to quantify and understand the relative improvements to the simulated climatology of the equatorial Pacific cold tongue region in an OGCM arising from increased horizontal resolution and the inclusion of the Galápagos Islands. For all of the ocean model experiments analyzed in Section 3.3, the meridional boundaries of the model grid are 40°N to 40°S, along which a sponge layer is used at the meridional open boundaries (see Chen et al. 1994), and Indonesian throughflow is closed off. Four one-year integrations under identical climatological forcing were carried out, beginning with a properly spun up state *for each case*. Climatological forcing consisted of 2° by 2° ECMWF operational analysis surface wind stress, base period 1985-2003 (Bengtsson et al. 1982), Xie and Arkin (1996) precipitation, base period 1979-2003, ISCCP cloud cover, base period 1983-1994 (Rossow and Schiffer 1991),

and ERBE shortwave radiation, base period 1984-1990 (Barkstrom 1984). A total of four cases are examined. The first case (*Coarse*) was run on a grid with uniform zonal resolution ($3/4^\circ$), meridional resolution stretching from $1/3^\circ$ at the equator to 1° at the meridional boundaries, without the Galápagos Islands. The second case (*Coarse+G*) was run on the same grid as *Coarse* plus the Galápagos Islands. The third case (*Fine*) was run on a grid with increased resolution in the eastern tropical Pacific: zonal stretching from $1/4^\circ$ in the east to 1° at the western boundary, meridional stretching from $1/4^\circ$ at the equator to 1° at the meridional boundaries, and no Galápagos Islands. The final case (*Fine+G*) was run on the same grid as *Fine* plus the Galápagos Islands. For computational efficiency, the meridional limits of the grids used in cases *Fine* and *Fine+G* were reduced to 30°N to 20°S . The *Fine* and *Fine+G* experiments are of similar horizontal resolution as those of ET-04.

Implementation of the Galápagos Islands is subject to the constraints of each model setup. The Galápagos Islands were implemented for *Fine+G* as land points on the model grid approximating the size and shape of Isla Isabela (Figure 3.1), and similarly for *Coarse+G* but with less detail (not shown). The model setup used in ET-04 included the partial cell topography improvements of Pacanowski and Gnanadesikan (1998), however, there is little if any variation with depth of the topography of the Galápagos Islands in ET-04. Similar is the case in the Gent-Cane OGCM, where all topography is constant in the vertical. However, as evinced by subsurface bathymetric measurements (Figure 3.1), this is a reasonable approximation in the upper few hundred meters of the ocean, where most of the interesting features of the equatorial circulation are at play.

For all of the ocean model experiments analyzed in Section 3.4, the meridional boundaries of the model grid are 30°N to 20°S . All experiments are run on a grid with higher resolution in the eastern tropical Pacific: zonal stretching from $1/4^\circ$ in the east to approximately 1° at the western boundary, and meridional stretching from $1/4^\circ$ near the equator to

approximately 1° at the meridional boundaries. Forcing in the idealized ENSO experiments analyzed in Section 3.3 is either climatological or climatological plus an idealized anomaly.

In the idealized forced setup, two main experiments were performed, which are designed to reveal the *total* effect of the Galápagos Islands on an El Niño event. Prior to both experiments, the model was spun up from the climatology of Levitus and Boyer (1994) for sixty years. The first of the two main experiments, *IC-Grid-*, was initialized with initial conditions that were produced by spinning up the model with the Galápagos excluded from the model grid. Thus, the mean state in *IC-Grid-* is the mean state that would exist if the Galápagos Islands did not exist. The model was then integrated for two years, saving 10-day mean fields, with the Galápagos withheld from the model grid. The second of the two main experiments, *IC+Grid+*, was initialized with initial conditions produced by spinning up the model with the Galápagos Islands included in the model grid. Thus, the mean state in *IC+Grid+* is the appropriate mean state accounting for the existence of the Galápagos. The model was then integrated for two years, with the Galápagos included in the model grid. By the naming convention, *IC-* versus *IC+* refers to whether the experiment was initialized with the non-Galápagos or Galápagos mean state, and *Grid-* versus *Grid+* refers to whether the island representing Galápagos was included in the model grid during the integration.

Each “experiment” (e.g., *IC-Grid-*) consists of two model runs: one forced by strictly climatological forcing (the “clim” run), and one forced by climatological forcing plus a westerly wind stress anomaly designed to induce a reasonable El Niño event (the “niño” run). Thus, anomalies for each experiment are taken as the difference between the niño and clim runs of that experiment. Section 3.3 was essentially a comparison of the clim runs of *IC-Grid-* and *IC+Grid+*. A westerly wind stress anomaly of 0.72 dyn cm^{-2} (equivalent to about 6 m s^{-1}) was applied to the climatological zonal wind stress over a box centered on the equator in the western Pacific (maximum at the equator, and tapers outward to 8°N and 8°S , 160°E and 160°W) from September through November of the first year of integration. The location, magnitude, timing

and duration of the idealized wind stress anomaly is reasonably similar to those preceding significant El Niño events in recent observed history.

One could imagine there are two ways by which the Galápagos Islands might influence the characteristics of an ocean anomaly such as those associated with an El Niño event. The first would be associated with the physical presence of the island- i.e., direct, physical flow-topography interaction with the island. The other type of effect would be associated with the fact that the existence of the Galápagos results in a different mean state. Therefore, if there are differences between *IC-Grid-* and *IC+Grid+*, it is necessary to understand if those differences are due to (a) the direct island effect, or (b) the different mean state. To isolate the direct island effect versus the effect of the mean state, two additional experiments, *IC-Grid+* and *IC+Grid-*, were conducted. Following convention, the experiment *IC-Grid+* was initialized with the non-Galápagos mean state, but the island was included in the model grid throughout the integrations. Conversely, the experiment *IC+Grid-* was initialized with the Galápagos mean state, but the island was excluded from the model grid throughout the integrations. In this manner, for example, one can compare experiments *IC+Grid+* and *IC+Grid-* to isolate the differences due to the direct island effect (in the context of the Galápagos mean state), or experiments *IC+Grid-* and *IC-Grid-* to isolate the effect of the mean state (in the context of the island not being present), and so on. The validity and limitations of this method are discussed at the end of the present section. A summary of these and other details of each of the four experiments and their constituent model runs can be found in Table 3.1.

Exp.	Model runs	Initial conditions	Grid config.	Forcing
<i>IC-Grid-</i>	IC-Grid- clim	Spun up without Galáp.	No Galáp.	Climatology
	IC-Grid- niño	Spun up without Galáp.	No Galáp.	Clim. plus anom.
<i>IC-Grid+</i>	IC-Grid+ clim	Spun up without Galáp.	Incl. Galáp.	Climatology
	IC-Grid+ niño	Spun up without Galáp.	Incl. Galáp.	Clim. plus anom.
<i>IC+Grid-</i>	IC+Grid- clim	Spun up with Galáp.	No Galáp.	Climatology
	IC+Grid- niño	Spun up with Galáp.	No Galáp.	Clim. plus anom.
<i>IC+Grid+</i>	IC+Grid+ clim	Spun up with Galáp.	Incl. Galáp.	Climatology

Table 3.1. Table outlining the main details of the model experiments relevant to the ‘idealized forced’ section, including the initial conditions, grid configuration, and forcing for each experiment and their constituent model runs.

For the second set of experiments in Section 3.4 (analyzed in Section 3.4.2), we use an identical model setup as that of the idealized forced experiments, with the exception that the ocean is coupled to the zonal wind stress field. The coupling is similar to that used in Sun et al. (2004), wherein the zonal wind stress anomaly is proportional to the zonal SST gradient in the equatorial Pacific:

$$(3.1) \quad \tau_x(\lambda, \varphi) = \tau_{x \text{ clim}}(\lambda, \varphi) - \mu(\varphi) (\Delta T - \Delta T_{\text{clim}})$$

where τ_x is zonal wind stress, λ is longitude, φ is latitude, $\tau_{x \text{ clim}}$ is the monthly climatological mean zonal wind stress, μ is the coupling coefficient, ΔT is the difference between area-averaged SST between the western (5°S-5°N, 130°E-180°) and eastern (5°S-5°N, 130°W-80°W) equatorial Pacific Ocean, and ΔT_{clim} is the monthly climatological mean ΔT . Thus, a positive SST anomaly in the eastern equatorial Pacific will result in a positive (westerly) zonal wind stress anomaly. In our model, we use a coupling coefficient of $\mu(0) = 0.065 \text{ dyn cm}^{-2} \text{ K}^{-1}$, decreasing with the cosine of latitude and diminishing at 15°N and S. This value of $\mu(0)$ is reasonably close to the range suggested by Sun et al. (2004).

Two 75-year simulations were produced, with the only difference being the existence of the Galápagos Islands in the model grid. Experiment “*No Galápagos*” was initialized with the spun-up state without Galápagos (the same initial conditions as those used in idealized forced experiment *IC-Grid-*) and integrated forward with the island absent from the model grid. Experiment “*Galápagos*” was initialized with the spun-up state that included the Galápagos Islands (the same initial conditions as those used in idealized forced experiment *IC+Grid+*) and integrated forward with the Galápagos present in the model grid. After removing the brief spin-

up period due to the introduction to the SST-wind stress coupling, 68 years of output is available for analysis.

One of the seemingly important assumptions in the idealized forced experiments is that El Niño events in the real world are triggered by westerly wind stress anomalies in the west-central Pacific. ENSO is an example of a truly coupled ocean-atmosphere phenomenon, and regardless if El Niño events are systematically triggered by westerly wind stress anomalies, it is clear that as the ocean-atmosphere system becomes coupled, there is usually a westerly wind stress anomaly present, and that is an integral part of the propagation and growth of the SST anomaly into a mature El Niño event. Therefore, since the purpose of this chapter is not to understand the genesis of ENSO events, but to quantify and understand the effect of the Galápagos Islands on the ocean's response to ENSO forcing, we suggest the method used to initiate El Niño events in the idealized forced experiments is of secondary importance.

Furthermore, the amplitude of the idealized El Niño event that is produced by the model is arbitrary. The greater the westerly wind stress anomaly we impose, the higher the amplitude of the ensuing El Niño event. The goal is not to accurately simulate a specific El Niño event as seen in observations, but to study aspects of the ocean's response to ENSO forcing that are dependent on the Galápagos Islands. For the same reason- that we are interested in differences- we can have confidence in the results even though the model is basically an ocean-only model (even the hybrid coupled model is only coupled to the atmosphere locally via heat fluxes and wind stress in a simplified manner) and thus the amplitude of an ENSO event may be somewhat different than had it been a fully coupled global ocean-atmosphere GCM.

An additional source of uncertainty pertains to the validity of the idealized forced experiments *IC-Grid+* and *IC+Grid-*. Throughout the two years of integration in the *IC-Grid+* experiment, for example, the mean state *began* as the non-Galápagos mean state, but could begin to shift toward the Galápagos mean state since the island is present in the model grid. However, two years is not sufficient time for such an adjustment to occur in the model. Rather,

we found that this takes at least twenty years. To be sure, however, we directly quantify how much the mean state began to shift throughout the two years of integration in the experiments *IC-Grid+* and *IC+Grid-* (not shown). We use the depth of the 20°C isotherm to represent the mean state because that is an indicator of the depth of the thermocline, which is an important factor not only to SST, but the sensitivity of SST to anomaly-generating processes (e.g., vertical motions, undulations of the thermocline, internal waves, surface Kelvin waves, etc.). The mean state remains sufficiently steady everywhere west of approximately 100°W over the two years of integration. East of 100°W- approaching the island and beyond- the island does begin to affect the mean state within the timeframe of a two-year integration. Thus, with respect to understanding the specific contribution of the direct island effect versus the effect of the mean state, we can only trust the results of *IC-Grid+* and *IC+Grid-* west of 100°W.

A final limitation is that introduced by observations. Observations of subsurface information are extremely limited east of 100°W. Inferring geostrophic currents from *in situ* dynamic height calculations is problematic in the presence of complicated, nonlinear flow such as that surrounding an island and coastline. This leaves us with satellite observations, specifically microwave, since spatial resolution is important in this case, for which we have limited record lengths and occasionally limited spatial coverage due to rain. Further, observations can only show the total effect of the Galápagos. No corroboration of results intended to isolate the direct island effect versus the effect of the mean state can be made with observations.

3.3. On the mean state of the equatorial Pacific Ocean

3.3.1. The effect of the Galápagos Islands on the equatorial Pacific Ocean: comparison of simulations and observations

The annual mean SST fields from the four simulations and TMI are shown in Figure 3.2. There appears to be very little difference when (a) adding the Galápagos Islands under coarse

resolution (i.e., *Coarse* vs. *Coarse+G*), or (b) increasing the horizontal resolution without the Galápagos Islands (i.e., *Coarse* vs. *Fine*). However, adding the Galápagos Islands under fine resolution (i.e., *Fine* vs. *Fine+G*) has the effect of reducing the westward extent of the CT. In fact, the westward extent of the CT appears *underestimated* when compared to the TMI climatology (base period 1998-2005), while the structure closer to the Galápagos Islands and the coast of South America is in better agreement than any other case.

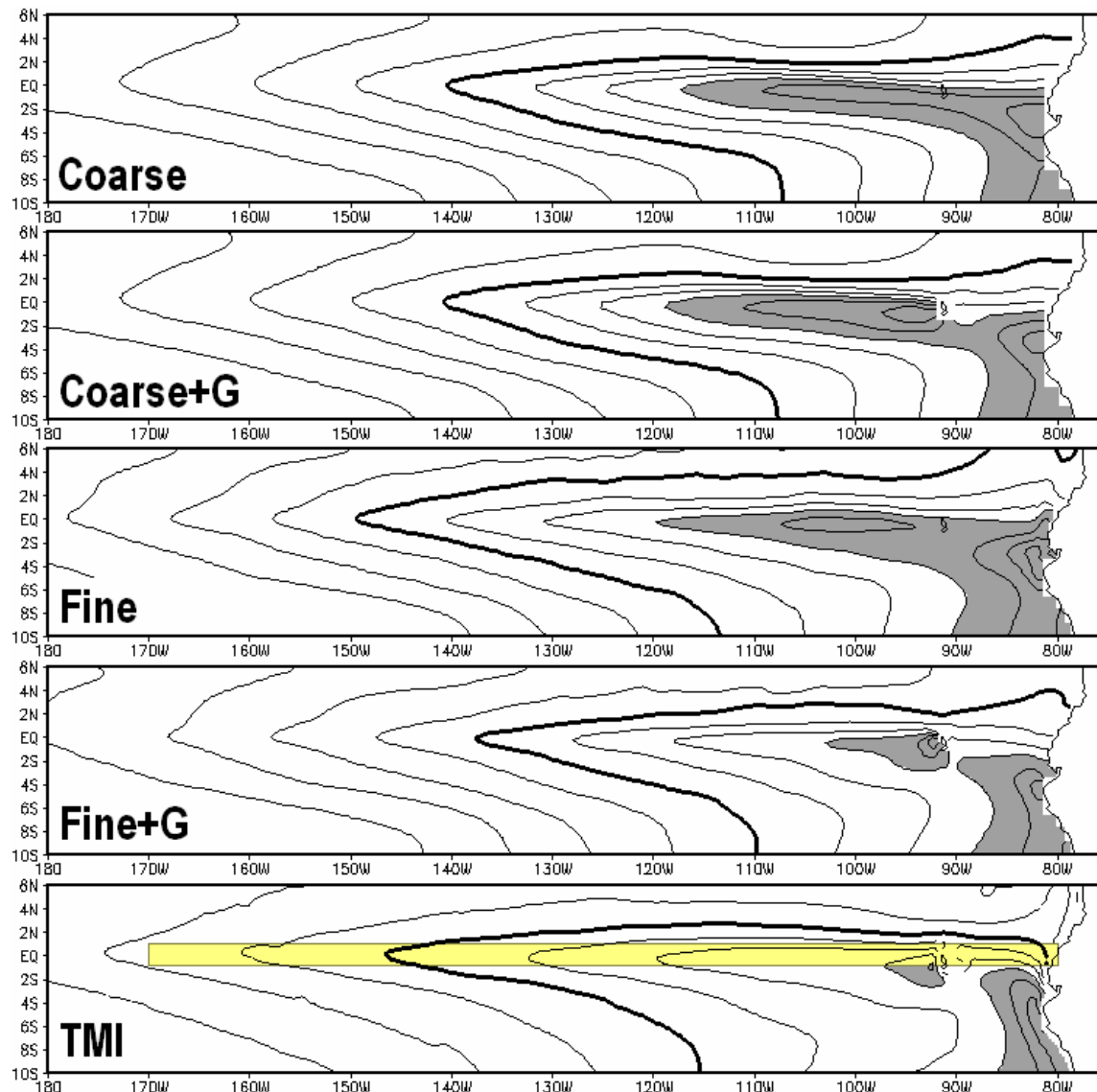


Figure 3.2. Annual mean SST (°C) in the equatorial Pacific Ocean for the four simulated cases and TMI. TMI based on the 1998-2005 climatology. Contour interval 1°C, the heavy contour is 26°C, and SST colder than 23°C is shaded. The yellow box indicates the index region used in the Figure 3.3.

To analyze the simulated mean seasonal cycle of SST in the CT region, an index was constructed as the area average SST from 170°W to the coast of South America, from 1°N to 1°S (indicated in Figure 3.2, bottom panel). The resulting seasonal cycles from all four cases and Reynolds OI are displayed in Figure 3.3.

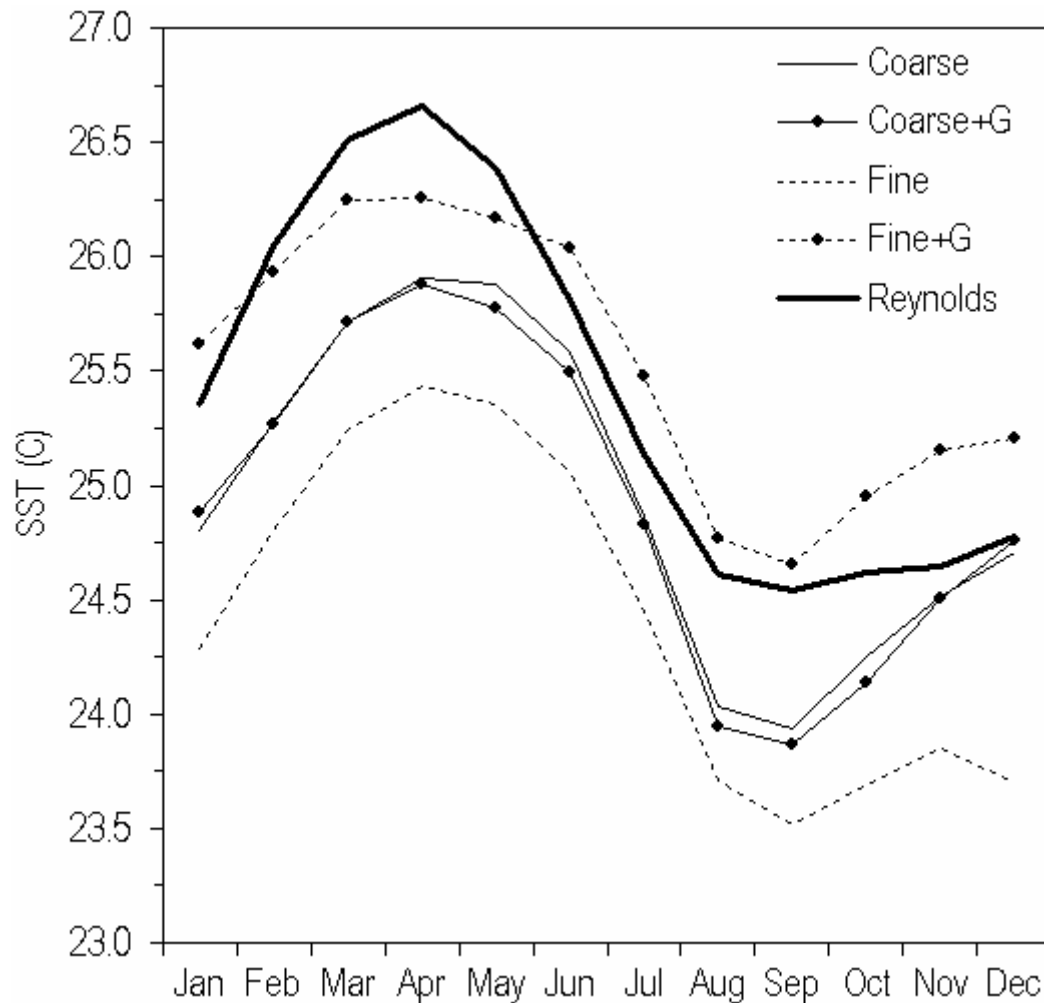


Figure 3.3. Mean seasonal cycle (monthly means) of SST (°C) in the cold tongue index region (1°S-1°N by 170°W-80°W) for the four simulated cases and the Reynolds SST climatology. Lines are as indicated on figure key.

Reynolds OI is used here because its longer temporal record should make it more representative of climatology while spatial comparisons are not needed. Under coarse resolution, the inclusion

of the Galápagos Islands made little difference; cases *Coarse* and *Coarse+G* exhibit a similar cold bias all year, which is more pronounced during the boreal spring and fall seasons and consistent with the global models (Stockdale et al. 1998). Under fine resolution, however, the Galápagos Islands have a warming effect on CT SST anywhere from 0.8°C to 1.5°C. Throughout the year, CT SST in *Fine+G* is closer to observations than in *Fine*; the root-mean-square error (RMSE) with respect to Reynolds OI is reduced from 1.0°C to 0.3°C (70% reduction). The longitudinal distribution of the biases in each case is shown in Figure 3.4. In the east-central part of the basin, there is little difference between cases *Coarse* and *Coarse+G*. East of the islands, however, the inclusion of the Galápagos Islands warms the SST anywhere from 0.25-1°C. In the fine resolution experiments, the effect of the Galápagos Islands is to warm SST everywhere except for a very narrow (~2° longitude wide) region immediately west of the islands. In the central region, a relatively strong warm bias (~1°C) actually develops in *Fine+G* than was only moderate (~0.5°C) in *Fine*, but everywhere east of ~140°W the cold bias is much reduced. For reference, the difference between TMI and Reynolds SST is also provided. TMI is clearly colder than Reynolds throughout the east-central equatorial Pacific, but it also resolves the cold (warm) signal immediately west (east) of the Galápagos Islands.

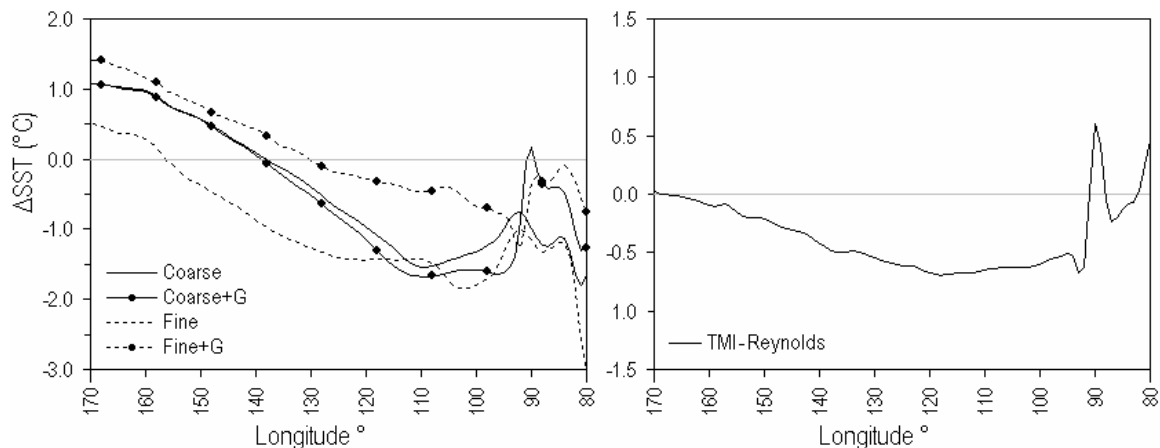


Figure 3.4. Left: Annual mean meridionally averaged (1°N-1°S) SST bias (°C, with respect to Reynolds) across the index area shown in Figure 3.2 of four simulated cases. Right: as in left but of TMI. Lines are as indicated on figure keys.

Diagnosing changes in seasonal variability between the simulations is not within the scope of this dissertation, but it is worthwhile to note that the seasonal variability of SST is also improved in the east-central region by including the Galápagos Islands under fine resolution (Figure 3.5). Under coarse resolution, there is some reduction of the westward extent of high seasonal variability (standard deviations of 1°C or more are shaded). However, the region of high seasonal variability in *Fine+G* is characterized as broader and shorter, similar to Reynolds, rather than narrow and long as in the other three experiments.

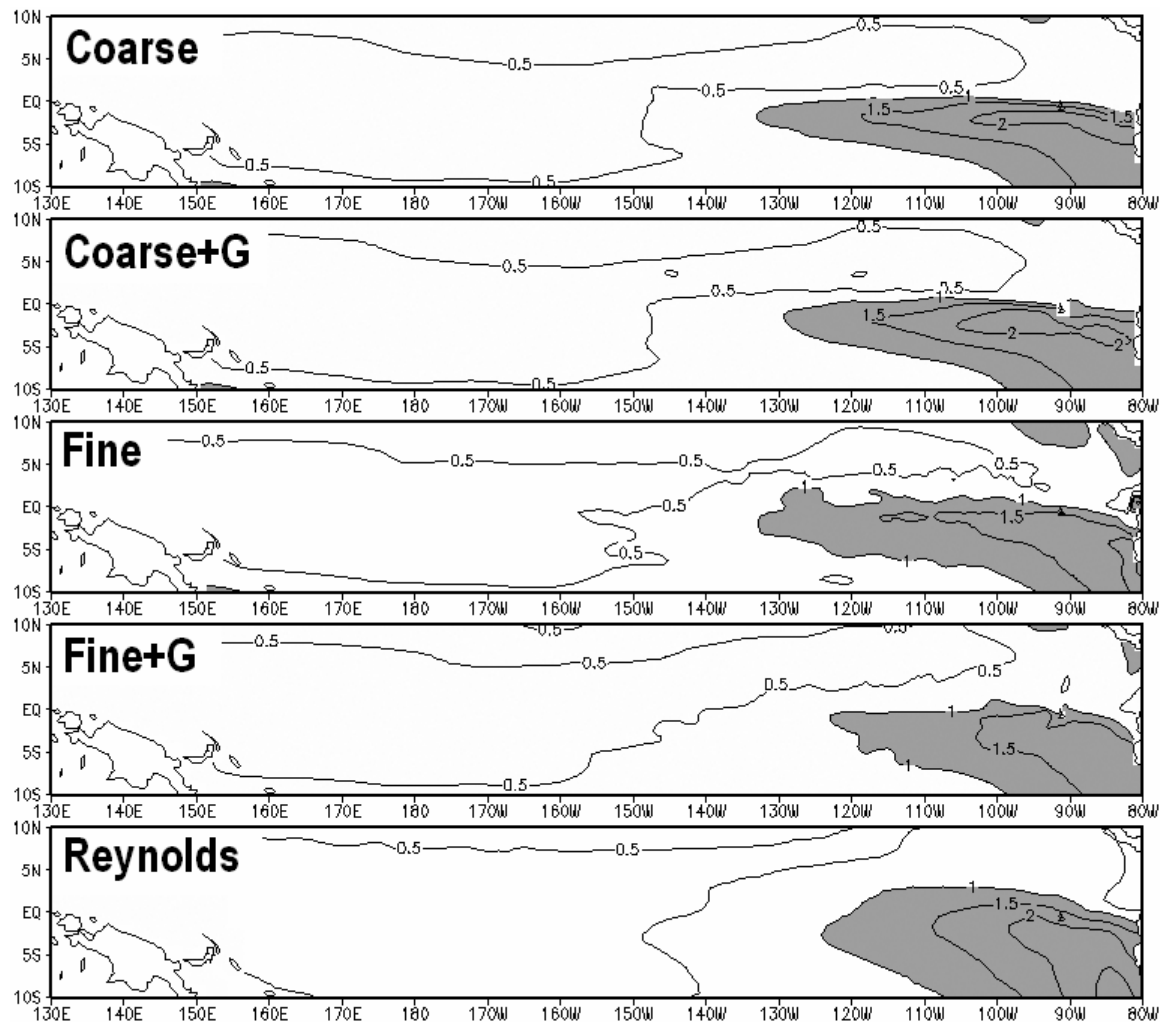


Figure 3.5. Standard deviation of the monthly SST (°C) seasonal cycle in the four simulated cases and Reynolds. Contour interval 0.5°C and standard deviations higher than 1.0°C are shaded.

The improvements in the cold tongue region by increased resolution and the Galápagos Islands are also evident upon comparing the spatial structure of seasonal mean SST fields. Based on observed climatology and output from all four simulated cases, the CT is least developed in terms of coastal and equatorial SST in boreal spring (MAM) and most developed in boreal fall (SON). Figure 3.6 (3.7) is a comparison of the mean MAM (SON) SST in the east-central equatorial Pacific Ocean between all four simulated cases and TMI observations. In both seasons, the combined effects of resolution and the Galápagos Islands are similar. Under coarse resolution, the improvements are local: slight warming immediately east of and cooling immediately west of the Galápagos Islands, while the coastal upwelling signal and westward extent of the CT are relatively unchanged. Under fine resolution, three improvements are found: the spatial structure of the CT immediately east and west of the Galápagos Islands, the structure of the coastal upwelling signal, and a reduction in the westward extent of the CT. Improvements from resolution alone are relatively minor. However, improvements due to the Galápagos Islands are only impressive under fine resolution.

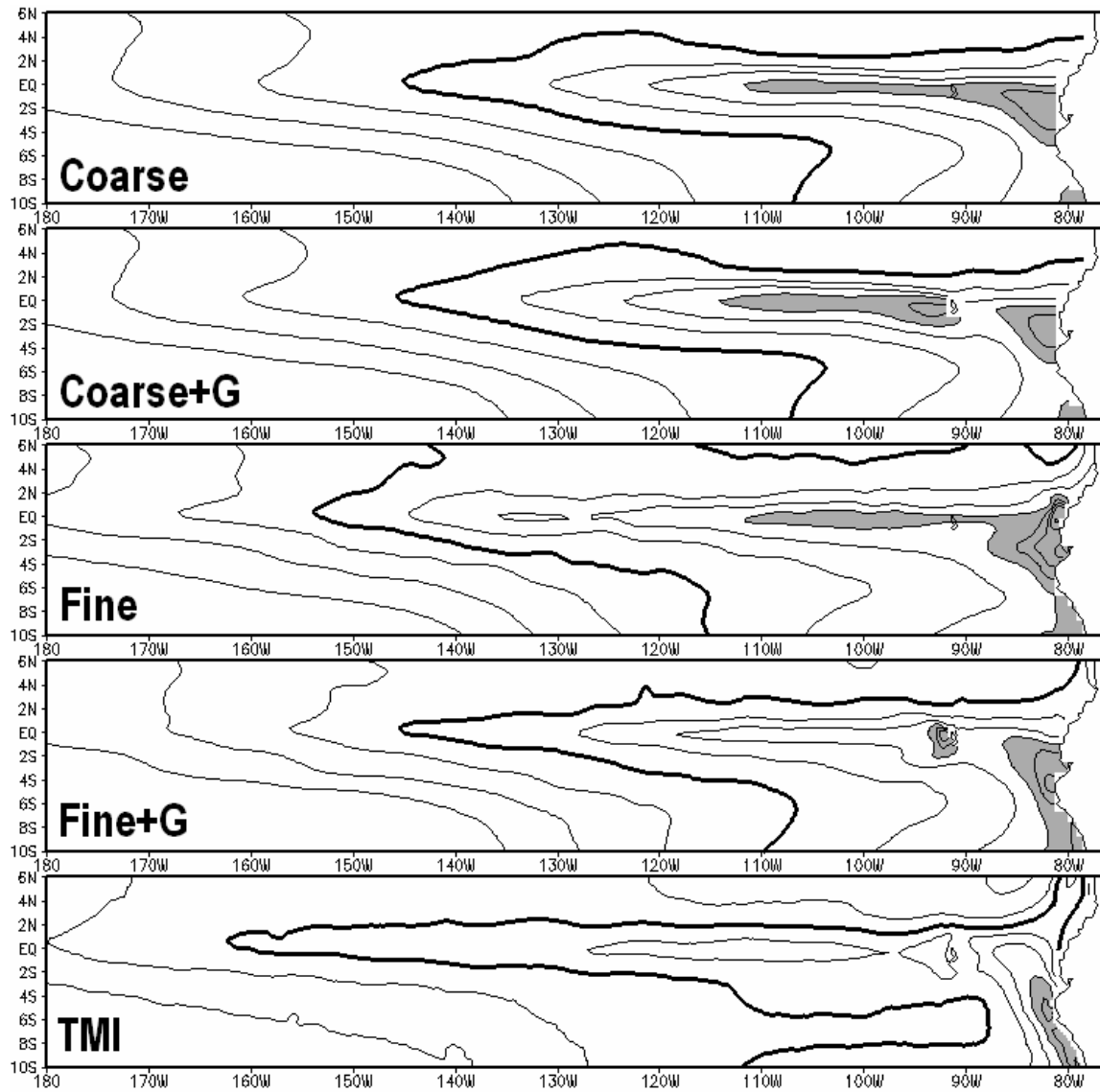


Figure 3.6. As in Figure 3.2 but for March-May, and the heavy contour is 27°C, and SST colder than 24°C is now shaded.

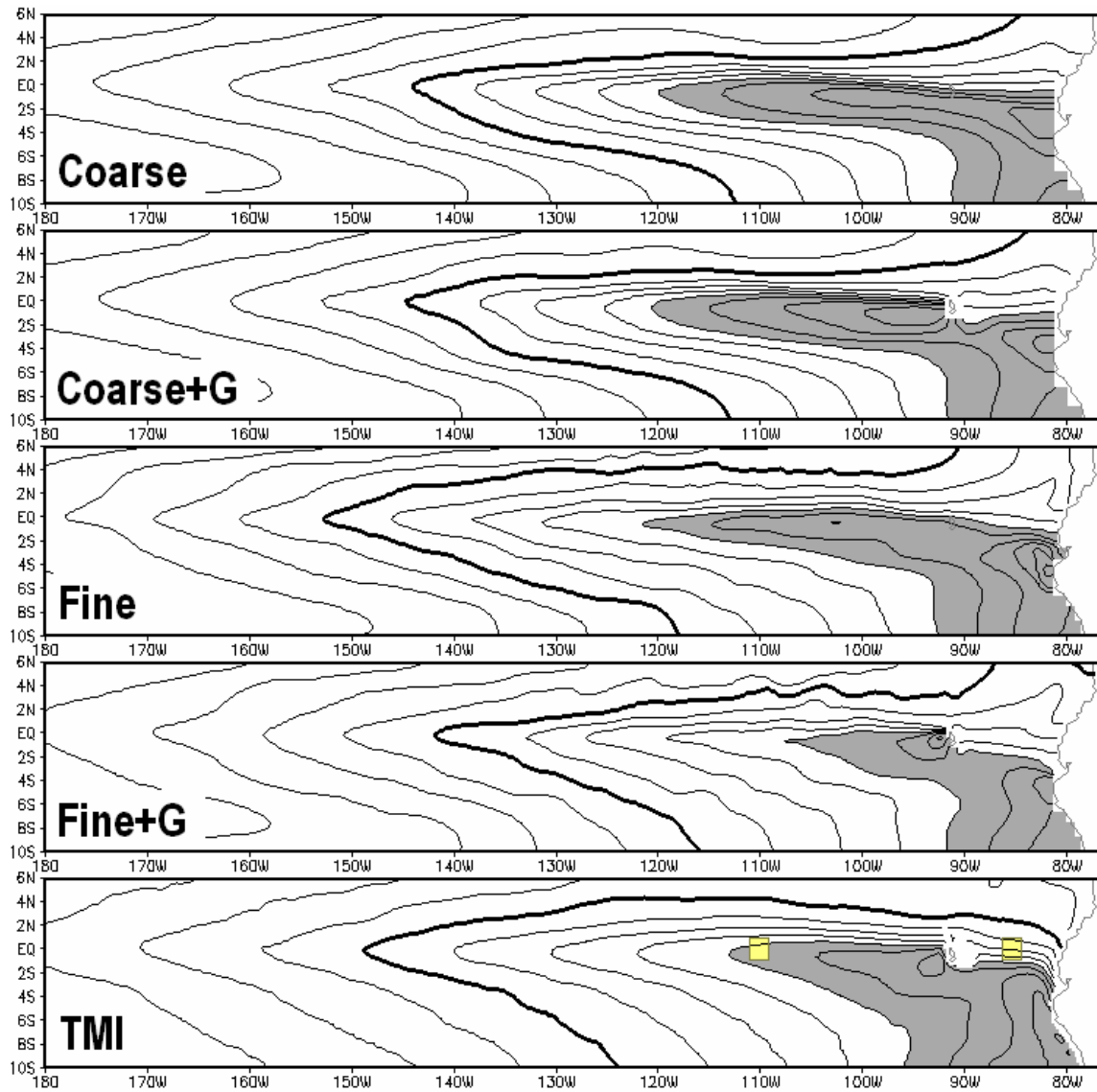


Figure 3.7. As in Figure 3.2 but for September-November, and the heavy contour is 26°C, and SST colder than 22°C is now shaded. The yellow boxes indicate the index regions used in Figures 3.8-3.9.

Different processes may be responsible for SST changes in the east-central part of the basin and in the region east of the Galápagos Islands. The CT index used thus far, spanning 90° longitude, is too broad for interpreting the response east and west of the Galápagos Islands. Therefore, two small (2° by 2°) boxes centered on the equator, one east of the Galápagos Islands (85°W) and one to the west (110°W), were chosen for comparison of simulated mean seasonal cycles of SST and Reynolds OI (indicated in Figure 3.7, bottom panel). Under coarse resolution

(Figure 3.8), there is little change in SST west of the islands, while at 85°W, the inclusion of the islands increases SST up to 1°C, bringing the simulated mean seasonal cycle in closer agreement with observations. This warming to the east of Galápagos is caused by a weakening of the thermocline and reduced entrainment-mixing and is similar to the changes in the *Fine+G* simulation. Under fine resolution, the simulated mean SST east and west of the Galápagos Islands is considerably improved (Figure 3.9). In addition to the surface, temperature differences in excess of 2°C between cases *Fine* and *Fine+G* are found at thermocline depth (Figure 3.10). Along the equator, the largest positive temperature difference between *Fine+G* minus *Fine* is found at approximately 75 m. Likewise along 110°W, the largest difference is found at 75 m, but differences of over 1.5°C extend to depths of 250 m or more, which is consistent with the changes in EUC and SEC noted in the following section.

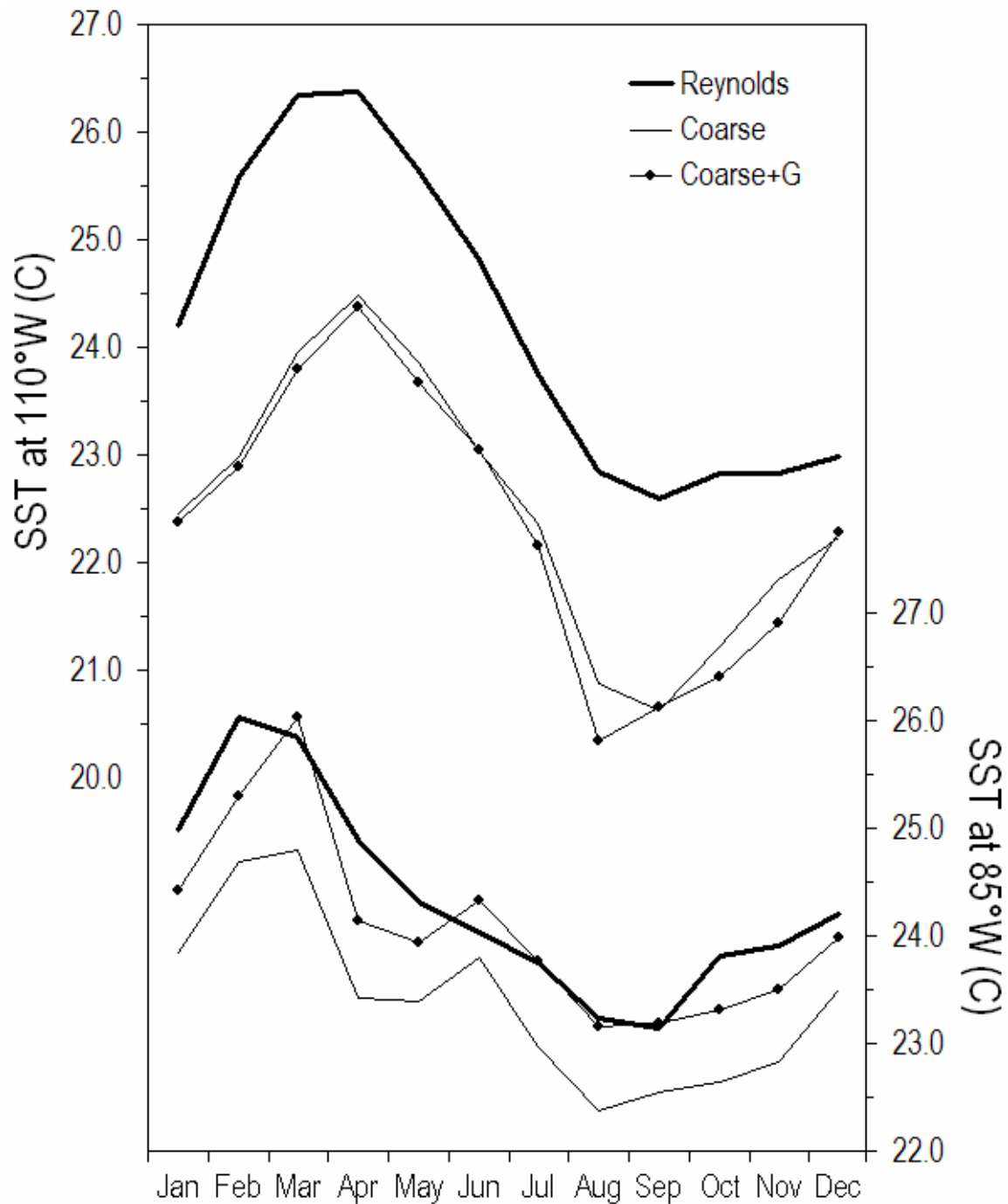


Figure 3.8. Mean seasonal cycle (monthly means) of SST (°C) at two 2° by 2° boxes (84°W-86°W by 1°S-1°N and 109°W-111°W by 1°S-1°N) for cases *Coarse* and *Coarse+G*, and the Reynolds SST climatology. Lines are as indicated on figure key.

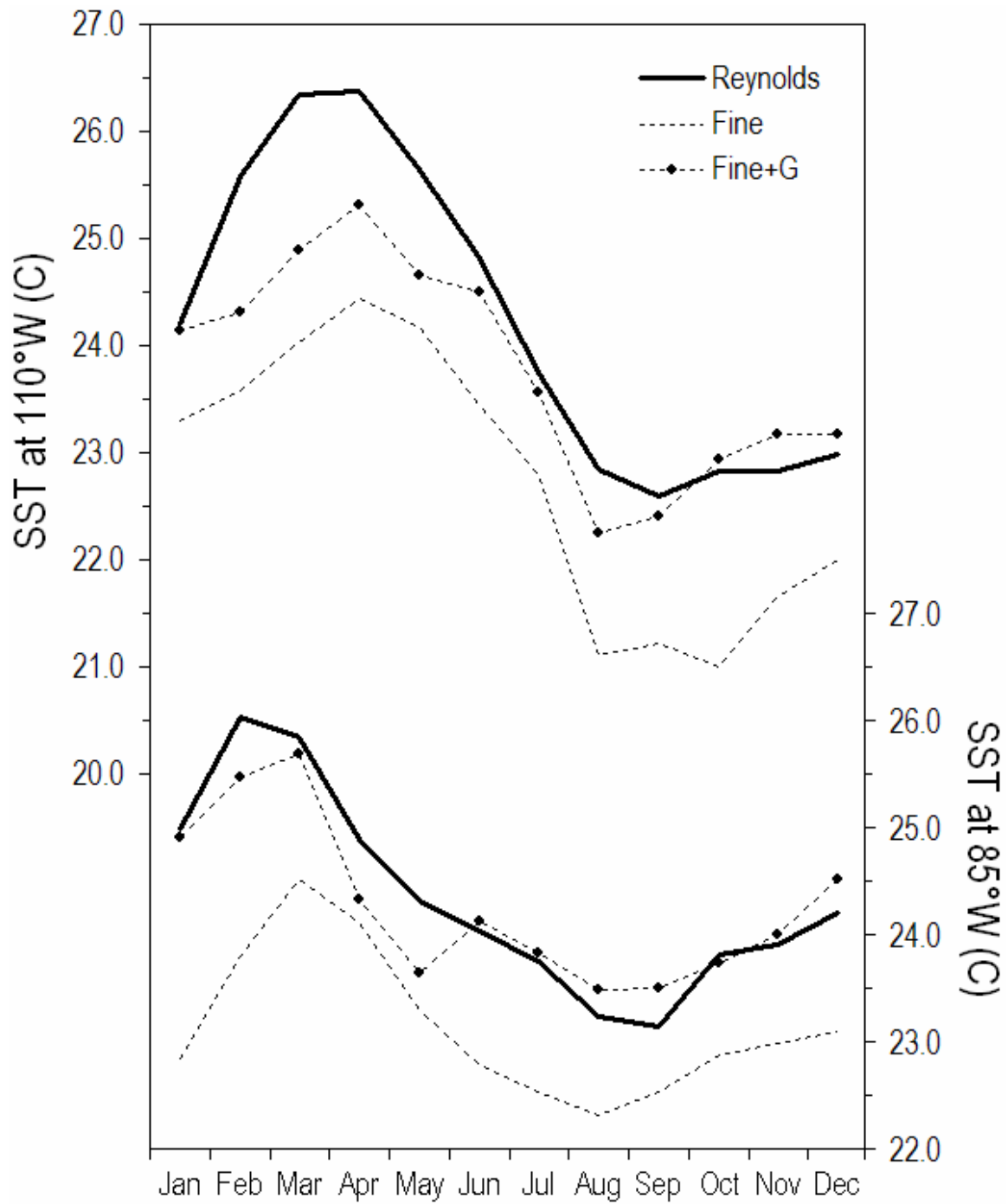


Figure 3.9. As in Figure 3.8 but for cases *Fine* and *Fine+G*.

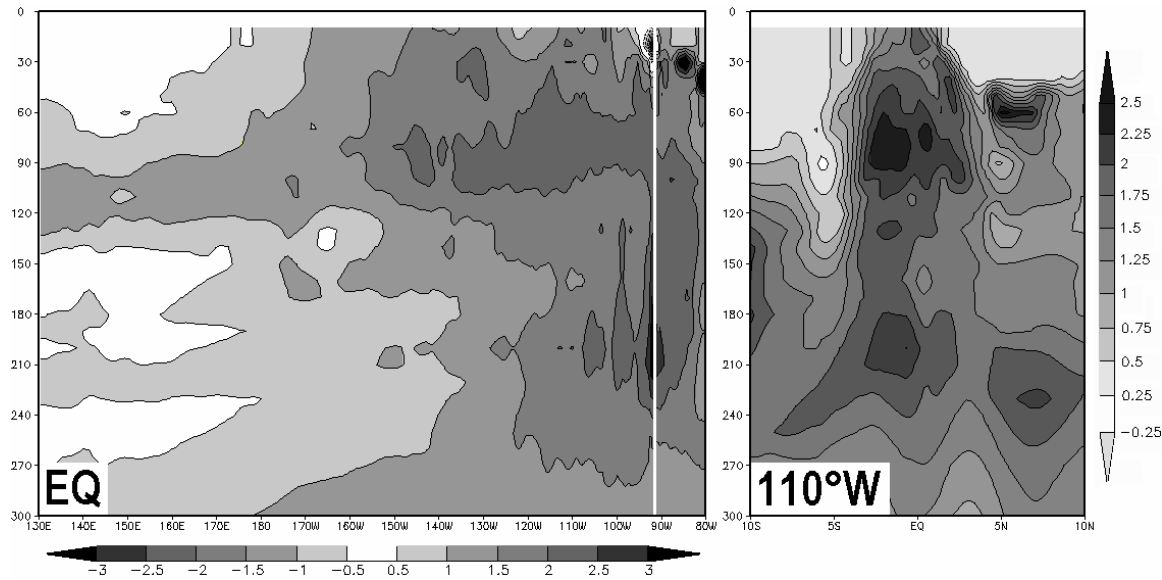


Figure 3.10. Zonal depth sections along the equator of September-November mean temperature ($^{\circ}\text{C}$) difference between cases *Fine+G* minus *Fine*, and the corresponding meridional section along 110°W .

In the equatorial Pacific Ocean, zonal transport is dominated by the eastward EUC and the westward South Equatorial Current (SEC). Changes to the EUC, a most vital component to the dynamical balance of the equatorial Pacific Ocean, are also noted under fine resolution. Presented in Figure 3.11 is a comparison of vertical profiles of zonal velocity at 110°W (about 20° longitude west of the Galápagos Islands) between the four simulated cases and available TAO depths. The effect of increased model resolution on zonal velocity at 110°W is to lower the core of the EUC by 10-20 m, and increase its speed by over 30 cm s^{-1} . The faster EUC in the fine resolution simulations could be partly attributed to stronger meridional gradients of zonal velocity, which has been shown to result in eastward advection of cyclonic relative vorticity and thus a stronger EUC than would be expected from the zonal pressure gradient alone (Kessler et al. 2003). Furthermore, near the core of the EUC (100 m), the inclusion of the Galápagos Islands under fine resolution (*Fine+G*) brings the simulated zonal velocity to within 2.4 cm s^{-1} of TAO observations. The profile of zonal velocity at 110°W from the climatology of the existing version of the NCEP GODAS is similar to the coarse resolution profiles in Figure 3.11 (Behringer

and Xue 2004, c.f. Figure 7). The SST improvements immediately east and west of the Galápagos Islands, as will be discussed in the following section, are related to the obstruction of the EUC by the Galápagos Islands in case *Fine+G*. We will also show that the improvements to the broader tropical cold bias problem are also due to the obstruction of the EUC, but further through a basin-wide dynamical and heat flux adjustment that effectively produces an SST warming across the east-central tropical Pacific Ocean.

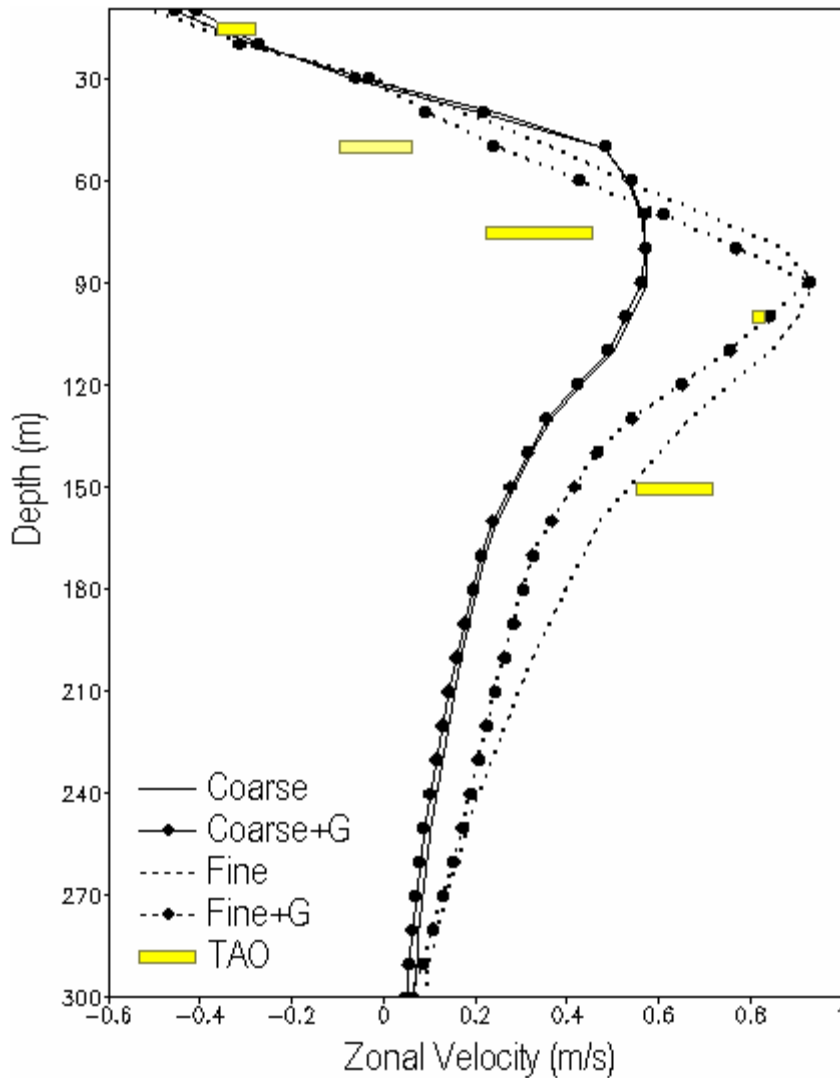


Figure 3.11. September-November mean vertical profiles of zonal velocity (m s^{-1}) at 0°N , 110°W for the four simulated cases. Yellow bands represent corresponding TAO zonal currents 15, 50, 75, 100, and 150 m. The width of the yellow bands represents the extent to which the values depend on the climatological base period used (i.e., 1980-1989, 1990-2005, or 1980-2005).

3.3.2. The influence of the Galápagos Islands on the Equatorial Undercurrent

A case is presented here that the simulated improvements to the tropical cold bias problem begin with the obstruction of the EUC by the Galápagos Islands at 92°W. From the comparison of vertical sections of temperature and zonal velocity along the equator (Figure 3.12), it can be seen that zonal velocity in the EUC approaches zero at the western edge of the Galápagos Islands in case *Fine+G*, while in case *Fine*, the EUC is allowed to continue unobstructed until reaching the continental shelf of South America. A similar reduction in the EUC approaching the Galápagos Islands is evident under coarse resolution, although much more gradual. The effect of obstructing the EUC on the upper ocean thermal structure east of the Galápagos Islands is a deeper thermocline; the 20°C isotherm is over 10 m deeper along the coast of South America in case *Fine+G* than in case *Fine*. Since the mean thermocline in the eastern equatorial Pacific is quite shallow to begin with, relatively small changes in the depth of the thermocline can have a large impact on SST. Comparing the subsurface thermal structure west of the Galápagos Islands, a given isotherm outcrops at least 10° longitude further to the east in *Fine+G* than in *Fine*, appreciably reducing the cold bias that is present without the Galápagos Islands.

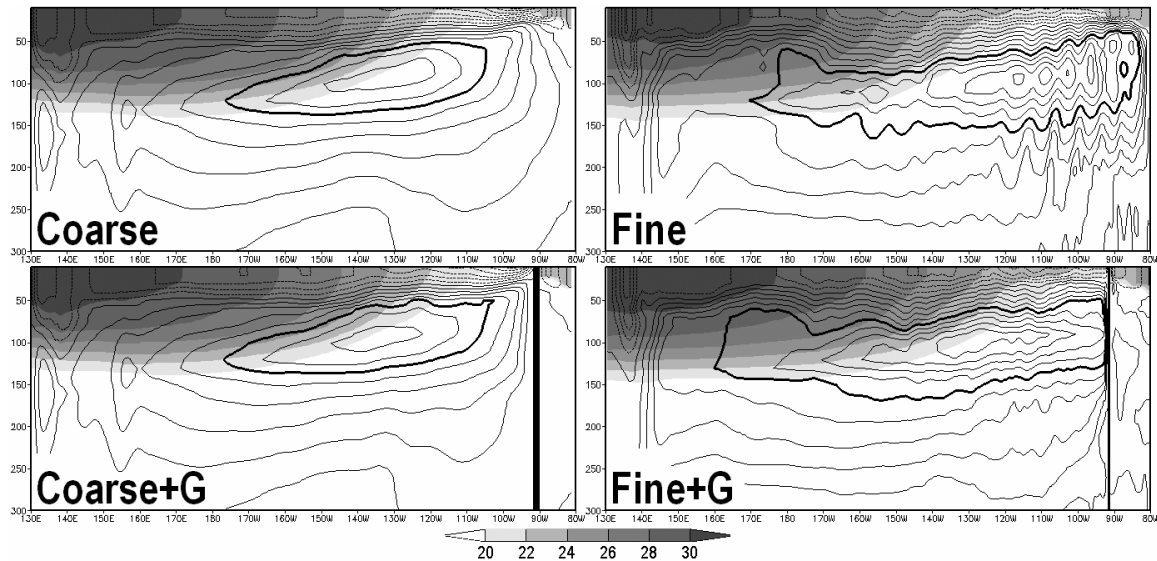


Figure 3.12. Vertical sections of September-November mean temperature ($^{\circ}\text{C}$) (shaded) and zonal current (m s^{-1}) (contoured) along the equator in the upper 300 m of the Pacific Ocean for simulated cases *Coarse* (A), *Coarse+G* (B), *Fine* (C), and *Fine+G* (D). Temperature warmer than 20°C is shaded every 2°C , zonal current contour interval 10 cm s^{-1} , and the heavy contour is 50 cm s^{-1} .

From a zonal depth section (e.g., Figure 3.12) one cannot determine if the EUC terminates, is deflected, or splits around the Galápagos Islands. ET-04 compared latitude-longitude plots of zonal velocity at 80 m depth in the eastern equatorial Pacific Ocean between simulations with and without the Galápagos Islands (c.f. Figure 3). In the model simulation of ET-04 that included the Galápagos Islands, the EUC is deflected northward around the island where it returns to the equator and continues on its original path. For that reason, ET-04 found only localized changes to the SST field (i.e., warming immediately east of and cooling immediately west of the Galápagos Islands). Figure 3.13 shows the analogous zonal velocity depiction for our experiments, comparing cases *Fine* and *Fine+G*. Clearly evident in case *Fine+G* is an obstruction or, at least zonally, a near termination of the EUC at the western boundary of the Galápagos Islands. This near termination of the zonal component of the EUC is further evident in Figure 3.14, which is a series of meridional sections of zonal velocity 2° west of, through, and 2° east of the Galápagos Islands. Along each of the meridians shown for case *Fine* (top), there is little change in the strength or location of the EUC. In *Fine+G* (bottom), as in *Fine*, the EUC has a core of roughly 70 cm s^{-1} at 93°W , but upon meeting Isla Isabela, a weak ($10\text{-}20 \text{ cm s}^{-1}$) branch is directed south of, and one is directed north of the barrier. At 89°W , all that remains of zonal velocity is a slightly deeper 10 cm s^{-1} lobe to the north of the original core.

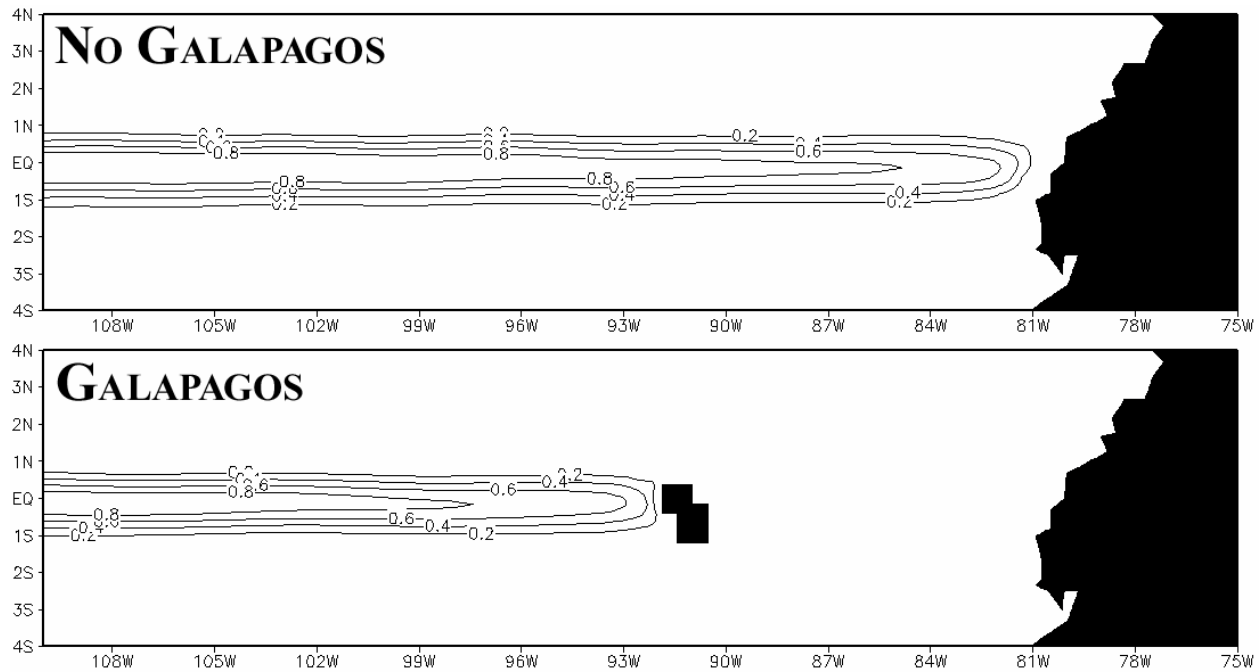


Figure 3.13. September-November mean 80 m zonal currents (m s^{-1}) in the eastern equatorial Pacific Ocean for simulated cases *Fine* (“*No Galápagos*”) and *Fine+G* (“*Galápagos*”). Contour interval 20 cm s^{-1} .

It is instructive to understand the fate of the EUC following its encounter with the Galápagos Islands. In terms of volume transport (integrated from 4°S to 4°N and 0-300m), eastward volume transport (T_x) is reduced by 62% between 95°W and 85°W . To estimate how much of that reduction in T_x is being compensated by poleward volume transport (T_y) versus vertical transport (T_z), T_y was calculated by integrating meridional velocity from 95°W to 85°W and 0-300m at 4°N and 4°S . Poleward transport, or the sum of northward T_y through the 4°N plane and southward T_y through the 4°S plane, only accounts for 15% of the amount by which eastward T_x was reduced across the Galápagos Islands. This implies that T_z , taken as the residual, accounts for the remaining 85% of the mass balance. Furthermore, 86% of the poleward transport is accounted for by the southward T_y , which becomes available to feed the Peru-Chile Undercurrent.

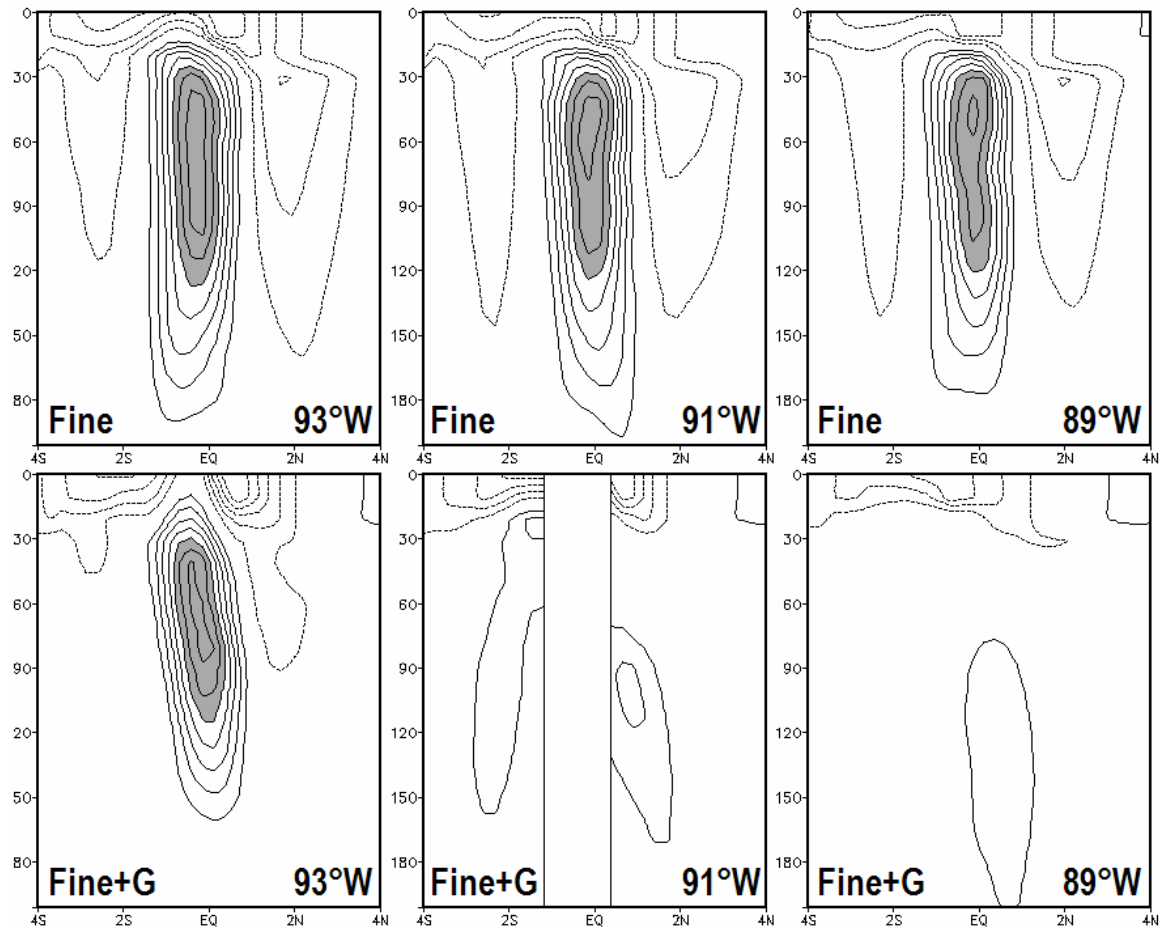


Figure 3.14. September–November mean meridional sections of zonal velocity (m s^{-1}) in cases *Fine* and *Fine+G* at 93°W , 91°W , and 89°W for the upper 200 m. Contour interval 10 cm s^{-1} , values greater than 50 cm s^{-1} are shaded, and negative values are dashed.

As demonstration of the improved modeling of subsurface flow due to the inclusion of the Galápagos Islands, a comparison is made with the seminal work of Lukas (1986). Lukas (1986) observed remnants of the EUC flowing southeastward from the Galápagos Islands to converge with the Southern Subsurface Countercurrent and form the Peru–Chile Undercurrent around 100 m depth. The location of the Peru–Chile Undercurrent was then corroborated with inferences from dynamic topography. Based on comparison of current vectors and speed at 100 m depth between cases *Fine* and *Fine+G* (Figure 3.15), the joining of the EUC remnants southeast of the Galápagos Islands with the Southern Subsurface Countercurrent and formation

of the Peru-Chile Undercurrent is evident in case *Fine+G*, confirming the important role of the interaction between the Galápagos Islands and the EUC in its formation. Both cases exhibit a narrow corridor of southward flow along the coast, but the connection with the EUC, as in the analyses of Lukas (1986; c.f. Figure 17), is only evident in case *Fine+G*.

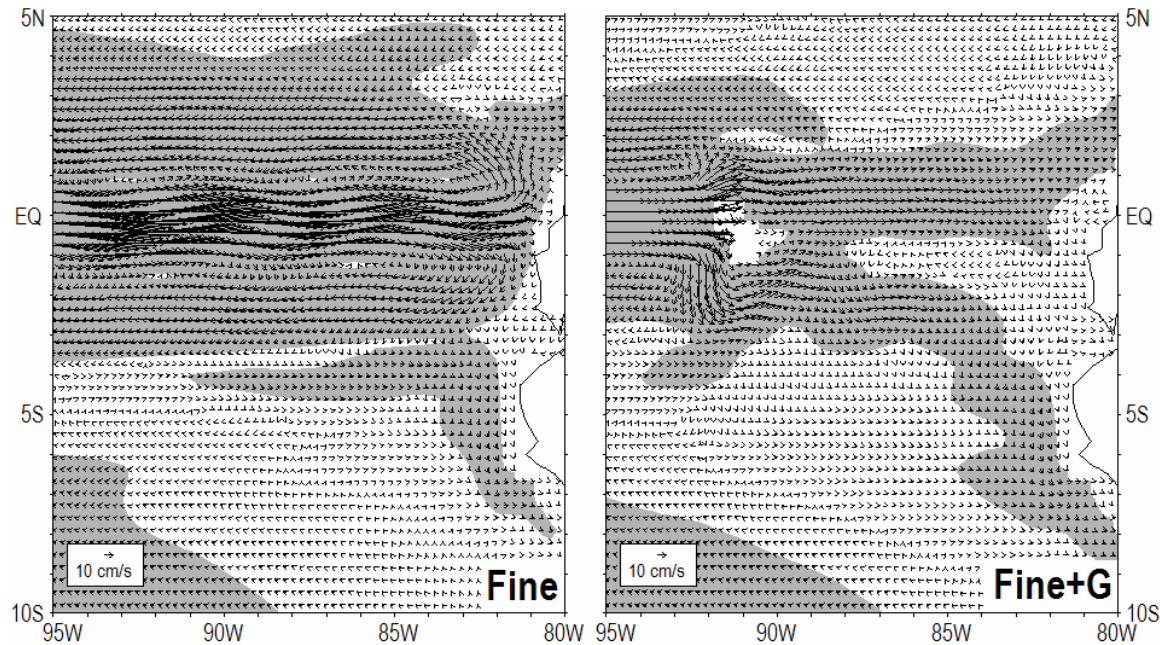


Figure 3.15. September-November mean velocity vectors at 100 m depth in the eastern equatorial Pacific Ocean for cases *Fine* and *Fine+G*. A reference vector for 10 cm s⁻¹ is provided. Shading indicates speeds greater than 2.5 cm s⁻¹.

3.3.3. Mechanisms for the reduction of the tropical cold bias

The more remarkable improvement to the simulated climatology of the tropical Pacific Ocean owing to the Galápagos Islands is not necessarily the fact that the EUC is blocked well short of the South American coast, but rather the positive mean SST difference throughout the east-central tropical Pacific. The existence of the Galápagos Islands has a warming effect on a broad region from 10°S to 10°N, up to 2°C (Figure 3.16a). Also shown in Figure 3.16a is the difference in ocean-atmosphere net heat flux (NHF) between cases *Fine+G* minus *Fine*. Differences of 10-20 W m⁻² are found across the east-central tropical Pacific. This points to the

important role of the feedback between SST and ocean-atmosphere heat flux, and could have an appreciable impact on the thermodynamics of the lower troposphere. A straightforward heat budget analysis was performed on the two small boxes used for the SST mean seasonal cycle comparison in the previous section. Each term was contrasted between cases *Fine* and *Fine+G* to determine what processes are responsible for the warming previously shown and discussed. In the 85°W box east of the Galápagos Islands, vertical entrainment-mixing is reduced; the difference in annual mean contribution to the mixed layer heat budget by entrainment-mixing is +15.8 W m⁻² (Figure 3.16b). Meridional and zonal thermal advection also contribute to the warming east of the Galápagos Islands (Figure 3.16c, d). West of the Galápagos Islands, the difference in contribution to the mixed layer heat budget by entrainment-mixing remains broad and positive (+13.4 W m⁻² in the 110°W box), while differences due to horizontal thermal advection represent the signal of westward propagating waves and average to zero over time and space.

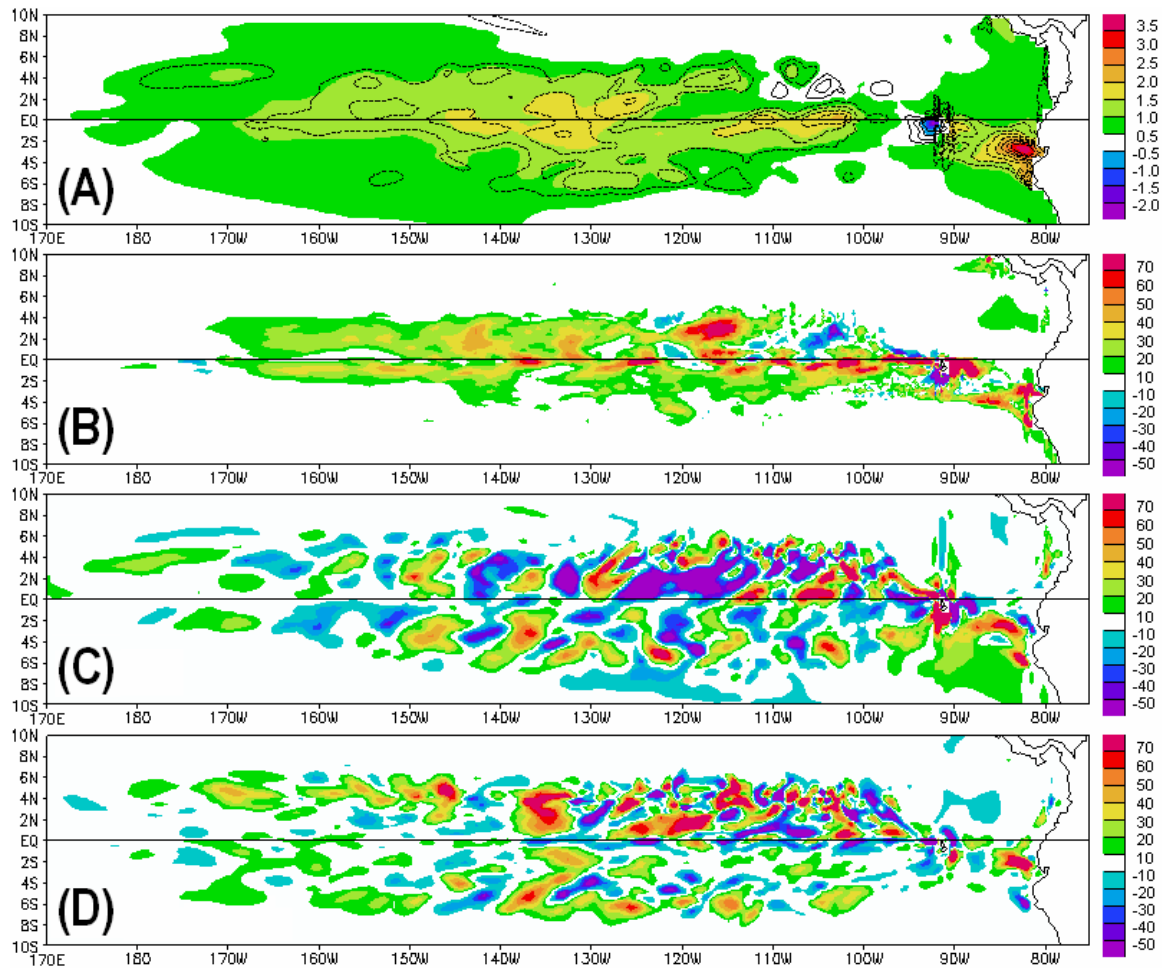


Figure 3.16. September-November mean SST difference ($^{\circ}\text{C}$) (shaded), net ocean-atmosphere heat flux difference (contour interval 10 W m^{-2}) (A), difference in contribution to the mixed layer heat budget by entrainment-mixing (W m^{-2}) (B), zonal thermal advection (C), and meridional thermal advection (D) for cases *Fine+G* minus *Fine*.

Given that reduced entrainment-mixing is the dominant term responsible for the positive SST difference between cases *Fine* and *Fine+G*, the remainder of this section is aimed at establishing why entrainment-mixing would be reduced in case *Fine+G*. Two important factors that determine the effectiveness of entrainment-mixing are the vertical gradient of temperature, particularly at the base of the mixed layer, and the depth of the thermocline. Across the entire east-central tropical Pacific, the vertical temperature gradient at the mixed layer depth is more

diffuse in *Fine+G* than in *Fine*. For example, using once again 110°W and averaged from 2°N to 2°S, the vertical temperature gradient at mixed layer depth is more diffuse in case *Fine+G* ($-0.10^{\circ}\text{C m}^{-1}$) than case *Fine* ($-0.13^{\circ}\text{C m}^{-1}$). While these differences appear small, note that these are the remaining differences as a net result of the large-scale dynamic and thermodynamic adjustments including shear mixing and entrainment under prescribed forcing.

For a given zonal wind stress and ocean geometry, there will be an equilibrium mass and energy balance. In the Pacific Ocean, the dynamical features maintaining this balance are the easterly trade winds, the westward SEC, southward interior Sverdrup flow, a thermocline that slopes up to the east, a sea surface that slopes up to the west (mirroring the thermocline), a westward zonal pressure gradient, and the EUC flowing eastward along the thermocline. After sufficient spin-up time, such is the case in a model. However, should one component of this balance become disrupted, a new, adjusted dynamical balance must follow. An attempt at illustrating this adjustment using output from the *Fine* and *Fine+G* simulations is presented in Figure 3.17. The disruption in this case is the obstruction of the EUC at the Galápagos Islands, which is evident in the difference in EUC core velocities around 92°W (“EUC core velocity” being the maximum positive zonal velocity found between 5°S and 5°N at any depth). In response to this disruption, equatorial sea level rises across the basin. However, since EUC transport is also reduced basin-wide, the change in sea level is nonuniform; the sea level rise in the west is less than that in the east, resulting in a more gradual sea surface slope. Also evident in Figure 3.17 is the fact that the SEC in the east-central region is approximately 10 cm s^{-1} slower in case *Fine+G*, or a roughly 25% reduction in SEC velocity between 160°W and 90°W (“SEC velocity” being surface zonal velocity averaged from 5°S to 5°N). Corresponding changes in the subsurface thermal structure are also evident; the base of the mixed layer is deeper between 170°W and 130°W, and the 20°C isotherm is deeper throughout the east-central region where positive SST differences were found. When compared with the climatology of September–November mean 20°C isotherm depth from TAO measurements, closer agreement is found with

Fine+G at all available longitudes (Figure 3.17). East of 180°W, the difference in 20°C isotherm depth represents an over 50% reduction in RMSE with respect to TAO measurements. The new, adjusted equilibrium state of the equatorial Pacific in *Fine+G* caused by the obstruction of the EUC at the Galápagos Islands, leading to reduced EUC-SEC shear, reduced westward advection of cold SST by the SEC, and a deeper thermocline lends itself to the positive SST differences found in nearly the same location as known SST cold biases. None of the aforementioned differences highlighting the zonal dynamical adjustment were discernable between cases *Coarse* and *Coarse+G*, which is undoubtedly because the EUC did not extend far enough to the east for the Galápagos Islands to actually obstruct it (e.g., Figure 3.12).

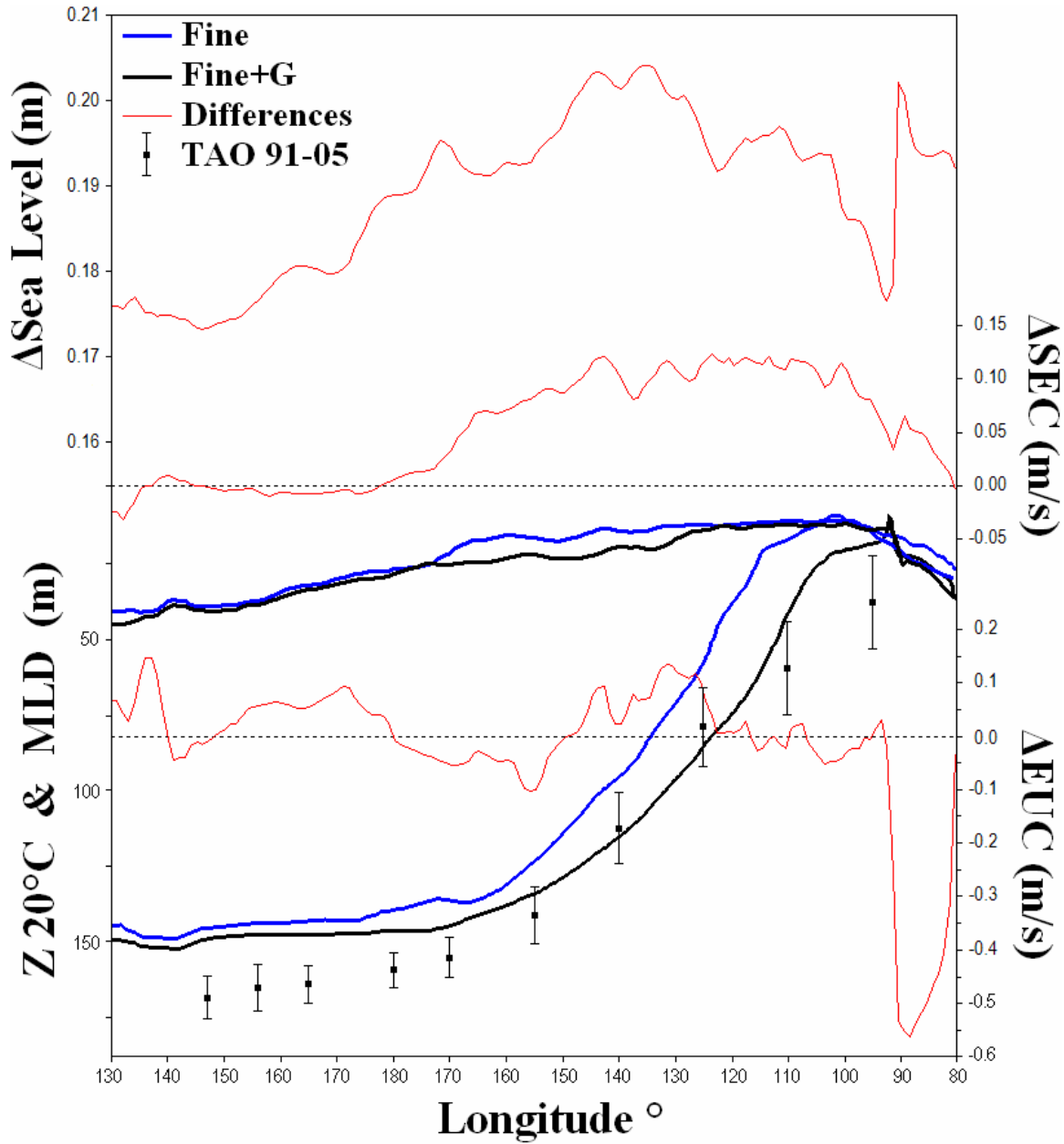


Figure 3.17. September-November mean values with respect to longitude along the equator of (from top to bottom) difference in sea level (m) between *Fine+G* minus *Fine*, difference in SEC velocity (m s^{-1}) between *Fine+G* minus *Fine*, mixed layer depth (m) for *Fine* and *Fine+G*, 20°C isotherm depth (m) for *Fine*, *Fine+G*, and TAO observations (error bars indicate one standard deviation), and difference in EUC core velocity (m s^{-1}) between *Fine+G* minus *Fine*.

Important differences in meridional circulation were also found between cases *Fine* and *Fine+G*, which are not unrelated to the zonal adjustment. The meridional circulation in the equatorial Pacific Ocean is characterized by import at thermocline depth and export at the surface. Given such a configuration, mass continuity mandates upwelling and entrainment of cold water at the equator. This circulation is present in both *Fine* and *Fine+G*, but is considerably slower in case *Fine+G*. At 4°N, averaged from 180°W to 100°W, the maximum southward velocity (import) is reduced by 15%, and the maximum northward velocity (export) is reduced by 65% from *Fine* to *Fine+G*. At 4°S, there is little change in maximum northward velocity (import), but maximum southward velocity (export) is reduced by 27%. Translating to an overall reduction in the rate of meridional equatorial overturning of roughly 25%, an increase in SST follows. As would be expected from a more diffuse thermocline, the aforementioned zonal adjustment, and reduced meridional circulation, entrainment-mixing is considerably weaker and less effective, resulting in a pattern of reduced cooling that approximates the pattern of SST warming (Figure 3.16b). The reader is reminded that the wind stress forcing was identical in all cases, thus any changes in circulation are independent of any wind-driven processes such as Ekman divergence. One could say that many aspects of the ocean's response to the surface winds that act to produce zonal inhomogeneities (e.g., 20°C isotherm depth, sea level, SST, etc) are lessened without requiring a change in zonal wind stress. Clearly a warmer CT and a reduced zonal SST gradient will have local and remote wind responses in a coupled model and as pointed out by Schneider and Zhu (1998), they will further alleviate the cold bias in the CT.

The objective of the present section was to assess the potential improvements to the equatorial Pacific cold tongue region resulting from higher spatial resolution and the inclusion of the Galápagos Islands. It was found that the Galápagos Islands obstruct the EUC, which prompts a basin-wide adjustment in the equatorial mass and energy balance. The result of the dynamical adjustment is a deeper and more diffuse thermocline, as well as reduced meridional

overturning at the equator. All of these results lead to reduced entrainment-mixing and therefore warmer SST. The feedback between SST and ocean-atmospheric heat flux also contributes to the warming.

In many respects, simply increasing the resolution *without* including the Galápagos Islands did not result in improvements, but instead exacerbated the cold bias and produced an EUC that is too strong east of where the islands should be. On the other hand, differences due to the Galápagos Islands without increasing the horizontal resolution were negligible. Only when the Galápagos Islands were given a proper treatment with sufficient horizontal resolution did a more realistic depiction of the CT and a reduction in the tropical cold bias problem emerge. In other words, the horizontal resolution must be fine enough to produce an EUC that extends far enough eastward, but the Galápagos Islands must be there to obstruct it.

In the experiments of ET-04, the EUC deflects north and promptly returns to its original path without extensive loss of zonal velocity. The reasons for such drastically different EUC responses to the Galápagos Islands between this dissertation and ET-04 are straightforward. Although there are differences in the OGCMs used in ET-04 and the present study (horizontal resolution is not one of them), it is thought that the differences in the results arise from the fact that the Galápagos Islands in ET-04 were too small (meridional extent about $3/4^\circ$), and entirely south of the equator (by about $1/4^\circ$). In the present study, the Galápagos Islands were implemented into the our OGCM with realistic meridional extent and location. Furthermore, the EUC in the ET-04 simulation that includes Galápagos is centered directly on the equator, rather than $1/4^\circ\text{S}$ where it is known to be. For these reasons, the EUC simply “glances” the Galápagos Islands in ET-04, which at least partially explains why ET-04 did not report a broader tropical SST warming. Differences in the surface heat flux formulation also contribute to the differences in the extent of air-sea interactions between the two models (see Murtugudde et al. 1996).

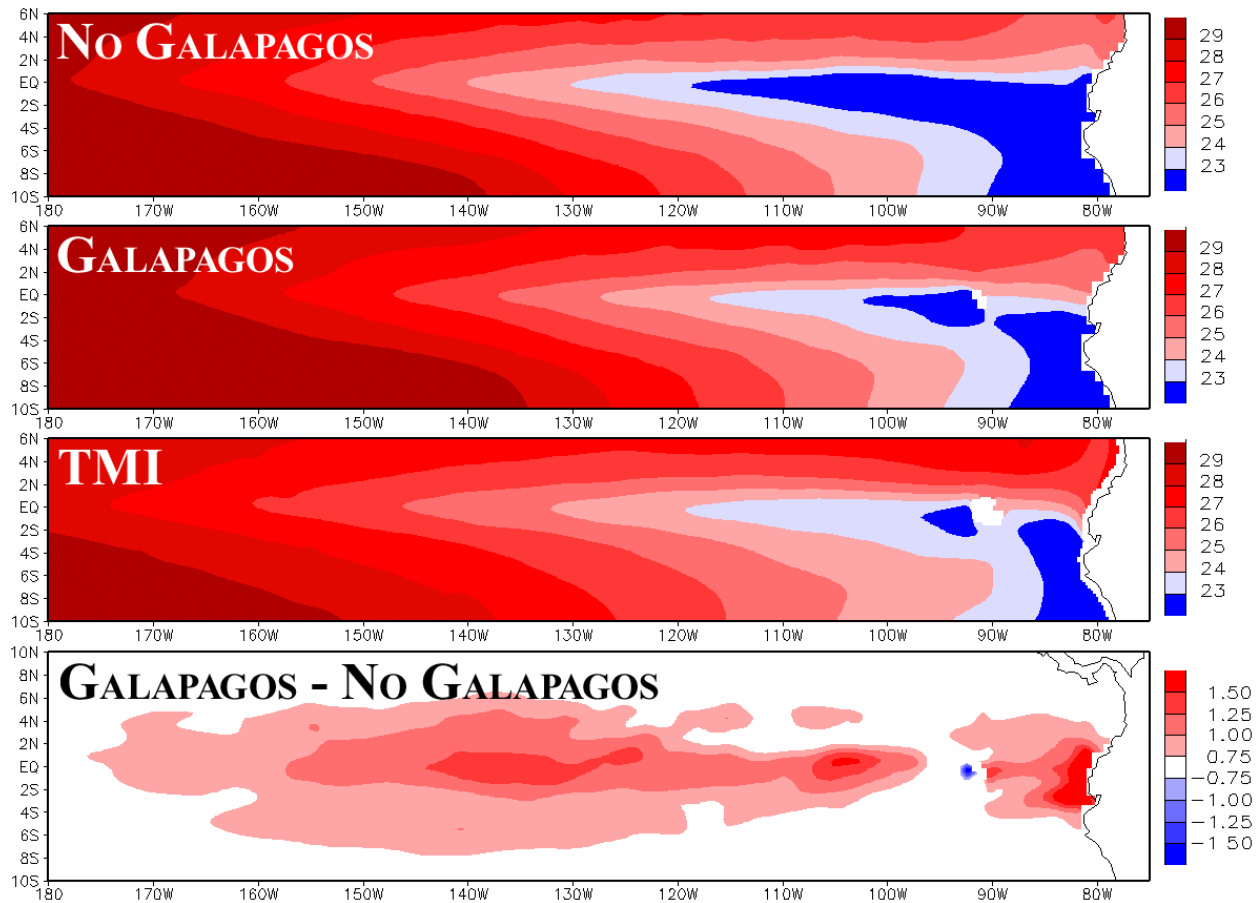


Figure 3.18. Annual mean SST ($^{\circ}\text{C}$) in the equatorial Pacific Ocean from model cases without Galápagos (*Fine*), with Galápagos (*Fine+G*), and TRMM (1998-2005), and the difference between model cases with and without the Galápagos Islands.

The spatial pattern of the SST difference *Fine+G* minus *Fine* is similar to the known biases in the MOM3 OGCM and the NCEP GODAS (Figure 3.18). It is thought that such an improvement, including the reduced atmosphere-ocean NHF, would have a considerable impact on the ability of coupled ocean-atmosphere and ocean-ecosystem models to produce realistic clouds, precipitation, biological activity, and carbon cycling in the tropical Pacific Ocean. It is clear that the effects of the Galápagos Islands on the Pacific Ocean beginning with equatorial currents cannot be ignored on the annual mean. Future work should be aimed at exploiting similar effects on interannual variability and the implications for the predictability of the couple

ocean-atmosphere system. In particular, the potential benefits to the predictive skill of, for example, future iterations of the NCEP GODAS and CFS by implementing the Galápagos Islands at sufficient resolution should be given serious consideration.

3.4. Improvements to the simulation of ENSO in forced and hybrid coupled models

3.4.1. The effect of the Galápagos Islands on an idealized El Niño

The next logical step is to understand what effect the Galápagos Islands have on interannual variability in the Pacific (i.e., ENSO) and subsequent predictability in a coupled climate context. There could also be important implications for the equatorial and coastal biological response to ENSO variability. The present section is aimed at quantifying and explaining the effect of the Galápagos Islands on ENSO amplitude and period. We consider the possibility that the Galápagos may exert an influence through either direct flow-topography interaction or through the fact that the Galápagos results in a different mean state upon which ENSO events operate. In this chapter, we use a combination of tools to explain the effects in terms of ocean mixed layer physics and equatorial wave dynamics: “idealized forced” experiments using the dynamically uncoupled ocean model also used in Section 3.3 (i.e., only coupled through surface heat flux), “hybrid coupled” experiments (i.e., coupled through surface heat flux *and* wind stress) to show the effect of the Galápagos on the intrinsic ENSO variability in the Pacific ocean-atmosphere system, and high-resolution satellite observations.

To illustrate the total effect of the Galápagos Islands on the El Niño events in the idealized forced experiments, it is necessary to choose indices that highlight the ocean response at key locations in the tropical Pacific Ocean. NINO4 (160°E-150°W, 5°S-5°N) represents the anomaly in the western equatorial Pacific, NINO3 (150°W-90°W, 5°S-5°N) in the eastern Pacific, and NINO1+2 (90°W-80°W, 10°S-Eq.) in the coastal upwelling region off the west coast of South America but east of the Galápagos Islands. The NINO4 region also closely resembles the domain over which the westerly wind stress anomaly was positioned for inducing the El

Niño events. The NINO3 region corresponds with the region in which a fully-mature ENSO event manifests itself in SST. For practical purposes, NINO3 is the appropriate measure of the peak amplitude of an ENSO event, while NINO4 is commonly thought to have predictive utility.

Area averaged SST and mixed layer heat content anomalies were computed for each of the aforementioned NINO indices, and are presented in Figure 3.19. The general expression for ocean heat content HC is

$$(3.2) \quad HC = C_p \rho \int_z^{\Delta z} T(z) dz$$

where C_p is the specific heat of water at constant pressure, ρ is the density of water, and $T(z)$ is the temperature at depth z . Thus, the heat content of an isothermal layer k is defined as

$$(3.3) \quad HC(k) = C_p \rho h(k) T(k)$$

where $h(k)$ is the depth of layer k . Since, in the present model formulation, the mixed layer is simply the first layer, mixed layer heat content HC_{ml} reduces to

$$(3.4) \quad HC_{ml} = C_p \rho h(1) T(1).$$

Thus, particularly in the eastern equatorial Pacific where the mixed layer is relatively shallow compared to the west, and where there are large interannual variations in the depth of the mixed layer, HC_{ml} contains important information about subsurface processes, and is highly sensitive to the depth of the mixed layer $h(1)$ compared to mixed layer temperature $T(1)$, since $h(1)$ is in units meters and variations are order 10m, whereas $T(1)$ is in units Kelvin and variations are order 1K.

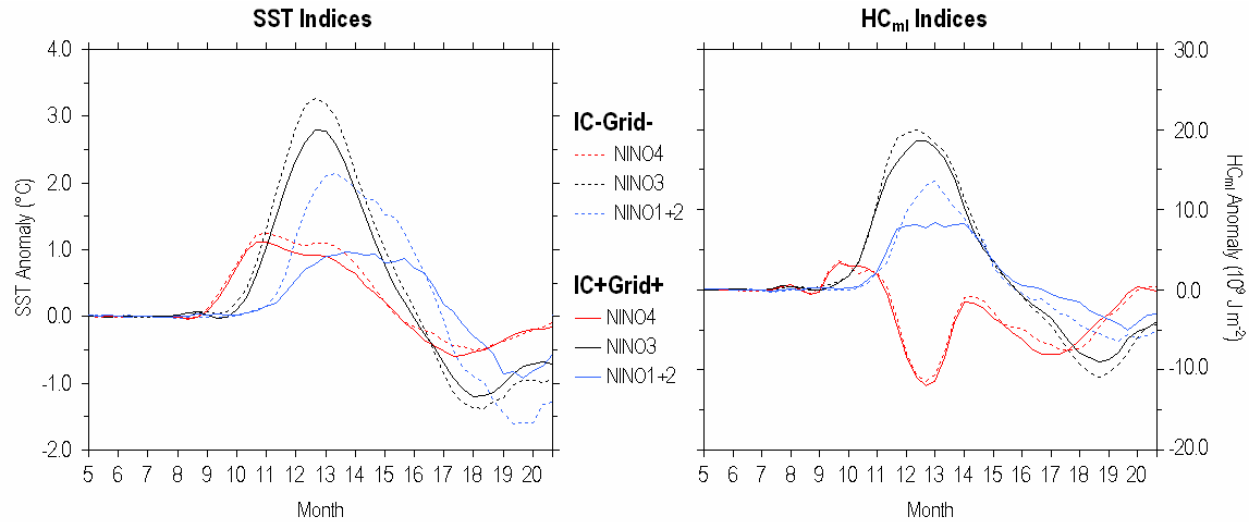


Figure 3.19. Temporal evolution of SST anomaly ($^{\circ}\text{C}$; left) and mixed layer heat content (HC_{ml} ; 10^9 J m^{-2} ; right) in the NINO4 (red), NINO3 (black) and NINO1+2 (blue) regions for idealized forced experiments *IC-Grid-* (dashed) and *IC+Grid+* (solid).

According to Figure 3.19, the peak SST anomaly in the NINO3 region is reduced by approximately 0.5°C by the Galápagos, or a 15% reduction in the anomaly over experiment *IC-Grid-*. The reduction of the anomaly in NINO4 is small. In NINO1+2, however, the SST anomaly is reduced by approximately half. The phasing between the three NINO indices is relatively unchanged between *IC-Grid-* and *IC+Grid+*, with both experiments exhibiting NINO4 leading, followed by NINO3, and finally NINO1+2. The result is similar in terms of HC_{ml} anomaly, with the largest difference being found in the NINO1+2 region.

In both experiments *IC-Grid-* and *IC+Grid+*, the peak of the event occurred in December and January. To examine the spatial distribution of the SST anomalies during the peak of the El Niño event, presented in Figure 3.20 are maps of Dec.-Jan. mean SST anomaly in experiments *IC-Grid-* and *IC+Grid+*, and the difference. In the east-central region of the equatorial Pacific, the SST anomaly is damped by the Galápagos by approximately 0.5°C . East of the Galápagos, the reduction of the SST anomaly is $1\text{-}2^{\circ}\text{C}$. The difference in net atmosphere-ocean heat flux anomaly is also displayed. A direct implication of a reduced SST anomaly is

reduced anomalous ocean-atmosphere heat flux, which would have strong consequences for the overall tropospheric response to an El Niño event. As will be discussed in the following section, the reduced NHF is largely due to reduced Q_{LH} . Thus, not only is the effect of the Galápagos transmitted through NHF, but through evaporative moisture flux as well.

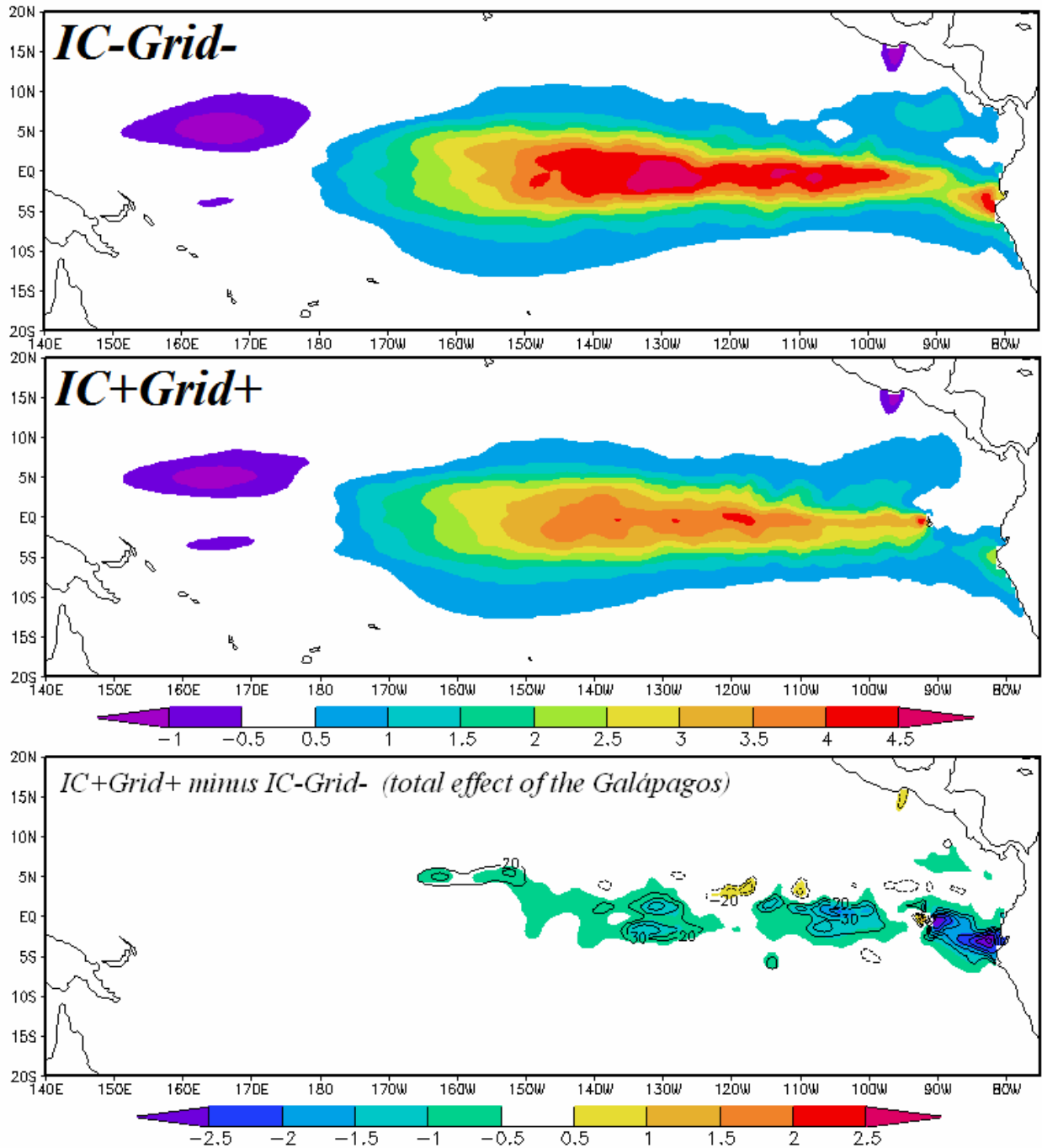


Figure 3.20. Maps of Dec.-Jan. mean SST anomaly ($^{\circ}\text{C}$) in the tropical Pacific Ocean for idealized forced experiments *IC-Grid-* (top), *IC+Grid+* (middle), and the difference, including the difference in net atmosphere-ocean heat flux anomaly (bottom; W m^{-2} ; contour interval 10 W m^{-2} beginning at $\pm 20 \text{ W m}^{-2}$).

Figure 3.21 shows the equatorial temperature anomaly at depth in *IC-Grid-* and *IC+Grid+*. The Dec.-Jan. mean temperature anomaly in *IC-Grid-* is in excess of 7°C , whereas the maximum temperature anomaly in *IC+Grid+* does not reach 6°C . Noting the broad outcropping of the 4°C temperature anomaly contour from approximately 140°W to 100°W in *IC-Grid-*, versus only a few localized outcroppings of the 4°C temperature anomaly contour in *IC+Grid+* helps to connect the difference in SST to the differences in the structure and magnitude of the temperature anomalies beneath the surface. Examining differences east of the Galápagos, one can notice the temperature anomaly in *IC-Grid-* spreads vertically as it approaches the coast of South America, whereas in *IC+Grid+* is not as great and does not spread vertically. Corresponding temperature sections at 2°N and 2°S look very similar (not shown).

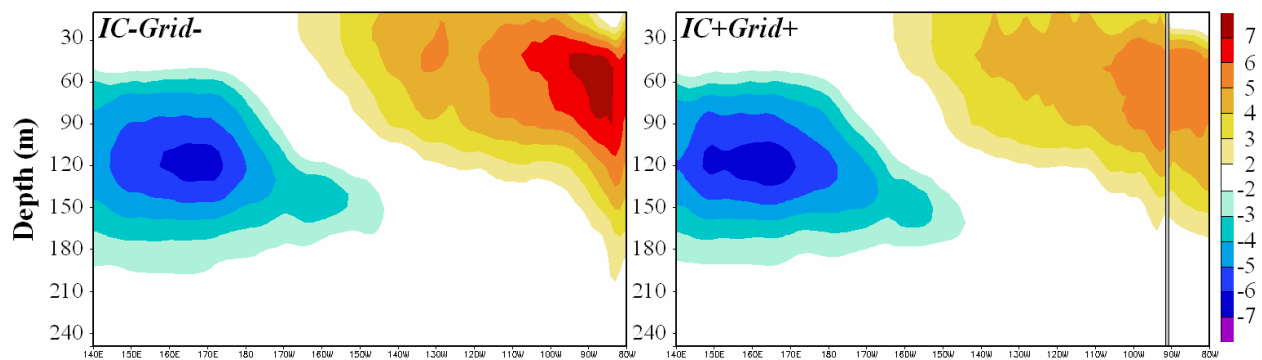


Figure 3.21. Vertical sections of Dec.-Jan. mean equatorial temperature anomaly ($^{\circ}\text{C}$) in the tropical Pacific Ocean for idealized forced experiments *IC-Grid-* (left), and *IC+Grid+* (right).

The results presented in the previous section represent the total effect of the Galápagos Islands on the magnitude and structure of heat content and temperature anomalies in an El Niño event. The results in this section are aimed at separating the roles of (1) the direct,

physical effect of the island through flow-topography interaction, and (2) the fact that the mean state of the equatorial Pacific is different due to the existence of the Galápagos Islands. Verification of this method mandates that only results west of 100°W be trusted, because the adjustment to the alternate equilibrium state cannot significantly progress over the course of a two-year model integration except east of the Galápagos Islands. Thus, we again focus on the NINO3 region.

The SST and mixed layer heat content indices previously discussed are shown again in Figure 3.22, but arranged to illustrate the specific contribution of the roles of the mean state versus the direct island effect. Panels A and B show the effect of the island’s presence (i.e., the “direct” island effect), within the context of the Non-Galápagos versus Galápagos mean state. Only within the context of the Galápagos mean state does the island’s presence have a discernable effect. Panels C and D show the effect of the mean state in the context of the island being absent or present. The mean state has the effect of damping SST and heat content anomalies whether the island is physically present or not. What is clear from Figure 3.22 is that the mean state resulting from the Galápagos Islands has a damping effect on the SST anomaly, but what is not clear is whether the direct island effect alone has a discernable effect.

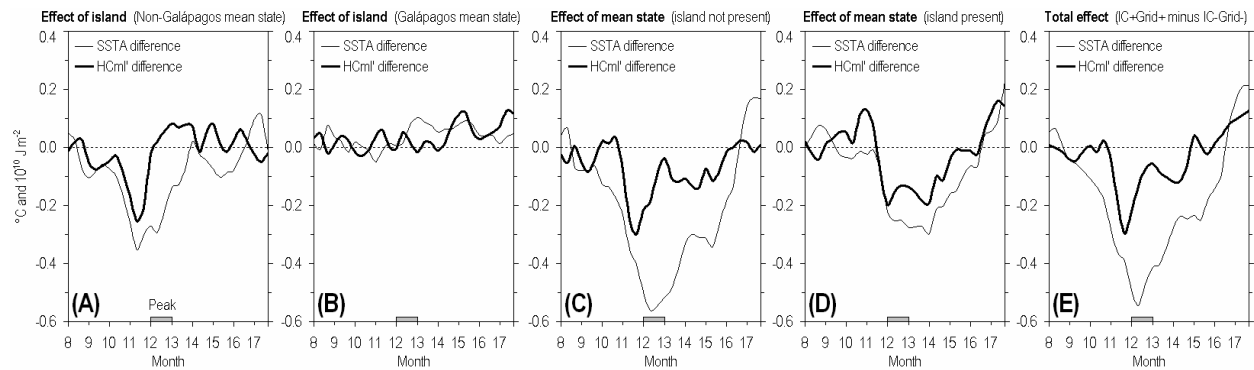


Figure 3.22. NINO3 SST anomaly ($^{\circ}\text{C}$) and mixed layer heat content anomaly (HC_{mi} ; 10^{10} J m^{-2}) differences intended to isolate the specific contribution of: the island in the non- Galápagos mean state (A), the island in the Galápagos mean state (B), the Galápagos mean state without the island present in the model grid (C), and the Galápagos mean state with the island present in the model grid (D). Also

shown is the total effect of the Galápagos Islands (i.e., idealized forced experiments $IC+Grid+$ minus $IC-Grid-$) (E).

When compared to satellite observations of SSTA throughout the 2002-03 El Niño (Figure 3.23), the $IC+Grid+$ results are a much better match, particularly with the equatorial SST anomaly being blocked at the Galápagos Islands until nearly the end of the warm phase, when the warm SST anomaly does develop between the island and the coast of South America. Every El Niño event in nature is different, however, and there are cases when an equatorial SST anomaly appears more or less continuous to the South American coast. Also shown for the 2002-03 El Niño event is the SeaWiFS surface chlorophyll-*a* concentration (Figure 3.24). Upwelling in the eastern tropical Pacific is reduced during an El Niño event, thus the vertical flux of nutrients is reduced and there is a negative chlorophyll anomaly associated with the observed El Niño. In spite of the missing patches of data, it is overwhelmingly clear in Figure 3.24 that the Galápagos Islands have *some* effect on the surface ocean biological response to ENSO. The characteristics and dynamics behind this response are beyond the scope of this dissertation, but it is nonetheless worthwhile to point out that further modeling that is directed toward understanding ocean biogeochemical response to ENSO should take into consideration the Galápagos Islands.

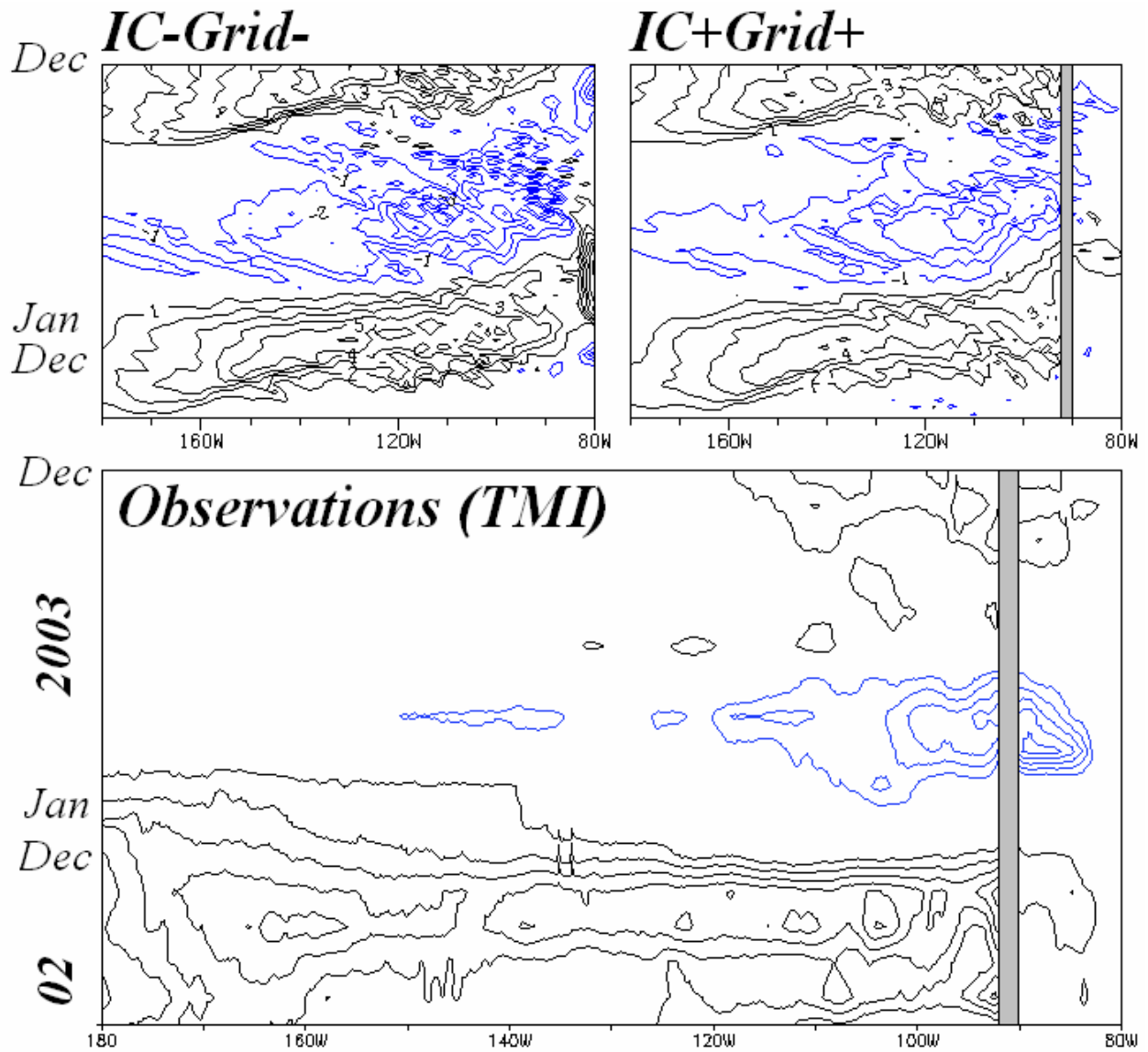


Figure 3.23. Time-longitude evolution of SST anomaly ($^{\circ}\text{C}$) across the equatorial Pacific Ocean (180° - 80°W) from approximately Sep. through the following Dec. for idealized forced experiments *IC-Grid-* (top left), *IC+Grid+* (top right) (contour interval 1°C) and that from observations (TMI) of Sep. 2002 through Dec. 2003 (bottom) (contour interval 0.5°C).

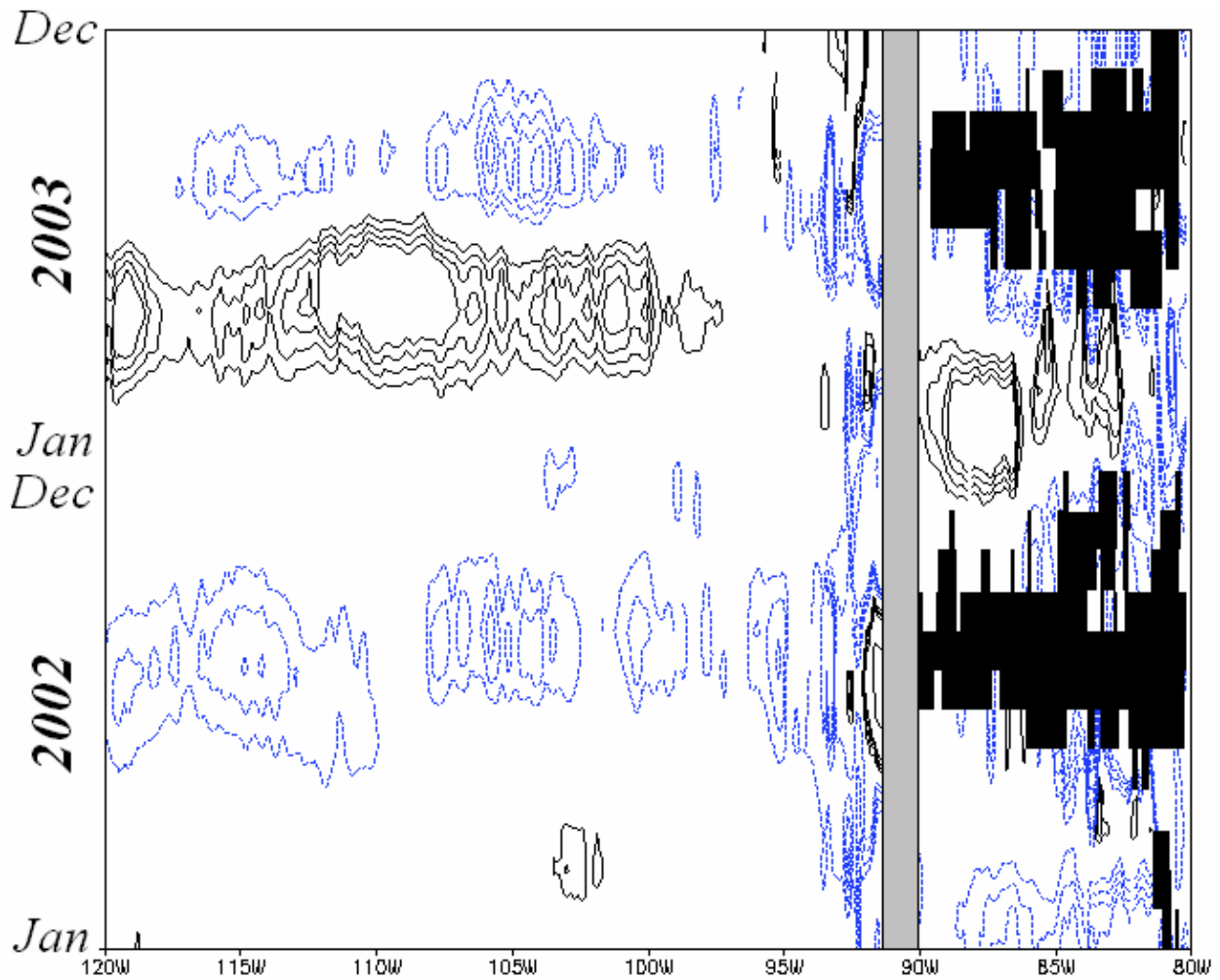


Figure 3.24. Time-longitude evolution of surface chlorophyll concentration anomaly (mg m^{-3}) across the equatorial Pacific Ocean from Jan. 2002 through Dec. 2003. Black regions indicate bad or missing data. Contour interval logarithmic, and include: 0.04, 0.06, 0.08, 0.1, 0.2, 0.4, 0.6, 0.8, 1, 2, 4, 6, 8, 10, 20, and corresponding negative values negatives.

Given that the mean state plays a dominant role in the overall effect of the Galápagos on ENSO amplitude, it is reasonable to guess that subsurface entrainment into the mixed layer and vertical mixing would be important in explaining the overall effect of the Galápagos on ENSO, since the efficiency of entrainment-mixing to affect the mixed layer heat budget and SST depends strongly on the depth and sharpness of the thermocline. The complete mixed layer heat budget is reviewed in Appendix A. The mixed layer heat budget anomalies throughout the

evolution of the El Niño events in the idealized forced experiments are shown in Figure 3.25. In both experiments, the processes responsible for the warming are dominantly Q_{ZA} and Q_{EMX} , with Q_{MA} also making a contribution. However, it is the Q_{EMX} term that is different between the two experiments. In experiment *IC-Grid-*, the Q_{EMX} anomaly reaches 55 W m^{-2} , while in experiment *IC+Grid+*, the Q_{EMX} anomaly levels off at 42 W m^{-2} . This suggests that entrainment-mixing is the process which is primarily responsible for the difference in the amplitude of the SST anomaly between experiments *IC-Grid-* and *IC+Grid+*, and that the anomalous net heat flux to the atmosphere, through latent heat flux, is reduced as well. On the mean, entrainment-mixing is a process that cools the mixed layer, thus for an El Niño event, the entrainment-mixing anomalies are positive; entrainment-mixing is cooling the mixed layer *less*.

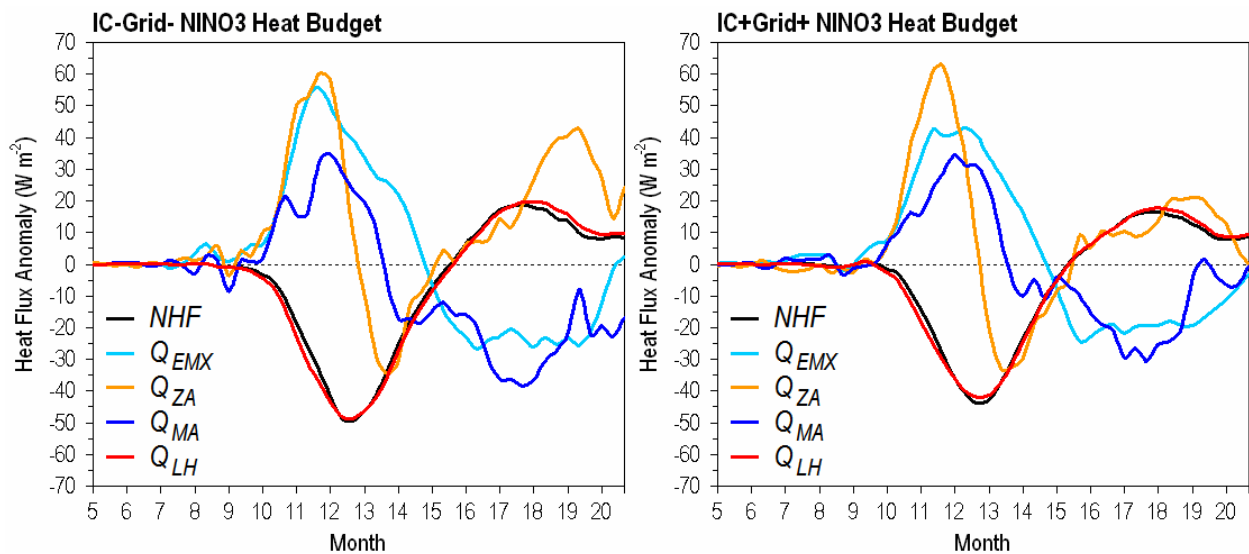


Figure 3.25. Time series of mixed layer heat budget anomalies (W m^{-2}) including net heat flux (NHF) in the NINO3 region for experiments *IC-Grid-* (left) and *IC+Grid+* (right). Q_{LW} and Q_{SH} anomalies are relatively small ($\pm 5 \text{ W m}^{-2}$) and thus omitted from the figure.

Figure 3.26 is a time-longitude depiction of the entrainment-mixing anomaly. In experiment *IC-Grid-*, the entrainment-mixing anomaly is positive and essentially propagates unimpeded to the coast of South America. However, in *IC+Grid+*, there is some reflection of the

entrainment-mixing anomaly off the island, beginning over 10° to the west of the island. Part of the SST anomaly west of the island to about 120°W is due to the reflections of the entrainment-mixing anomaly off the island. This is obviously not possible in *IC-Grid-* since the island is not present. Averaged over the growth phase of the El Niño event (Sep.-Nov.), the entrainment-mixing anomaly is also larger in the broader east-central part of the basin (Figure 3.27).

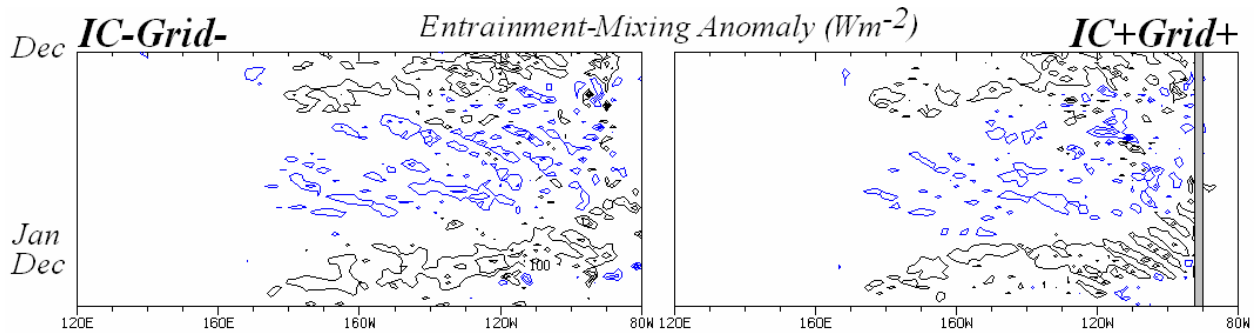


Figure 3.26. Time-longitude evolution of the contribution to the mixed layer heat budget by the entrainment-mixing term (anomaly; $W m^{-2}$; contour interval $100 W m^{-2}$) across the equatorial Pacific Ocean from approximately Sep. through the following Dec. for idealized forced experiment *IC-Grid-* (left) and *IC+Grid+* (right).

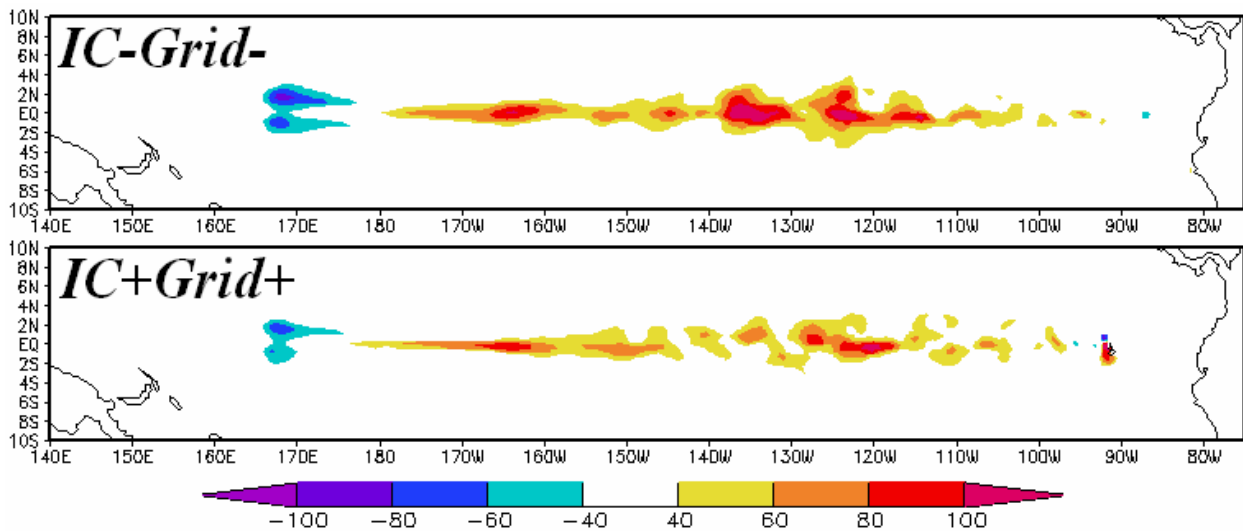


Figure 3.27. Contribution to the mixed layer heat budget by Q_{EMX} (anomaly; $W m^{-2}$) for Sep.-Nov. of the first year of idealized forced experiments *IC-Grid-* (top) and *IC+Grid+* (bottom).

The Galápagos can also exert an influence on El Niño via the mixed layer heat budget by modifying the overall level of activity of tropical instability waves (TIWs). TIWs are westward-propagating signatures in the near-surface momentum and heat balances along the northern and southern front of the equatorial cold tongue. TIWs arise from vigorous horizontal and vertical current shear (Philander 1987, Chelton et al. 2003). TIWs result in a net equatorward heat transport; recent work by Jochum and Murtugudde (2006) suggest a surprisingly large warming contribution of TIWs to the mean equatorial mixed layer heat budget. The impact of the Galápagos Islands on TIW activity in the eastern equatorial Pacific was recently shown by Eden and Timmerman (2004), who found reduced TIW activity in the vicinity of the island, a large enhancement to the northwest (between 105°-95°W), followed by a strong and broad suppression of TIW activity extending the remainder of the basin, with the exception of another localized enhancement between 140°-130°W. It is also generally known that El Niño (La Niña) events suppress (enhance) TIW activity. Thus, it could be said that the suppressing (enhancing) of TIWs during an El Niño (La Niña) event acts as a negative feedback on the warm (cool) SST anomaly. Therefore, it is of interest to understand what impact the Galápagos Islands have on TIW activity in the context of an El Niño event.

The 10-day mean simulated SSTs were filtered for TIWs by removing the 12° zonal mean (6° in each direction) from the total SST value at each point. Our results are highly consistent with the pattern shown by Eden and Timmerman (2004), with the exception that our strong and broad TIW suppression extending west of 105°W is mostly uninterrupted by localized enhancements. We compute an index as the TIW-filtered SST, averaged from the equator to 3°N along 110°W, which is shown in Figure 3.28. The longitude 110°W was chosen because it coincides with a region of high TIW activity in both experiments. During the boreal winter months (here Nov. through Feb.) of the clim runs, TIWs are of lower amplitude in *IC+Grid+* than *IC-Grid-*. The variance of the TIW-filtered SST at 110°W over the boreal winter months in *IC+Grid+* is 23% lower than that of *IC-Grid-*. During the El Niño events, TIW activity drops to

nearly zero in both experiments. The implication is that, when an El Niño event occurs and TIWs activity goes to zero, the *change* is less- or the negative feedback to the SST anomaly would not be as strong due to the Galápagos, and the SST anomaly would tend to be greater. Since the amplitude of the SST anomaly in the idealized forced experiments is larger *without* the Galápagos, its modification of the TIW feedback is not of primary importance in the mixed layer response to an El Niño event. The isolation of the contributions of the direct island effect versus the mean state to this effect (not shown) confirm that it is the Galápagos mean state, rather than the physical presence of the island, that accounts for the reduction of TIWs at 110°W.

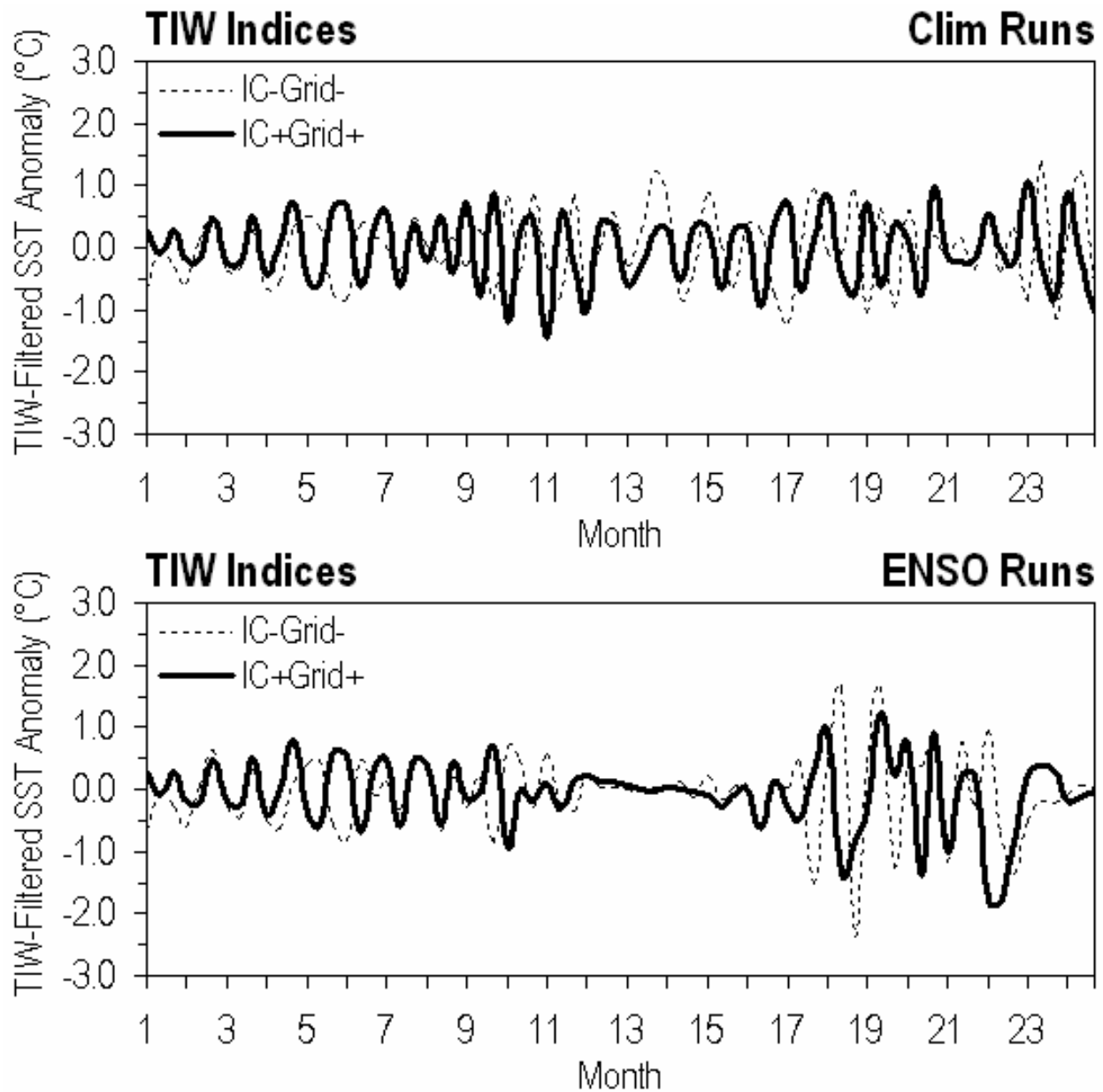


Figure 3.28. Time series of SST across Eq-3°N at 110°W, after being filtered to highlight variability due to tropical instability waves (TIW's). The TIW filtering technique consists of subtracting the 12° zonal mean (6° in either direction) from the total SST value at each point. Top: idealized forced clim runs, bottom: idealized forced niño runs.

3.4.2. The effect of the Galápagos Islands on the timescale of ENSO in hybrid coupled experiments

In this section, we discuss the effect of the Galápagos Islands on intrinsic ENSO variability with the ocean model coupled to the atmosphere through zonal wind stress. Specifically, we are interested in any changes in the timescale of ENSO, as the idealized experiments served to show that, given an identical perturbation in the wind field, the amplitude of the SST response should be damped in the case with the Galápagos Islands. Recall that the only difference between hybrid coupled experiments *No Galápagos* and *Galápagos* is the existence of the Island in the ocean model grid. Again, we focus on the interannual variability in the NINO3 region. It is well known that ENSO events tend to peak in boreal winter. To confirm that the interannual variability in the hybrid coupled model is phase-locked with the annual cycle, as it is quite strongly in nature, Figure 3.29 is a depiction of the variance of SST anomalies as a function of calendar month. Indeed the hybrid coupled model in both *Galápagos* and *No Galápagos* simulations captures nicely the phase-locking of the amplitude of interannual variability with the annual cycle. This provides some confidence that the mechanisms behind ENSO events in our hybrid coupled model have some basis rooted in nature.

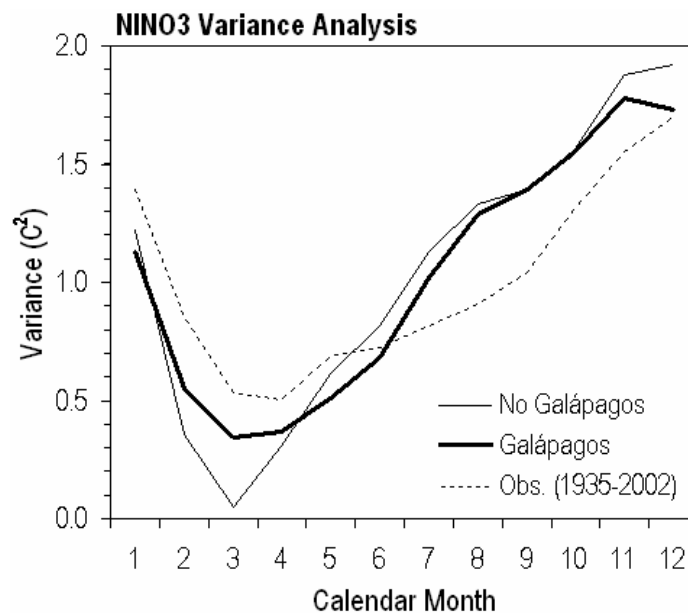


Figure 3.29. Variance of monthly NINO3 (150°W-90°W, 5°S-5°N) SSTA (°C²) as a function of calendar month for 68 years of integration from hybrid coupled experiments *No Galápagos*, *Galápagos*, and 68 years (1935-2002) of observationally-based SST data (Smith and Reynolds 2004).

Figure 3.30 (top panel) shows the time series of NINO3 SST anomaly throughout the model integrations. Also shown in Figure 3.30 (bottom panel) are the power spectra computed by discrete Fourier transform (DFT) for NINO3 SSTA in experiments *No Galápagos*, *Galápagos*, and the last 68 years (1935-2002) of the NOAA Extended Reconstructed SST v.2 dataset (Smith and Reynolds 2004). A brief mathematical description of the DFT methodology used is provided in Appendix B. To avoid spurious spectral features (i.e., those of period close to the length of the time series), we only show power spectra from the fourth harmonic and beyond (i.e., period not longer than one quarter the length of the time series). Examining the power spectrum for the *No Galápagos* experiment, there is one dominant spectral peak, which is found at the 2-year period. This can be confirmed intuitively by counting the number of warm events in any 10-year interval of the *No Galápagos* NINO3 time series; there will be exactly 5. This is classic “biennial ENSO” behavior exhibited by some ocean and coupled climate models. Such strictly biennial regularity is not realistic, as ENSO in nature at present is neither perfectly regular nor significantly biennial. In our coupled model simulations, the Galápagos Islands have the effect of significantly reducing the biennial peak and giving rise to a preferred timescale near 3 years. Moreover, a closer look at the *Galápagos* NINO3 time series reveals that the system also has the ability to transition into and out of a biennial ENSO regime; between years 20-40, the ENSO periodicity in the *Galápagos* experiment is nearly biennial. It is also interesting to note that during that period, the amplitude is smaller than surrounding periods. In *No Galápagos*, ENSO is strictly biennial throughout, with relatively consistent amplitude.

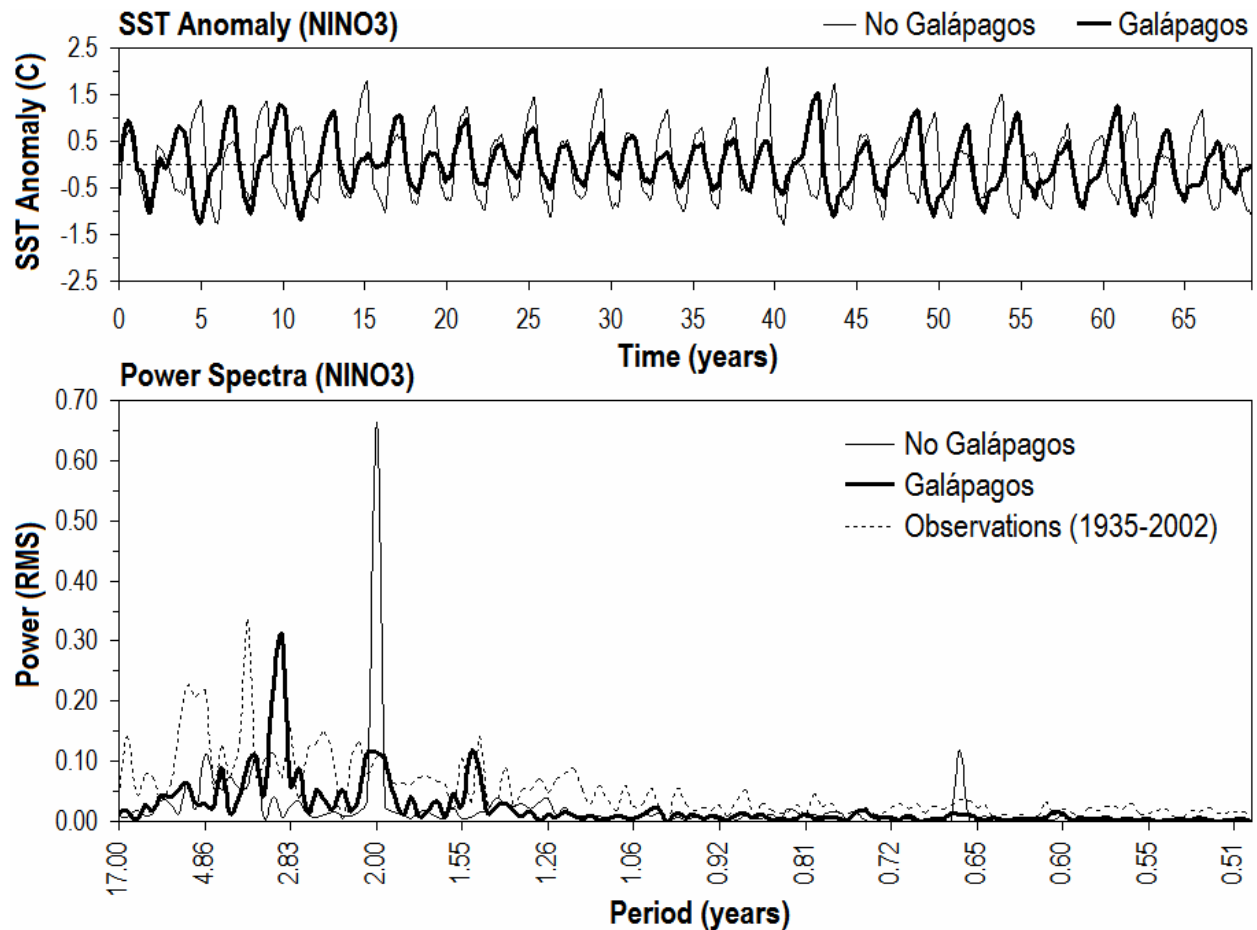


Figure 3.30. Top: monthly time series of NINO3 (150°W - 90°W , 5°S - 5°N) SSTA ($^{\circ}\text{C}$) for 68 years of integration from hybrid coupled experiments *No Galápagos* and *Galápagos*. Bottom: power spectra (RMS as a function of period [years]) for the time series in the top panel plus that of 68 years (1935-2002) of observationally-based SST data (Smith and Reynolds 2004). Time series not normalized.

As evident by comparing simulated and observed power spectra (Figure 3.30, bottom panel), the overall effect of reducing the biennial peak and increasing spectral power at lower interannual frequencies represents a considerable improvement in the representation of ENSO, even within a relatively simple coupled context. An alternative technique for computing power spectra which readily lends itself to understanding the statistical significance of spectral peaks is the multi-taper method (available in UCLA SSA-MTM Toolkit for Spectral Analysis, useful mathematical discussion in Ghil et al. 2002). From the MTM method, the basic features of the

No Galápagos and *Galápagos* NINO3 power spectra are very similar to those resulting from DFT. In the *No Galápagos* NINO3 power spectrum, the two-year peak is the only interannual peak significant at the 99% confidence level. In the *Galápagos* power spectrum, a broad swath of three peaks (from approximately 3-1.5 years) are significant at the 99% confidence level.

To illuminate why the Galápagos Islands would lead to a shift in the ENSO timescale from strictly biennial to lower frequency, we begin by analyzing composite ENSO events and how they unfold. We perform an Empirical Orthogonal Function-Principal Component (EOF-PC) analysis on model SST for the 68 years of output, which is presented in Figure 3.31. In our hybrid coupled model, the only “real” mode of variability should be ENSO. There is no interannual forcing being applied to the system that would justify otherwise; the model is in fact running freely. Despite the requirement of orthogonality, the process of EOF-PC calculation can lead to multiple “propagating” modes, i.e., two statistical modes representing different aspects of a single physical mode. The first EOF of SSTA in both *No Galápagos* and *Galápagos* experiments represents the fully mature ENSO event, portrayed in its warm phase in Figure 3.31. This is evident by the fact that the first PC and the NINO3 index in each experiment are correlated > 0.99 for years 42-68 (Figure 3.31, lower-left panel). The second (and third, in the case of *Galápagos*) mode of SSTA represents the transition between positive and negative phases of ENSO, i.e., the warming period preceding an El Niño event, and cooling which follows. The warming and cooling periods surrounding mature ENSO events are akin to the process described as recharging and discharging heat from the equatorial Pacific (e.g., Jin 1997); these secondary modes of SSTA variability could be said to correspond with the recharge-discharge process. Spatially, there are only minor differences in SST modes between experiments *No Galápagos* and *Galápagos*. The exception is a break in the EOF loading at the western edge of the Galápagos Islands, which is found further toward the coast of South America in the *No Galápagos* case.

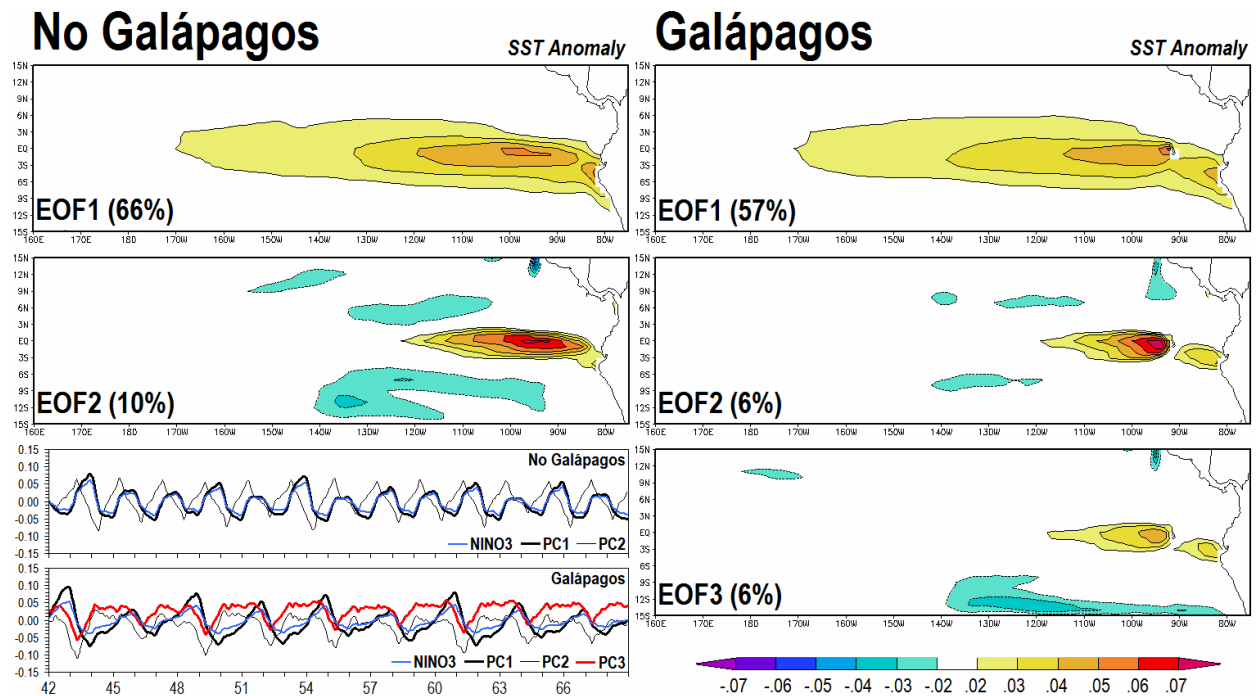


Figure 3.31. First two (three) EOF patterns of SSTA for hybrid coupled experiments *No Galápagos* (*Galápagos*), computed over the full 68 years of integration in each experiment. Also shown (bottom left) are the corresponding principal components and NINO3 SSTA indices for each experiment. Time indices only shown for the final 27 years of integration for legibility.

Temporally, differences in the EOF-PC analysis shed light on an important distinction in the nature of ENSO in the coupled experiments. In both experiments, the secondary PCs are maximum while the PC1/NINO3 signal is growing, and minimum while the PC1/NINO3 signal is decaying (again, because they represent the warming and cooling periods surrounding mature ENSO events). However, in the *Galápagos* experiment, the positive phases in the PC2 are persistent, consistent with a slower growth of PC1/NINO3 signal. Conversely, the PC2 signal in the *No Galápagos* experiment grows as rapidly as it decays, and does not persist in either phase. Hence the ENSO events themselves in the *No Galápagos* experiment grow and decay similarly, resulting in a shorter period or preferred timescale than in the case with the Galápagos Islands. The difference in the warming period preceding El Niño events between the two experiments is

also evident in an EOF analysis of sea level anomaly (Figure 3.32). The total sea level anomaly (SLA) is subject to the effects of propagating Kelvin and Rossby waves characteristic of the delayed oscillator paradigm of ENSO, and the heat content changes associated with the recharge-discharge process of ENSO, particularly in the eastern equatorial Pacific where the broader thermocline variations are large. As with SSTA, the leading PC of SLA corresponds with the phase of ENSO in both experiments (Figure 3.32, bottom panels), but the warming phase is more slowly evolving in the *Galápagos* experiment.

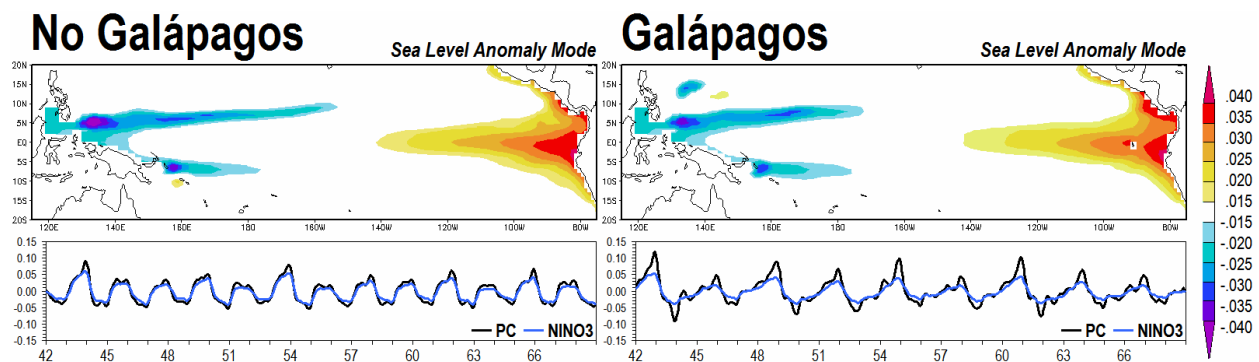


Figure 3.32. Leading mode of sea level anomaly for hybrid coupled experiments (*No Galápagos* left) and *Galápagos* (right), computed over the full 68 years of integration in each experiment. Also shown (bottom) are the corresponding principal components and NINO3 SSTA indices for each experiment. Time indices only shown for the final 27 years of integration for legibility.

To summarize the differences in the time evolution of ENSO events between the two hybrid coupled experiments, Figure 3.33 portrays the composite (over years 42-68) evolution of NINO3 SSTA, SLA PC, SSTA PCs, as well as the time rate of change of NINO3 mixed layer heat content anomaly [$d(HC_{ml}')/dt$] and the zonal wind stress anomaly averaged from 5°S to 5°N. The basic message is that NINO3 SSTA, the sea level pattern, SSTA PC1, and zonal wind stress anomaly track very closely, but grow much more rapidly in the *No Galápagos* experiment. This is consistent with the fact that the maxima in the secondary SSTA mode, which represents the warming preceding El Niño events, and the change in mixed layer heat content itself, are shorter

lived in the *No Galápagos* experiment and essentially mirror the minima following the event. In the *Galápagos* case, the warming mode persists longer, and changes the mixed layer heat content more gradually (i.e., a smaller rate of change over a longer period of time). A direct comparison of the composite SST anomaly in the eastern equatorial Pacific is shown in Figure 3.33c, and reveals a slower growth but ultimately the same amplitude. When this slower and more subtle growth of the warm anomaly is compared to a composite of observed El Niño events (Figure 3.33d), it is clearly an improvement in the representation of ENSO evolution. The mechanisms behind the slower growth of warm ENSO events in the hybrid coupled model, which lead to a longer preferred timescale for ENSO, and how they relate the Galápagos Islands, are discussed in the following subsection.

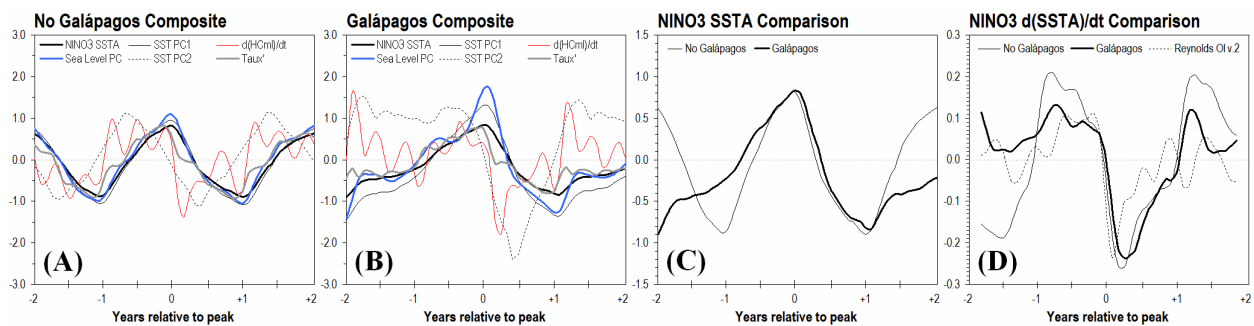


Figure 3.33. Composite evolution of NINO3 SSTA ($^{\circ}\text{C}$), SLA PC, SST PC1 and PC2, time rate of change of NINO3 mixed layer heat content ($10^9 \text{ J m}^{-2} \text{ s}^{-1}$), and zonal wind stress anomaly (averaged 5°S - 5°N ; dyn cm^{-2}) for the last 27 years of hybrid coupled experiments *No Galápagos* (A) and *Galápagos* (B). Also shown is a simultaneous comparison of the NINO3 SSTA composites for the two experiments (C), and that for the time rate of change of the composite NINO3 SSTA, including that computed from observations (Reynolds and Smith 2002; D). Composite time zero refers to the month in which the maximum NINO3 SSTA was simulated or observed. Lines are as marked on the figure.

In this subsection, we discuss the mechanism for the change in ENSO timescale. There are a handful of important theories for the oscillatory nature of ENSO. The delayed oscillator (DO) mechanism (McCreary 1983, Suarez and Schopf 1988) begins with a downwelling Kelvin

wave propagating eastward along the equator, which produces a positive SST anomaly. The DO mechanism then relies on the reflection of Rossby waves at the western boundary to return as upwelling Kelvin waves for decay. Zebiak and Cane (1987) and Battisti and Hirst (1989) demonstrated that the DO mechanism can explain many of the salient aspects of ENSO. One shortfall of the DO mechanism in explaining the full variability of ENSO is that it would predict a perfectly regular ENSO cycle, with a period of approximately two years. The DO-driven ENSO period of two years is based on the estimated basin crossing times of Kelvin and Rossby waves. *Strictly* within the context of the DO mechanism and its constituent equatorial waves, there are two ways by which the introduction of the Galápagos Islands to the hybrid coupled model could lead to a change in the ENSO period: (1) the speed of the Kelvin or Rossby waves change, thereby changing the basin crossing times, or (2) the Galápagos Islands changes the effective width of the ocean basin, by acting as an effective eastern boundary, thereby changing the basin crossing times of the equatorial waves. The latter is not a plausible explanation for two reasons. While the Galápagos Islands are wide enough in the meridional direction to significantly obstruct the EUC and cause a shift in the mean state (as shown in Section 3.3), they are not wide enough to cause any appreciable reflection of Kelvin wave energy. Secondly, if the Galápagos Islands were wide enough to act as an effective eastern boundary and reflect Kelvin waves, this would result in *shorter* crossing times for the equatorial waves and translate into a shorter ENSO period- the opposite of which is the case.

The other possible explanation for the Galápagos Islands leading to a change in the period of ENSO through the DO mechanism and the characteristics of its waves- that the basin crossing time is changed because the speed of the waves are changed- is also not plausible. Examining the equatorial Kelvin wave, the complete solution is (Gill 1982):

$$(3.5) \quad \eta_K = \exp(-\beta y^2 / 2c) G(x - ct),$$

$$(3.6) \quad u_K = g'/c \exp(-\beta y^2 / 2c) G(x - ct),$$

$$(3.7) \quad v_K = 0,$$

$$(3.8) \quad \text{where } c = \sqrt{g'H}$$

where η_K is the sea level perturbation, β is the beta coefficient (the change in the Coriolis parameter with latitude), G is a sinusoidal function, u_K is the geostrophic zonal current perturbation, g' is reduced gravity (the acceleration due to gravity, g^* , reduced by the percent difference between upper and lower layer density), v_K is the geostrophic meridional current perturbation, and H is the fluid depth. Equatorial Kelvin waves have approximately the dispersive characteristics of ordinary shallow-water gravity waves (Matsuno 1966, Holton 1992), and thus they travel at a speed proportional to the square root of depth H (Equation 3.8). In the case of a Kelvin wave, H is the effective upper-layer depth, which we will approximate using the depth of the thermocline. To examine the dependence of zonal current u_K and phase speed c on upper-layer depth H , we simply graph the solutions to Equations (3.6) and (3.8) using common values for g' ($0.003 g^*$, where $g^* = 9.81 \text{ m s}^{-2}$), and β ($2.3 \cdot 10^{-11} \text{ m}^{-1} \text{ s}^{-1}$) (Gill 1982). We also drop the G function from Equation (3.8) and use a y^2 of 1 m. The results, shown in Figure 3.34, illustrate how a deeper H will lead to a faster, yet damped, Kelvin wave signal.

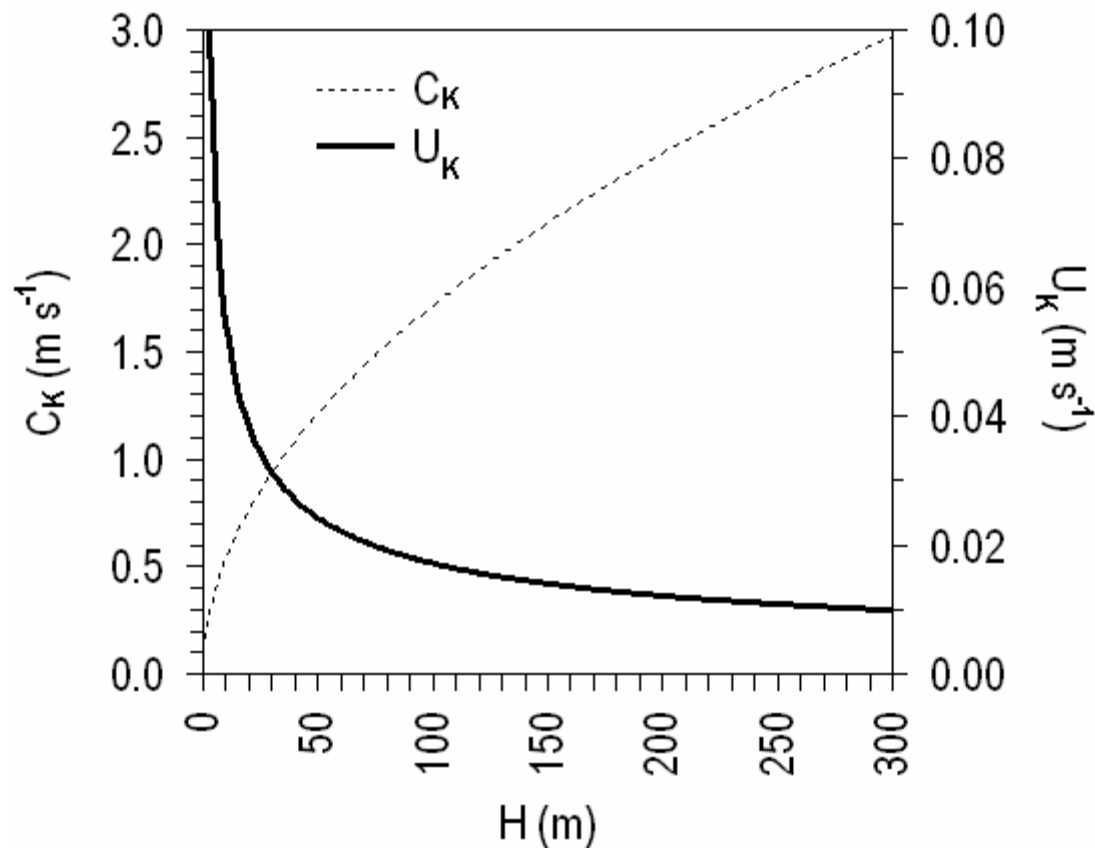


Figure 3.34. Solutions to Equations (3.6) and (3.8), illustrating the dependence of Kelvin wave phase speed (c_K ; dashed) and Kelvin wave zonal geostrophic current anomaly (u_K ; bold) on the depth of the upper layer (H).

It was demonstrated in Section 3.3 that the introduction of the Galápagos Islands into an OGCM leads to a change in the equatorial mean state, specifically a deeper thermocline and mixed layer. Thus, in the case of *Galápagos*, we would expect a greater H and faster Kelvin wave phase speed. This is indeed the result in both the idealized forced and the hybrid coupled experiments; Kelvin wave speed is very slightly higher in the simulations that included the Galápagos Islands in the model. Figure 3.35 shows that the Kelvin wave generated by an identical wind stress perturbation is faster in the idealized forced experiment *IC+Grid+* than *IC-Grid-* (as evident by the positive difference at the leading edge of the Kelvin wave signal), and damped (as evident by the negative difference in the core of the Kelvin wave signal). Thus,

the change in Kelvin wave crossing time cannot explain the change in ENSO period. Rather, if it were up to the Kelvin wave phase speed, the period of ENSO would shorten, as it would have if the Galápagos were an effective eastern boundary to Kelvin waves.

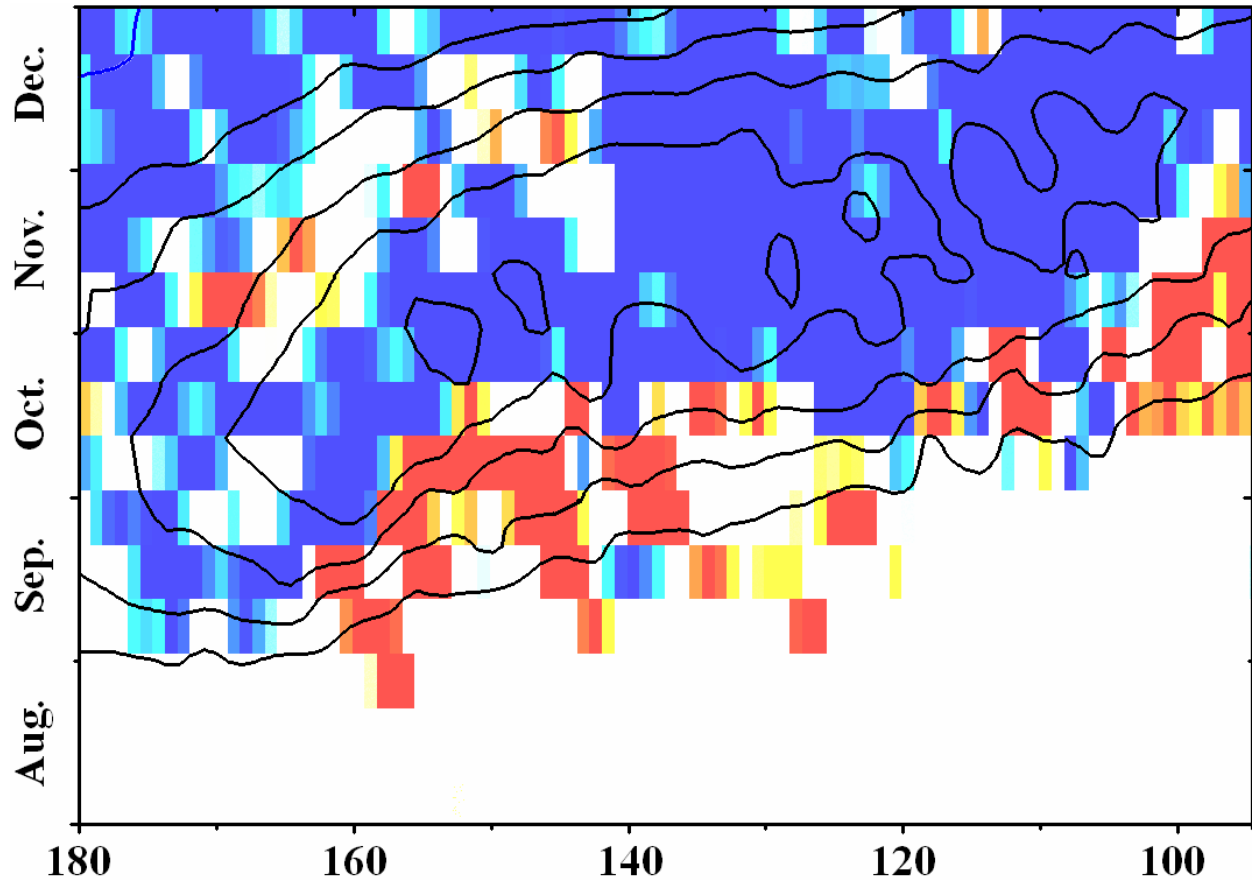


Figure 3.35. Equatorial time-longitude plot of the projection of Kelvin waves onto zonal geostrophic current (contour interval 0.2 m s^{-1}) in the idealized forced experiment *IC-Grid-*, and the difference between cases *IC+Grid+* minus *IC-Grid-*.

Rather than explaining the change in ENSO period as a result of the Galápagos Islands from the standpoint of the DO set by the speed of its constituent waves, we consider the behavior of the fully coupled system and its response to the Kelvin waves under different mean states, particularly the role of the Bjerknes feedback (Bjerknes 1969), while invoking aspects of other leading theories for the oscillatory nature of ENSO, including the recharge-discharge mechanism (Jin 1997) and the advective-reflective model (Picaut et al. 1997). From Equation

(3.6) and its solution illustrated in Figure 3.34, the solution for the zonal geostrophic current associated with an equatorial Kelvin wave is damped in the presence of a larger H , which is the case in the *Galápagos* mean state. Whether an equatorial Kelvin wave is of the downwelling or upwelling variety is defined by the u_K field; a convergent u_K field results in downwelling and a divergent u_K field results in an upwelling signal propagating along with the wave energy. Similarly, a lower amplitude convergent u_K imparts weaker downwelling and therefore results in a smaller SST anomaly. This in part helps to explain the damped SST anomaly response to identical wind stress perturbations in the idealized forced experiments. However, in the coupled context, this has further implications for the growth of the SST anomaly in time.

To analyze the behavior (amplitude and temporal characteristics) of Kelvin waves in the hybrid coupled model experiments, we compute the projection of Kelvin waves onto geostrophic current anomaly. Figure 3.36 (top) shows the ratio of the variability of the Kelvin wave signal along the equator from 180° - 100° W in experiments *No Galápagos* and *Galápagos*. Also shown in Figure 3.36 (bottom) is the difference in the mean state (equatorial temperature) with minus without the Galápagos Islands (annual mean).

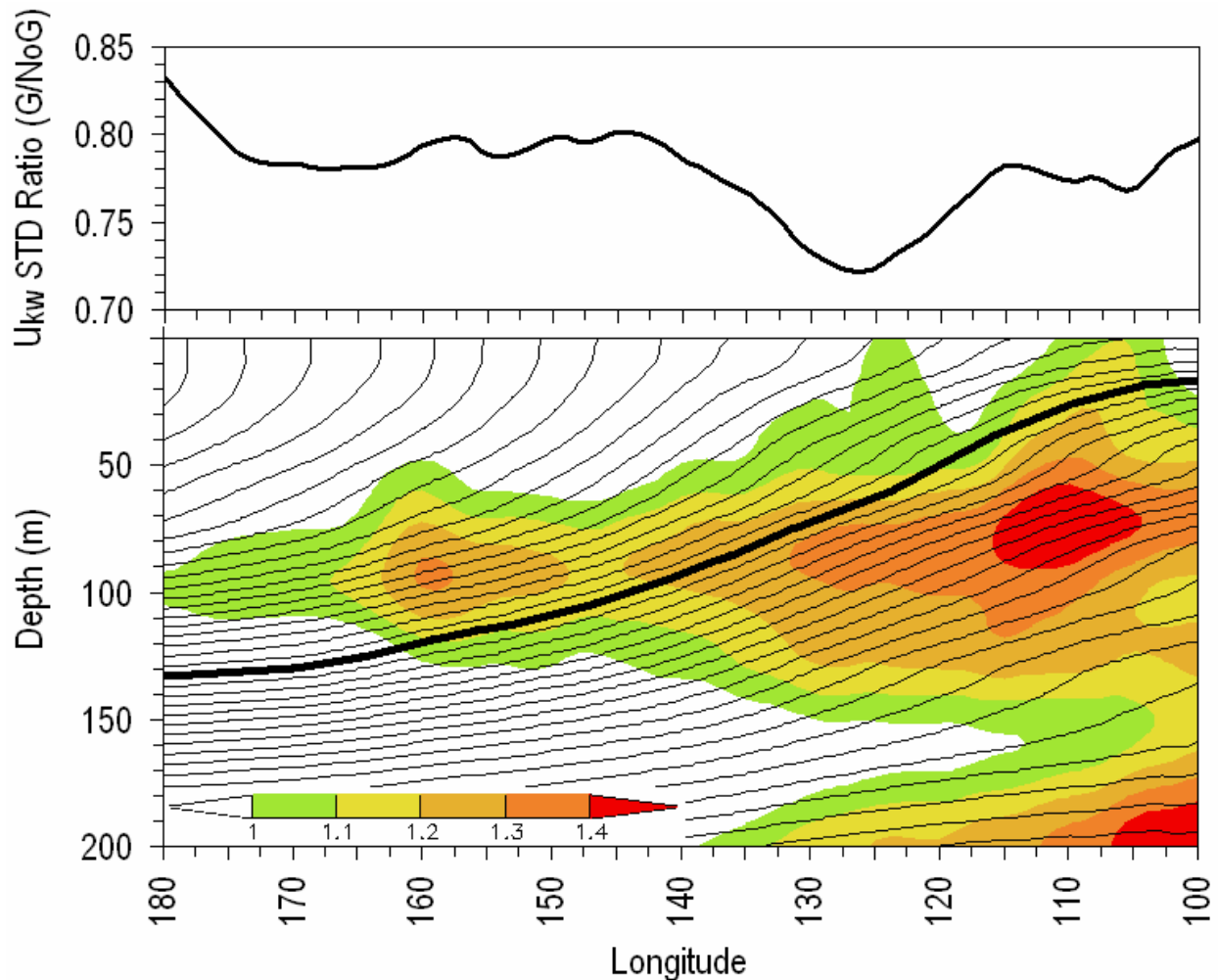


Figure 3.36. Ratio of the standard deviation of the Kelvin wave zonal geostrophic velocity anomaly signal as a function of longitude for experiments *Galápagos* to *No Galápagos* (top), and an illustration of the difference in the mean state of the equatorial Pacific with and without the Galápagos Islands (bottom): annual mean difference in temperature at depth (shaded) and the annual mean distribution of isotherms in the *No Galápagos* case (contour interval 0.5°C). The heavy black line is the 20°C isotherm.

Because the interannual variability inherent to the coupled experiments would be aliased into any long-term mean calculations, we rely on the difference in annual means derived from the climatological runs of the idealized forced experiments. As is expected from theoretical considerations (Figure 3.34), the Kelvin wave variability is damped by up to 28% by Galápagos, which appears to be stronger where the thermocline difference is greater (e.g., note similarities

at 105°W and 125°W). Note that standard deviation is only dependent on amplitude- not frequency, thus the result in Figure 3.36 is independent of the fact that there are fewer full ENSO cycles in the *Galápagos* case. Eastward of the Galápagos Islands (i.e., between the island and the coast of South America), the thermocline is much deeper in the Galápagos mean state. We therefore theorize that the Kelvin wave is damped further in that region, although this cannot be confirmed due to problems with calculating projections near a concave coastline. Presented in Figure 3.37 (3.38) is a time-longitude depiction of the projection of equatorial Kelvin (Rossby mode 1 along 3.8°N) waves onto zonal geostrophic current anomaly (sea level anomaly) for the last 27 years simulated in the hybrid coupled experiments. There are some clear and important differences in the Kelvin wave projections in the *Galápagos* and *No Galápagos* results. Again, the amplitude in *Galápagos* is damped compared to the *No Galápagos* results. Secondly, the sequencing of the events is different; in the *No Galápagos* projection, there is an annual Kelvin wave signal, with each successive Kelvin wave being of the opposite sign, thus resulting in a strong biennial periodicity. In the *Galápagos* projection, the sequence is as follows: zero, a gradually increasing positive Kelvin wave signal, a negative Kelvin wave signal immediately following, and another lull before the next gradual increase toward a robust positive Kelvin wave signal. The differences in the Rossby wave projections are similar, since they are reflections of the Kelvin wave energy incident upon the eastern boundary; amplitude is reduced and sequencing asymmetrical. Also shown on Figures 3.37 and 3.38 are the trajectories of hypothetical “drifters” released at 180° and 160°W (released one year before Figures 3.37 and 3.38 begin). The procedure for calculating drifter trajectory follows Picaut et al. (1995), where they are allowed to drift freely, governed by the zonal geostrophic current averaged from 4°S to 4°N. The drifters represent the zonal migration of the eastern front of the west Pacific warm pool, the advection of which by Kelvin and Rossby waves is the critical mechanism of the periodicity of ENSO in the advective-reflective model (Picaut et al. 1997). The biennial versus irregular (~3 year) periods are evident in the Kelvin and Rossby wave

projections. In essence, the advective-reflective model describes the implications of a DO mechanism operating on top of an important mean state. Picaut et al. (1997) also noted that the convergence of drifters over some period of time is a fundamentally important feature of the circulation and interannual variability thereof, which only occurs in the *Galápagos* results.

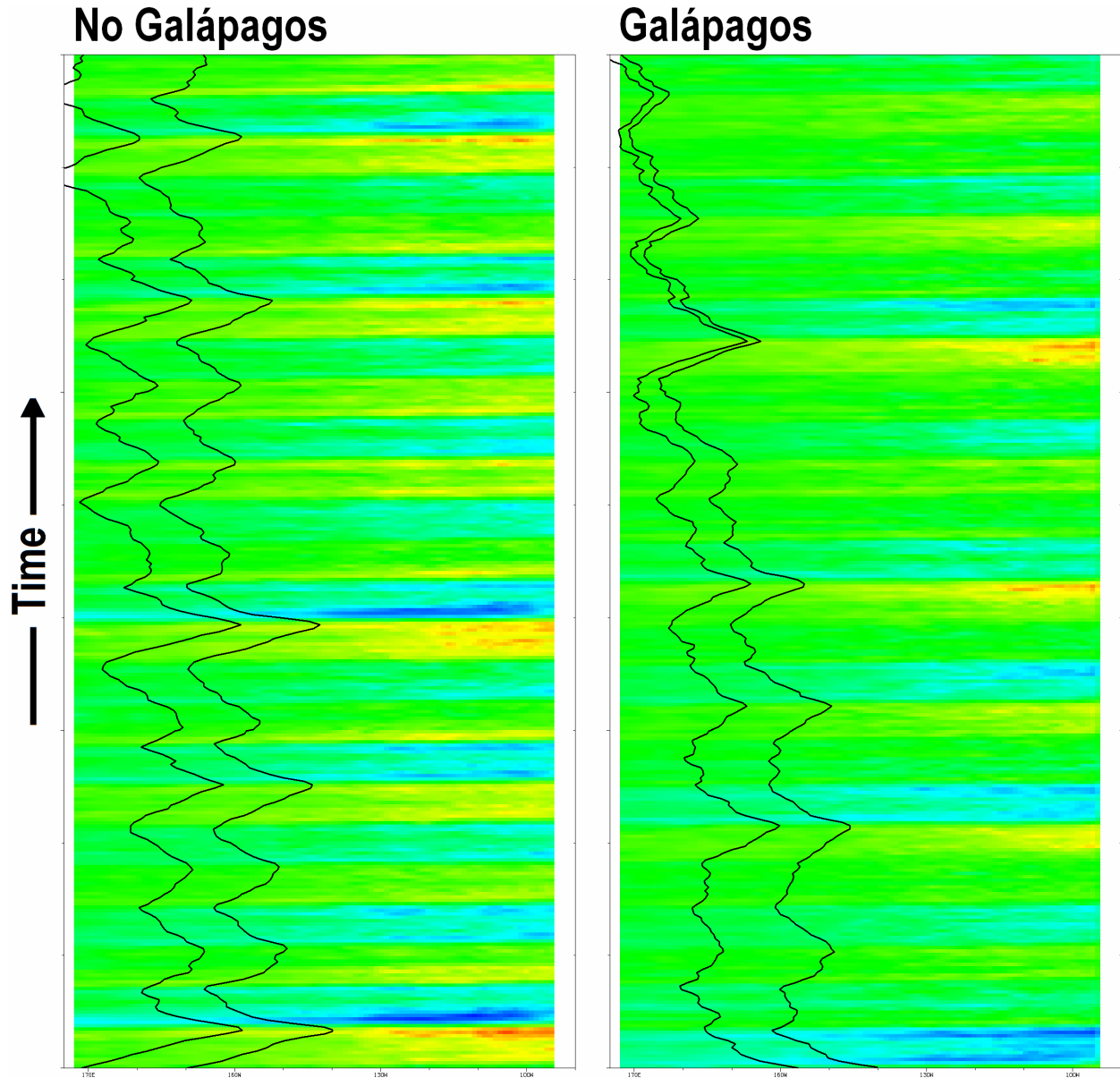


Figure 3.37. Time-longitude (time increasing along the positive y-axis) depictions of the Kelvin wave projection onto zonal geostrophic current (shaded -0.4 m s^{-1} to 0.4 m s^{-1}) along the equator for hybrid coupled experiments *No Galápagos* (left) and *Galápagos* (right) (25 years shown). Shown in solid black lines are the trajectories of hypothetical “drifters” released at 180° and 160°W one year preceding the first

time in the figure. The paths of the drifters are governed by the full zonal geostrophic current anomaly averaged between 4°S and 4°N.

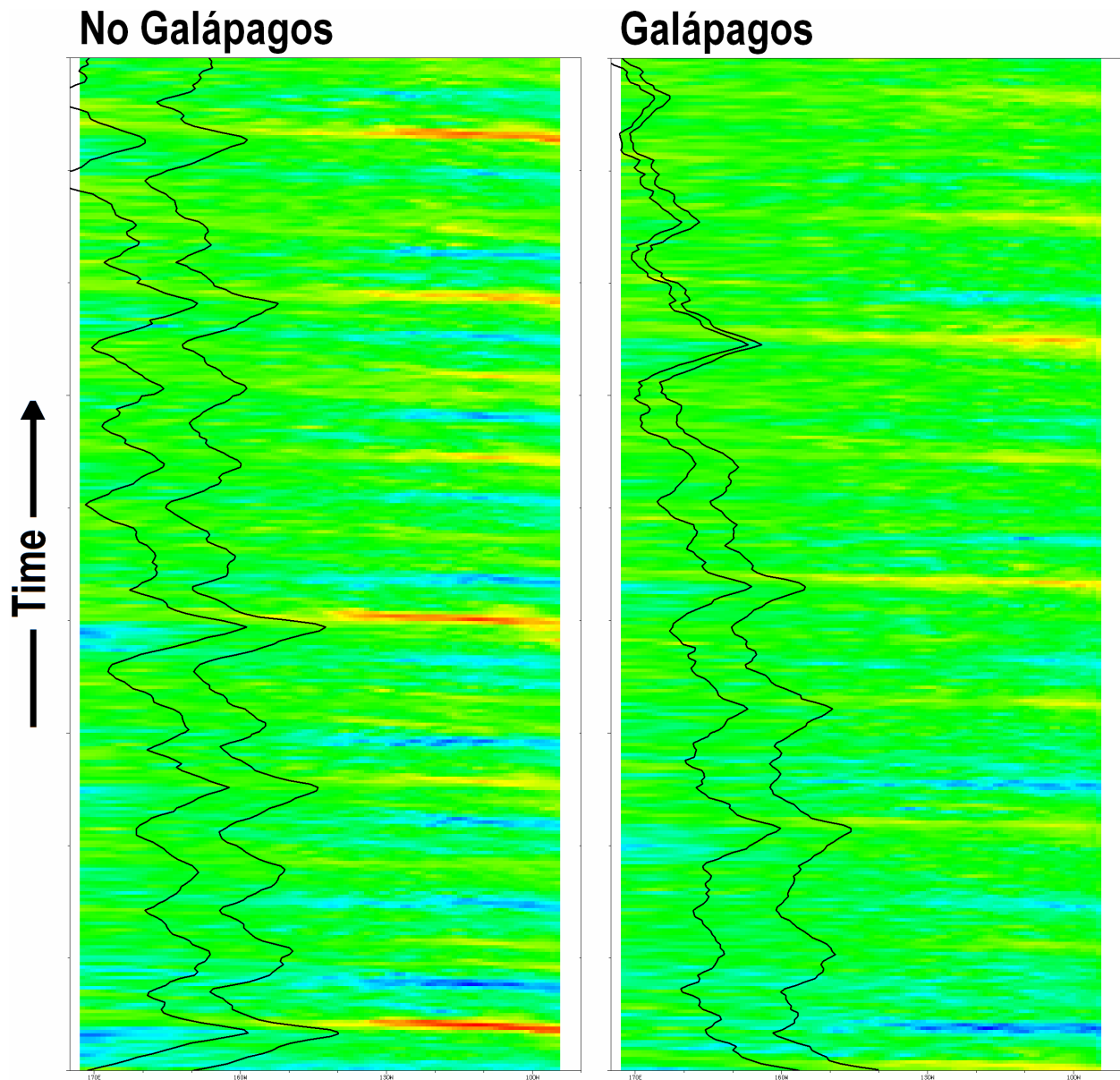


Figure 3.38. Time-longitude (time increasing along the positive y-axis) depictions of the Rossby wave (mode 1) projection onto sea level anomaly (shaded -0.07 m to 0.07 m) along 3.8°N for hybrid coupled experiments *No Galápagos* (left) and *Galápagos* (right) (25 years shown). Shown in solid black lines are the trajectories of hypothetical “drifters” released at 180° and 160°W one year preceding the first time in the figure. The paths of the drifters are governed by the full zonal geostrophic current anomaly averaged between 4°S and 4°N.

Using theoretical calculations and analysis of idealized forced and hybrid coupled experiments, we have shown that the equatorial Kelvin waves involved in ENSO in experiments which included the Galápagos Islands are damped. We have also shown that the longer ENSO period in the *Galápagos* simulation is a result of a longer, more gradual warming period leading to the peak El Niño event. The key question is thus: why the slower anomaly growth and hence longer ENSO period with the Galápagos Islands? The answer is directly related to the fact that the SST anomaly imparted by the Kelvin wave is damped initially, and relies on the Bjerknes feedback, which is easily extracted from our model given the simplified ocean-atmosphere coupling scheme. The feedback hypothesized by Bjerknes is that an SST anomaly in the eastern equatorial Pacific leads to a positive zonal wind stress anomaly, which further acts to amplify the initial SST anomaly. From the coupling mechanism described in Equation (3.1), the rate of growth of the SST anomaly beyond the initial SST perturbation by the downwelling Kelvin wave is strongly dependent on the amplitude of the initial SST perturbation. Equation (3.1) can be rewritten in terms of anomalies and expanded:

$$(3.9) \quad \tau_x' = -\mu [(\mathbf{T}_{\text{west}} - \{ \mathbf{T}_{\text{east}} + T'_{\text{east}} \}) - \Delta\mathbf{T}_{\text{clim}}]$$

where primes (') denote anomalies, $\Delta\mathbf{T}_{\text{clim}}$ is the average ΔT_{clim} in experiments *Galápagos* and *No Galápagos* (5.7°C), and similarly, \mathbf{T}_{west} is the average T_{west} (32.8°C) and \mathbf{T}_{east} is the average T_{east} (27.1°C). To illustrate this dependence, we initialize Equation (3.9) with a T'_{east} of 0.5°C, calculate the resulting zonal wind stress anomaly τ_x' , and assume the growth of the SST anomaly by the next time step will be proportional to that zonal wind stress anomaly. We then carry this out twelve time steps, and repeat the process for alternative values of T'_{east} of 1.0, 1.5, and 2.0°C. The results of the sensitivity exercise are presented in Figure 3.39. Noting the difference between the growth rate lines for an initial SST anomaly of 0.5°C versus 1.0°C, for example, the growth rate via the Bjerknes feedback alone is over four times faster for the larger initial SST anomaly. Recall that the idealized forced results led to a damping of the SST anomaly of about

0.5°C, yet the rate of the growth of the anomaly did not change, because there was no dynamical coupling with the atmosphere and therefore no Bjerknes feedback. Hence, the dependence of the strength of the Bjerknes feedback on the amplitude of the initial anomaly explains why the growth phase of El Niño events would be slower in the *Galápagos* simulation, while the rate of decay of the El Niño events would remain unchanged.

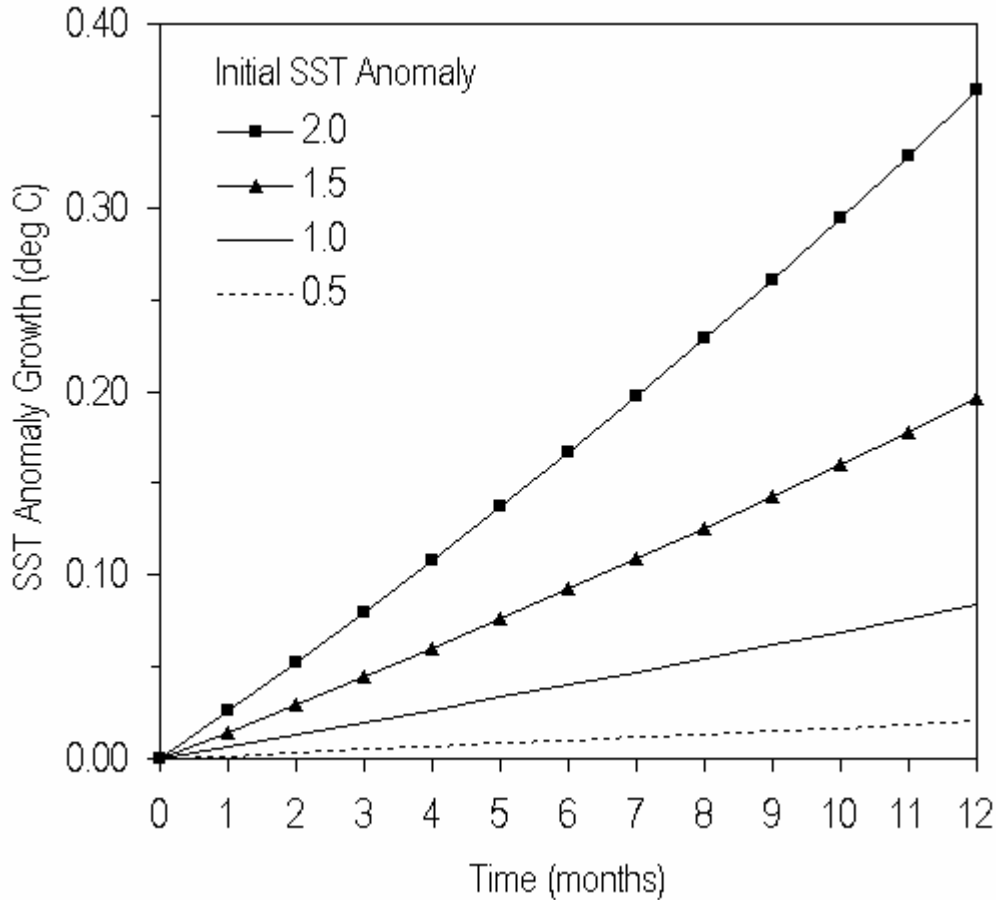


Figure 3.39. Solutions to Equation (3.9), initialized for values of T'_{east} of 0.5, 1.0, 1.5, and 2.0°C. Lines are as marked on the figure.

With the rate of anomaly growth and thus timescale difference reconciled, the remaining curiosity is why, if the Kelvin wave SST response is damped, would the amplitude of the fully mature warm ENSO event be similar (e.g., the composite events shown in Figure 3.33c)? As previously alluded to, ENSO and its oscillatory nature have been described as a series of

recharge and discharge phases (Jin 1997). The meridional circulation in the tropical-subtropical Pacific Ocean is defined by wind-driven subtropical cells: vigorous upwelling at the equator, poleward surface transport, subduction, and equatorward return flow along the thermocline. Variations in transport convergence in the upper pycnocline by Pacific subtropical cells have recently gained attention due to their possible role in modulating decadal variability (McPhaden and Zhang 2002, 2004). Greater transport convergence is associated with cooler equatorial SST, and vice versa, because the equatorward flow in the upper pycnocline is a branch in the same circuit as the equatorial upwelling. Likewise, suppressed transport convergence indicates reduced equatorial upwelling of cold water and would lead to a warmer equatorial SST. In this context, we examine the role of mass transport convergence in the upper pycnocline in affecting differences between the simulated ENSO in our hybrid coupled experiments. Our methodology is identical to that of McPhaden and Zhang (2002, 2004). Based on the vertical structure of the “upper pycnocline” described by McPhaden and Zhang, and vertical variations of mass transport, in either hemisphere and for either coupled simulation, we choose density surfaces between which we vertically integrate mass transport. In experiment *No Galápagos*, we use 21.18-25.19 kg m⁻³ (21.71-25.06 kg m⁻³) for the Northern (Southern) Hemisphere, and in experiment *Galápagos*, we use 21.16-24.85 kg m⁻³ (21.71-24.68 kg m⁻³) for the Northern (Southern) Hemisphere. Finally, along 6°N (6°S), we integrate from 145°E-90°W (160°E-85°W), and obtain upper pycnocline convergence (UPC) by taking the difference between the northward transport at 6°S and the southward transport at 6°N.

We again construct a picture of the composite El Niño event, in terms of UPC (Figure 3.40). The unfolding of events in the *No Galápagos* composite is as follows: a large SSTA develops at an early stage because the mean state is one in which SSTA is highly sensitive to Kelvin waves, a strong Bjerknes feedback drives a rapid growth of both the SSTA and zonal wind stress anomaly (recall from Figure 3.33a, b that the SSTA and zonal wind stress anomaly lines are nearly identical), and UPC is immediately and strongly suppressed. In effect, the DO and

Bjerknes feedback are operating in high synchrony, and the UPC is simply responding to the fluctuating zonal wind stress. Over the 68 years simulated, the UPC anomaly and SSTA time series are anticorrelated -0.82. This is indicative of a strong positive feedback between UPC and SST during the warming phase: the suppressed UPC results in reduced upwelling, which acts to increase the warming already in progress. Also from the *No Galápagos* composite (Figure 3.40a), UPC is in quadrature with $d(HC_{ml})/dt$, meaning the UPC does not have an impact on the warming; it is simply driven by the same process that drives the warming, i.e., the winds.

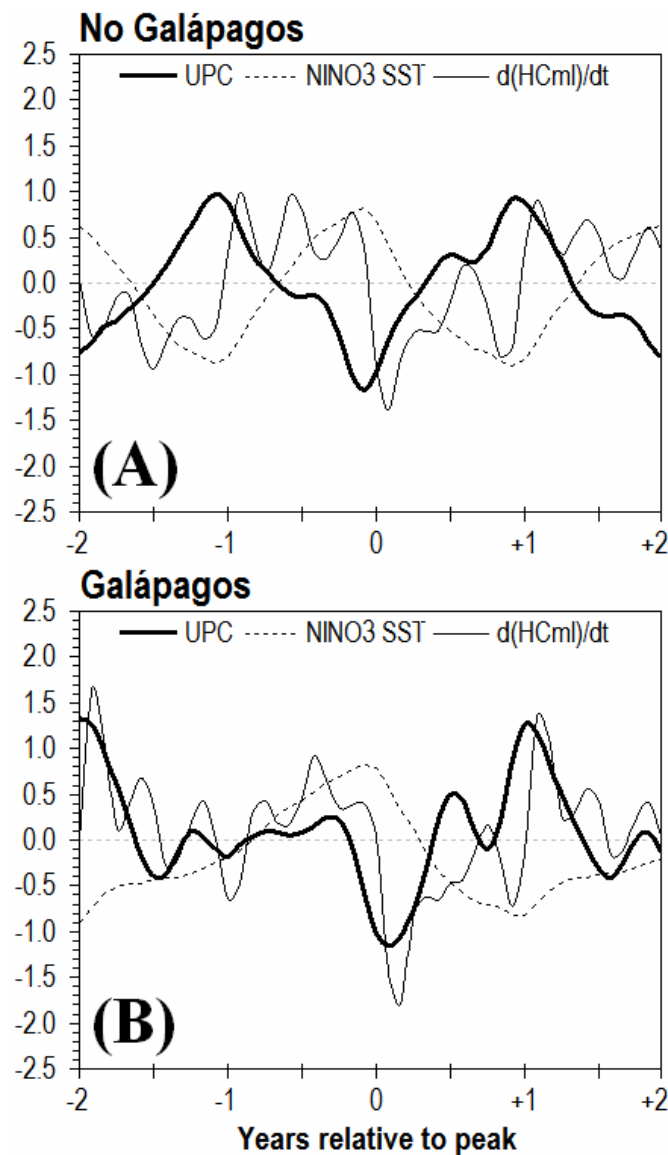


Figure 3.40. Composite evolution of upper pycnocline mass convergence (UPC; normalized units), NINO3 SSTA ($^{\circ}\text{C}$), and the time rate of change of NINO3 mixed layer heat content ($10^9 \text{ J m}^{-2} \text{ s}^{-1}$) for the last 27 years of hybrid coupled experiments *No Galápagos* (A) and *Galápagos* (B). Composite time zero refers to the month of the maximum NINO3 SSTA. Lines are as marked on the figure.

The evolution of UPC in the *Galápagos* composite is quite different: a smaller SSTA develops in the early stages because the mean state is somewhat more resilient to Kelvin waves, and a weaker Bjerknes feedback drives a slower growth of the SSTA and zonal wind stress anomaly. However, the wind stress anomaly was too weak throughout most of the warming period to cause a change in the wind-driven UPC. Not only is the UPC anomaly small, but positive, which means that UPC actually has a counteracting effect on the SSTA growth, further contributing to the slowness of the warming phase. Hence, $d(\text{HC}_{\text{ml}})/dt$ remains small but steady positive approaching the peak of the El Niño event. Finally, at the end of the warming phase, the zonal wind stress anomaly is strong enough suppress the UPC and drive the NINO SSTA to an amplitude roughly equal to that in the *No Galápagos* composite. As evident in the composite, there is strong association between UPC and the time rate of change of mixed layer heat content, meaning that UPC is having an effect on the warming: a negative one throughout the composite event.

The recharge-discharge paradigm of ENSO was also discussed by Kessler (2002) using observations, who portrayed the ENSO cycle as an evolution of the state of the equatorial system through phase space defined by basin-wide mean 20°C isotherm depth and NINO3 SST. In a similar fashion, Figure 3.41 depicts the coupled ENSO cycle as an evolution through phase space defined by NINO3 SSTA and zonal wind stress anomaly (averaged 5°N to 5°S). In the *No Galápagos* case (Figure 3.41a), the system undergoes a rapid growth/warming (quadrant IV to quadrant I), and immediately undergoes a rapid decay/cooling (quadrant II to quadrant III), with little time spent near the origin. Conceptually, this is the DO mechanism operating upon a

submissive mean state, with Bjerknes on the accelerator. In Kessler’s phase diagram depicting the recharge-discharge process, this would resemble a constant circular orbit through the four quadrants of phase space, with nearly equal time spent in each state, rather than an abundance of points near the origin or in the recharge phase. In contrast, and more consistent with observations, the *Galápagos* phase diagram (Figure 3.41b) depicts a DO mechanism operating on a more resistant mean state, with the Bjerknes feedback acting more subtly until the equatorial system is completely discharged and promptly returns to gradually recharge (i.e., more data points are found near the origin and in quadrant III). Such an evolution through the coupled phase space is more realistic with respect to an equal number of years (1935-2002) of observationally-based data (Figure 3.41c).

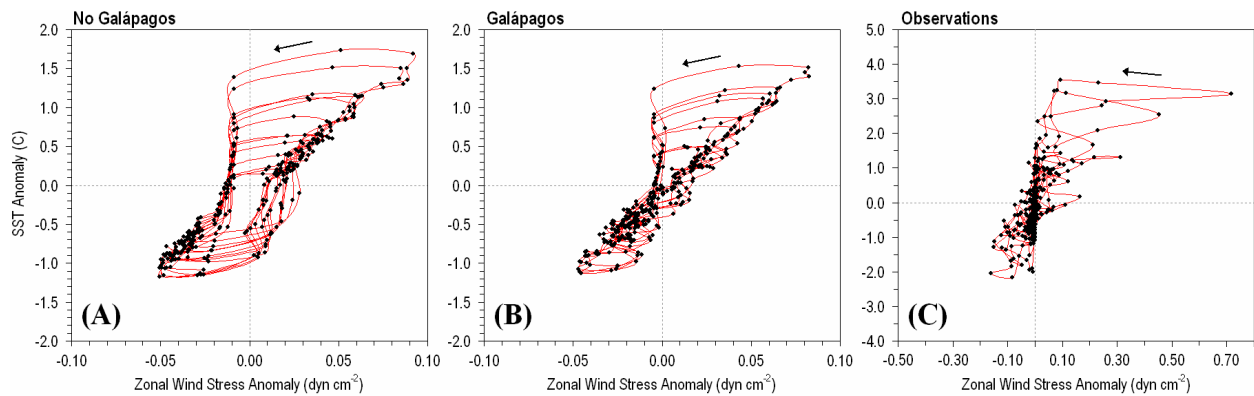


Figure 3.41. Phase diagram (scatterplot with consecutive points connected by lines) defined by NINO3 SSTA (°C) along the y-axis, and zonal wind stress anomaly (averaged 5°S-5°N; dyn cm⁻²) along the x-axis, for 27 years of hybrid coupled experiments *No Galápagos* (A), *Galápagos* (B), and that derived from 25 years (1982-2006) of observations (Reynolds and Smith 2002; C).

3.5. Summary

In this chapter, we use an ocean model to describe the effect of the Galápagos Islands on forced El Niño events and coupled ENSO variability. The Galápagos results in a damped temperature anomaly in response to the forced El Niño throughout the equatorial Pacific, but especially east of the island and beneath the surface, which is primarily due to the different

mean state, i.e., a deeper and more diffuse thermocline. The eastward propagating equatorial warm SST anomaly appears blocked by the island until the latter stage, when it finally propagates fully eastward to the coast of South America. This is a close match with the 2002-03 El Niño as seen in TMI observations. The Galápagos also appears to play an equally important role in the distribution of surface chlorophyll anomalies throughout the 2002-03 as seen in SeaWiFS observations. In terms of the mixed layer heat budget, entrainment-mixing is the underlying process for the above three points. Net surface heat flux responds accordingly, largely through latent heat flux. TIWs, which have a warming effect on the equatorial mixed layer, diminish during El Niño. Since boreal winter TIWs are reduced on the mean with Galápagos, the *reduction* in warming is less with Galápagos. Thus, through the El Niño-induced change in TIWs, the SST anomaly should be larger with Galápagos. Since it is not, the Galápagos-induced damping of wintertime TIWs in the mean is of secondary importance to the effect of the background mean state.

The power spectrum of the hybrid coupled experiment without the Galápagos Islands is dominated by a peak at two years, which is the classic biennial ENSO characteristic of many ocean and coupled climate models. Two such examples are the NCAR CCSM3 (Collins et al. 2006) and the ECHAM4 (Bacher et al. 1998). Such strictly biennial regularity is not realistic, as ENSO in nature is neither perfectly regular nor significantly biennial. The Galápagos Islands have the effect of significantly reducing the biennial peak and generating a preferred timescale of roughly 3 years, which is a closer match to the observed spectra. We explain the shift in ENSO period in the context of current paradigms for the oscillatory nature of ENSO. The delayed oscillator model of ENSO would dictate a two year period of ENSO. However, given a damped SST anomaly, which is the overall effect of the Galápagos mean state, the growth of the SST anomaly through the Bjerknes feedback is slowed. A slower warming translates into a longer complete cycle as measured between crests or troughs in a time series of, say, NINO3 SST anomaly. Had the Galápagos Islands also resulted in a more gradual cooling period following an

El Niño event, the change in period may well have been not from 2 to 3 years, but from 2 to 4 years. Fedorov and Philander (2000) discussed the relationship between thermocline depth in the mean state and the period of ENSO; our results are highly consistent with their notion that a deeper mean thermocline results in a longer period of the most unstable mode in the tropical Pacific coupled ocean-atmosphere system.

The Pacific subtropical cells also contribute to the slowness of the warming preceding the peak El Niño. Since the transport convergence is related to the strength of the equatorial winds, a gentle weakening of the trades, as is the case in the coupled experiment that included the Galápagos Islands, does not lead to suppression of the subsurface transport convergence and therefore does not contribute to the warming. The amplitude of the peak event in either of the coupled experiments is roughly the same, however, because the transport convergence is eventually suppressed once the zonal wind stress anomaly is finally strong enough to affect a change in the subsurface meridional transport convergence.

The most general implication is that ENSO frequency is sensitive to the true mean state, and if one is to properly simulate ENSO variability in even a simple coupled model, it is particularly crucial to accurately represent the thermocline depth and mixed layer physics. In our case, and based on the spatial patterns of SST biases in other models, it is the introduction of the Galápagos Islands that seems to bring about the right thermocline change to enable important aspects of tropical ocean-atmosphere dynamics and, ultimately, a more reasonable ENSO frequency. There are examples of coupled models that are plagued by the usual equatorial cold bias, while exhibiting reasonable ENSO frequency, such as the GFDL CM2.0/2.1 (Wittenberg et al. 2006). In ocean models that already have an excessively diffuse thermocline (e.g., some z -coordinate models), it is not clear whether the Galápagos Islands would lead to improvements or further biases. It has also been argued that some coupled GCMs produce a biennial ENSO because of an over-sensitivity to interactions between the Pacific and Indian Oceans (Yu 2005). The Galápagos Islands were not included in the model grid of Yu (2005).

We do not suggest that our results conflict with those of Yu (2005); strong Indo-Pacific interactions could be responsible for an excessively biennial ENSO in some coupled models. However, such interactions in models are sensitive to the treatment of Indonesian throughflow and the highly complex topography which acts as a partial barrier between the Indian and Pacific Oceans. Our model, as set up for the present experiments, does not include any form of Indo-Pacific interaction.

Such a change in the overall amplitude and timescale for ENSO, at least as contained within the Pacific basin, should have a considerable impact on the role of- and response to ENSO in the broader global atmospheric circulation. The atmosphere is also known to be a large source of stochastic forcing in the Pacific coupled ocean-atmosphere system, but in global models which are plagued by a strong biennial ENSO such as CCSM3 and ECHAM4, inclusion of the Galápagos Islands seems a likely solution. In terms of operational predictions of the coupled system, The NOAA Environmental Modeling Center (EMC) is currently assessing the impact of the Galápagos in the Climate Forecast System (CFS) (Jiande Wang, personal communication, 2007). This also applies to physical-ecosystem modeling, since we show that the Galápagos Islands impact the propagation of coastally trapped Kelvin waves through the east Pacific warm pool and Costa Rica Dome- a region of high and complex surface ocean biological activity.

The fact that the Galápagos Islands appear to have such a strong impact on both the mean state of the tropical Pacific and the period of Earth's dominant interannual climate signal raises the issue of the Galápagos playing an important role in paleoclimate. Put simply, nowhere else could an island structure as small as the Galápagos have such a profound global impact. Studies have been conducted which relate Earth's climate fluctuations on timescales of millions of years to thermocline depth and therefore ENSO periodicity (e.g., Philander and Fedorov 2003). It is generally accepted that the Galápagos Islands have existed near their present position for millions of years. However, it would take little horizontal translation or change in vertical structure for the Galápagos Islands to become a non-factor, since the most

dramatic consequences seem to rely on the Galápagos obstructing the equatorially-confined EUC. Therefore, a paleoclimate question that could be explored as motivated by the present chapter is simulating a regime shift that occurred when the islands breached the depth of the EUC, or moved into its path from an off-equatorial position. This would seem to cause a “sudden” change in the mean state, and therefore a change in some key aspects of ENSO as shown in this chapter. In terms of the scenario posed by Philander and Fedorov (2003), the resultant deeper thermocline would mean a climate regime with a longer ENSO period. Such a hypothesis could be tested by using a model to simulate the changes as the Galápagos Islands rise from 200 m depth (i.e., an early period), to 80 m (i.e., a transitional period), 30 m (i.e., a later period), and finally breaching the sea surface (i.e., the present), although model resolution must be fine enough to correctly implement the Galápagos Islands.

Naturally, one would also want to re-think the issue of contemporary sea level rise in the context of the relationship between the sea surface and the Galápagos Islands. However, the Galápagos Islands are volcanic formations, meaning the slope of the surface elevation is very drastic. Initial analysis suggests that even a 50 meter sea level rise would result in only minor loss of the total surface area of the Galápagos Islands. Though the Galápagos Islands may not play an important role in future climate change by way of topographic effects on equatorial currents, the more general results of the present chapter do add, if inadvertently, to the ongoing debate on the effects global warming will have characteristics of ENSO such as its amplitude and period. If future projections include a deeper thermocline in the equatorial Pacific, then we have accidentally simulated that. If global warming is to result in a shallower mean thermocline, we have simulated the opposite. Interpretation of our results in this light should, however, be taken with caution as even our hybrid coupled model is confined to the tropical Pacific, whereas the full response of the Earth's climate will undoubtedly involve adjacent basins and the extratropics.

Chapter 4: The Role of SST in the Eastern Tropical Pacific Ocean in the Interannual Variability of Central American Rainfall

4.1. Introduction and prior work

Central America and its 50 million human inhabitants lay snug between the warm waters of the tropical Pacific Ocean and the Caribbean Sea. The majority of mountainous Central America is less than 400 km wide from coast to coast; in some countries such as Costa Rica and Panama, it is much narrower (Figure 4.1). It is also interesting to examine the spatial distribution of population density in Central America; a greater portion of the Mexican population lives on the Gulf coast, while throughout Central America south of the Yucatan Peninsula, population density heavily favors the Pacific coast. Clearly elevation plays a role in shaping the distribution of population in a region such as Central America, where outward expansion is not possible. Recall from Chapter 1, Section 2 that this has been identified as a region particularly susceptible to rain-induced landslides (Hong et al. 2006, 2007a, 2007b, Nadim et al. 2006).

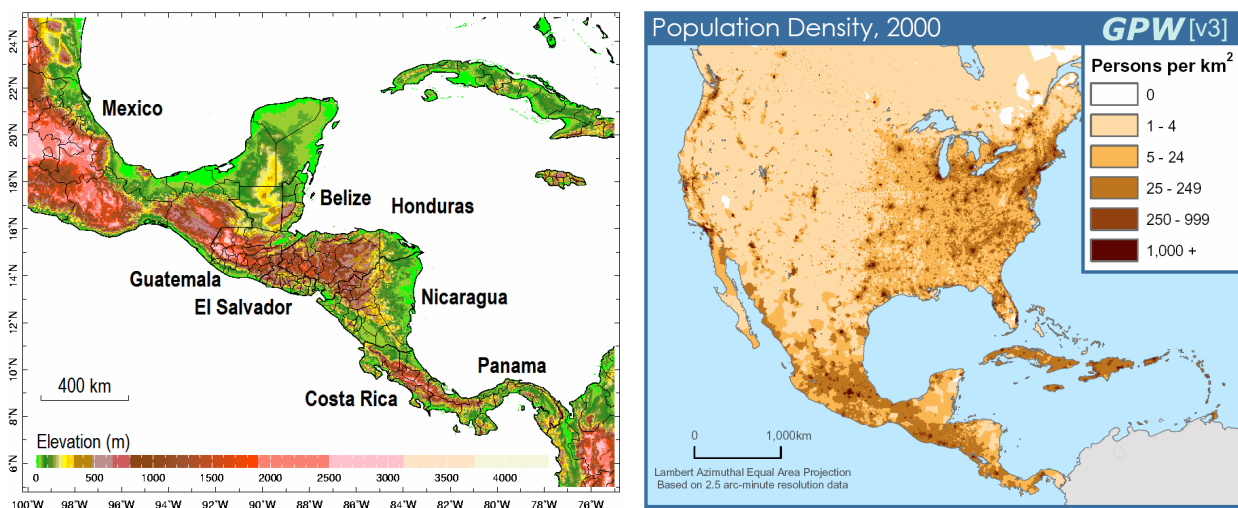


Figure 4.1. Maps of elevation (left) and North & Central American population density in 2000 (right). Elevation data are from the NOAA NGDC GLOBE (Hastings and Dunbar 1999), and population data are from the Columbia University Gridded Population of the World (GPW) v.3.

When a molecule of water lands on the Central American Cordillera or coastal plains, where was it prior to participating in the intricate microphysical metamorphosis that transforms buoyant water vapor to liquid drops which fall from the sky? Was this representative water molecule evaporated directly from the land surface beneath? Was it evaporated from a nearby or remote ocean surface and then transported inland by the general atmospheric circulation? The surface-atmosphere water balance in a narrow maritime landmass such as Central America will undoubtedly be a different picture than that of e.g., the U.S. Great Plains, where direct land surface evaporation exerts a first-order control on hydroclimate variability (e.g., Koster et al. 2004). Other than potentially contributing to the water vapor necessary to produce rainfall, what role does the east Pacific warm pool play in the atmospheric circulation that is relevant to rainfall? Moreover, do interannual variations in the mean sea surface temperature of the EPWP contribute to the interannual variations in rainfall over Central America?

While a vast body of literature concerning rainfall and its interannual variations exists for North and South America, the literature regarding that of Central America can be summed up in a small handful of key studies. The pioneering work of Stefan Hastenrath (1966a, 1966b) considered the seasonal moisture and energy budgets over the Caribbean Sea and Gulf of Mexico. While these works neither included the tropical Pacific sector nor directly addressed rainfall in Central America, they motivated another pioneering study by Hastenrath (1976) on the interannual variations of extreme climate events in the Caribbean and Central America. Hastenrath (1976) averaged stations from southern Mexico, northern South America, and the entire Caribbean basin (to 60°W), and analyzed composite maps of observed SLP, wind speed, and SST associated with extreme wet and dry events in that region. While Hastenrath (1976) had precious little data available from the tropical Pacific, he did make some interesting observations which highlighted the potential importance of processes based in the tropical Pacific. The focus of Hastenrath (1976) was divided between the Atlantic and Pacific, but with

regard to the eastern tropical Pacific, Hastenrath identified the makeup of wet and dry events in the Central America-Caribbean region as summarized in Table 4.1.

Rainfall Anomaly	Season	Equatorial Pacific	ITCZ
Wet	Winter preceding	Warm	Poleward
	Summer of	Cold	Poleward
Dry	Winter preceding	Cold	Equatorward
	Summer of	Warm	Equatorward

Table 4.1. Summary of the characteristics of equatorial Pacific climate associated with anomalously wet and dry rainy seasons in Central America and the Caribbean identified by Hastenrath (1976).

That wet (dry) events corresponded to a poleward (equatorward) displaced ITCZ, and that summertime poleward (equatorward) displacements of the ITCZ corresponded to cold (warm) equatorial Pacific SST makes sense on first principles. However, that wintertime poleward (equatorward) displacements of the ITCZ corresponded to warm (cold) equatorial Pacific SST does not seem to fit within first principles, including the modern day picture of ENSO events as a coupled phenomenon. Hastenrath left this unresolved, perhaps in part due to the lack of observations from the eastern tropical Pacific from which he constructed composite maps. Also, the magnitudes of the warm and cold equatorial Pacific SSTs were only on the order of $\pm 0.5^{\circ}\text{C}$ (except up to 1.0°C for the warm SST in the summer of a dry event). All composite departures were less pronounced for wet events. Mechanisms linking SST anomalies, the ITCZ, and rainfall in Central America-Caribbean were also left unresolved. Once again, however, given that Hastenrath's analyses were performed entirely before the satellite era, the foundations he laid for further study are remarkable.

Still focusing on the Central America-Caribbean region, Hastenrath (1978) used principal component analysis to identify leading modes of sea level pressure (SLP) and SST in the Atlantic and eastern Pacific, and compare with rainfall variability in the Central America-Caribbean region and elsewhere in the tropics. Hastenrath found that the first modes of SLP

and SST, accounting for 43% and 42% of field variance, respectively, were highly correlated with one another, and with SST at the coast of Ecuador and Peru. However, the pair of modes that corresponded to rainfall variability in the Central America-Caribbean region was the fourth mode of SLP and the third mode of SST (each explaining 10% of the variance of their respective field). This would seem to suggest greater complexity in the relationship between ENSO and rainfall in the Central America-Caribbean region. The major result from Hastenrath (1978) was that tropics-wide mass exchanges appear to play an important role in tropical climate anomalies.

Using a very similar domain (Central America, northern South America, and the Caribbean out to 60°W), Giannini et al. (2000) returned to the question of the role of the Atlantic and Pacific basins in the seasonal and interannual variability of rainfall in that region. Their overarching goal was similar to that of Hastenrath- to understand the large-scale tropical interactions between ENSO in the Pacific and tropical Atlantic variability. With regard to the role of the Pacific, Giannini et al. (2000) found that dry conditions tend to prevail in the rainy season preceding an El Niño event, and wet conditions in the following rainy season. The mechanism proposed for the latter is that in the spring following the El Niño event, the Caribbean basin is still anomalously warm, which contributes to the positive rainfall anomaly in that season. This mechanism is quite physically viable because the rainfall index covers such a broad region, primarily encompassing the Caribbean. Whether this mechanism could explain the response of Central American precipitation to eastern tropical Pacific SST variability is unknown. The authors also did not address the fact that, in the maps that revealed the positive Caribbean SST anomaly persisting into the spring following an El Niño event, there is also a comparable SST anomaly in a region outlining the EPWP.

It is suggested here that the role of the eastern tropical Pacific in the interannual variability of rainfall in Central America (strictly speaking) may be at the very least underestimated, because most prior work has only considered Central America as a part of a

much larger region, and assuming some amount of homogeneity across the entire Caribbean and even the western Atlantic.

More recently, Peña and Douglas (2002) took a different approach to that of Hastenrath (1976, 1978) and Giannini et al. (2002). Peña and Douglas (2002) analyzed the mean synoptic atmospheric fields associated with six years of wet and dry spells along the Pacific coast of southern Central America (Nicaragua, Costa Rica, and Panama). In contrast to the aforementioned studies, wet (dry) spells could in this case be as short as a day, so long as at least 75% (65%) of the stations in that region did (did not) report rainfall. Peña and Douglas (2002) found that wet spells were characterized by weakened Caribbean trades and stronger cross-equatorial flow over the eastern Pacific toward Central America, and the opposite for dry spells. The authors also noted that composite OLR maps of wet and dry spells reveal convective cloudiness anomalies extending from Central America westward, well into the eastern Pacific. This fresh perspective paints a very different picture of Central American precipitation than that of the aforementioned studies.

Although SSTs were not discussed in Peña and Douglas (2002), it is here noticed that said OLR anomalies are collocated to near perfection with the EPWP. It is also worthwhile to point out that cross-equatorial flow toward Central America implies flow *over* the EPWP. The authors did point out that there was interannual variation in the number of wet and dry spells, but this subject was not within the scope of the paper or feasible given the length of the dataset. Nonetheless, the first question posed in the concluding remarks of Peña and Douglas (2002) was: what are the processes modulating the lower-frequency variations in wet and dry spells?

Chapter 2 utilized ocean general circulation modeling and multiple forms of observations to understand what governs the interannual variability in the EPWP. One of the hypotheses that motivated such an understanding was that there is a connection between the interannual variability of the EPWP and that of Central American precipitation. Furthermore, if there is a robust mechanistic connection between the EPWP and Central American precipitation, and the

EPWP is well-understood, then there is the potential for useful seasonal-to-interannual predictability of Central American hydroclimate. The first sections of Chapter 4 are devoted to describing the interannual variability of Central American precipitation, including its temporal and spatial scales, and determining if observations suggest a connection between the interannual variability of Central American precipitation and SST in the eastern tropical Pacific Ocean. The latter sections of Chapter 4 are devoted to understanding the physical mechanisms underpinning the observed (or not observed) covariability of Central American precipitation and the EPWP, and whether this contributes to the potential predictability of Central American precipitation. Clearly one of the more challenging issues is how to isolate the specific role or relationships associated with the EPWP from the potentially dominant influence of ENSO.

4.2. Observed scales of interannual variability of Central American rainfall

4.2.1. Global context

The purpose of section 4.2 is to describe the interannual variability of precipitation in Central America, and understand its spatial and temporal scales. Within the broader global context (Figure 4.2), Central America is in very close proximity to a major center of precipitation. The ITCZ over the EPWP is in boreal summer the rainiest place on Earth. On average, up to 50 cm of rain falls on the EPWP between May and July, which rivals the Indo-Pacific warm pool and Indian monsoon.

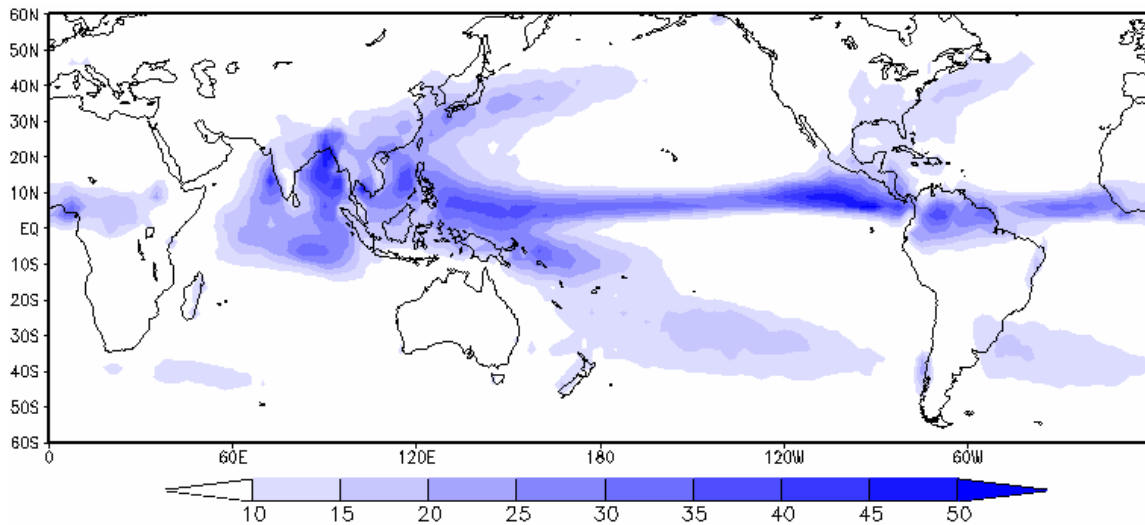


Figure 4.2. Climatological mean global precipitation for early boreal summer (May-July; cm) over the period 1979-2006 from the CPC Merged Analysis of Precipitation (CMAP, Xie and Arkin 1997).

In terms of a first order spatial scale, the ITCZ over the EPWP is part of a tropics-wide belt of heavy precipitation, and therefore rainfall over Central America must be considered in that context. As a brief aside, the east Pacific ITCZ is northward displaced from the equator because it tends to follow the *thermal* equator. In the eastern Pacific, the equatorial cold tongue together with the EPWP to the north generates a marked northward “kink” in the thermal equator. Interannual variations in this arrangement, such as ENSO events, can cause this to change considerably.

4.2.2. Precipitation datasets

Given the complex and narrow geography characteristic of Central America, a brief evaluation of available precipitation datasets is required before serious use in that region. In this subsection, precipitation data from six sources are briefly analyzed for mean and variability in order to select the most appropriate dataset(s) for use in the present study. The basic details of each dataset considered are outlined in Table 4.2. Horizontal resolution is especially

important since the southern stretch of Central America itself (Costa Rica and Panama) is nearly “subgridscale” from the perspective of global reanalyses and some satellite-based analyses.

Dataset	Resolution	Temporal coverage	Key reference
DEKLIM	0.5°	1951-2002	Beck et al. (2005)
UNAM v.0705	0.5°	1901-2002	UNAM
U-Del	0.5°	1950-1999	Willmott and Matsuura (1995)
NARR	1°	1979-2002	Mesinger et al. (2005)
CMAP	2.5°	1979-pres.	Xie and Arkin (1997)
NCEP Reanalysis	~2°	1948-pres.	Kalnay et al. (1996)

Table 4.2. Name, horizontal resolution, temporal coverage, and key reference for each of the six precipitation datasets considered in the present subsection.

Of primary importance is the apparent performance of land precipitation over Central America, rather than the broader precipitation field including the ocean. To ensure a fair comparison, only the 21-year period 1979-1999 is used, as that is the range common to all six datasets. Shown in Figure 4.3 is the annual mean land precipitation over Central America in all six datasets. The top three panels are strictly *in situ* observations (DEKLIM, UNAM, and U-Del), while the bottom row shows a regional reanalysis (NARR), satellite observations (CMAP), and a global reanalysis (NCEP). From the three 0.5° observational datasets (top row), it is clear that precipitation datasets suitable for Central America should include some spatial variability between the Pacific and northeast coasts, as well as variation with latitude. Based on UNAM and U-Del, neither of the reanalyses nor CMAP appears to capture this without severe underestimates or overestimates of annual mean precipitation. In terms of variability (Figure 4.4), it is clear that neither DEKLIM, NARR, CMAP, nor NCEP exhibits variability beyond about one half the magnitude indicated by UNAM and U-Del. In the mean and variability figures, UNAM and U-Del appear to have very similar characteristics. Both are land-only products, but U-Del is available for all land surfaces globally which could be potentially useful for setting regional anomalies within the context of tropics-wide or extratropical anomalies. Therefore, U-

Del precipitation will be used for land precipitation in Central America, complemented by the satellite observations of CMAP over nearby ocean regions where U-Del has no data.

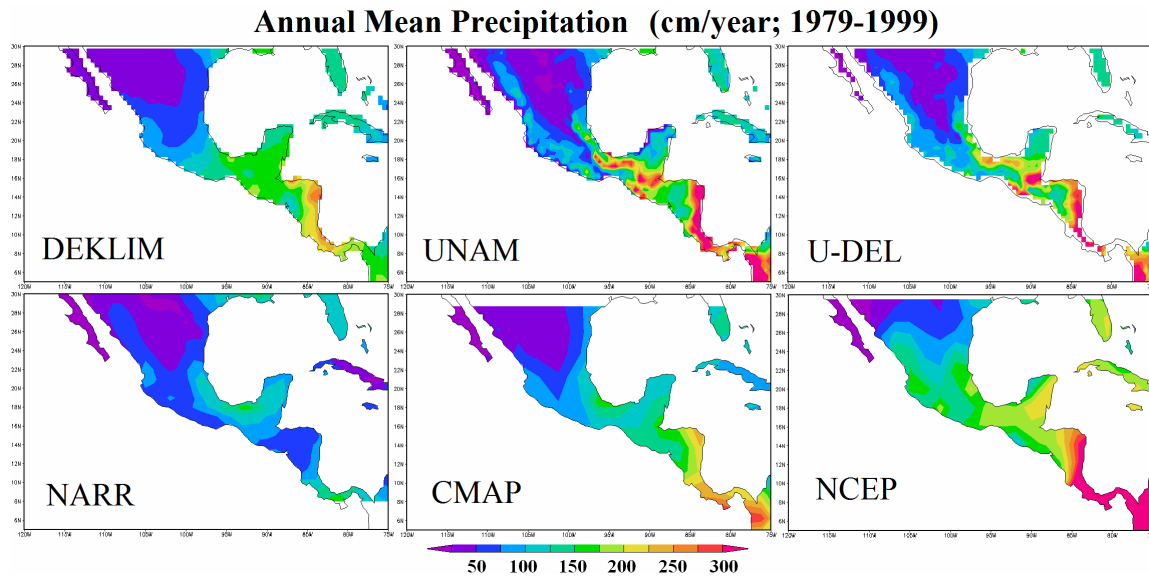


Figure 4.3. Comparison of the 1979-1999 annual mean precipitation (cm yr⁻¹) from the six precipitation products as explained in the main text.

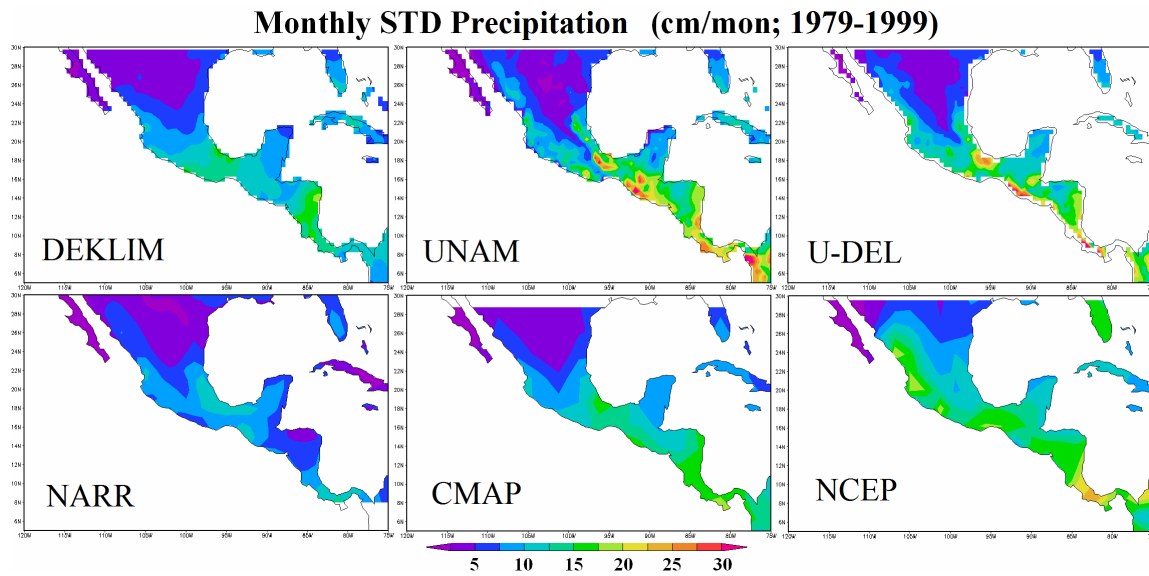


Figure 4.4. Comparison of the standard deviation of monthly precipitation anomalies over the period 1979-1999 (cm month⁻¹) from the six precipitation products as explained in the main text.

4.2.3. Seasonality and indices

Next, a rainy season must be defined. Shown in Figure 4.5 is the monthly climatology of precipitation in Central America from U-Del (all land between 6°N and 22°N). The midsummer relative minimum in precipitation as described in Magaña (1999) is evident even in such a broad region. The rainy season for Central America will be defined as May through November. This is a fairly liberal definition, but is necessary because (a) early onsets and late progressing rainy seasons can be accounted for, and (b) the climatology show in Figure 4.5 is for a wide range of latitude; the seasonal cycle at different latitudes may include more or less precipitation toward the limits of our definition. Furthermore, the rainy season will be split between an early rainy season (May-July) and a late rainy season (September-November). The spatial context of the early versus late rainy seasons, and their interannual covariability are analyzed in the paragraphs to follow.

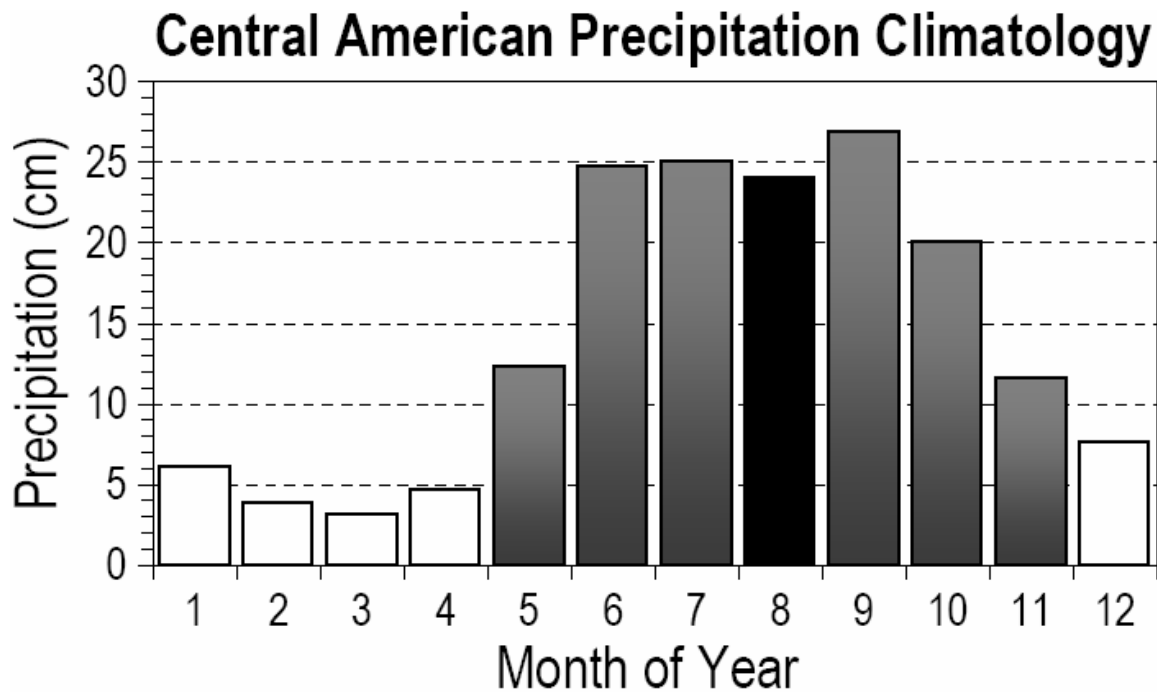


Figure 4.5. Monthly climatology of precipitation (cm) in Central America (area average of all land precipitation within 105°W-80°W x 6°N-22°N) from U-Del precipitation (1950-1999). White bars are not included in “rainy season” calculations. The two separate groups of gray bars delineate the early from the late rainy season in Central America.

Shown in Figure 4.6a is the observed climatological mean rainy season precipitation in Central America. Similar to the annual mean from a shorter period that was discussed in Figure 4.3, there is considerable spatial variability in the distribution of rainfall over Central America. In southern Mexico, rainfall tends to favor the Gulf coast (as does population; Figure 4.1), while in the rest of Central American rainfall is found on both sides of the isthmus. Figure 4.6b shows the difference between rainfall in the late and early rainy seasons. Compared to the early rainy season, rainfall in the late season increases over parts of the Gulf and Caribbean coast, decreases over much of the Pacific coast, but increases along the Pacific side of Nicaragua, Costa Rica, and Panama. CMAP, which is not limited to land, does appear to capture much of the observed spatial seasonality (Figure 4.6c), which foretells its potential utility in understanding the broader (ocean) context of land precipitation variability in Central America.

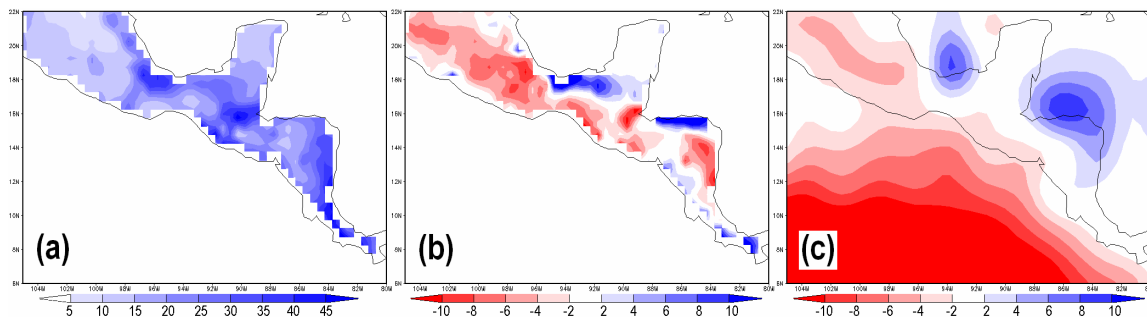


Figure 4.6. Climatological mean rainy season (May-November) precipitation in Central America (cm) from U-Del precipitation (1950-1999; a), mean precipitation difference (cm) between the late (September-November) and early rainy season (May-July) from U-Del precipitation (b), and as in (b) but for CMAP precipitation (1979-2006; c).

Given the observed spatial variability discussed above, it is clear that insightful analysis of rainfall variability over Central America requires a regional perspective. Shown in Figure 4.7 is the U-Del data grid (and long-term mean rainy season precipitation field), along with outlines of the five precipitation indices that will be analyzed. These will be referred to as P#, where # is

the number indicated on the map in Figure 4.7. P1 and P2 are effectively the Pacific and Gulf coasts of southern Mexico, P3 and P4 are effectively the Pacific and Caribbean coasts of Central America from Nicaragua through the Yucatan Peninsula, and P5 is effectively Panama and Costa Rica, which are too narrow in comparison to the resolution of U-Del precipitation to be split into Pacific and Caribbean sides. The following analysis of a series of scatterplots comparing the variability of precipitation among the five precipitation indices is meant to elucidate which indices are necessary to keep, and which are essentially explained by an adjacent region.

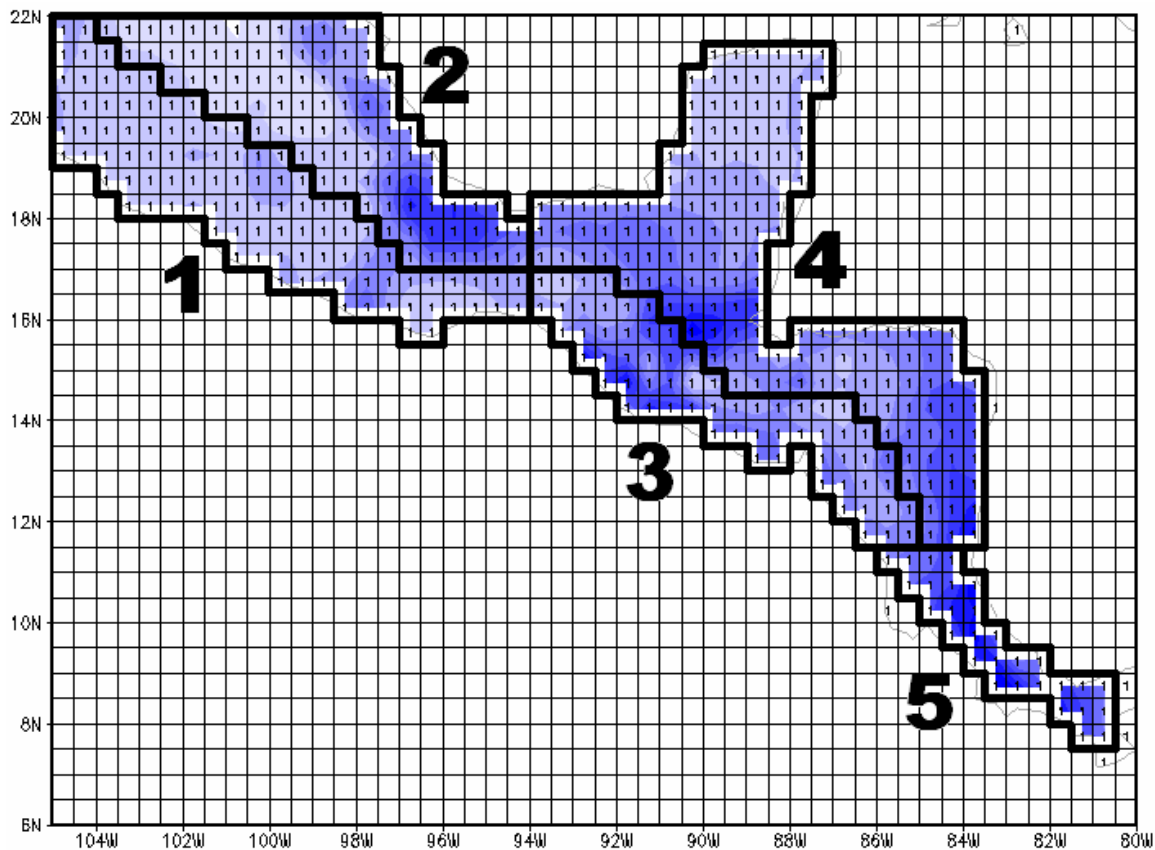


Figure 4.7. Map of Central America, the mean rainy season (May-November) precipitation (cm) from U-Del precipitation (1950-1999), the 0.5° x 0.5° grid on which the U-Del precipitation dataset is arranged, and the five precipitation index regions discussed in the main text.

The scatterplots arranged in Figure 4.8 compare rainfall interannual variability on the Pacific side of the isthmus versus the Gulf or Caribbean side. The question addressed is: how

different are the Pacific and Gulf or Caribbean coasts in U-Del precipitation? As expected, the coasts are not altogether independent from one another. The percent variance of a given index that is explained by its neighbor across the isthmus ranges from 56-72%, depending on whether the full, early or late rainy season is considered. There is also a general tendency for the cross-isthmus correspondence to weaken (i.e., data points straying further from the linear best-fit line) toward higher values of rainfall. This hints that “extreme” wet years (as yet undefined) are in fact more restricted to one coast or the other, rather than being a blanket event across the isthmus. These differences warrant keeping the Pacific and Gulf or Caribbean coasts separate in analysis of rainfall interannual variability.

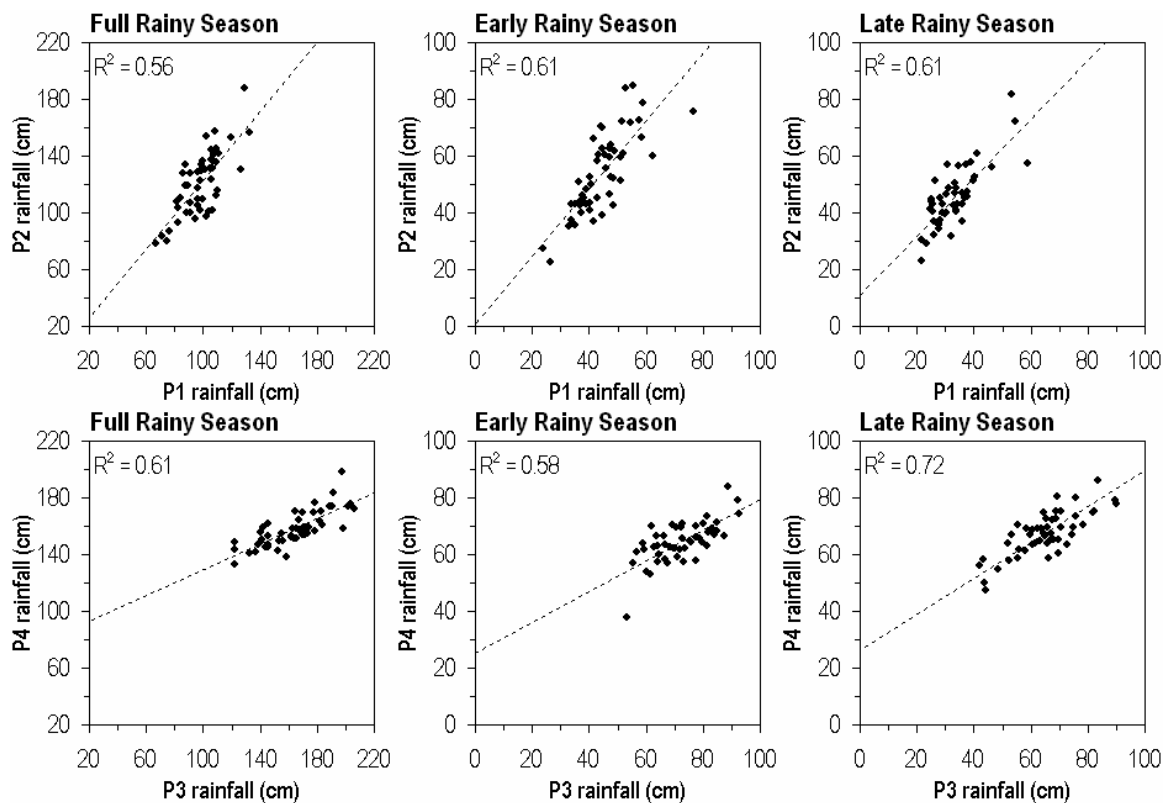


Figure 4.8. Scatterplots of P1 vs. P2 (top) and P3 vs. P4 (bottom) precipitation (cm) for the full rainy season (left), the early rainy season (center), and the late rainy season (right) from U-Del precipitation (1950-1999). Indices are defined in Figure 4.7.

Next, we consider how independently the northern versus southern stretches of the Pacific and Gulf or Caribbean coasts vary on interannual timescales. As evident in Figure 4.9, an index of “Pacific Central American,” or “Gulf-Caribbean Central American” rainfall would make little sense. The percent variance of one index that is explained by its neighbor along the coast ranges from 5-24%. Therefore, regions of Central America are much more independent from neighbors *along a coast* than from neighbors of *across the isthmus*. Interestingly, the distribution of population is the opposite (Figure 4.1); there is more population variation between the coasts than along the coast. In other words, citizens of a country, who are generally bounded to the north or south by national borders, heavily favor living on one *side* or the other, within their latitudinal restriction (national borders). Since this cannot be explained by topography alone (the mountains run through the center, leaving ample space on either coastal side), this may be an indication of the perceived importance of the seemingly subtle differences in rainfall variability between the Pacific and Gulf or Caribbean coasts.

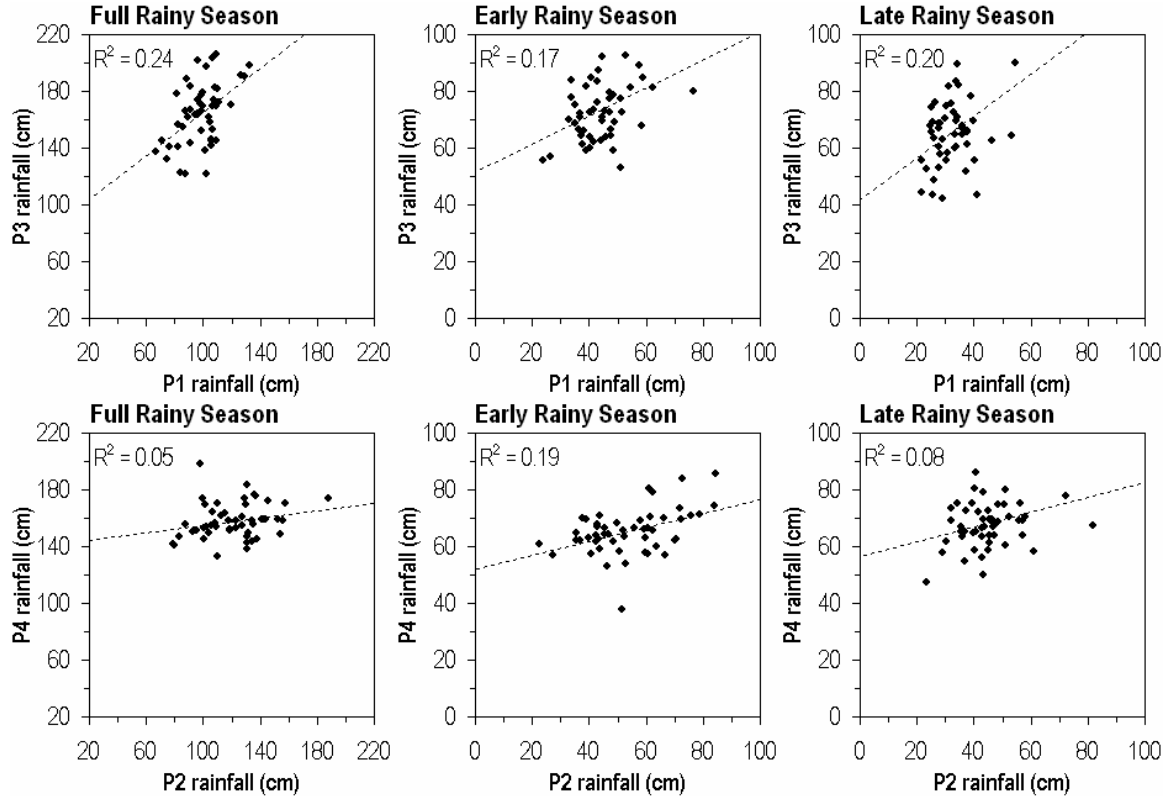


Figure 4.9. Scatterplots of P1 vs. P3 (top) and P2 vs. P4 (bottom) precipitation (cm) for the full rainy season (left), the early rainy season (center), and the late rainy season (right) from U-Del precipitation (1950-1999). Indices are defined in Figure 4.7.

Since Costa Rica and Panama (P5) are so narrow, and cannot sensibly be split into Pacific and Caribbean halves, a logical question is: where does P5 belong? Can it be grouped with P3 on the Pacific coast, or P4 on the Caribbean coast? From Figure 4.10, it is clear that P5 is almost completely independent from both of its northern neighbors. Percent variance explained ranges from 0-21%. The highest percent variance explained is found in the late rainy season (21% versus 5% on the Pacific side; 10% versus 0% on the Caribbean side). Given the relatively important factor that latitude plays (i.e., comparison of P1 vs. P3 or P2 vs. P4 in Figure 4.9), this does not necessarily suggest that P5 is influenced by both basins equally. The interannual variability of rainfall in P5 could be dominated by either the Pacific or Caribbean/Atlantic sector, but the strong latitudinal heterogeneity prevents Figure 4.10 from being interpreted for that purpose.

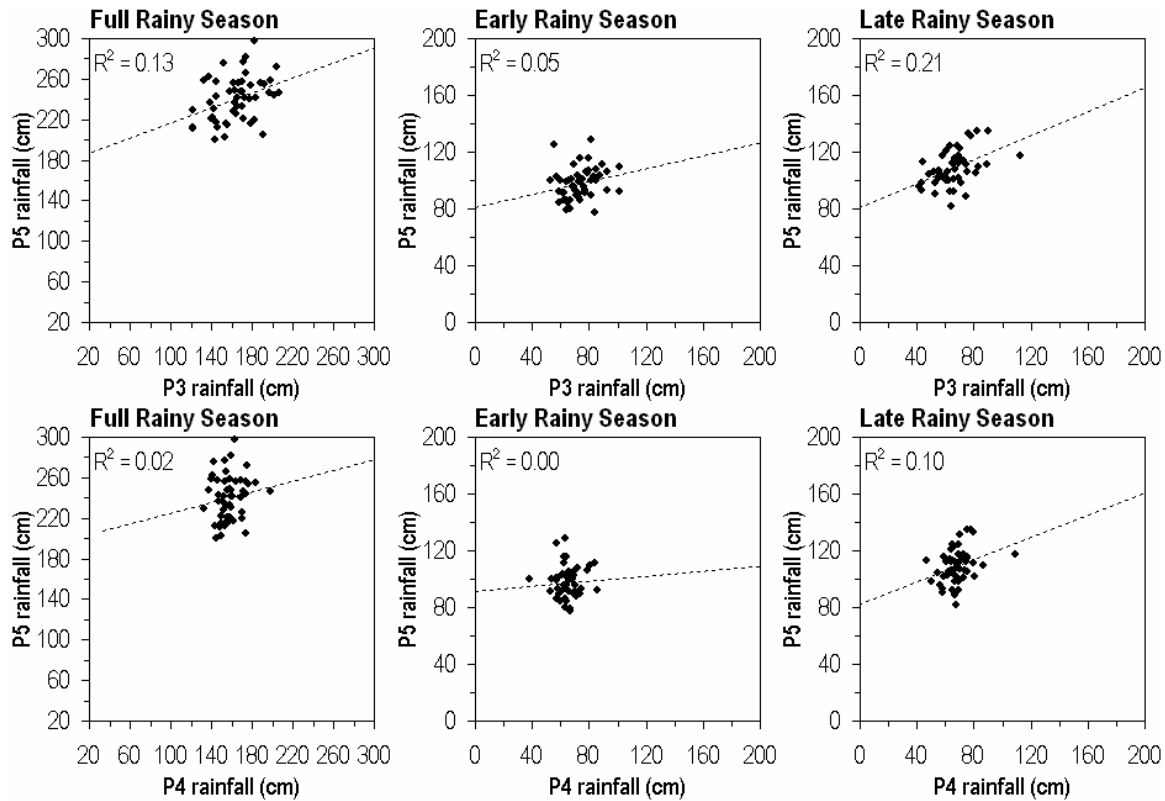


Figure 4.10. Scatterplots of P3 vs. P5 (top) and P4 vs. P5 (bottom) precipitation (cm) for the full rainy season (left), the early rainy season (center), and the late rainy season (right) from U-Del precipitation (1950-1999). Indices are defined in Figure 4.7.

A final covariance analysis of the proposed indices focuses on the seasonality of interannual variations. Shown in Figure 4.11 are one scatterplot for each of the five indices, and the data being compared within each scatterplot are the early versus late rainy season rainfall. The question being addressed is: does anomalous rainfall (either positive or negative) during the early rainy season correspond to (or foretell similar-) anomalous rainfall later in the rainy season? If so, indices stratified by early versus late rainy season would not be necessary. On the contrary, rainfall in the early and late rainy season *appears* completely independent of one another. In light of this, not only is it not sensible to combine the early and late rainy seasons, it is not even sensible to show or discuss further the interannual variability of rainfall in the broader rainy season. All results and discussion must be stratified by early and late season. As

an interesting corollary, a seasonal prediction of rainfall in Central America based on persistence would be rivaled by a coin-flip!

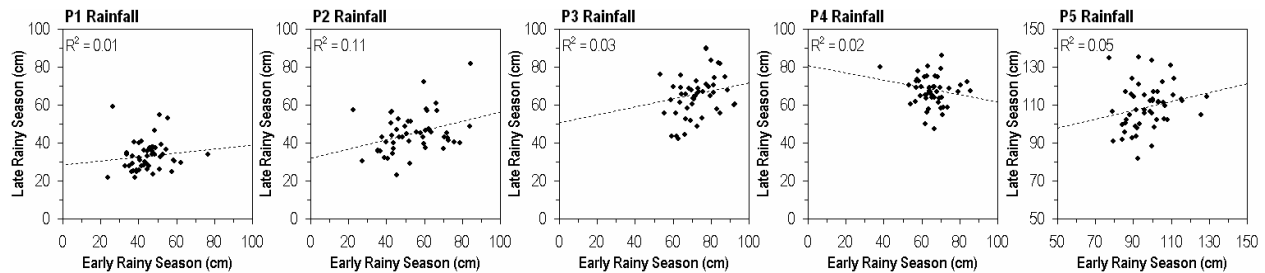


Figure 4.11. Scatterplots of early rainy season vs. late rainy season precipitation (cm) for indices P1-P5 (left to right) from U-Del precipitation (1950-1999). Indices are defined in Figure 4.7.

4.2.4. Observed interannual variability

The covariance analyses in the previous subsection suggest that none of the five proposed precipitation indices can be discarded or combined with a neighboring index. The exception to this is that spatial or temporal portrayals of the entire rainy season lack representativeness of the early or late rainy season in Central America. Shown in Figure 4.12 are time series of early rainy season rainfall (departure from mean) for rainfall indices P1-P5. There are considerable year-to-year fluctuations in each of the indices. The rainfall anomalies, as a percentage of the mean, tend to decrease southward toward P5 (i.e., P5 bars are similar to P1 bars, but the P5 mean is over twice the P1 mean). Given only 50 years of data, spectral analysis cannot be performed with adequate statistical significance. An alternative way of characterizing the temporal scale of variability is to simply compute the average number of years an anomaly persists on either side of zero. It is noted that the average persistence is a very crude estimate since clearly there are examples of rainfall departures persisting for fewer or more years than the average persistence suggests. Linear trends in the precipitation indices may also affect the average persistence.

While Figure 4.12 is a depiction of the temporal characteristics of the early rainy season rainfall in Central America, it is also of interest to understand the spatial scale associated with

such rainfall departures. This is where CMAP is most useful, since U-Del precipitation is only available over land. CMAP can add the broader spatial context to the picture of regional rainfall departures in Central America. Using a threshold of ± 10 cm, wet and dry composites were selected for such departures in each rainfall index. As visual inspection revealed that the wet and dry composites are approximately symmetric (not shown), shown in Figure 4.13 are the differences between the wet and dry composites. This also serves as an internal consistency check of the representativeness of each index to rainfall in that region; each index nicely captured land precipitation patterns strongly affecting that region, and in some cases unique to that region. The CMAP overlays show the larger-scale precipitation concurrent with the land precipitation, such as the east Pacific ITCZ and western Caribbean rainfall. Diagnostics of mechanisms behind these rainfall departures are reserved for the following sections, but it should be pointed out that the east Pacific ITCZ appears to be *most* relevant in the P3 and P4 composites (i.e., Pacific and Caribbean side of Central America south of the Yucatan Peninsula). CMAP precipitation anomalies are found over the northeastern tropical Pacific that are of comparable magnitude to those over the Central American index regions themselves.

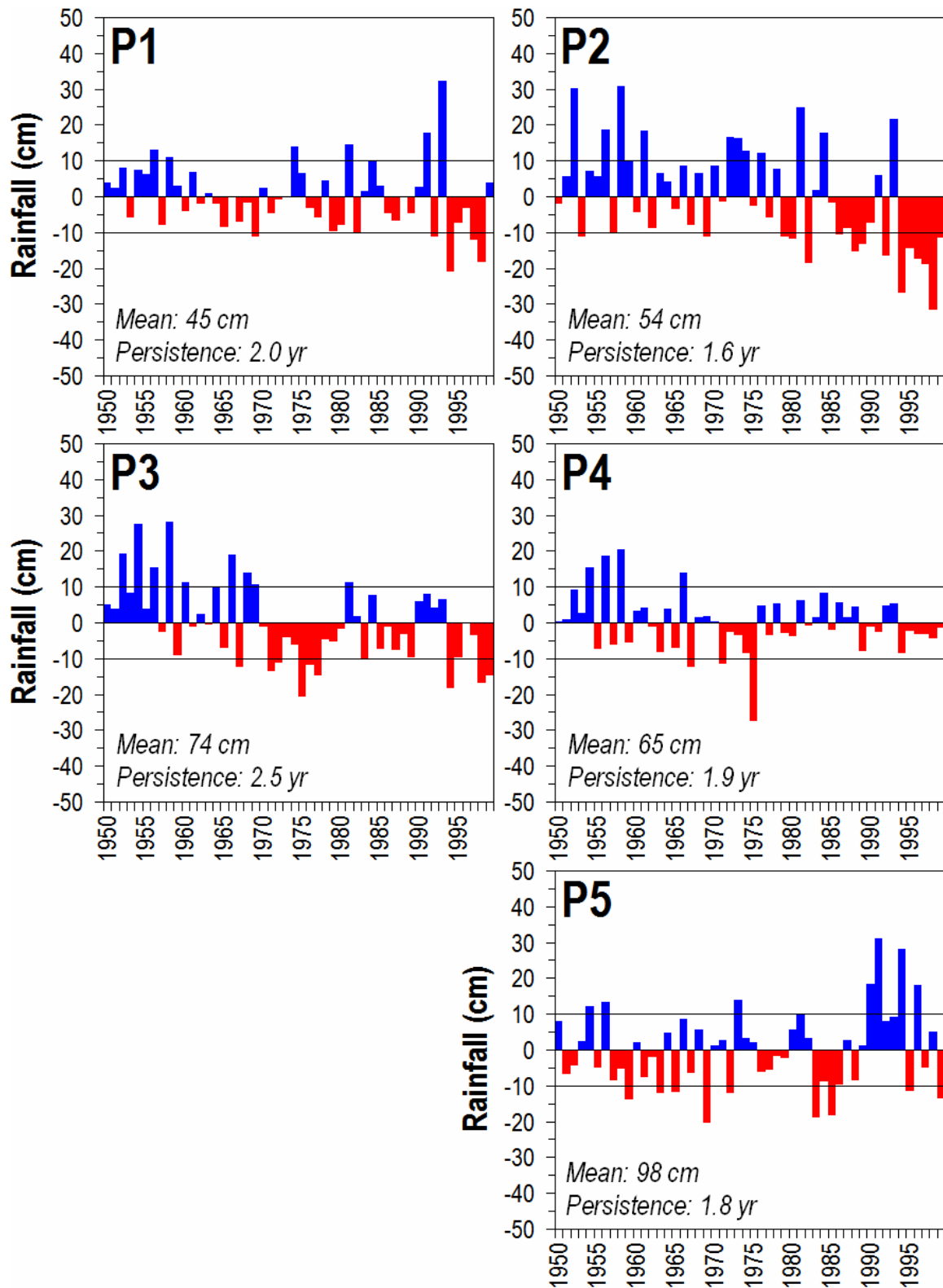


Figure 4.12. Time series of early rainy season precipitation (departure from mean; cm) for indices P1 through P5 from U-Del precipitation (1950-1999). Time series mean and average persistence are

displayed on each panel. Black lines at ± 10 cm indicate the threshold for the composites shown in Figures 4.14 and 4.16 and discussed in the main text.

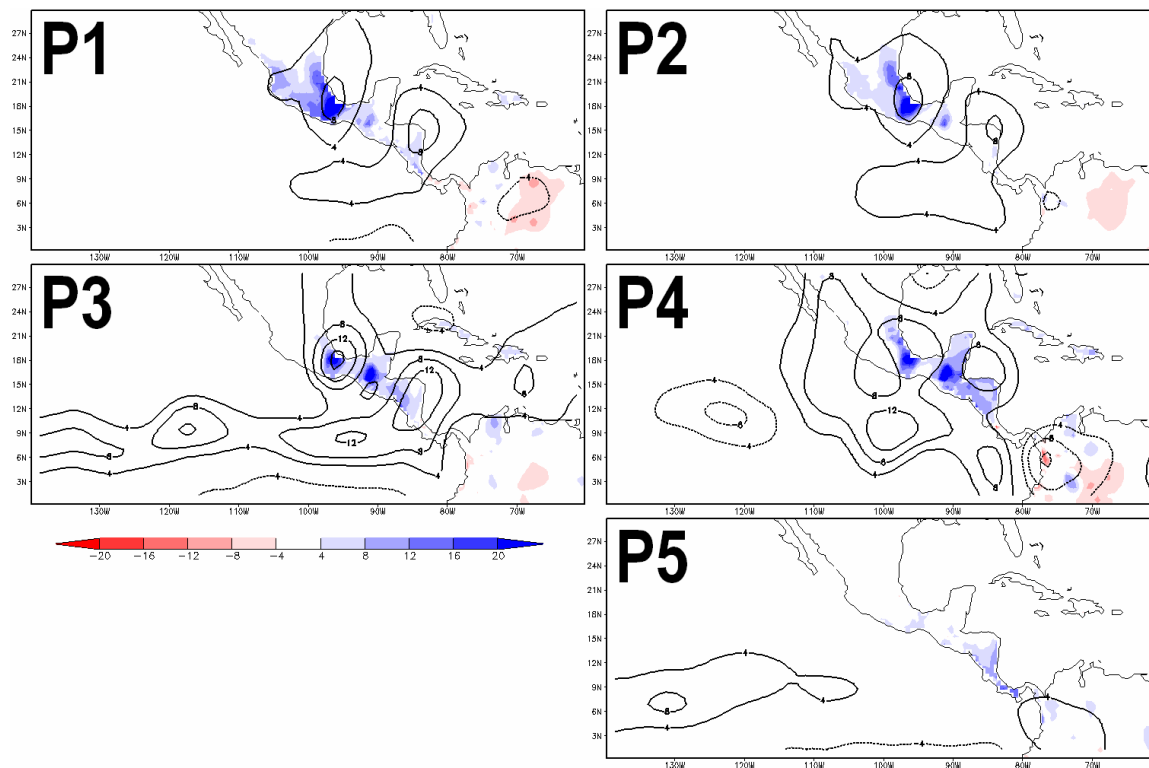


Figure 4.13. Composite early rainy season precipitation anomaly differences (cm; wet – dry) in the Inter-Americas region from U-Del precipitation (1950-1999; color shading) and CMAP precipitation (1979-1999; heavy black contours) for indices P1 through P5.

Shown in Figure 4.14 is the same time series depiction as Figure 4.12, but for late rainy season rainfall departures. As expected from the covariance analysis between early versus late rainy seasons at individual regions, the picture is very different from the early rainy season time series, including the average persistence. For example, the average persistence for P5 is 2.3 years in the late rainy season, versus 1.8 years in the early rainy season. Composite wet–dry precipitation maps corresponding with the indices in Figure 4.14 are shown in Figure 4.15. What is different in the composites of late rainy season precipitation from those of the early rainy season is the apparent spatial extent and involvement of larger scale precipitation patterns

like the ITCZ. In the early rainy season composites, CMAP revealed the east Pacific ITCZ to be a relevant feature for primarily P3 and P4 rainfall departures. In the late rainy season composites, heavy involvement of the eastern tropical Pacific is seen in each composite, while reduced in P3 and P4.

Are mechanisms different than those governing the rainfall departures during the early rainy season? What role does the EPWP play in those processes? These questions are addressed in the following sections.

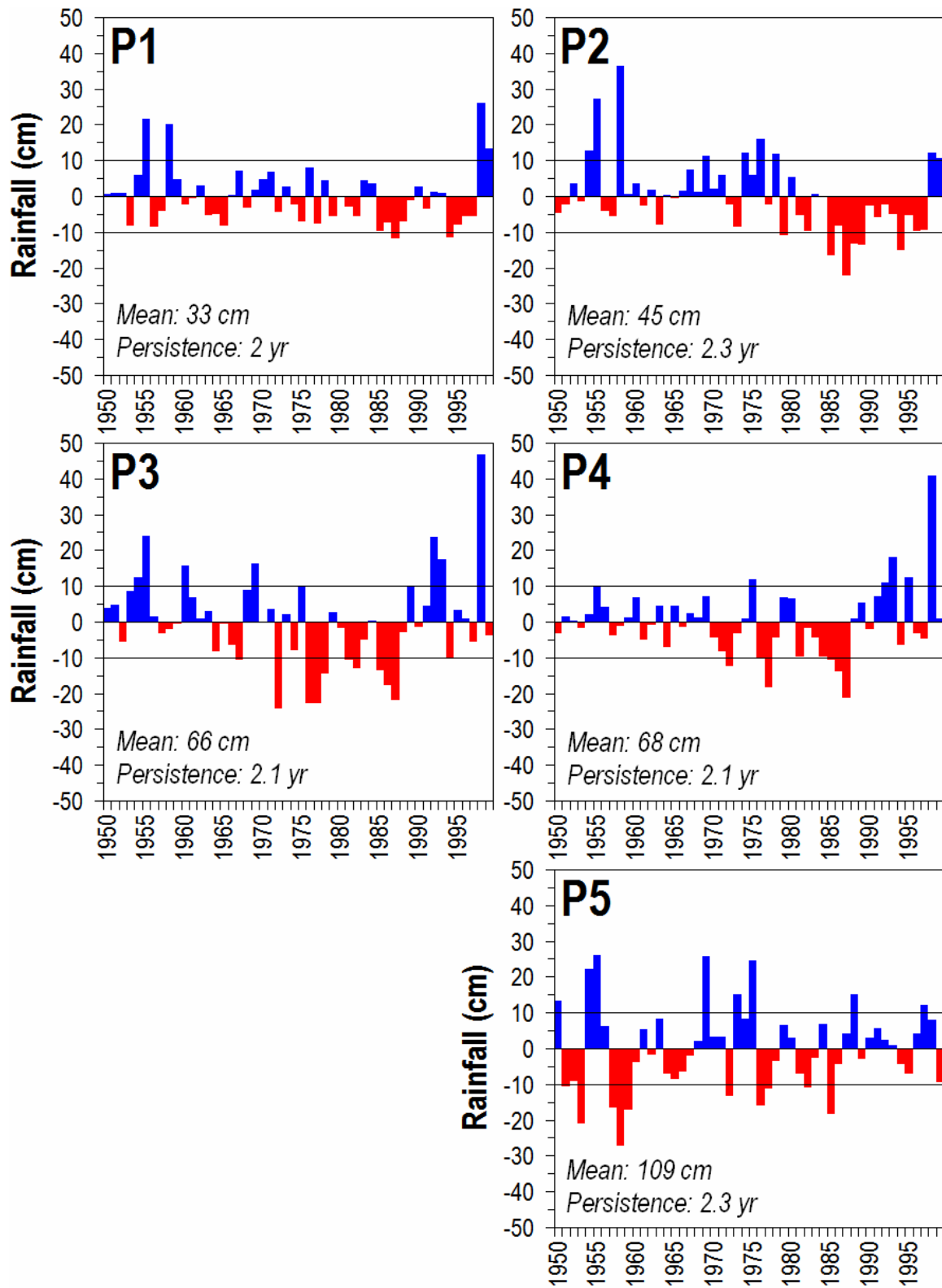


Figure 4.14. As in Figure 4.12 but for the late rainy season.

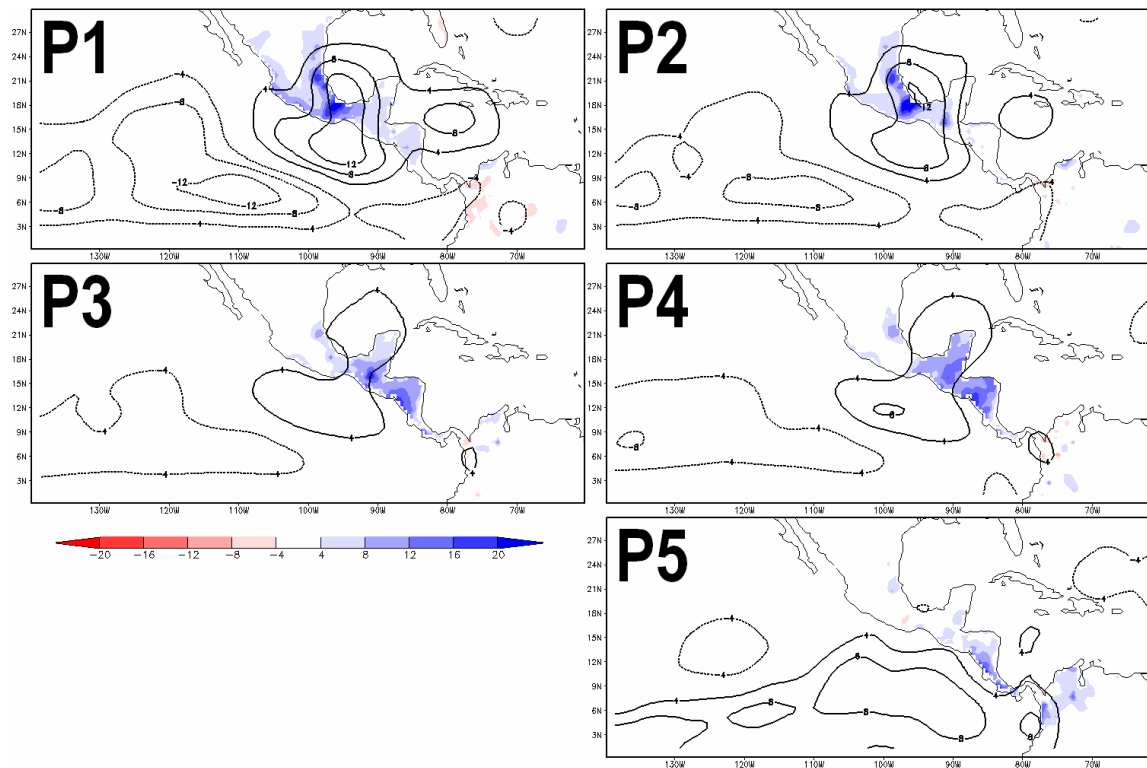


Figure 4.15. As in Figure 4.13 but for the late rainy season.

4.3. Observed covariability with SST in the eastern tropical Pacific Ocean

The previous section (4.2) described the important spatial and temporal aspects of precipitation over Central America using U-Del (*in situ* observations) and CMAP (satellite observations) precipitation. One of the more interesting results was that composite rainfall differences over Central America appear to be related to rainfall variability within the east Pacific ITCZ, the majority of which is nominally situated over the EPWP adjacent to Central America. Also, Central America appears to have some complex heterogeneity in terms of interannual rainfall variability, which suggests that rainfall over Central America as a whole cannot be averaged together, let alone together with the Caribbean and western Atlantic as has been the method in some prior studies. The objective of the present section is simply to highlight the observable evidence of a role of the eastern tropical Pacific Ocean in the interannual variability of rainfall in Central America. As has been previously shown (Section

2.3), the interannual variability of SST in the EPWP is highly correlated and mechanistically linked to ENSO. Furthermore, SST anomalies in the EPWP tend to lag ENSO and persist well beyond the related equatorial SST anomaly. One would thus presume that the role of the EPWP in the interannual variability of Central American rainfall would ultimately include, or be manifest as, some interaction with ENSO.

Describing the nature and processes linking SST in the EPWP to interannual variations in Central American rainfall is the focus of the following section. Thinking ahead, however, it should be noted that “evidence” for a relationship between the eastern tropical Pacific Ocean and Central American rainfall variability does not necessarily mean a positive linear correlation between indices of SST and precipitation. There are potential mechanisms by which the EPWP could play a role in generating a positive precipitation anomaly in Central America following an El Niño event. For example, if anomalously warm equatorial SSTs retreat before the rainy season, the east Pacific ITCZ can march northward to its usual boreal summertime position (i.e., over the EPWP and Central America). If the EPWP is still anomalously warm, however, the EPWP could further enhance the ITCZ (e.g., Zhang 1993) and therefore lead to a positive precipitation anomaly. This mechanism could be characterized as a low-frequency amplification of the annual cycle. On the other hand, there are conceivable ways in which the EPWP could play a role in generating an anomalously *dry* rainy season in response to the same El Niño event. For example, an anomalously warm EPWP (a result of the *large scale* descent and increased shortwave heating) may operate on the *local scale* by reducing the daytime land-sea temperature contrast. Such a configuration would tend to retard the three dimensional land-sea circulation which is an important aspect of tropical Americas rainfall on daily timescales (e.g., Garreaud and Wallace 1997).

Finally, there may be circumstances under which the specific role that the EPWP plays, and the sign of the rainfall anomaly to follow, depends on competing influences or remote matters. For example, if an El Niño event persists into the rainy season, the northward annual

march of the ITCZ could be inhibited and the EPWP would not have the opportunity to interact with the ITCZ. Also under some circumstances, conditions in the Caribbean and Atlantic sector could overrule the Pacific, or generate significant rainfall anomalies when conditions in the Pacific are normal. In other words, the interannual variability of Central American rainfall is subject to multiple and nonlinear influences.

Scatterplots of ENSO indices (e.g., NINO3 SSTA) versus precipitation indices such as those defined in the previous section yield very little evidence of any role of the eastern tropical Pacific Ocean in the interannual variability of rainfall in Central America. For example, shown in Figure 4.16 is one such scatterplot, in this case using early rainy season precipitation on the Pacific coast of southern Mexico (P1 index). The linear correlation coefficient is only -0.2 (not statistically significant at the 90% confidence level), which implies that ENSO explains a mere 4% of the rainfall variability in that region. All other regions yield similar results in terms of direct linear correlation. However, what is being masked is the fact that a NINO3 anomaly of one sign might strongly correspond in time with a positive rainfall anomaly during some years, while strongly correspond with a negative rainfall anomaly during other years.

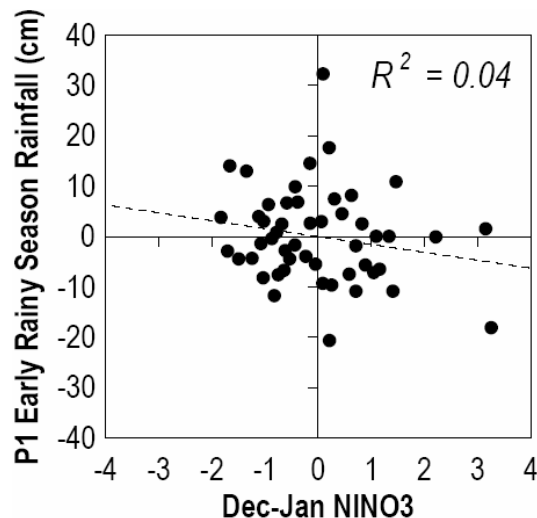


Figure 4.16. Scatterplot of December-January mean NINO3 SSTA (°C) versus early rainy season precipitation anomaly (cm) in the P1 region (U-Del; 1950-1999). Indices are defined in Figure 4.7.

One simple way to compare the timing of large rainfall anomalies of either sign with NINO3 anomalies of either sign is simply to square and standardize the indices. This has the effect of giving all anomalies a positive sign, emphasizing the larger anomalies over the smaller ones, and offering ease of visual comparison. Shown in Figures 4.17 and 4.18 are such comparisons; Figure 4.17 (18) compares early (late) rainy season indices with the preceding wintertime NINO3. Some interesting features associated with the rainfall and ENSO indices are the inactive period during the 1960's, and the higher amplitude ENSO events (1956, 1958, 1966, 1973, 1976, 1983, 1989, 1992, and 1998). Some rainfall anomalies within the Central American regions appear to not correspond to any ENSO event whatsoever (e.g., early rainy season 1975 in P4, early rainy season 1993 in P1). However, many large rainfall anomalies of some sign do correspond to ENSO events. It is particularly interesting to compare the well-known 1982-83 and 1997-98 El Niño events. The 1982-83 ENSO event only appears to correspond with a rainfall anomaly in Costa Rica and Panama (P5), in the early rainy season. In contrast, the 1997-98 ENSO event appears to have affected regions P1-P4. There are rainfall anomalies in P1-P3 in the early 1998 rainy season, and in P1, P3, and P4 in the late 1998 rainy season. Knowing that the 1982-83 and 1997-98 ENSO events were both strong El Niño events, and had similar magnitudes in terms of SST anomaly, how can one so strongly affect Central America but the other not?

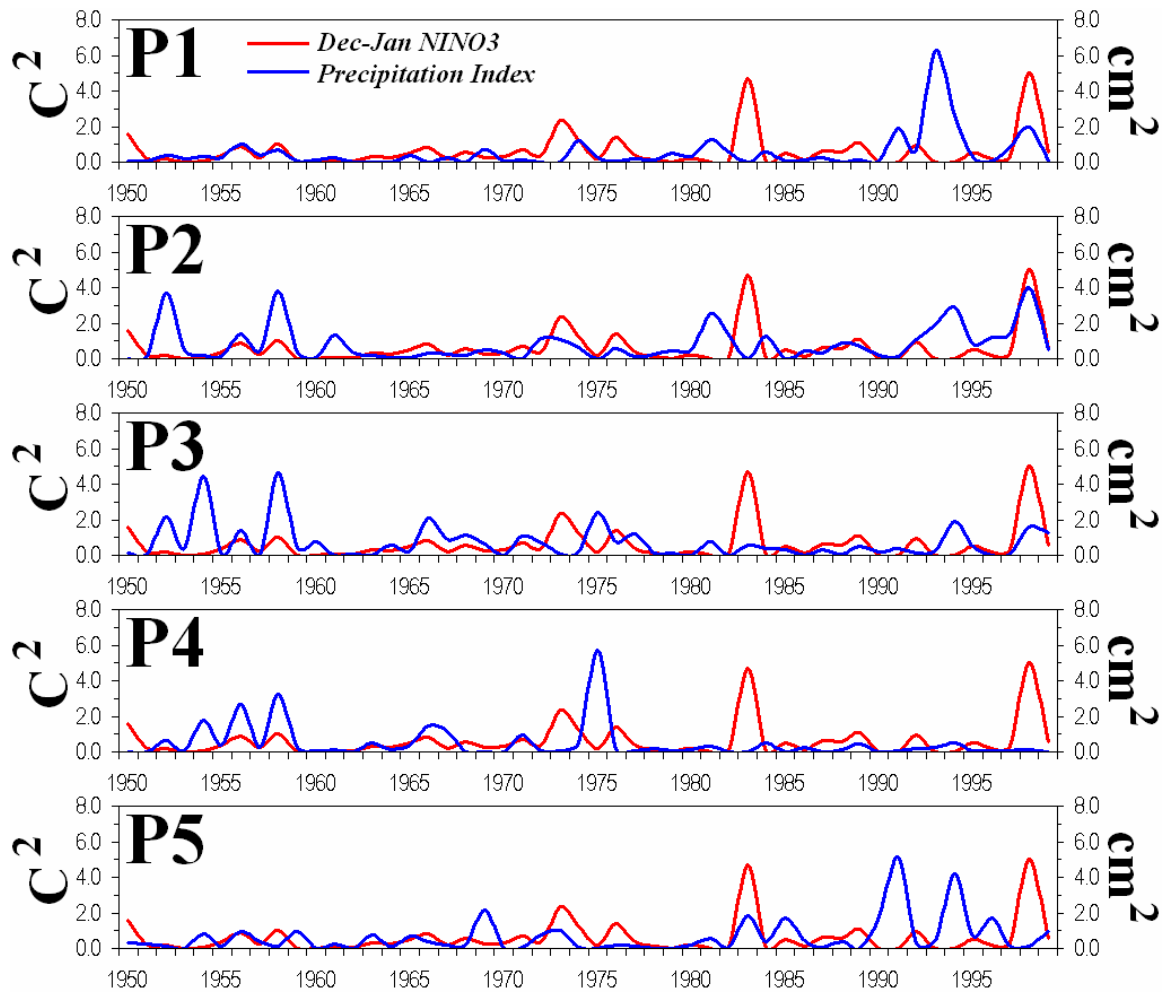


Figure 4.17. Time series of squared and normalized early rainy season precipitation (cm^2) in the five Central American index regions defined in Figure 4.7 (blue) and December-January mean NINO3 SST anomaly (C^2 ; red).

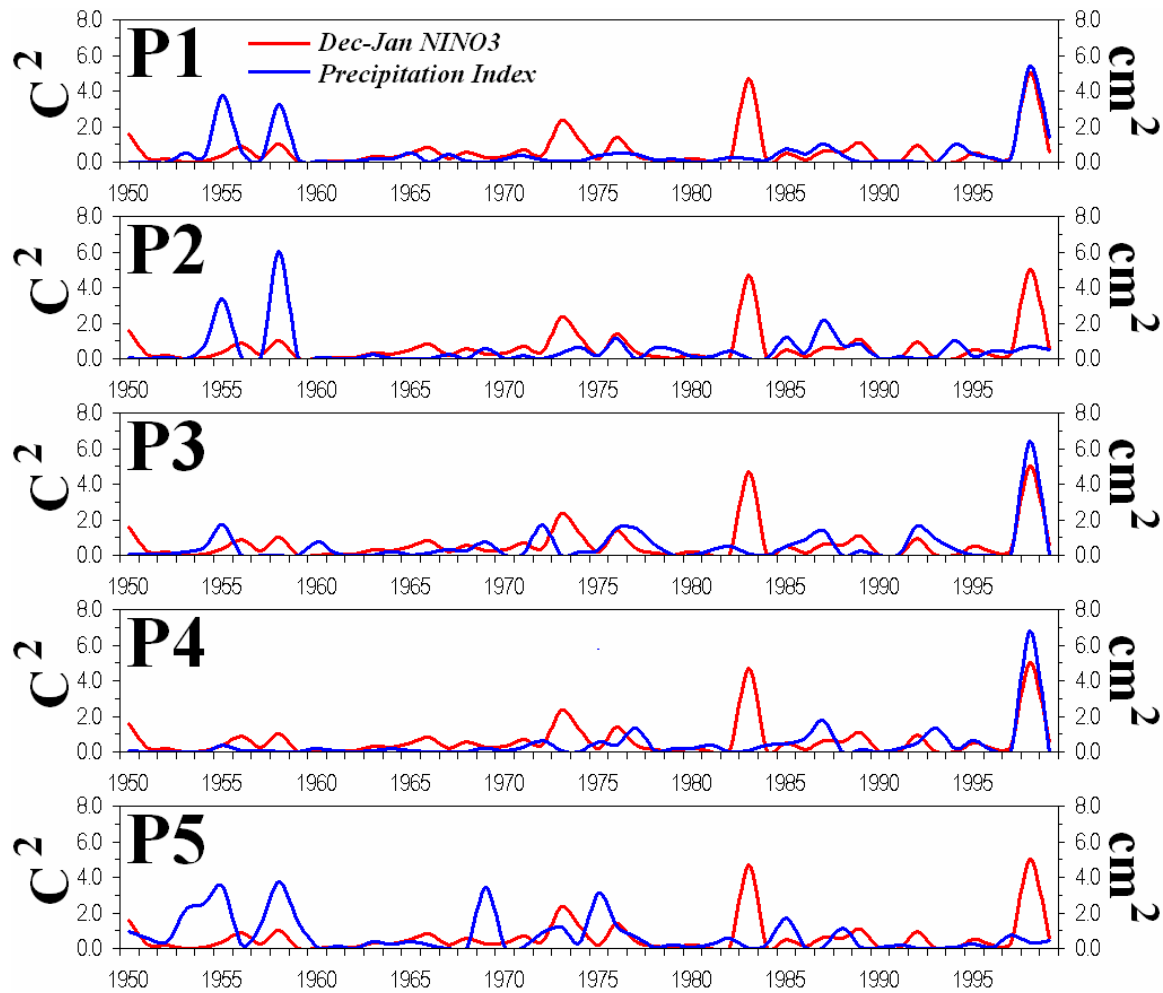


Figure 4.18. As in Figure 4.17 but for late rainy season.

To obtain a more detailed picture of the changes in precipitation potentially associated with variability in the eastern tropical Pacific Ocean, shown in Figure 4.19 are composite seasonal cycles for each rainfall index, stratified by the phase of ENSO. An ENSO warm (cold) event was defined as a case when the NINO3 index exceeded positive (negative) 1.5 standard deviations. ENSO warm events included [1957-58, 1965-66, 1972-73, 1982-83, 1987-88, 1991-92, 1997-98]; ENSO cold events included [1955-56, 1967-68, 1970-71, 1973-74, 1975-76, 1988-89]. Regions P1–P3 indicate substantial and similar responses to ENSO, primarily manifest during the rainy season preceding the peak ENSO event. During the rainy season preceding an ENSO warm (cold) event, monthly rainfall is reduced (enhanced) by 5 cm, which is equivalent to

~25% of the monthly rainfall during the rainiest months at P1 (June through September). During the late rainy season at P1 following an ENSO warm event, rainfall tends to be a few cm higher than normal. Some, but not all, of the differences seen in the seasonal cycle composites are consistent with Giannini et al. (2000) and Hastenrath (1976).

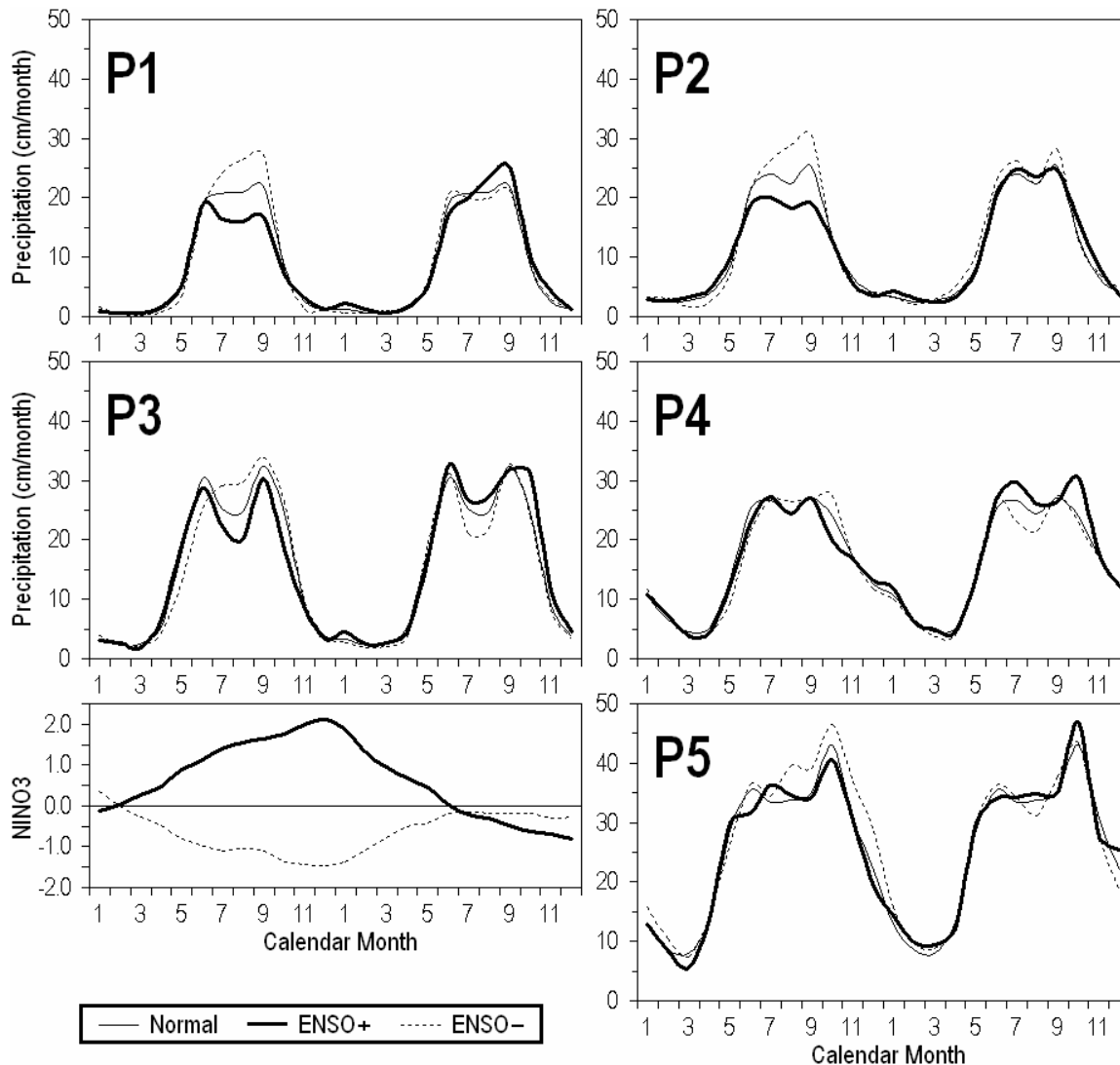


Figure 4.19. Composite seasonal cycles of monthly U-Del (1950-1999) precipitation (cm month^{-1}) in Central American index regions P1–P5 (defined in Figure 4.7) for normal (thin solid), ENSO warm (thick solid), and ENSO cold (dashed) events. The composite calendar years before and after the peak of the ENSO event are shown. An ENSO warm (cold) event was defined as a case when the NINO3 index exceeded positive (negative) 1.5 standard deviations. The corresponding composite evolutions of NINO3 SST anomaly ($^{\circ}\text{C}$) are shown in the lower-left corner.

Other major differences in the seasonal cycle composites stratified by ENSO phase are primarily manifest as changes in the midsummer rainfall minimum in July-August. For example, very substantial changes in the “midsummer drought” are observed in P3 corresponding to ENSO events. The composite differences in rainfall at the height of the early or late rainy season at P3 are very small, however, the differences in July and August are again on the order of 5 cm- equivalent to ~20% of the rainfall during those months. During the rainy season preceding the peak event, ENSO warm events tend to enhance the “midsummer drought” (reduce precipitation in July-August), while ENSO cold events appear to remove that otherwise prominent feature in the seasonal cycle. During the rainy season following the peak event, the opposite is the case.

The composite evolution of the NINO3 index (Figure 4.19, lower left panel) indicates that SST in the eastern equatorial Pacific is anomalously warm or cold throughout the *entire* rainy season preceding the peak ENSO event. However, in the calendar year following the peak ENSO event, the SST anomaly in the eastern equatorial Pacific decays more rapidly than it grew, hence crossing the zero line by June. Therefore, during the late rainy season following the peak ENSO event, although precipitation changes are noted (e.g., Figures 4.17–4.19), the equatorial SST anomaly is no longer present. One may thus expect that mechanisms linking SST in the eastern tropical Pacific with the rainy season in Central American be different before versus after peak ENSO events. Similarly, how long an equatorial SST anomaly persists into the second calendar year, on a case-by-case basis, might determine the way the eastern tropical Pacific influences that rainy season. Does this explain why *composite* rainfall differences in the rainy season following the peak ENSO event tend to be smaller than those in the rainy season preceding the peak ENSO event?

To further compare the spatio-temporal variability of Central American rainfall with SST in the eastern tropical Pacific Ocean, the leading empirical orthogonal functions (EOFs) and

principal components (PCs) of monthly precipitation (seasonal cycle removed) were computed for Central America from the U-Del precipitation. Shown in Figure 4.20 are the leading two EOFs of monthly precipitation. The first EOF appears to be a rainfall monopole with higher loading from southern Mexico through Nicaragua. The first EOF, which explains 25.5% of the overall variance of monthly precipitation, essentially describes a state of either wet or dry conditions throughout Central America. The second EOF, explaining 12.1% of the variance of precipitation, appears to be a rainfall dipole. When wet conditions prevail north of the Isthmus of Tehuantepec, the opposite conditions prevail from the Yucatan Peninsula through Panama. Strictly to provide a qualitative sense of validation of the U-Del EOFs, shown in Figure 4.21 are regression maps of CMAP precipitation onto the PC time series corresponding to the leading two U-Del precipitation EOFs. The regression maps suggest that the EOF-PC analysis of U-Del precipitation does harmonize within the larger scale picture of the precipitation field as inferred from satellite observations. The precipitation index regions (Figure 4.7) were defined such that P1 and P2 to the northwest were split with P3 and P4 to the southeast at 94°W. The loading pattern of EOF2 confirms that was a good choice, and partially explains why P1 is so independent from P3, and P2 from P4.

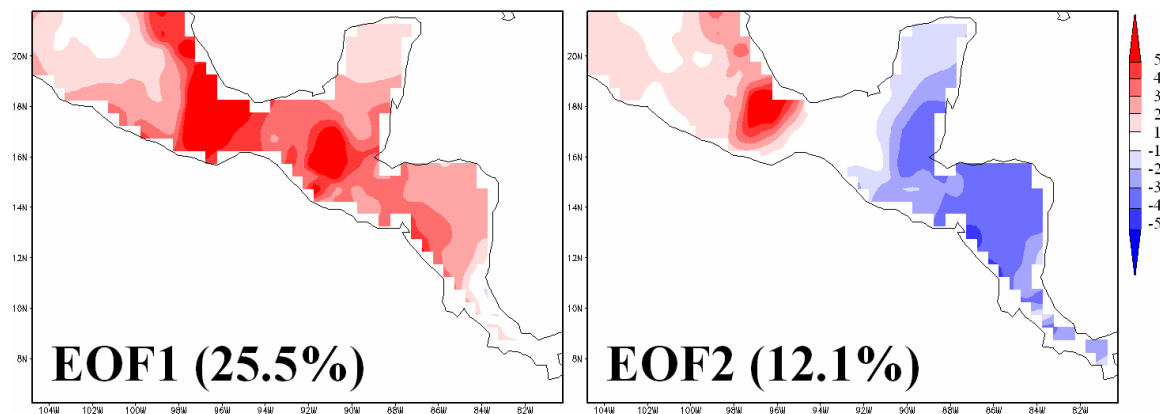


Figure 4.20. The leading two Empirical Orthogonal Functions of monthly precipitation (seasonal cycle removed) from U-Del precipitation (1950-1999), using the domain shown in the figure.

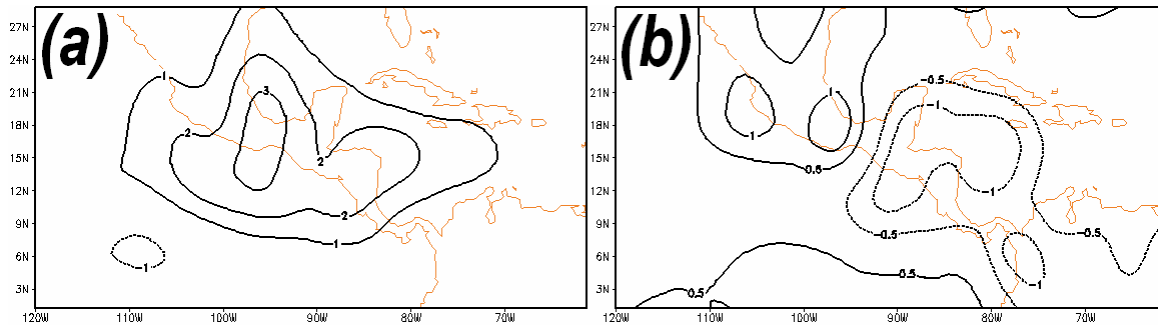


Figure 4.21. Linear regression of monthly CMAP precipitation anomaly (cm month^{-1}) onto the first (a) and second (b) principal components of U-Del precipitation (seasonal cycle removed), 1979-1999.

A depiction of the preferred seasonality of the two EOF patterns shown in Figure 4.20 are displayed in Figure 4.22. Figure 4.22 is a comparison of the variance as a function of calendar month of the principal components matching the EOF patterns shown in Figure 4.20. Both EOFs have higher variance throughout the rainy season as defined in the previous section (May through November), including a midsummer minimum. In fact, the seasonality of PC1 appears very similar to the mean seasonal cycle of precipitation itself. Thus, EOF1 and PC1 represent the interannual modulation of the annual cycle. In contrast, EOF2 shows preference for the late rainy season. In this dipole mode, the peak variance is found in October.

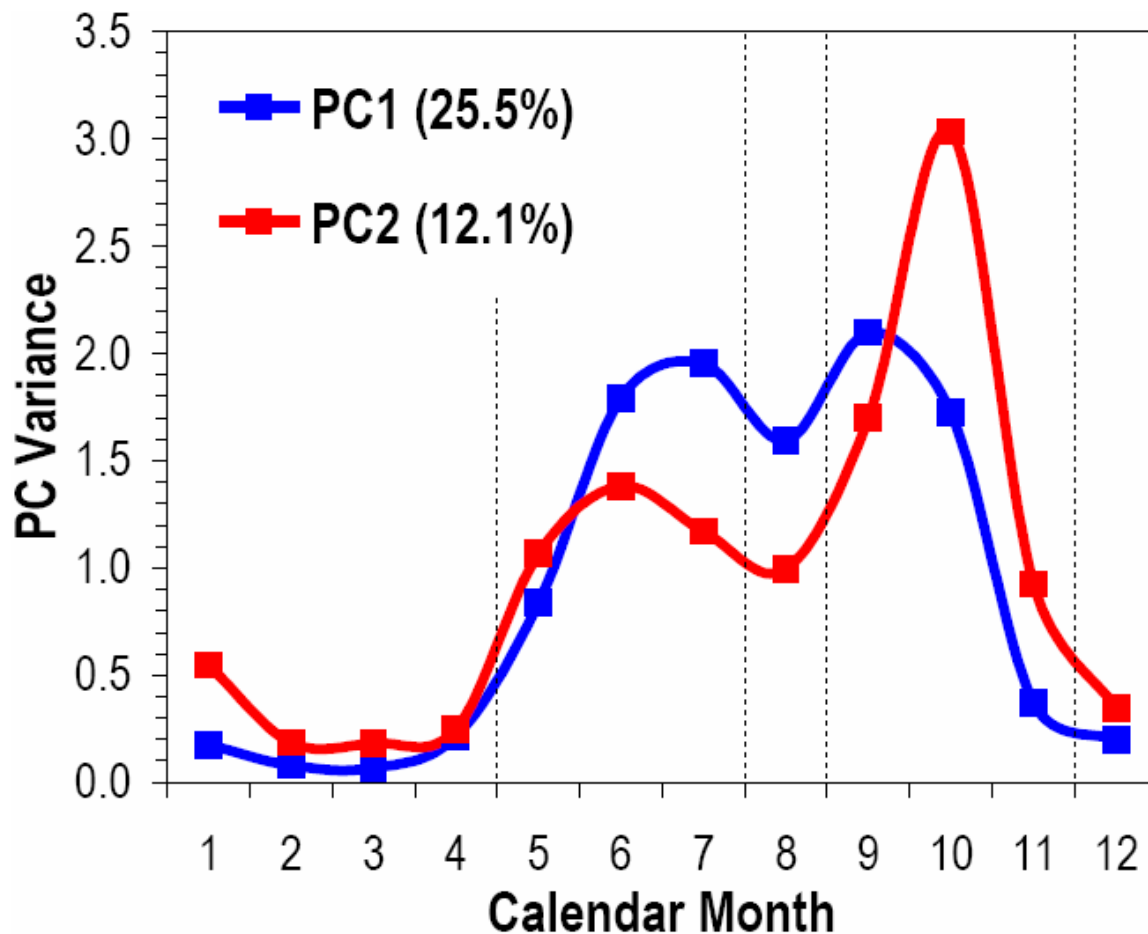


Figure 4.22. Variance as a function of calendar month of the first two principal components of monthly precipitation (seasonal cycle removed) in Central America from U-Del precipitation (1950-1999). Dotted lines denote the early and late rainy seasons as discussed in the main text.

Finally, we compare the time evolution of the two leading patterns of precipitation in Central America with that of equatorial Pacific SST. Shown in Figure 4.23 are time series comparisons of the precipitation PCs and the NINO3 index. Although not visually impressive, statistically significant (90%) correlations are found between the PC2 (full rainy season; not shown) and NINO3, and between the PC2 early rainy season and NINO3 (Figure 4.23c). Again comparing the 1982-83 and 1997-98 El Niño events, none of the PC indices shown in Figure 4.23 appear to have a feature at 1982 or 1983, but all four PC indices do show a strong feature at 1998. By interpreting the EOF patterns (Figure 4.20) and the corresponding PC features (Figure

4.23), the precipitation field in 1998 would be characterized as slightly dry (because $PC1_{early} < 0$) but *more* dry north of the Isthmus of Tehuantepec (because $PC2_{early} < 0$) in the early rainy season, and very wet (because $PC1_{late} >> 0$) but *more* wet from the Yucatan Peninsula southward (because $PC2_{late} << 0$) in the late rainy season.

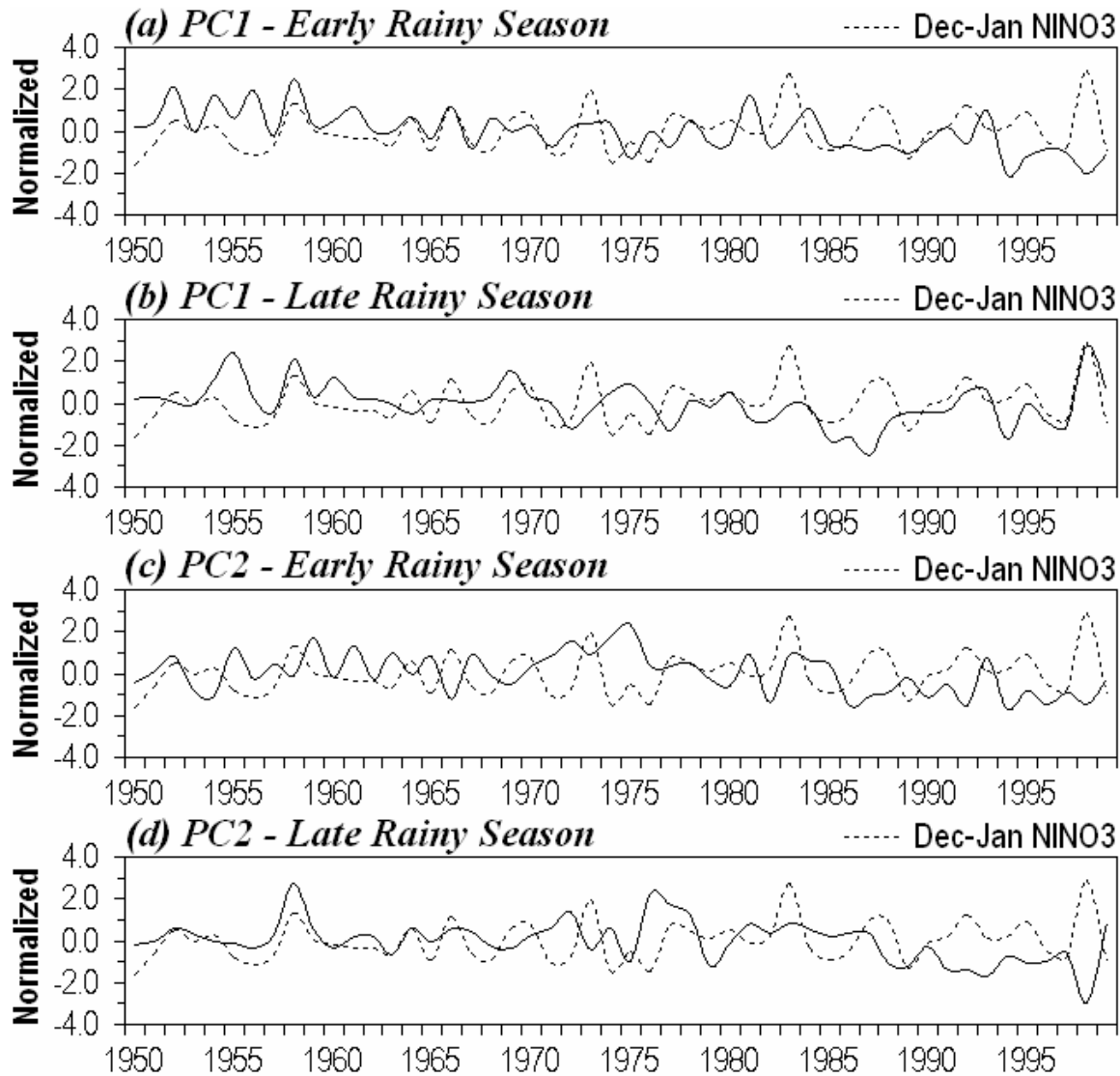


Figure 4.23. Normalized time series of the first principal component of precipitation averaged over the early (a) and late rainy season (b), and the second principal component averaged over the early (c) and late (d) rainy season. Also on each panel (a) – (d) is the December-January mean NINO3 index.

The present section was a presentation of the spatio-temporal variability of precipitation in Central America with comparison to the primary mode of SST interannual variability of the eastern tropical Pacific Ocean. The objective was to highlight observable evidence of a potential role of the EPWP in the interannual variability of Central American rainfall, if only by virtue of interactions with ENSO. No inferences into mechanisms or processes were made regarding the role of the eastern tropical Pacific Ocean, which is the focus of the following section. It is concluded that sufficient observable evidence exists, which is also supported by previous studies (e.g., Hastenrath 1976, 1978, Giannini et al. 2000), to warrant further investigation into the *nature* of the relationship between SST in the eastern tropical Pacific Ocean and rainfall in Central America.

Analyses discussed in sections 4.2-4.3, as well as some of the previous studies, can be used to organize and motivate hypotheses for the role of the EPWP in the interannual variability of rainfall in Central America. Specifically, studies by Hastenrath (1976) and Peña and Douglas (2002), as well as most spatial aspects of the analyses presented thus far would suggest the role of the east Pacific ITCZ deserves closer consideration. Furthermore, further analyses are directed toward understanding what factors influence the unfolding of events and subsequent precipitation anomalies during the rainy season following peak ENSO events.

4.4. On the relationship between SST in the eastern tropical Pacific Ocean and Central American rainfall

The objective of the present section is to describe the primary role of the east Pacific warm pool in the interannual variability of rainfall in Central America. It should be noted that the goal is not to “explain” the full interannual variability of Central American rainfall. Certainly, rainfall in Central America is potentially subject to multiple and nonlinear influences, including that from the Caribbean Sea, broader Atlantic basin, and from the continents situated north and south of Central America. Moreover, multiple temporal scales are likely at play.

Influences from outside the Pacific basin and temporal scales other than interannual are beyond the scope of this chapter. In this section, the specific focus is on understanding the role of the EPWP in the interannual variability of Central American rainfall.

In Chapter 2, the primary mechanisms for the interannual variability of the EPWP itself were described. It was found that the evolution of SST anomaly in the EPWP follows very closely to that of the eastern equatorial Pacific, i.e., it is driven by ENSO. Ocean mixed layer heat budgets and atmospheric analyses indicated that the major process by which the ENSO signal is communicated to the EPWP is by way of an atmospheric link; SST anomalies on the equator strongly modify the distribution of vertical motions in the atmosphere, which helps dictate cloud cover and thus the distribution of shortwave radiation reaching the surface. One could say the EPWP “happens” to be situated beneath the region of the troposphere where vertical motions balance those of the opposite sign over the equator. In the region of interest, this boils down to the meridional variations and strength of the east Pacific ITCZ. The physical interpretation of “ascent over the eastern equatorial Pacific / descent over the EPWP, during an El Niño event” is that the ITCZ is displaced equatorward from its nominal position over the EPWP.

Given that SST in the EPWP is driven by ENSO, it is reasonable to assume that the role of the EPWP in Central American rainfall is primarily as an instrument in the way ENSO events unfold in the northeastern tropical Pacific. During the growth phase of an El Niño event, for example, (which normally includes the rainy season preceding the peak) Central America and the EPWP are both subject to strong tropospheric descent, as the warm equatorial SSTs are forcing the ITCZ southward of its normal position. During that period, one would expect less rainfall in Central America and a warming EPWP. As shown in Figure 4.19 (and supported by previous studies), most of Central America does experience dry conditions during the rainy season preceding the peak El Niño event. Thus, during the rainy season preceding the peak event, the EPWP does not play an important role in the concurrent rainfall anomaly. Both

phenomena are simply responding to the same remote forcing based on equatorial Pacific SST anomalies. However, it will be shown in this section that the EPWP does play a major role in Central American rainfall anomalies during rainy seasons following peak ENSO events. It is hypothesized that, depending on when the equatorial SSTs relinquish control over the ITCZ, the EPWP modulates the strength of the ITCZ which is a major contributor to rainfall over Central America.

Although no two ENSO events are exactly the same, one important commonality is that the variance of SST anomalies in the eastern equatorial Pacific tends to peak during December (see Section 3.4.2). However, there is a large amount of variability in the persistence of the anomaly beyond December. This fact is exemplified in Figure 4.24. Each point in the scatterplot represents one ENSO event, and where the point falls within the Cartesian plane represents its persistence. For clarity, only ENSO events in which the December SSTA exceeded ± 1 standard deviation are shown. For example, points falling within the dashed box in quadrant I represent El Niño events that persisted (maintained an SSTA greater than 0.5°C) into the following July. In contrast, points falling within quadrant IV represent El Niño events in which, by the following July, the SSTA was of the opposite sign by at least 0.5°C (i.e., an antipersisting El Niño). Points that do not fall within any of the four dashed boxes are ENSO events in which the SSTA decayed to near zero by July. What is particularly interesting is that, out of the 13 large ENSO events in the period 1950-1999, the distribution based on this persistence characteristic is spread quite evenly. There were two each of persisting El Niños, decaying El Niños, persisting La Niñas, decaying La Niñas, and antipersisting La Niñas, and three antipersisting El Niños. As will be shown, this is the characteristic of the ENSO event that determines the timing and strength of the impact of the EPWP on the interannual precipitation anomaly during the following rainy season.

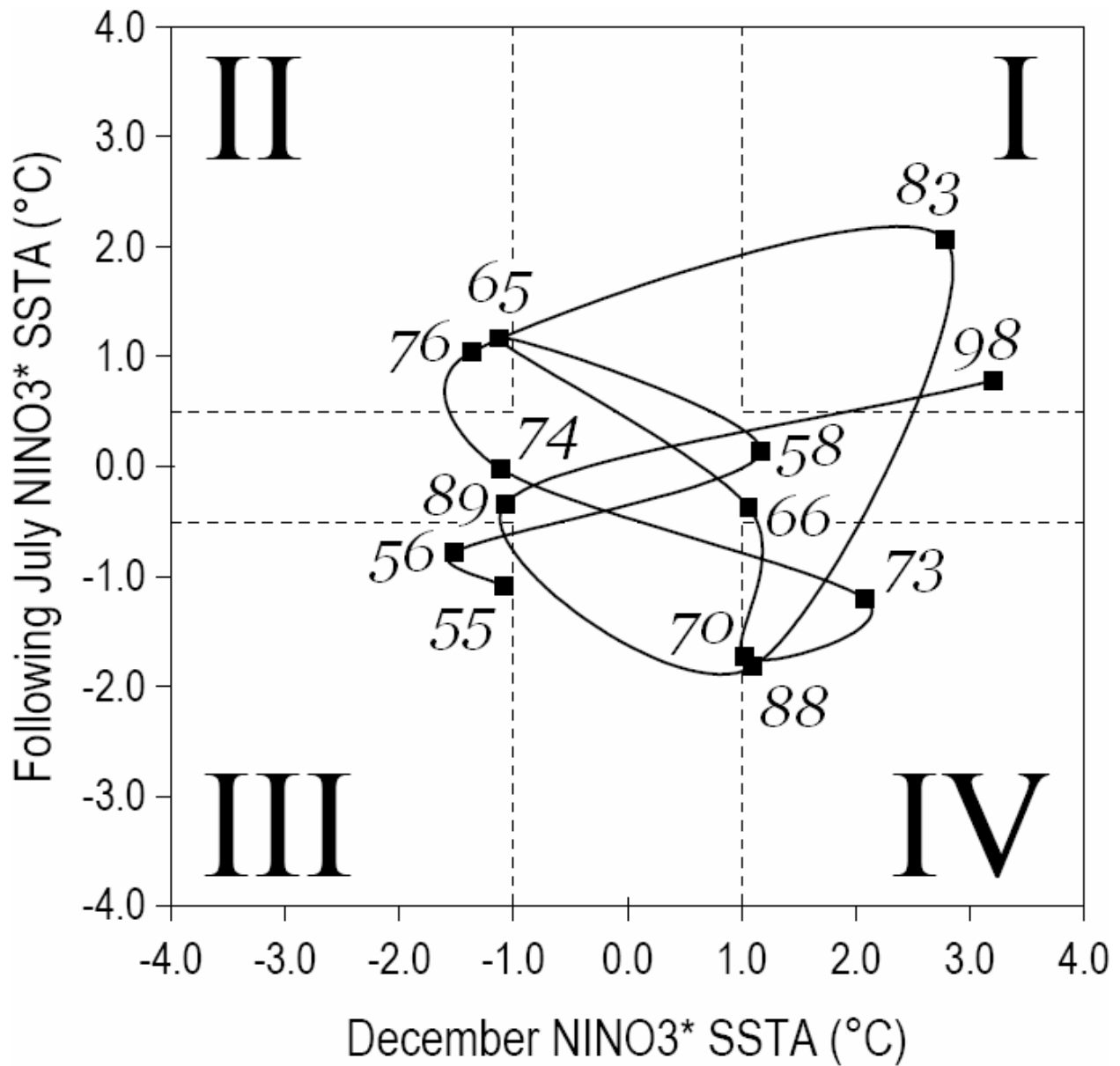


Figure 4.24. Scatterplot of SST anomaly (°C; Reynolds ERSST, 1950-1999) in the NINO3* region (eastern half of the standard NINO3 index region) in December (x-axis) and in the following July (y-axis) for all cases where the December NINO3* SST anomaly exceeded +/- 1 standard deviation. Points falling within dashed boxes I and III are considered “persisting” ENSO+ and ENSO- events, respectively. Points falling within dashed boxes II and IV are considered “antipersisting” ENSO- and ENSO+ events, respectively. Points near zero on the y-axis (not falling within any dashed box) are considered “decaying” ENSO events. The number next to each point indicates the calendar year of following July (“19” omitted).

To help illustrate the interplay between SST, vertical motion, and precipitation anomaly, and where the EPWP fits into that interplay, we examine the unfolding of the 1997-98 El Niño event. The 1997-98 El Niño was chosen because it was quite strong and fell within the period for which CMAP precipitation observations are available. From Figure 4.24, the 1997-98 ENSO event is characterized as a strong, moderately persisting El Niño. The December 1997 SST anomaly in the eastern equatorial Pacific was 3.2°C, and in July 1998 was still 0.8°C. Shown in Figure 4.25 is a schematic of how the SST, vertical motions, and precipitation anomalies are analyzed. SST is zonally averaged across 100°W to 85°W, from 5°S northward to where there is no more Pacific Ocean between that longitudinal band. Vertical motion is analyzed in the same manner, except all the way northward throughout Central America (25°N), using 850 hPa omega from the NCEP Reanalysis, and precipitation anomalies using CMAP with the seasonal cycle removed. The bounds of the zonal averaging were chosen so that they encompass the equatorial belt, the EPWP, and Central America, while minimizing contamination from other basins.

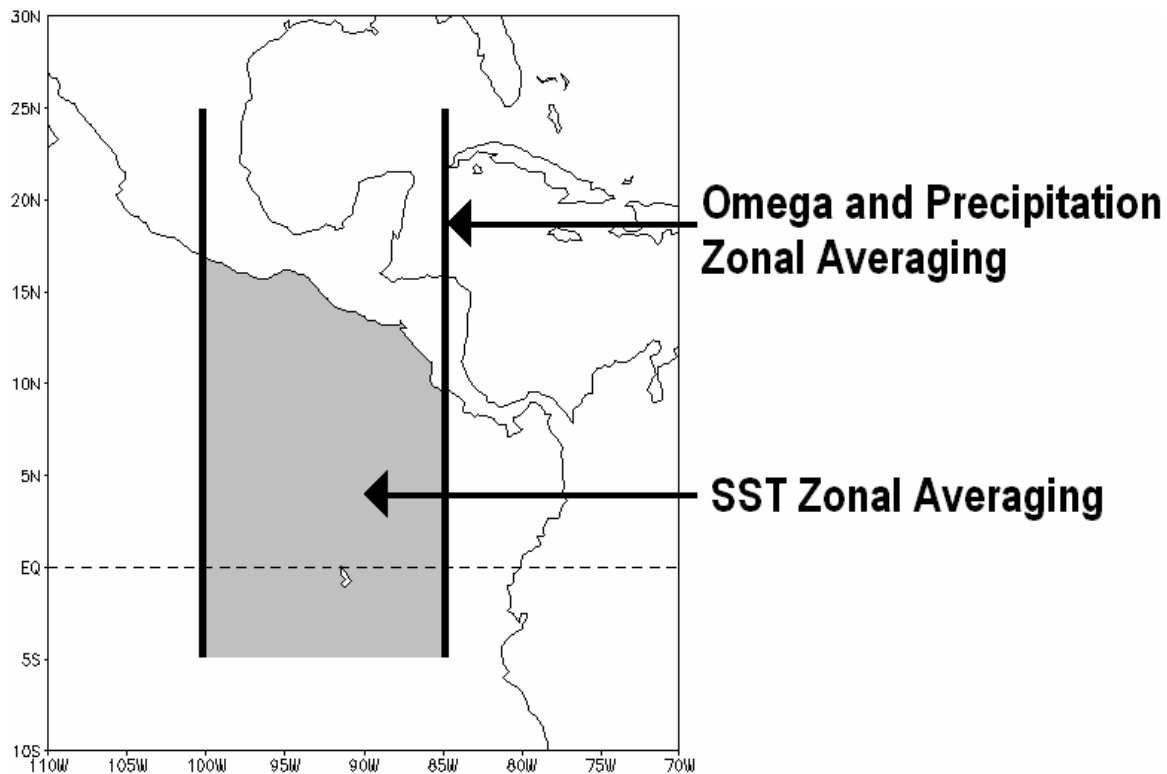


Figure 4.25. Schematic depiction of the time-latitude plots of zonally averaged 850 hPa omega, precipitation anomaly, and SST shown in Figure 4.26. Atmospheric fields (omega and precipitation anomaly) from 5°S to 25°N are zonally averaged between 100°W to 85°W, and SST is zonally averaged between the same limits but ends at ~16°N due to land.

The results for the evolution of SST, vertical motion, and precipitation anomaly are presented in Figure 4.26.¹ The gray region to the north represents latitudes at which there is no Pacific Ocean between 100°W and 85°W. (*It should be noted however, that this does not mean there is no land south of the gray region!*) For reference, the climatological mean (1950-1999) SST and vertical motion is shown in the top left panel. From the climatology panel, it can be seen that the ITCZ (maximum ascent) remains over the warmer waters to the north of the equator throughout the year (i.e., over the EPWP), except during February and March when the ITCZ diffuses and migrates southward in response to a slight seasonal warming (cooling) of equatorial (EPWP) SST. Note that SST in the EPWP and equator are seasonally out of phase. Turning to the progression of SST and vertical motion throughout 1997-98 (Figure 4.26, top right panel), important differences are noted during the rainy season preceding the peak event. During the 1997 rainy season, the developing El Niño causes the ITCZ to be displaced southward toward the equator. Also, the meridional gradient of vertical motion is more diffuse than the climatology, and the magnitude reduced. A weaker, more diffuse, and southward-displaced ITCZ is the result. Hence Central America tends to receive less rainfall during rainy seasons preceding El Niño events. At the same time, SST in the EPWP is warmer than normal. If the EPWP were playing a major role in the rainy season preceding the peak ENSO event, it would be forcing a thermally direct circulation and thus increase the overlying tropospheric ascent. As previously mentioned, during this time the EPWP and vertical motions over Central America are

¹ Although the omega dataset is the same (NCEP Reanalysis), some inconsistency with Figure 2.22 is to be expected; recall the omega depictions in Figure 2.22 are cross-sections directly along 100°W, while the omega depiction in Figure 4.26 is zonally averaged between 100-85°W.

simply being driven by the same, overwhelming remote influence (i.e., anomalously warm equatorial SST). However, based on the same argument- that vertical motions in the tropics tend to follow the warmer SSTs, it is likely that the ITCZ would be shifted even further southward toward the equator if the EPWP weren't anomalously warm during that time. In this sense, it could be speculated that the EPWP serves to buffer the otherwise-higher-amplitude effect of ENSO on the vertical motions over Central America during rainy seasons preceding peak ENSO events.

During the rainy season following the peak of the 1997-98 El Niño, a very different story emerges. After July 1998, as the equatorial SST returns to normal, the EPWP is still anomalously warm. Recall from Section 2.3 that the NINO3-EPWP cross-correlation exceeds the NINO3 autocorrelation after month 4, and does not decay beyond e^{-1} until month 9. When the ITCZ finally moves northward toward its nominal boreal summertime position, a rapid enhancement of the ITCZ is triggered by the very warm EPWP ($SST > 29^{\circ}\text{C}$; Zhang 1993). This can be seen by the strong gradient of vertical motion along the temporal axis coinciding with the warmest SSTs between 5°N and land. The core of the ITCZ is roughly 22% stronger than normal in the late rainy season of 1998. Throughout this process, the EPWP is expending energy and thus cooler SSTs emerge at the same point on the temporal axis as when the ITCZ ceases to intensify. Again referring to the cross- and autocorrelation analyses in Section 2.3, this is consistent with the more rapid decorrelation of the EPWP index within the first few months; ocean-atmosphere energy exchange beneath the ITCZ is expediting the decay of the positive SST anomaly in the EPWP. As a natural characteristic of a “persisting” ENSO event, there is no cold SST anomaly on the equator to contribute to the northward displacement or enhancement of the ITCZ (Figure 4.26; compare equatorial SST in July-December 1998 versus the climatology panel). Thus, the response of the ITCZ was forced locally by the EPWP.

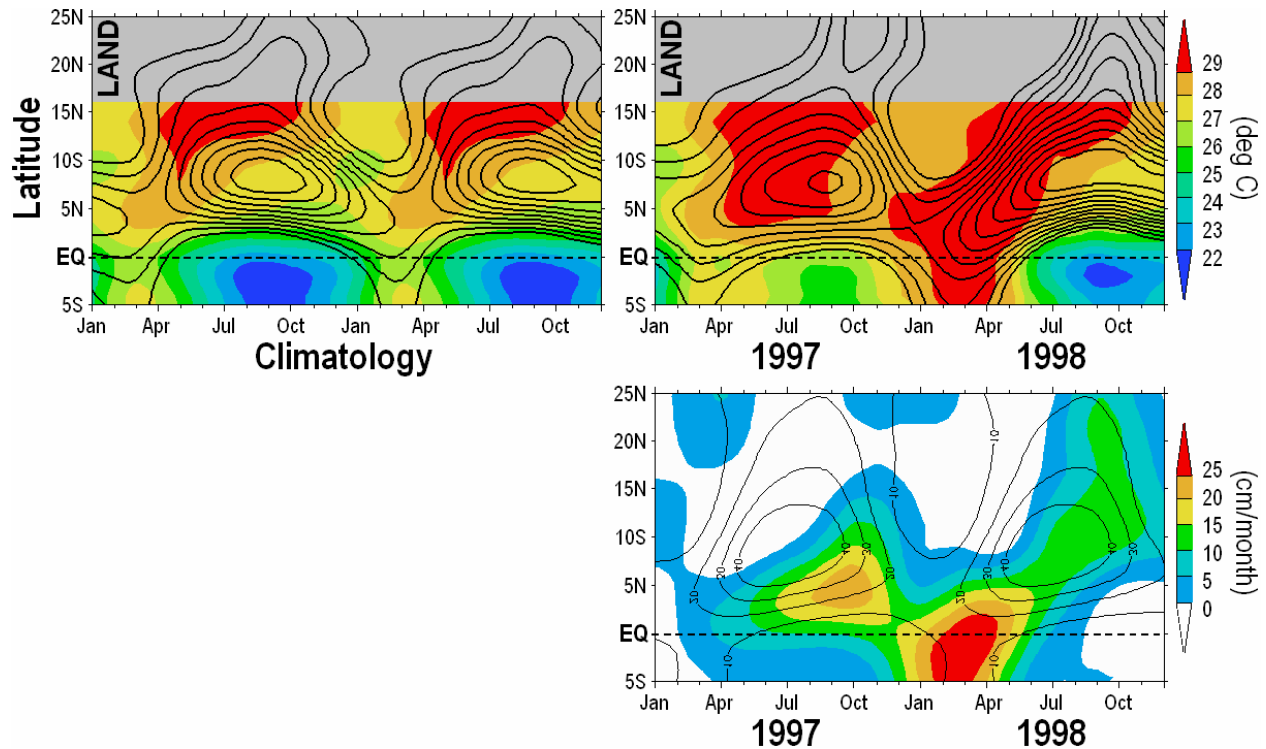


Figure 4.26. Top: Time-latitude plot of SST ($^{\circ}\text{C}$; shaded; Reynolds ERSST) and 850 hPa $-\omega$ (Pa sec^{-1} ; contour interval 0.01 Pa sec^{-1} beginning at 0.01 Pa sec^{-1} [negative contours omitted]; NCEP Reanalysis) for the 1950-1999 climatology (left) and 1997-98 period (right) zonally averaged between 100°W - 85°W . Bottom: Time-latitude plot of CMAP precipitation anomaly (cm month^{-1} ; shaded) and climatology (cm month^{-1} ; contour interval 10 cm month^{-1} beginning at 10 cm month^{-1}) averaged between 100°W - 85°W .

During boreal summer 1998, the meridional gradient of vertical motion on the south edge of the ITCZ is sharpened, and on the north edge is more diffuse. As can be seen in the gray region north of the SST data, this translates into a northward propagation of the intensification of the ITCZ well into Central America north of the EPWP. Finally, the much intensified ITCZ lasts beyond December 1998 (off the graph). The implication for precipitation anomalies in the late rainy season is obvious: just after the ITCZ undergoes a rapid and northward intensification, precipitation between latitudes 5 - 25°N is up to 75% higher than normal (Figure 4.26, bottom right panel).

To illustrate the spatial distribution of the land precipitation anomaly at the height of the late rainy season in 1998, shown in Figure 4.27 (4.28) is the U-Del precipitation anomaly (NCEP 850 hPa vertical motion anomaly) for October 1998. The precipitation anomaly is up to 50 cm along the Pacific Coast of Central America, strongest in the P3 rainfall region. If any portion of the precipitation anomaly over Central America in October 1998 were due to an influence from the Caribbean, and *not* due to the SST-enhanced east Pacific ITCZ, one would expect to observe the precipitation anomalies hugging the Caribbean coast of Central America, or at the very least see similar rainfall or ascent anomalies elsewhere in the Caribbean. On the contrary, *no* rainfall anomalies greater than 10 cm are observed anywhere else in the Caribbean basin even though U-Del data exists for most of the Caribbean including Cuba and Hispaniola. The spatial pattern of the precipitation anomaly is also consistent with the enhanced ITCZ uniquely located over the EPWP (Figure 2.28).

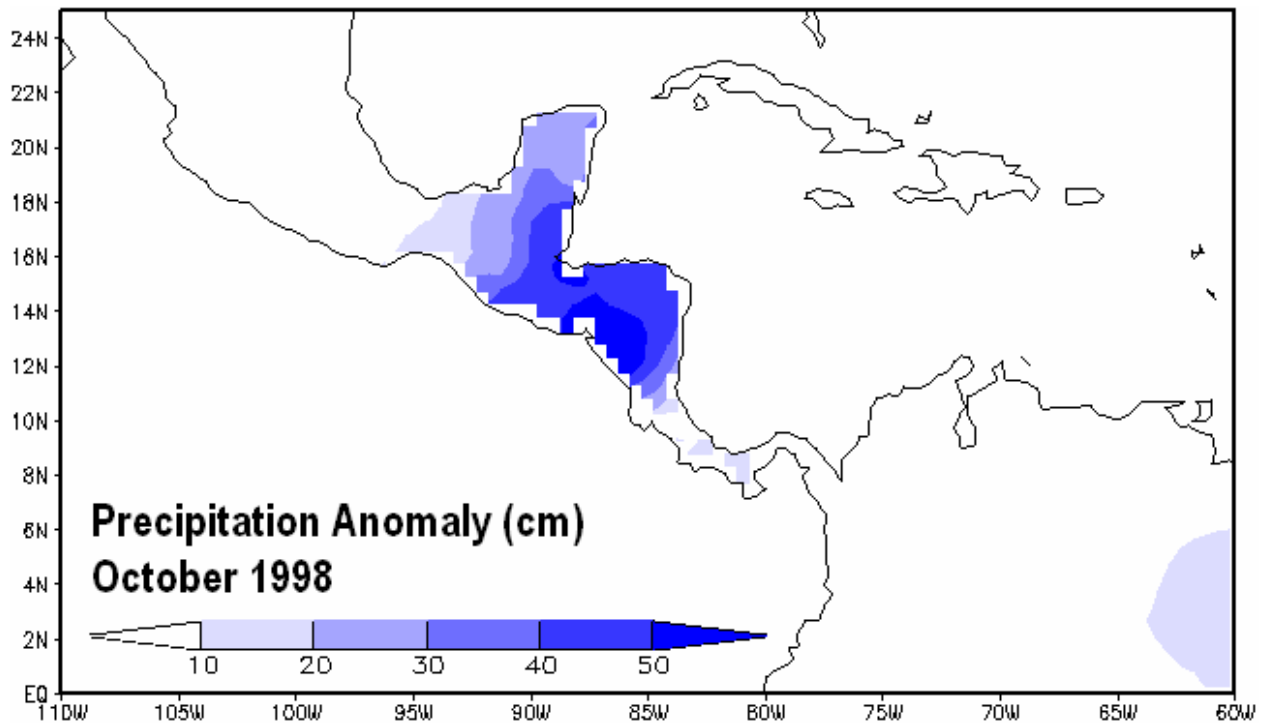


Figure 4.27. U-Del precipitation anomaly (cm) for October 1998.

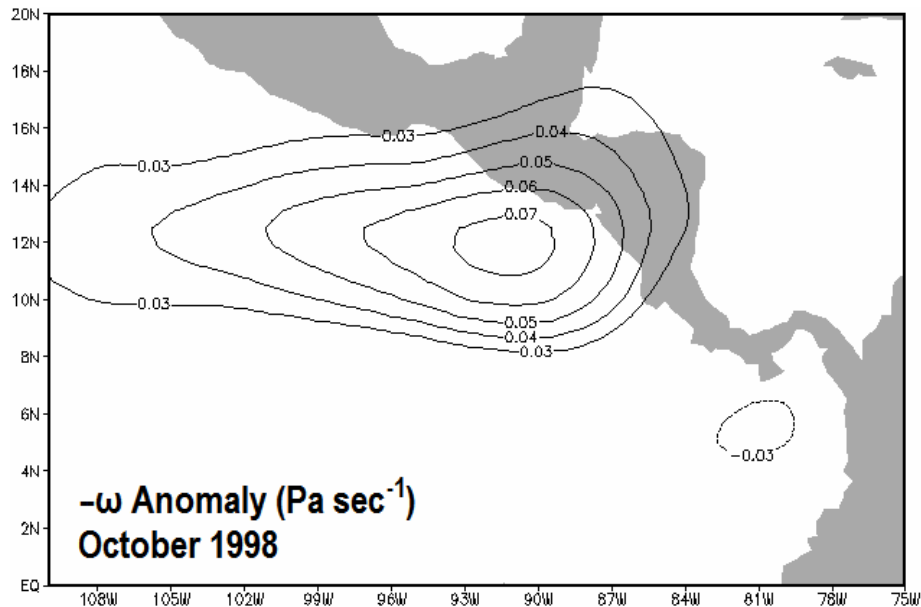


Figure 4.28. 850 hPa $-\omega$ (Pa sec⁻¹; contour interval 0.01 Pa sec⁻¹ beginning at 0.03 Pa sec⁻¹; NCEP Reanalysis) for October 1998.

As discussed in Chapter 1, tropical cyclones are beyond the scope of this dissertation. However, for those familiar with the hurricane season of 1998, it would be reasonable to question whether or not tropical cyclones have an appreciable effect on the results presented in this section. The short answer is that they do not, but for good measure, this issue is addressed in detail in Appendix C.

The specific role of the EPWP in the interannual variations of rainfall in Central America has been identified as a modulation of the strength of the ITCZ, being most important in rainy seasons following peak ENSO events. In the case of the 1997-98 El Niño, which was a strong and “persisting” ENSO event, the ITCZ intensified and resulted in a large rainfall anomaly somewhat later in the year (the late rainy season). Returning to the differences in ENSO events based on their persistence characteristics, it would thus follow that ENSO events which do not persist well into the rainy season might produce rainfall anomalies by the same mechanism earlier in the year. Composite seasonal cycles of precipitation before and after the ENSO events represented in Figure 4.24 (i.e., stratified by warm or cold and persisting or antipersisting) were

constructed for each of the Central American precipitation indices P1–P5. The results, compared with the climatological mean (1950–1999) seasonal cycles, are shown in Figure 4.29.

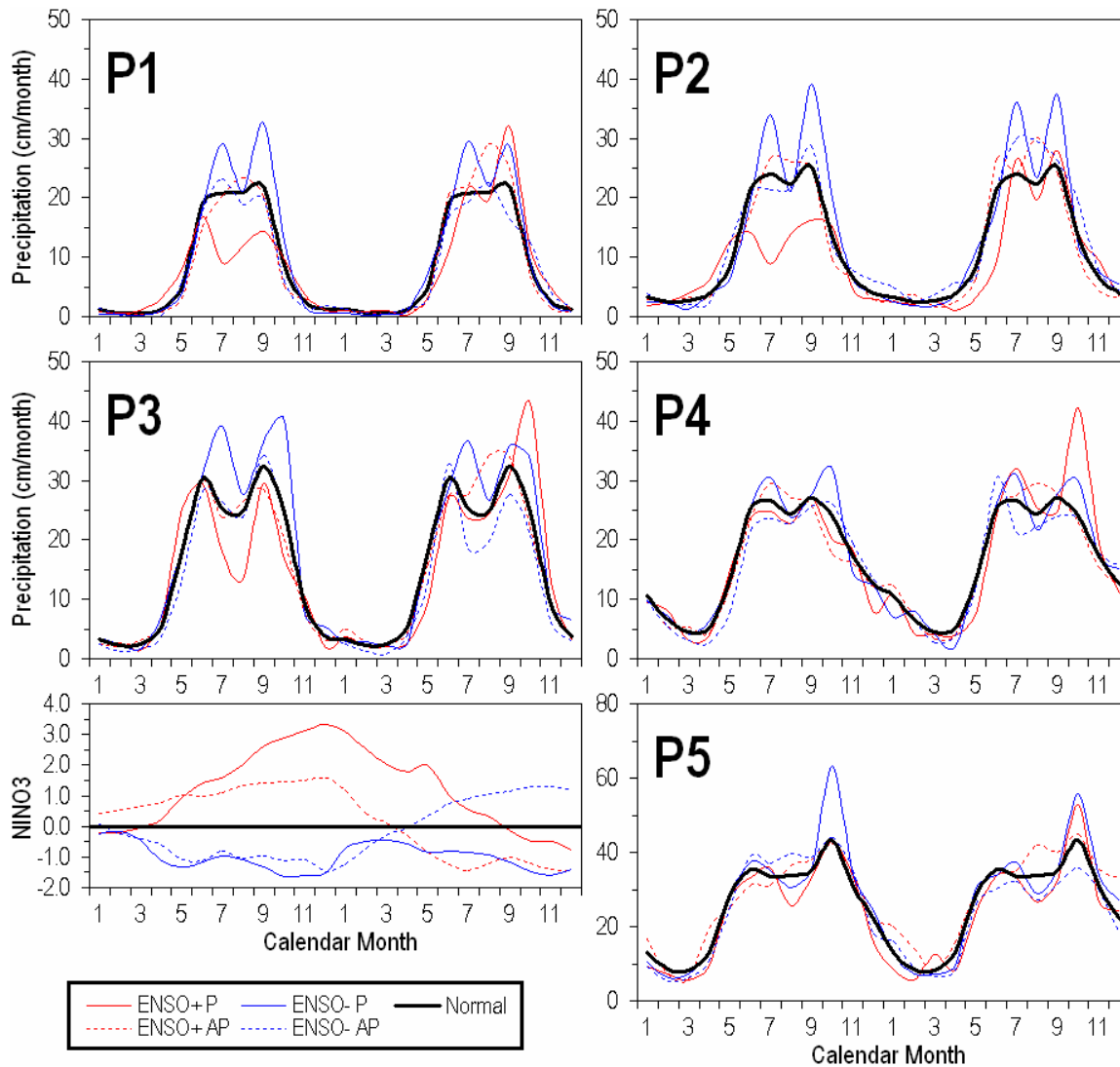


Figure 4.29. Composite seasonal cycles of monthly U-Del (1950–1999) precipitation (cm month⁻¹) in Central American index regions P1–P5 for ENSO events stratified by warm (+; red), cold (–; blue), persisting (P; solid), antipersisting (AP; dashed), and climatology (heavy black). The composite calendar years before and after the peak of the ENSO event are shown. The corresponding composite evolutions of NINO3 SST anomaly (°C) are shown in the lower-left corner.

In each of the Central American regions, it can be seen that rainy seasons preceding peak El Niños are anomalously dry, and rainy seasons preceding peak La Niños are anomalously wet.

This observation is less clear in P4, which highlights further difference between P3 and P4, which are merely adjacent regions on either side of a very narrow landmass. During the rainy seasons *following* peak ENSO events, however, the evolution as stratified by persisting or antipersisting ENSO events is exactly as expected from the SST-enhanced east Pacific ITCZ mechanism. Focusing on P3 (each region looks similar with respect to the following discussion), persisting El Niños result in slightly reduced precipitation in the early rainy season, normal precipitation in the midsummer minimum, and much increased rainfall in the late rainy season. The fact that the large peak in the late rainy season is not evident in P2 is actually consistent with the SST-enhanced east Pacific ITCZ mechanism; P2 is by far the most remote region from the EPWP. In contrast, antipersisting El Niños result in a positive rainfall anomaly toward the middle of the rainy season (or during the midsummer minimum). This occurs because the equatorial SST anomaly retreats earlier, releases the ITCZ northward earlier, thereby allowing the ITCZ to pass over the anomalously warm EPWP and intensify earlier. The mechanism is the same, but the timing depends on the persistence characteristic of the ENSO event.

Quite telling is the fact that the midsummer rainfall anomaly associated with the antipersisting El Niño events is not as large as the late rainy season rainfall anomaly associated with the persisting El Niño events (again, only in regions P1, P3, P4 and P5). Since the persistence of the El Niño event dictates how much time the EPWP receives anomalous shortwave radiation, the longer the El Niño event persists- the warmer the EPWP will be when the ITCZ eventually *does* migrate northward. This concept is analogous to a slingshot, where the elastic band is the ITCZ, the projectile is rainfall, the hand pulling the band is ENSO, and the target is Central America. The longer the hand (ENSO) pulls back on the band (the ITCZ), the greater the tension in the band (the warmth of the EPWP) will become. If the hand releases sooner, the projectile will arrive at the target sooner but with less force. If the hand pulls back longer before releasing, the projectile will arrive at the target later but with greater force.

4.5. Summary and implications for predictability

Almost all previous studies on the interannual variability of rainfall in Central America have focused on the broader Caribbean region. One of the first outcomes of the present chapter was a strong sense of heterogeneity within Central America; let alone what that implies about the Caribbean region as a whole. This observation, analyses of composite precipitation fields over and near Central America, and the work of Peña and Douglas (2002) which focused on the Pacific coast of Central America, motivated a hypothesis that the interannual variability of rainfall in Central America might be explained mechanistically different than that of the Caribbean. The present study complements the work of Hastenrath, Giannini, and Peña and Douglas by providing a more comprehensive understanding of the role of the eastern tropical Pacific Ocean in the interannual variability of Central American rainfall, including the as-yet underestimated role of the EPWP.

The major goals of the present chapter were to describe the scales of interannual variability of precipitation in Central America and understand the role of SST in the eastern tropical Pacific Ocean, with particular focus on the EPWP. The fact that one of the major outcomes of Chapter 2 was that the EPWP is driven by ENSO, and through an atmospheric field that also strongly influences precipitation, proposed mechanisms connecting the EPWP with rainfall variations in Central America could never have been framed independently of ENSO. In fact, interannual rainfall variations occurring in rainy seasons preceding peak ENSO events are an example of such codependence; the EPWP has no major role in those rainy seasons because both the EPWP *and* rainfall are being strongly forced by the same “third-party” phenomenon (SST anomalies on the equator).

However, the EPWP does play a major role in rainy seasons *following* peak ENSO events. This is consistent with Section 2.3; the EPWP tends to lag ENSO and propagate SST anomalies originating on the equator forward in time. Furthermore, the correlation between EPWP SSTA and NINO3 as a function of calendar month reveals that, from April through June,

the correlation is smaller than the correlation when all months are included (0.61 in April versus 0.72 overall). This suggests that, on average, boreal spring is when the EPWP and equator begin to diverge in terms of SST anomaly. Depending on when the equatorial SST anomaly retreats and allows the ITCZ to resume its seasonal march northward, the EPWP acts to trigger a rapid enhancement of the ITCZ as seen in such fields as vertical motions. The rapid enhancement occurs over the warmest SSTs in the EPWP, and eventually leads to a cooler EPWP. As the persistence of the ENSO event tends to correspond with the magnitude of the eventual precipitation anomaly in Central America, the SST-enhanced east Pacific ITCZ mechanism can be thought of like a slingshot. The longer equatorial SSTs force the ITCZ southward, the longer the EPWP is subject to anomalous shortwave radiation, and the greater the intensification of the ITCZ will be once it migrates northward over the EPWP. The critical aspect of this mechanism is the relative timing of SST anomalies between the equator and the EPWP.

These results seem to suggest that improvements in the prediction of rainfall over Central America will depend on improvements in the ability to predict when an ENSO event will retreat. If, in December, one knows the magnitude of the SST anomaly in the NINO3 region, then one presumably knows the approximate magnitude of the *peak* SST anomaly associated with that ENSO event. If one has a forecast of how far into the following calendar year that anomaly will persist, however, then one could conceivably make a useful prediction of the rainfall anomaly in the upcoming year, including its timing. In a place like Central America, where the seasonal cycle of rainfall has a marked bimodal distribution, the difference between a rainfall anomaly in August versus in October has important societal implications. To know that the midsummer minimum will be not a minimum at all, but a wet spell, could help guide the agricultural sector which hedges its investments annually based on the midsummer minimum. Similarly, to know that the midsummer minimum will be especially dry, but shortly thereafter will be a considerable wet spell could be very useful to those involved in both agriculture *and* disaster management, as Central America is especially prone to landslides.

The SST-enhanced east Pacific ITCZ mechanism is applicable to the problem of predictability of Central American rainfall. As evident in the sensitive time-dependent relationships between equatorial SST, the overlying atmosphere, SST in the EPWP, and, once again, the overlying atmosphere, a simple index of, say, SST would be of little use. Put very generally, rainfall depends on two factors: water vapor availability and a lifting mechanism. One of the many possible lifting mechanisms is ascent associated with the ITCZ. The results of Section 4.4 describe a mechanism which can modulate the strength of that lifting mechanism.

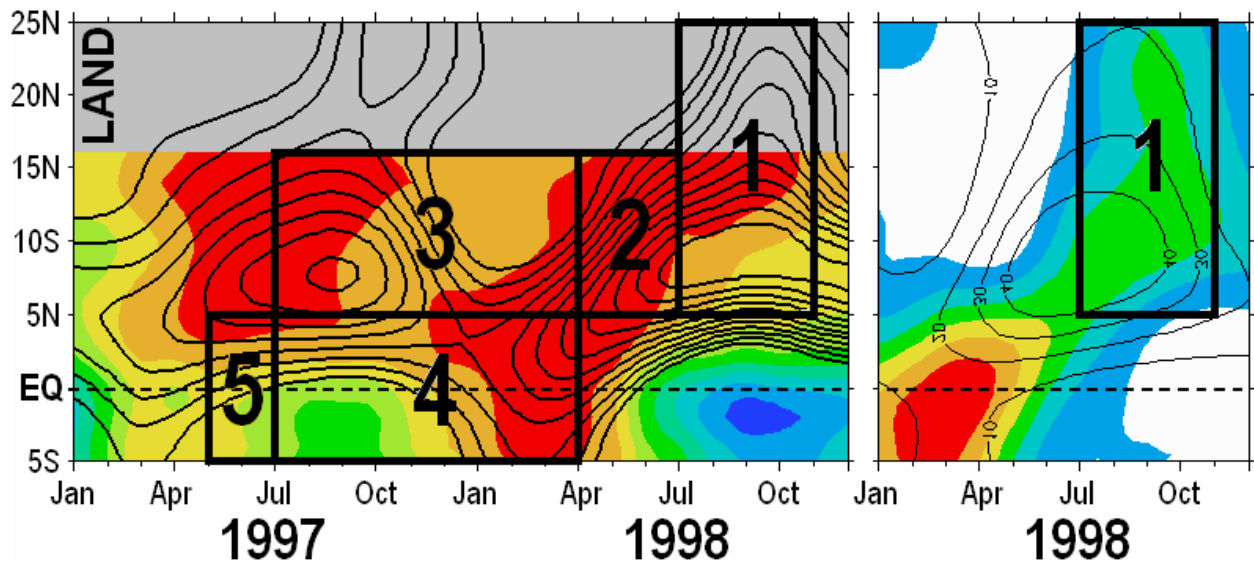


Figure 4.30. Reproduction of the right two panels of Figure 4.26, annotated with numbered boxes discussed in main text.

Regarding the applicability of the results of the present chapter to the problem of predictability (and climate monitoring and diagnostic analysis), the following is offered, which refers to Figure 4.30:

- a. To predict rainfall at [1], one must predict ω at [1];
- b. To predict ω at [1], one must predict $\partial\omega/\partial t$ at [2];
- c. To predict $\partial\omega/\partial t$ at [2], one must predict SST at [2];

- d.* To predict SST at [2], one must predict $d(\text{SST})/dt$ at [3];
- e.* To predict $d(\text{SST})/dt$ at [3], one must predict SSTA at [4];
- f.* To predict SSTA at [4], one must use SST at [5] as part of the set of initial conditions to be applied to a statistical or coupled general circulation model.

Statements *a-c* follow primarily from the results of the present chapter, and statements *d-e* follow primarily from the results of Chapter 2. Results in Chapter 3 have implications for statement *f*. As a prediction plan, the above statements are highly simplified and, for a perfect prediction, must assume that the SST-enhanced ITCZ is the only mechanism that can cause interannual variations in Central American rainfall. In practice, of course, several other factors require attention. However, it was established that the SST-enhanced ITCZ mechanism is dominant on interannual timescales, and serves to connect ENSO with Central American rainfall.

Recall the question posed in Section 4.3: “Knowing that the 1982-83 and 1997-98 ENSO events were both strong El Niño events, and had similar magnitudes in terms of SST anomaly, how can one so strongly affect Central America but the other not?” From Figure 4.24 in Section 4.4, both events were objectively characterized as persistent El Niños, based on the criterion that the NINO3 SST anomaly in the following July remain at least $+0.5^{\circ}\text{C}$. Shown in Figure 4.31 are the time series of NINO3 SSTA throughout 1982-83 and 1997-98, relative to the mean seasonal cycle of rainfall in the P3 region. Although both events were “persistent,” the 1982-83 event persisted *longer*- apparently just long enough to miss the late rainy season completely. With respect to predictability, clearly one critical aspect of the SST-enhanced east Pacific ITCZ mechanism is how long the ENSO event is expected to persist.

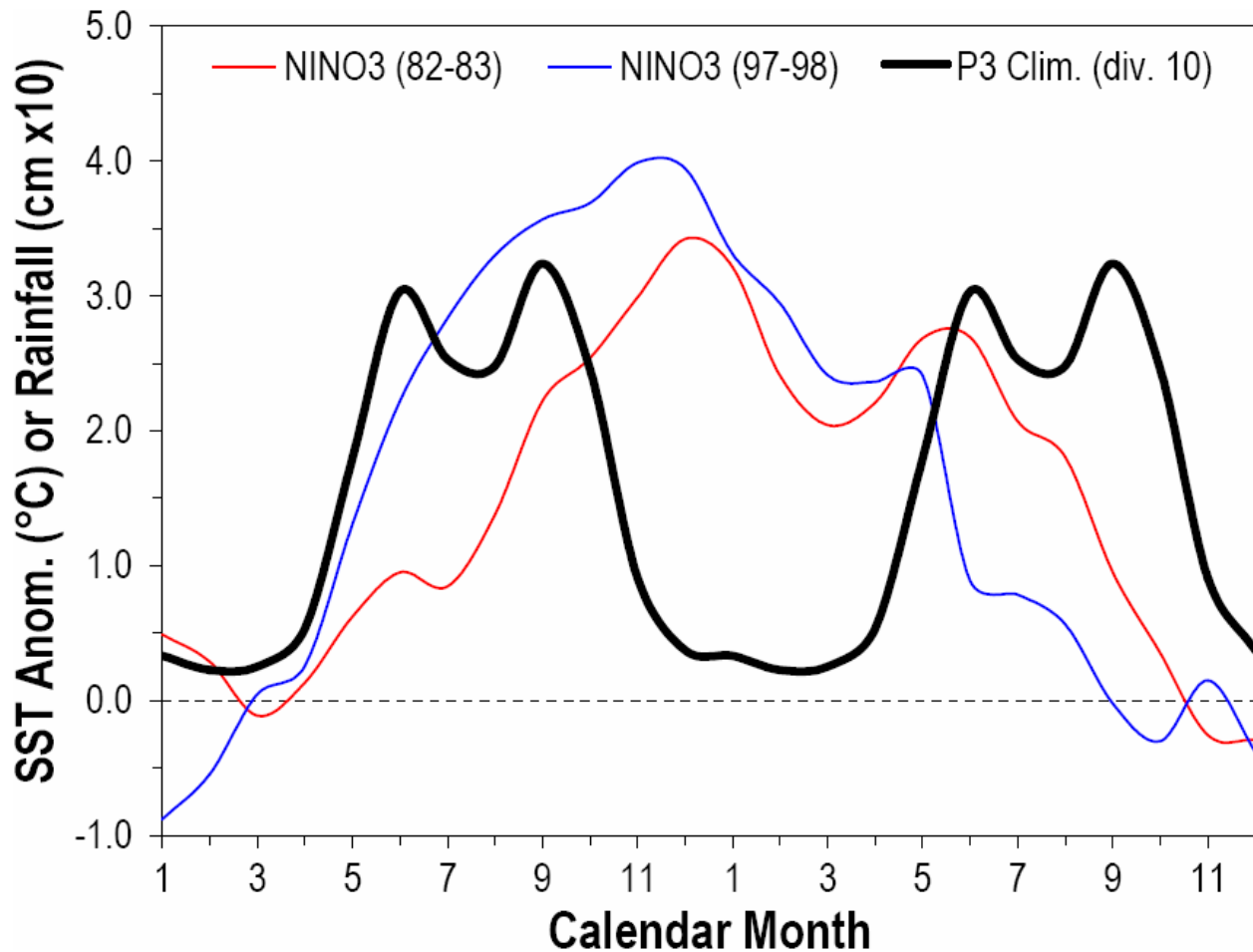


Figure 4.31. NINO3 SST ($^{\circ}\text{C}$; ERSST) throughout 1982-83 (thin red line) and 1997-98 (thin blue line), and the mean seasonal cycle of U-Del rainfall (10^{-1} cm). Base period 1950-1999 used for SST anomalies and rainfall climatology.

From the preceding discussion of predictability, two important inferences regarding seasonal and interannual prediction of Central American rainfall can be extracted by this simple prediction plan. For *interannual* prediction of Central American rainfall, predictive skill relies heavily on the skill of ENSO forecasts, especially amplitude and persistence into the following rainy season (follows statement *f*). Interannual predictions, including those for analogous regional tropical climates, also depend on the quality of the representation of regional tropical atmospheric circulation cells of only a few degrees in horizontal scale (follows statements *a-e*). For example, if the representation of the atmospheric mechanism connecting equatorial SST

with SST in the EPWP is deficient, or SST in the EPWP is not coupled correctly with the overlying vertical motion field, then the model and thus prediction cannot account for one of the dominant mechanisms influencing the interannual variability of Central American rainfall.

Finally, *seasonal* prediction of Central American rainfall depends critically on climate monitoring capabilities in the eastern tropical Pacific region, particularly *north* of the equator. Assuming a “seasonal” prediction means it is late winter or early spring, and one wishes to make a prediction for the upcoming rainy season, then one absolutely requires high quality observations of SST and other relevant variables that serve to couple the lower troposphere to the tropical sea surface. Provided high quality observations of SST in the equatorial *and* northeastern tropical Pacific, it can be demonstrated that there is potential for rainfall predictions several months in advance without the use of a coupled GCM. Based on the notion that the timing between SST anomalies on the equator and in the EPWP is the critical factor in determining the timing and strength of the SST-enhanced ITCZ, a simple index can be defined as the difference between normalized SST anomalies in the EPWP and the NINO3 region. The rationale is that the Δ SSTA index will be positive if the EPWP is anomalously warm, but can be overruled if the eastern equatorial Pacific is also anomalously warm. In other words, the most important variable is SST in the EPWP *at* the point in time when the equatorial SST anomaly is returning to zero, which is precisely what Δ SSTA captures. It is thus not surprising that the best match between Δ SSTA and P3 rainfall is found when Δ SSTA leads by 4 months.

Shown in Figure 4.32 is the Δ SSTA index (shifted 4 months forward in time), and the P3 rainfall anomaly index. Data outside the rainy season (May-November) are omitted. Comparing the P3 rainfall anomalies with the Δ SSTA index (versus with the NINO3 index alone; also shown in Figure 4.32) suggests that the Δ SSTA index provides critical and unique information, including the anomalous SST in the EPWP, particularly at the point in time when the equatorial SST anomaly retreats and allows the ITCZ to migrate northward over the EPWP. Combined with coupled model forecasts of the evolving SST field and regional atmospheric

response (i.e., the ITCZ), it is suggested that seasonal predictions of Central American rainfall could benefit from (a) explicit consideration of the SST-enhanced east Pacific ITCZ mechanism, and (b) improved and sustained *in situ* observations of SST in the eastern equatorial and northeastern tropical Pacific Ocean. An in-depth, practical analysis of the potential predictability of Central American rainfall from information such as that provided by the Δ SSTA index, in tandem with other considerations (e.g., the state of the Caribbean sector), is an important area of opportunity for future work.

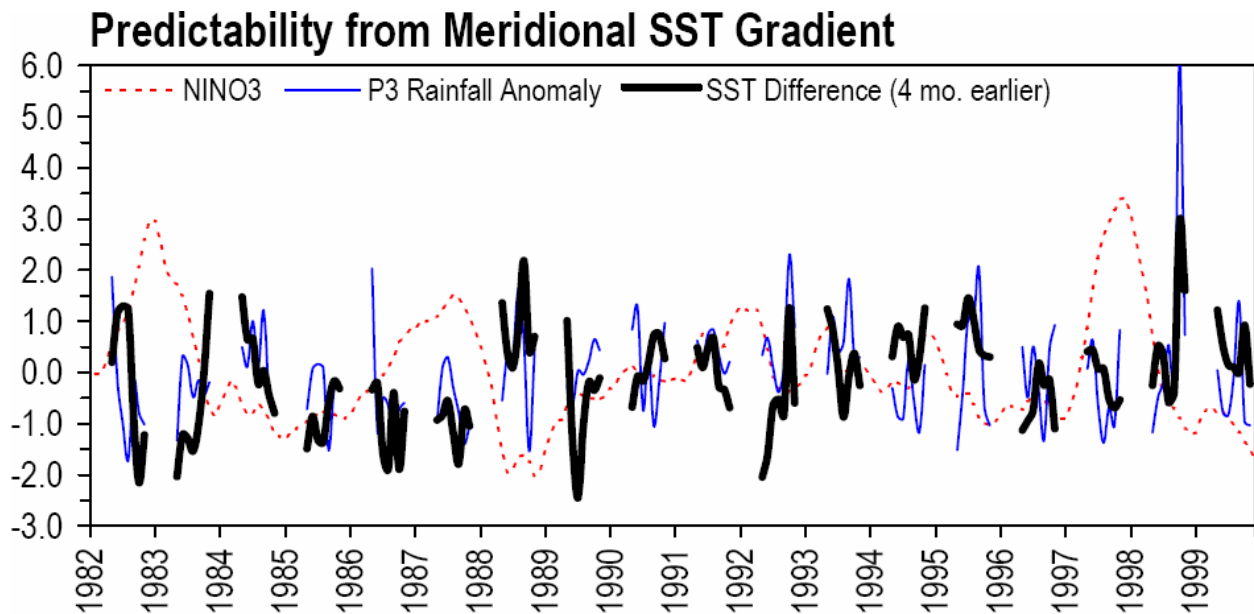


Figure 4.32. Normalized time series of the NINO3 index (dashed red), P3 rainfall anomaly (thin blue; only May–November shown), and Δ SSTA four months earlier (heavy black). Δ SSTA is defined as the difference between normalized SST anomalies in the EPWP and NINO3 region using Reynolds OI v.2 SST.

The TAO array in the eastern tropical Pacific extends to 95°W, which is probably far enough east to be useful in the prediction of Central American rainfall from the perspective described in the present chapter. However, data availability north of 8°N is extremely limited. The availability of SST observations at 95°W was discussed in Section 2.3; the availability of collocated shortwave radiation observations is similar (spans 2000 through 2003). SST

observations at 95°N, 8°W have since resumed, but it would be worthwhile to extend ongoing measurements to 10°N and 12°N as well, including shortwave radiation. Although it is understood that moorings in close proximity to the coast and in popular fishing regions are problematic for numerous reasons, such *in situ* observations would be very helpful for monitoring and predicting Central American rainfall. Advances in high-resolution satellite remote sensing, such as microwave SST observations from TRMM and AMSR-E, and passive estimates from sensors like MODIS, can make up for some deficiencies in *in situ* observing platforms. However, “ground” validation of satellite observations are necessary because even modern satellite retrievals are affected by heavy precipitation. Finally, with respect to the SST-enhanced east Pacific ITCZ mechanism, more work dedicated to understanding and observing the Central American gap winds is warranted, given their strong ability to modulate the flux of energy from the EPWP to the overlying troposphere.

Chapter 5: Summary and Concluding Remarks

The overall focus of this dissertation was the interannual variability of sea surface temperature in the eastern tropical Pacific Ocean, and the impact of that variability on rainfall in Central America. The eastern tropical Pacific Ocean includes the EPWP and the equatorial Pacific cold tongue. Although this work was originally intended to focus primarily on the EPWP, results clearly necessitated broadening the focus to also include processes in the eastern equatorial Pacific.

Chapter 2 was aimed at identifying the physical oceanographic and atmospheric processes governing the interannual variability of SST in the EPWP. Analysis of SST from satellite observations and a forced ocean model clearly indicated that SST in the EPWP is closely tied to ENSO. The majority of the interannual variability of SST in the EPWP is, in fact, explained by ENSO. Given the close proximity of the EPWP to the equatorial Pacific Ocean, the center of the ENSO universe, this was not surprising. What was surprising was that the ENSO signal is largely communicated from the equatorial Pacific Ocean to the EPWP *not* through a direct ocean pathway, but through an atmospheric link.

The mechanism is simple; upward vertical motion in the atmosphere, which results in cloud cover, follows warm water in the tropics. Cloud cover reduces solar heating of the surface, while clear skies allow passage of shortwave radiation and thus abundant surface solar heating. The east Pacific *warm* pool is therefore typically a cloudy and rainy region. However, when the equatorial Pacific Ocean is anomalously warm (such as during an El Niño event), cloud cover usually anchored over the western tropical Pacific Ocean and the EPWP is instead situated over the eastern equatorial Pacific Ocean. When such an event occurs, massive anomalous upward vertical motion also occurs over the eastern equatorial Pacific Ocean. Akin to other thermally-forced large-scale features of the atmospheric general circulation such as the Hadley or Walker cells, ascent somewhere is balanced by descent elsewhere. One of the major regions in which

such compensating descent occurs is over the EPWP. Thus, anomalously warm SST in the eastern equatorial Pacific Ocean forces anomalously warm SST in the EPWP using the atmospheric meridional-vertical circulation cell as a link. One potential uncertainty which could not have been addressed using the approach developed in this dissertation is the role of cloud cover in modulating net longwave radiation. In the OGCM experiments discussed in Chapter 2, the shortwave forcing implicitly includes the effect of interannual cloud cover, while net longwave radiation was computed by the modeled SSTs and atmospheric mixed layer properties, and climatological cloud cover. Thus, one area of future research would be to quantify the contribution of the feedback between SST and longwave radiation via cloud cover. This could be achieved by using a regional coupled model that explicitly includes such feedbacks.

While the aforementioned mechanism for communicating the ENSO signal from the equatorial Pacific Ocean to the EPWP is plausible, it does not by itself prove that ocean transport is unimportant. However, analysis of the ocean mixed layer heat budget and poleward heat transport in this dissertation suggests that is the case. Also, it is highly consistent with the conspicuous lack of poleward heat transport convergence between the equatorial Pacific and the northern tropics, while to the south of the equator, poleward heat transports are large.

Since the results of Chapter 2 clearly highlighted the importance of the equatorial Pacific and ENSO in the interannual variability of the EPWP, a further examination of present capabilities of modeling the equatorial Pacific and ENSO was warranted. One of the deficiencies characteristic of several coupled models is an overly-regular biennial ENSO. As opposed to something like amplitude, the period of an oscillation as influential as ENSO is extremely important since it sets the pace of other aspects of the Earth's physical-ecological climate system. In a sense, ENSO is truly one of the Earth's natural "clocks." If the clock is not ticking at the correct pace in a model, this means, among many other things, that the EPWP will not exhibit realistic interannual variability.

The ocean model experiments conducted in Chapter 2 had the correct period of ENSO because that answer was built into the solution; the ocean model was forced by *observed* atmospheric variability. Observed forcing such as winds and surface shortwave radiation in the tropical Pacific Ocean presumably has the correct (observed) ENSO signal contained within. However, it is in coupled (unforced) ocean-atmosphere modeling that the biennial ENSO is a problem. Chapter 3 represents a contribution to the problem of coupled ocean-atmosphere modeling of ENSO by illustrating one relatively simple, yet physically-based, modification that led to (1) improved representation of the *mean* state of the equatorial Pacific Ocean, and (2) subsequent improvements in the simulation of ENSO, including a significant reduction of the biennial ENSO problem. Returning to the original objective of this dissertation, these improvements would undoubtedly lead to improvements in the interannual variability of SST in the EPWP in coupled ocean-atmosphere models.

The final major body chapter of this dissertation was focused on clarifying the role of the eastern tropical Pacific Ocean in the interannual variability of rainfall in Central America. It was first noted that, although many previous studies have addressed rainfall variability in Central America within the context of the broader Caribbean region, the east Pacific ITCZ is among the rainiest places on Earth during boreal summer. The east Pacific ITCZ is of course situated over the EPWP, but also tends to cover portions of Central America. Thus, the motivated hypothesis was that Central American rainfall variations are inextricably linked to the east Pacific ITCZ, and that the EPWP can influence the strength of the east Pacific ITCZ and therefore Central American rainfall. It was concluded that the EPWP serves to trigger a rapid enhancement of the east Pacific ITCZ (in the case that the EPWP is anomalously warm), which is subsequently manifest as interannual rainfall anomalies over Central America.

Moreover, the timing and amplitude of the SST-enhanced east Pacific ITCZ depends on the persistence characteristics of SST anomalies in the eastern equatorial Pacific Ocean or ENSO. The longer the equatorial SST anomaly persists, the longer the EPWP is warmed by

shortwave radiation and thus the greater the subsequent SST-enhancement of the ITCZ. This concept is analogous to a slingshot, where the elastic band is the ITCZ, the projectile is rainfall, the hand pulling the band is ENSO, and the target is Central America. The longer the hand (ENSO) pulls back on the band (the ITCZ), the greater the tension in the band (the warmth of the EPWP) will become. If the hand releases sooner, the projectile will arrive at the target sooner but with less force. If the hand pulls back longer before releasing, the projectile will arrive at the target later but with greater force. The notion of Central America remaining dry as long as the anomalously warm equatorial SSTs are locking the ITCZ equatorward is consistent with the mechanism proposed by Eltahir and Gong (1996) for West African rainfall variability, except in that case there is no *later* intensification of the ITCZ by a coastal warm pool which would serve to reverse the rainfall anomaly later in the same year.

One important aspect of the large-scale climate system that could have an effect on both SST in the EPWP and rainfall anomalies in Central America is the North Pacific subtropical anticyclone. Variations in the position and intensity of the North Pacific subtropical anticyclone could have substantial effects on the position of the east Pacific ITCZ, coastal upwelling immediately north of the EPWP, and other processes relevant to the EPWP region. Understanding the specific role of the North Pacific subtropical anticyclone and its variability remains an important area open for future research.

One of the most fascinating outcomes of this dissertation is that one of the major ways in which ENSO exerts its influence on Central American rainfall is *through* the EPWP. ENSO influences the EPWP through the atmosphere, and the EPWP in turn influences Central American rainfall through the atmosphere. The conclusions of Chapters 2 and 4, while arrived at somewhat independently, are mutually consistent and reinforce one another; the mechanism by which ENSO influences the EPWP is part of what determines how much the EPWP will subsequently influence Central American rainfall. One exciting opportunity motivated by this outcome is the focused use of SST observations and coupled modeling to improve seasonal

predictions of Central American rainfall. This dissertation provides a new understanding of the important role of the EPWP in the Central American region which, in tandem with mechanisms identified by other investigators, could result in a more complete picture of an important regional climate and overall improved predictions of what is critical to the well-being of its inhabitants: the seasonal cycle of rainfall.

Appendix A: The Ocean Mixed Layer Heat Budget

Several sections of this dissertation include diagnostic analyses of the ocean mixed layer heat budget. Appendix A is aimed to provide a unified overview of the ocean mixed layer heat budget and heat flux formulations in terms of traditional formulae, the Gent-Cane OGCM, and *in situ* estimates using the TAO array. The complete ocean mixed layer heat budget can be expressed as: $\partial T/\partial t = Q_{SW} - Q_{PEN} - Q_{LW} - Q_{LH} - Q_{SH} + Q_{ZA} + Q_{MA} - Q_{EMX}$ where Q_{SW} is net surface downward shortwave radiation, Q_{PEN} is the shortwave radiation penetrating through the mixed layer, Q_{LW} is the net upward longwave radiation, Q_{LH} is latent heat flux, Q_{SH} is sensible heat flux, Q_{ZA} and Q_{MA} are zonal and meridional heat advection, respectively, and Q_{EMX} is the net heat flux effect of subsurface entrainment and mixing across the base of the mixed layer. $\partial T/\partial t$ is the time rate of change of mixed layer temperature; with knowledge of mixed layer depth this can be expressed in terms of heat flux. Generally in the tropics, the effect of Q_{SW} is always warming; the effects of Q_{PEN} , Q_{LW} , Q_{LH} , Q_{SH} , and Q_{EMX} are always cooling, and the effects of Q_{ZA} and Q_{MA} depend on circulation and upper-ocean heat distribution.

Shortwave radiation Q_{SW}

Traditional: $Q_{SW} = S (1 - \alpha) - X$ where S is the solar constant 1367 Wm^{-2} , α is planetary albedo, and X is a constant to account for absorption by O_3 and other atmospheric constituents.

Model: Climatological or interannual surface downward shortwave radiation is prescribed.

TAO: Q_{SW} is measured directly by shortwave radiometers.

Penetrative shortwave radiation Q_{PEN}

Traditional: $Q_{PEN} = Q_{SW} \gamma e^{-k z}$ where γ is an empirical coefficient, k is attenuation of photosynthetically active radiation, and z is ocean depth.

Model: $Q_{PEN} = (Q_{SW} \gamma e^{-h/a}) / b$ where $\gamma = 0.33$, h is mixed layer depth, $a = 17$, b is a flux conversion factor $4.12 \cdot 10^6$.

Longwave radiation Q_{LW}

Traditional: $Q_{LW} = \varepsilon \sigma_B T_S^4$ where ε is ocean surface emissivity, σ_B is the Stefan-Boltzmann constant $5.67 \cdot 10^{-8} \text{ W m}^{-2} \text{ K}^{-4}$ and T_S is SST in Kelvin.

Model: $Q_{LW} = \varepsilon \sigma_B T_S^4 (0.417 - 0.0486 (1000 q_A / 0.622)^{1/2}) (1 - a C^2) + 4 \varepsilon \sigma_B T_S^3 (T_S - T_A)$ where $\varepsilon = 0.97$, q_A is atmospheric mixed layer specific humidity, $a = 0.4$ if $T_S > 301.15$ and 0.8 if $T_S < 301.15$, C is observed cloud fraction, and T_A is low level air temperature.

TAO: Q_{LW} was calculated using the same equation and parameters as in the model formulation. Observations of C were derived from ICOADS (Woodruff et al. 1987), with temporal gaps filled using a blending of NCEP Reanalysis (25%) and linear interpolation (75%).

Latent heat flux Q_{LH}

Traditional: $Q_{LH} = L_V \rho_{air} C_M U_A (q_S - q_A)$ where L_V is the latent heat of vaporization $2.5 \cdot 10^6 \text{ J kg}^{-1}$, ρ_{air} is the density of air, C_M is the aerodynamic transfer coefficient for moisture $1.35 \cdot 10^{-3}$, U_A is scalar low level wind speed relative to surface ocean velocity, q_S is specific humidity of air at the ocean surface, and q_A is specific humidity of low level air.

Model: $Q_{LH} = L_V \rho_{air} C_M U_A (q_S - q_A)$ where $L_V = 2.5 \cdot 10^6 \text{ J kg}^{-1}$, $\rho_{air} = 1.225 \text{ kg m}^{-3}$, $C_M = 1.4 \cdot 10^{-3}$. U_A not corrected for surface ocean velocity.

TAO: Q_{LH} was calculated using the same equation and parameters as in the model formulation. q_S and q_A were calculated using observed temperature and relative humidity together with the set of moisture equations derived from Gill (1982; Appendix A.1).

* Note that a necessary model parameter is U_{A-Min} , which is set to 5 m s^{-1} . Thus, model Q_{LH} appears to have a high mean bias with muted variability.

Sensible heat flux Q_{SH}

Traditional: $Q_{SH} = C_P \rho_{air} C_H U_A (T_S - T_A)$ where C_P is heat capacity of water $4 \times 10^3 \text{ m J kg}^{-1} \text{ K}^{-1}$, ρ_{air} is the density of air, C_H is the aerodynamic transfer coefficient for heat 0.9×10^{-3} , U_A is scalar low level wind speed relative to surface ocean velocity, T_S is SST, and T_A is low level air temperature.

Model: $Q_{SH} = C_P \rho_{air} C_H U_A (T_S - T_A)$ where $C_P = 1004 \text{ J kg}^{-1} \text{ K}^{-1}$, $\rho_{air} = 1.225 \text{ kg m}^{-3}$, and $C_H = 1.4 \times 10^{-3}$. U_A not corrected for surface ocean velocity.

TAO: Q_{SH} was calculated using the same equation and parameters as in the model formulation.

Zonal heat advection Q_{ZA}

Traditional: $Q_{ZA} = -u \partial T / \partial x$ where u is zonal ocean velocity, and $\partial T / \partial x$ is the zonal SST gradient.

Model: $Q_{ZA} = -h u \partial T / \partial x$ (treated as flux of heat content) where h = mixed layer depth.

Meridional heat advection Q_{MA}

Traditional: $Q_{MA} = -v \partial T / \partial y$ where v is meridional ocean velocity and $\partial T / \partial y$ is the meridional SST gradient.

Model: $Q_{MA} = -h v \partial T / \partial y$ (treated as flux of heat content) where h = mixed layer depth.

Entrainment-mixing Q_{EMX}

Traditional: $Q_{EMX} = K_Z \partial^2 T / \partial z^2$ or $w \partial T / \partial z$ where K_Z is vertical eddy diffusivity, $\partial^2 T / \partial z^2$ is the second derivative of temperature T with respect to depth z , w is vertical velocity, and $\partial T / \partial z$ is the vertical temperature gradient.

Model: See Chen et al. (1994).

Appendix B. Discrete Fourier Transform (DFT) Methodology

All time series can be decomposed into a linear combination of sinusoidal components, each of which may be expressed as:

$$\sqrt{2} * A * \cos\left(2\Pi * f * t + \frac{\Pi * \Theta}{180}\right)$$

where A is root mean square (RMS) of the amplitude of the component,

f is the frequency of the component,

t is the time, and

Θ is the phase angle.

The DFT equation:

$$f_c(k) = \frac{1}{N} \sum_{n=0}^{N-1} t(n) * W_N^{kn}$$

where

$$W_N = \exp\left(-\frac{2\Pi i}{N}\right),$$

$f_c(k)$ is the complex frequency at frequency point k ,

$t(n)$ is time at time point n ,

N is the number of time points beginning with zero, and

$$i = \sqrt{-1}$$

is solved for the RMS amplitude

$$A(k) = \frac{1}{\sqrt{2}} * \sqrt{f_{c_real}(k)^2 + f_{c_imag}(k)^2} \text{ and graphed as a function of period } T = \frac{1}{f}.$$

Appendix C. October 1998 Tropical Cyclones

Tropical cyclones form and propagate over the northeastern tropical Pacific Ocean every year. Such tropical cyclones travel roughly parallel to the coast of Central America and Mexico, usually remaining sufficiently offshore as to not directly affect Central America. Additionally, Atlantic tropical cyclones can occasionally make landfall on Central America (normally 1-3 per year).

As discussed in Chapter 1, tropical cyclones are beyond the scope of this dissertation. However, for those familiar with the hurricane season of 1998, it would be reasonable to question whether or not tropical cyclones have an appreciable effect on the results of Chapter 4, particularly the depictions and discussion of the SST-enhanced east Pacific ITCZ mechanism. Given that the rainfall anomaly over Central America during October 1998 was among the largest in the U-Del precipitation record, we find it necessary to provide a closer look at any tropical cyclones in close proximity to Central America during that month.

During October 1998, there were three named storms in the eastern Pacific basin: Hurricanes Kay, Lester, and Madeline. Hurricanes Kay (Oct. 13-16) and Madeline (Oct. 16-20) were short-lived, and formed, propagated, and decayed far from Central America (west of 150°W). Hurricane Lester, however, formed offshore south of Guatemala, and lasted 26 days (Oct. 15-26). Also during October 1998, one named Atlantic storm came within close proximity of Central America: Hurricane Mitch (Oct. 22-Nov. 5). Hurricane Mitch remains among the deadliest and most powerful in the Atlantic basin. For reference, the paths of Hurricanes Lester and Mitch are shown on Figure C.1. Although tropical cyclones undoubtedly contributed to the total rainfall over Central America and southern Mexico during October 1998, this appendix provides three simple lines of observational evidence confirming that neither Lester nor Mitch had an appreciable impact on the interpretation of the results of Chapter 4 with regard to the

SST-enhanced ITCZ mechanism, and that October 1998 would have been an anomalous rainy season in Central America without them.

1. Presented in Figure C.1 is the CMAP precipitation anomaly for October 1998. Over land areas, there is excellent agreement with the corresponding gauge-based anomaly (Figure 4.27). Overlaid onto Figure C.1 is the anomalous 850 hPa vertical motion field for October 1998 (solid contours for ascent). Clearly the precipitation anomalies, especially those on the Pacific side of Central America, are associated with the large-scale anomalous ascent in the ITCZ over the EPWP, consistent with the SST-enhanced east Pacific ITCZ mechanism described in Section 4.4. It is highly unlikely that a single hurricane such as Lester could result in such a robust feature in the monthly vertical motion field. Even if it could, the hurricane track diverges from the ascent anomaly (Figure C.1). On the contrary, one could better argue that the anomalously warm EPWP played a role in Hurricane Lester. From that perspective, if tropical cyclones result from organized deep convection, and the ITCZ is deep convection, which the EPWP enhances by providing warm SSTs, then the genesis of Hurricane Lester is not altogether separable from the SST-enhanced ITCZ. The difference is that the deep convection making up Hurricane Lester became organized and eventually began to rotate. After all, the deep tropical convection that can morph into tropical cyclones is part of the time-mean ITCZ.

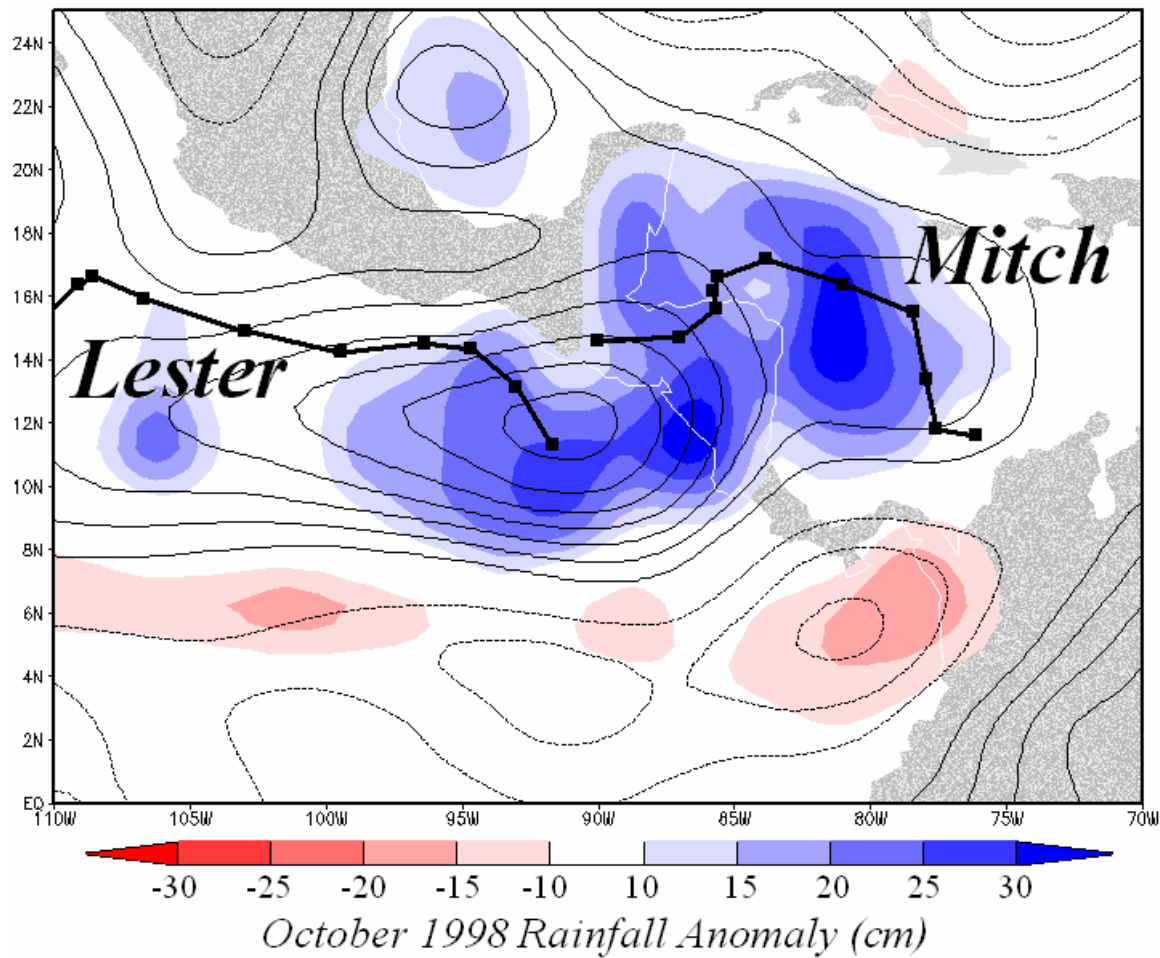


Figure C.1. October 1998 CMAP precipitation anomaly (cm; shades) and NCEP Reanalysis 850 hPa – omega anomaly (contour interval 0.01 Pa sec⁻¹ beginning at +/- 0.01 Pa sec⁻¹), and NOAA best-tracks for Hurricanes Lester and Mitch (tracks outside October 1998 omitted). Black squares on the hurricane tracks represents time intervals of one day.

2. The majority of the rainfall over the P3 region of Central America in October 1998 fell during the first half of that month, while both Hurricanes Lester and Mitch did not exist until the second half. Shown in the top panel of Figure C.2 is the total CMAP rainfall during October 1998. When the total monthly precipitation is broken down between that which fell during the first half of the month (Oct. 1-15) versus the second half of the month (Oct. 16-30; Oct. 31 not included because that day is part of the first pentad in November 1998), it is evident that the

majority of the rainfall over the EPWP in October 1998 (i.e., the rainfall collocated with the large ascent anomaly) fell during the first half of the month.

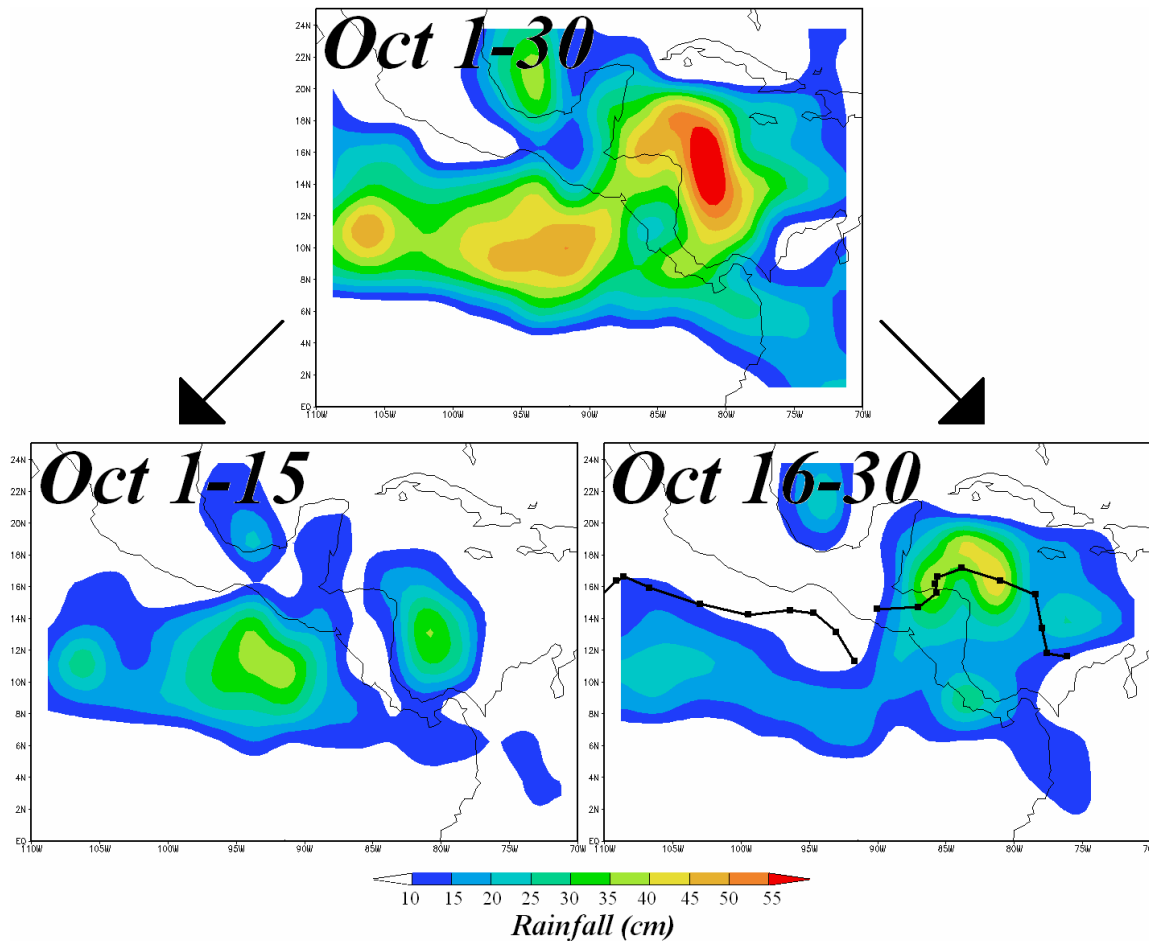


Figure C.2. Top: CMAP total precipitation for October 1998 (cm), Bottom-left: as in top but for Oct. 1-15, Bottom-right: as in top but for Oct 16-30, and NOAA best-tracks for Hurricanes Lester and Mitch (tracks outside October 1998 omitted).

Additionally, referring to Figure 4.26, the zonally averaged (between 100-85°W) rainfall anomaly during 1998 clearly propagates northward in time, and actually peaks during September. Thus, the SST-enhanced east Pacific ITCZ mechanism was already set in motion, and neither Hurricanes Lester nor Mitch could have an effect on that depiction. During the second half of the month (Figure C.2, bottom-right), there is obvious correspondence between rainfall and the track of Hurricane Mitch- primarily on the Atlantic side of Central America.

3. Instantaneous visible and infrared satellite images also confirm that deep convection was occurring over the EPWP in October 1998, and that such convection was unrelated to Hurricanes Lester and Mitch. Figure C.3 shows infrared geostationary satellite images of Central America and surrounding seas at 1145 UTC on Oct. 23, 1998, and at the same time three days later. On Oct. 23, Atlantic Hurricane Mitch was gaining strength off the northwest coast of South America, and Pacific Hurricane Lester was long gone. Also on Oct. 23, a broad region of deep convection is found over the EPWP, which was not related to an imminent tropical cyclone. Three days later, Hurricane Mitch is nearly at full strength off the coast of Honduras (Figure C.3, right), while deep convection continues in the Pacific.

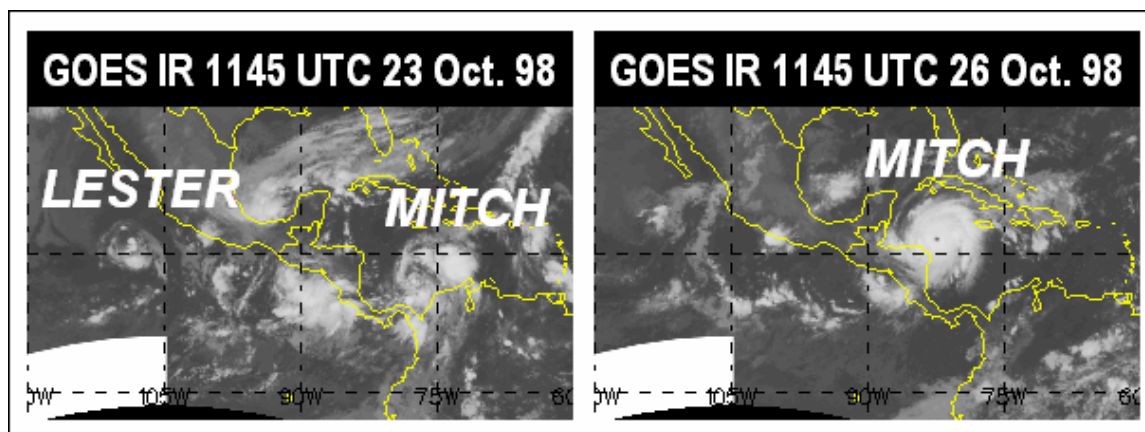


Figure C.3. Infrared satellite images over the tropical Americas at 1145 UTC on Oct. 23 (left) and Oct. 26 (right), 1998. Cloud formations associated with Hurricanes Lester and Mitch are labeled. Satellite images available from the Unisys weather image archive: <http://weather.unisys.com/archive/>.

Two higher-resolution visible and infrared satellite images are provided in Figure C.4 to further illustrate that the deep convection over the EPWP was not related to Hurricane Mitch, even while Hurricane Mitch was near peak intensity. Infrared imagery, unlike visible, provides an indication of the height of the cloud tops, by virtue of the fact that clouds higher in the atmosphere are colder than those lower in the atmosphere. The bright white cloud structure

over the EPWP in the infrared imagery, coupled with the overshooting tops evident in the visible imagery, suggests deep tropical convection, clearly separate from Hurricane Mitch.

In summary, tropical cyclones do not have an appreciable impact on the interpretation of the result of Chapter 4 with respect to the depictions and discussion of the SST-enhanced east Pacific ITCZ mechanism. Although Atlantic Hurricane Mitch produced considerable amounts of precipitation in the Caribbean and parts of Central America and southern Mexico, that was spatially and temporally separate from the anomalous rainfall associated with the SST-enhanced ITCZ over the eastern Pacific Ocean. Pacific Hurricane Lester also occurred after the peak in east Pacific ITCZ rainfall, and is not the reason for the anomalous ascent over the EPWP. On the contrary, the anomalously warm SSTs in the EPWP and resulting ascent may have helped precondition the environment so that when the tropical wave that was to become Hurricane Lester (and Madeline, for that matter) crossed Central America, a hurricane was formed. Hurricane Kay was not traced to a wave crossing Central America, but a tropical disturbance that originated within- and broke away from- the east Pacific ITCZ itself (Avila and Guiney 2000).

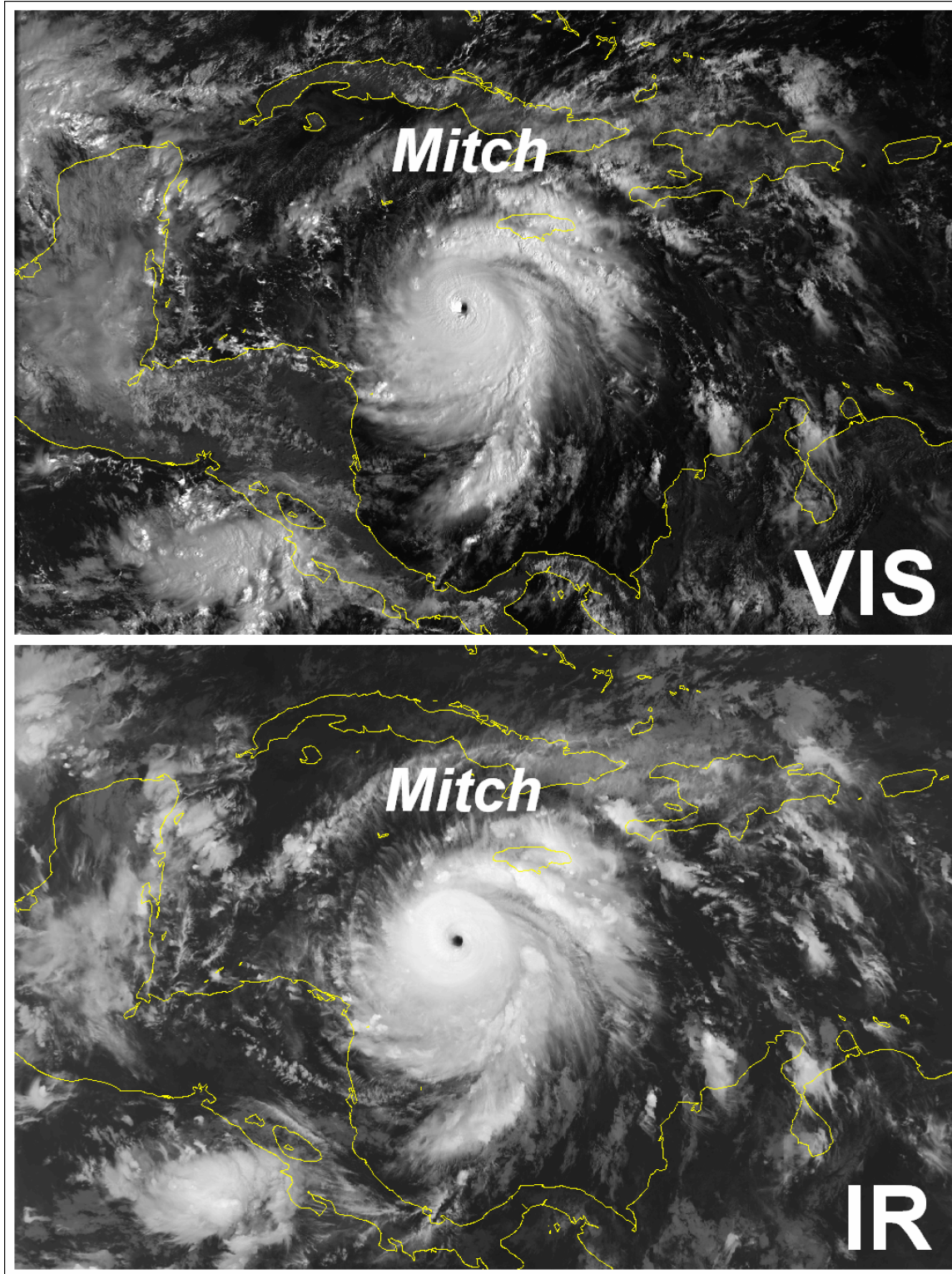


Figure C.4. Visible (top) and infrared (bottom) satellite images of Hurricane Mitch on October 26. Satellite images courtesy Earth Observing Group, Defense Meteorological Satellite Program, Boulder, CO: <http://www.ngdc.noaa.gov/dmsp/hurricanes/hurricanes.html>.

List of References

- Amador, J.A., Alfaro, E.J., Lizano, O.G., Magaña, V.O., 2006. Atmospheric forcing of the eastern tropical Pacific: a review. *Progr. Oceanogr.*, **69** (2–4), 101–142.
- Atlas, R., R.N. Hoffman, S.C. Bloom, J.C. Jusem, and J. Ardizzone, 1996: A multiyear global surface wind velocity dataset using SSM/I wind observations. *Bull. Amer. Meteor. Soc.*, **77**, 869–882.
- Avila, L.A., and J.L. Guiney, 2000: Eastern North Pacific Hurricane Season of 1998. *Mon. Wea. Rev.*, **128**, 2990–3000.
- Bacher A., Oberhuber J.M., Roeckner E., 1998: ENSO dynamics and seasonal cycle in the Tropical Pacific as simulated by the ECHAM4/OPYC3 coupled general circulation model. *Clim. Dyn.*, **14**, 431–450.
- Barkstrom, B.R., 1984. The Earth Radiation Budget Experiment (ERBE). *Bull. Amer. Meteor. Soc.*, **65**, 1170–1186.
- Battisti, D.S., and A.C. Hirst, 1989: Interannual variability in a tropical atmosphere–ocean model: Influence of the basic state, ocean geometry and nonlinearity. *J. Atmos. Sci.*, **46**, 1687–1712.
- Beck, C., J. Grieser and B. Rudolf (2005): A New Monthly Precipitation Climatology for the Global Land Areas for the Period 1951 to 2000. (To be published in Climate Status Report 2004, German Weather Service, Offenbach, Germany.)
- Behringer, D. and Y. Xue, 2004: Evaluation of the global ocean data assimilation system at NCEP: The Pacific Ocean. Proceedings of Eighth Symposium on Integrated Observing and Assimilation Systems for Atmosphere, Ocean, and Land Surface, Seattle, Washington, 2004.
- Bengtsson L., Kanamitsu M., Kallberg P. and S. Uppala, 1982: FGGE 4- dimensional data assimilation at ECMWF. *Bull. Amer. Meteor. Soc.*, **63**, 29– 43.
- Bjerknes, J. 1969: Atmospheric teleconnections from the equatorial Pacific. *Mon. Wea. Rev.*, **97**: 163–172.
- Black, T.L., 1994: The new NMC mesoscale eta model: Description and forecast samples. *Weather Forecasting*, **9**, 265–278.
- Bosilovich, M.G., 2002: On the vertical distribution of local and remote sources of water for precipitation. *Met. Atmos. Phys.*, **80**, 31–41.
- Bourassa, M.A., D.G. Vincent, and W.L. Wood, 1999: A Flux Parameterization Including the Effects of Capillary Waves and Sea State. *J. Atmos. Sci.*, **56**, 1123–1139.
- Broccoli, A.J., and S. Manabe, 1992: The effects of orography on midlatitude Northern Hemisphere dry climates. *J. Climate.*, **5**, 1181–201.
- Busalacchi, A.J., and J.J. O'Brien, 1980: The seasonal variability in a model of the tropical Pacific. *J. Phys. Oceanogr.*, **10**, 1929–1951.
- Busalacchi, A.J., and J.J. O'Brien, 1981: Interannual variability in the equatorial Pacific in the 1960's. *J. Geophys. Res.*, **86**, 10901–10907.
- Busalacchi, A.J. and J. Picaut, 1983: Seasonal variability from a model of the tropical Atlantic Ocean. *J. Phys. Oceanogr.*, **13**, 1564–1588.
- Cane, M.A., 1984: Modeling sea level during El Niño. *J. Phys. Oceanogr.*, **14**, 1864–1874.
- Carton, J.A., and B. Huang, 1994: Warm events in the tropical Atlantic. *J. Phys. Oceanogr.*, **24**, 888–903.
- Carton, J.A., G. Chepurin, X. Cao, and B.S. Giese, 2000: A SODA analysis of the global upper ocean 1950–1995, Part 1: methodology. *J. Phys. Oceanogr.*, **30**, 294–309.
- Center for International Earth Science Information Network (CIESIN), Columbia University; and Centro Internacional de Agricultura Tropical (CIAT). 2005. Gridded Population of the World Version 3 (GPWv3): Population Density Grids. Palisades, NY: Socioeconomic Data

- and Applications Center (SEDAC), Columbia University. Available at <http://sedac.ciesin.columbia.edu/gpw>. (date of download).
- Cerveny, R.S., 2005: Charles Darwin's meteorological observations aboard the H.M.S. Beagle. *Bull. Amer. Meteor. Soc.*, **86**, 1295-1301.
- Charney, J., 1959: On the general circulation of the atmosphere. *The Atmosphere and the Sea in Motion*, New York, Rockefeller Institute Press, 178-193.
- Chelton, D.B., M.H. Freilich and S.K. Esbensen, 2000a: Satellite observations of the wind jets off the Pacific coast of Central America, Part I: Case studies and statistical characteristics. *Mon. Wea. Rev.*, **128**, 1993-2018.
- Chelton, D.B., M.H. Freilich and S.K. Esbensen, 2000b: Satellite observations of the wind jets off the Pacific coast of Central America, Part II: Regional relationships and dynamical considerations. *Mon. Wea. Rev.*, **128**, 2019-2043.
- Chelton, D.B., Schlax, M.G., Lyman, J.M., and G.C. Johnson, 2003. Equatorially-trapped Rossby waves in the presence of meridionally-sheared baroclinic flow in the Pacific. *Progr. Oceanogr.*, **56**, 323-380.
- Chelton, D.B., Schlax M.G., Freilich M.H., and R.F. Milliff, 2004: Satellite measurements reveal persistent small-scale features in ocean winds. *Science*, **303**, 978-983.
- Chen, D., A.J. Busalacchi and L.M. Rothstein, 1994: The Roles of Vertical Mixing, Solar-Radiation, and Wind Stress in a Model Simulation of the Sea-Surface Temperature Seasonal Cycle in the Tropical Pacific-Ocean. *J. Geophys. Res.*, **99**(C10): 20345-20359.
- Chen, D., L.M. Rothstein, and A.J. Busalacchi, 1994: A Hybrid Vertical Mixing Scheme and Its Application to Tropical Ocean Models. *J. Phys. Oceanogr.*, **24**, 2156-2179.
- Chiang, J.C.H., and D.J. Vimont, 2003: Analogous meridional modes of atmosphere-ocean variability in the tropical Pacific and tropical Atlantic. *J. Climate*. **17**, 4143-4158.
- Christensen, N., Jr., 1971: Observations of the Cromwell Current near the Galápagos Islands. *Deep-Sea Res.*, **18**, 27-33.
- Clarke A.J., 1988: Inertial wind path and sea surface temperature patterns near the Gulf of Tehuantepec and Gulf of Papagayo. *J. Geophys. Res.*, **93**, 15491-15501.
- CLIVAR NAME: <http://www.usclivar.org/name-index.html>
- Collins, M., 2000: The El Niño-Southern Oscillation in the Second Hadley Centre Coupled Model and Its Response to Greenhouse Warming. *J. Climate*, **13**, 1299-1312.
- Collins, W.D., C.M. Bitz, M.L. Blackmon, G.B. Bonan, C.S. Bretherton, J.A. Carton, P. Chang, S.C. Doney, J.J. Hack, T.B. Henderson, J.T. Kiehl, W.G. Large, D.S. McKenna, B.D. Santer, and R.D. Smith, 2006: The Community Climate System Model Version 3 (CCSM3). *J. Climate*, **19**, 2122-2143.
- Curry, R.G., and M.S. McCartney, 2001: Ocean gyre circulation changes associated with the North Atlantic Oscillation. *J. Phys. Oceanogr.*, **31**, 3374-3400.
- Czaja A., and C. Frankignoul, 2002: Observed impact of North Atlantic SST anomalies on the North Atlantic Oscillation. *J. Climate.*, **15**, 606-623.
- Czaja, A. and J. Marshall, 2006: The Partitioning of Poleward Heat Transport between the Atmosphere and Ocean. *J. Atmos. Sci.*, **63** (5), 1498-1511.
- Darwin, C., 1839: *J. of Researches into the Geology and Natural History*. (1952; reprint of 1st ed. Hafner Publishing Company, 615 pp.).
- Darwin, C., 1897: *J. of Researches into the Natural History and Geology of the Countries Visited during the Voyage of the H.M.S. Beagle Round the World, under the Command of Capt. Fitz Roy, R.N.*, 2nd ed., D. Appleton and Company, 519 pp.
- daSilva, A, Young, A.C. and S. Levitus, 1994: Atlas of surface marine data 1994, volume 1.: Algorithms and procedures. Tech. Rep. 6, U.S. Department of Commerce, NOAA, NESDIS.
- Deser, C., and J.M. Wallace, 1990: Large-scale atmospheric circulation features of warm and cold episodes in the tropical Pacific. *J. Climate*, **3**, 1254-1281.

- Deser, C., and M.L. Blackmon, 1993: Surface climate variations over the North Atlantic Ocean during winter: 1900-1993. *J. Climate.*, **6**,1743-1753.
- Deser, C., and M.S. Timlin, 1997: Atmosphere-Ocean Interaction on Weekly Timescales in the North Atlantic and Pacific. *J. Climate.*, **10**, 393-408.
- Eden C., and T. Jung, 2001: North Atlantic interdecadal variability: oceanic response to the North Atlantic Oscillation (1865–1997). *J. Climate.*, **14**, 676–691.
- Eden, C., and A. Timmerman. 2004. The influence of the Galápagos Islands on tropical temperatures, currents and the generation of tropical instability waves. *Geophys. Res. Lett.*, **31**, 1-4.
- Eltahir, E.A.B., and C. Gong, 1996: Dynamics of Wet and Dry Years in West Africa. *J. Climate*, **9**, 1030–1042.
- Enfield, D., and J. Allen, 1980: On the Structure and Dynamics of Monthly Mean Sea Level Anomalies along the Pacific Coast of North and South America. *J. Phys. Oceanogr.*, **10**, 557–578.
- Enfield, D.B., and J. Allen, 1983: The Generation and Propagation of Sea Level Variability Along the Pacific Coast of Mexico. *J. Phys. Oceanogr.*, **13**, 1012–1033.
- Enfield, D.B. and D.A. Mayer, 1997: Tropical Atlantic SST variability and its relation to El Niño-Southern Oscillation, *J. Geophys. Res.*, **102**, 929-945.
- Enfield, D.B., and S.K. Lee, 2005: The Heat Balance of the Western Hemisphere Warm Pool. *J. Climate*, **18**, 2662–2681.
- Enfield, D.B., S.-K. Lee, and C. Wang, 2006: How are large western hemisphere warm pools formed? *Progr. Oceanogr.*, **70**, 346-365.
- EPIC: <http://www.physics.nmt.edu/~raymond/epic2001/overview/>
- Farber-Lorda, J., Lavin M.F., Zapatero, M.A., Robles, J.M., 1994: Distribution and abundance of Euphausiids in the Gulf of Tehuantepec during wind forcing. *Deep Sea Res.*, **38**, 359–367.
- Farrara, J.D. and J.-Y. Yu, 2003: Interannual variations in the North American monsoon and SST anomalies: A general circulation model study. *J. Climate*, **16**, 1703-1720.
- Fedorov, A.V., and S.G.H. Philander, 2000: Is El Niño changing? *Science*, **288**, 1997-2002.
- Fiedler, P.C., 1994: Seasonal and interannual variability of coastal zone color scanner phytoplankton pigments and winds in the eastern tropical Pacific. *J. Geophys. Res.*, **99**, 18,371-18,384.
- Fiedler, P.C., 2002a: The annual cycle and biological effects of the Costa Rica Dome. *Deep Sea Res.*, **49**, 321-338.
- Fiedler, P.C., 2002b: Environmental change in the eastern tropical Pacific Ocean: Review of ENSO and decadal variability. *Mar. Ecol. Progr. Ser.*, **244**, 265-283.
- Fu, L.-L., E.J. Christensen, C.A. Yamarone, Jr., M. Lefebvre, Y. Ménard, M. Dorrer, and P. Escudier, 1994: TOPEX/POSEIDON mission overview, *J. Geophys. Res.*, **99** (C12), 24,369-24,382.
- Garreaud, R.D., and J.M. Wallace, 1997: The Diurnal March of Convective Cloudiness over the Americas. *Mon. Wea. Rev.*, **125**, 3157–3171.
- Gent, P.R., K. O'Neill, and M.A. Cane, 1983: A model of the semiannual oscillation in the equatorial Indian Ocean. *J. Phys. Oceanogr.*, **13**, 2148-2160.
- Gent, P.R., and M.A. Cane, 1989: A Reduced Gravity, Primitive Equation Model of the Upper Equatorial Ocean. *J. Comput. Phys.*, **81**, 444-480.
- GEWEX Americas: <http://www.ogp.noaa.gov/mpe/gapp/>
- Ghil M., R.M. Allen, M.D. Dettinger, K. Ide, D. Kondrashov, M.E. Mann, A. Robertson, A. Saunders, Y. Tian, F. Varadi, and P. Yiou, 2002: Advanced spectral methods for climatic time series, *Rev. Geophys.*, **40**, 3.1-3.41.
- Giannini, A., Y. Kushnir, and M.A. Cane, 2000: Interannual Variability of Caribbean Rainfall, ENSO, and the Atlantic Ocean. *J. Climate*, **13**, 297–311.
- Gill, A.E., 1982: Atmosphere-Ocean Dynamics. Academic Press.

- Goldenberg, S.B., and L.J. Shapiro, 1996: Physical Mechanisms for the Association of El Niño and West African Rainfall with Atlantic Major Hurricane Activity. *J. Climate*, **9**, 1169–1187.
- Gordon, C.T., A. Rosati and R. Gudgel. 2000: Tropical Sensitivity of a Coupled Model to Specified ISCCP Low Clouds. *J. Climate*, **13** (13), 2239–2260.
- Graham, N.E., and T.P. Barnett, 1987: Observations of sea surface temperatures, convection and surface wind divergence over tropical oceans, *Science*, **238**, 657-659.
- Haney, R.L., 1971: Surface Thermal Boundary Condition for Ocean Circulation Models. *J. Phys. Oceanogr.*, **1**, 241-248.
- Harrison, M.J., Rosati, A., Soden, B. J., Galanti, E., Tziperman, E., 2002: An Evaluation of Air–Sea Flux Products for ENSO Simulation and Prediction. *Mon. Weather Rev.*, **130**, 723-732.
- Hastenrath, S.L., 1966a: On General Circulation and Energy Budget in the Area of the Central American Seas. *J. Atmos. Sci.*, **23**, 694–711.
- Hastenrath, S.L., 1966a: The Flux of Atmospheric Water Vapor over the Caribbean Sea and the Gulf of Mexico. *J. Appl. Meteor.*, **5**, 778–788.
- Hastenrath, S., 1976: Variations in Low-Latitude Circulation and Extreme Climatic Events in the Tropical Americas. *J. Atmos. Sci.*, **33**, 202–215.
- Hastenrath, S., 1978: On Modes of Tropical Circulation and Climate Anomalies. *J. Atmos. Sci.*, **35**, 2222–2231.
- Hastenrath, S., 2006: Circulation and teleconnection mechanisms of Northeast Brazil droughts. *Progr. Oceanogr.*, **70**, 407-415.
- Hastings, D.A., and P.K. Dunbar, 1999. Global Land One-kilometer Base Elevation (GLOBE) Digital Elevation Model, Documentation, Volume 1.0. Key to Geophysical Records Documentation (KGRD) 34. National Oceanic and Atmospheric Administration, National Geophysical Data Center, 325 Broadway, Boulder, Colorado 80303, U.S.A.
- Hayes, S.P., L.J. Mangum, J. Picaut, A. Sumi and K. Takeuchi, 1991: TOGA-TAO: A moored array for real-time measurements in the tropical Pacific Ocean. *Bull. Amer. Meteor. Soc.*, **72**, 339-347.
- Higgins, R., K. Mo, and Y. Yao, 1998: Interannual variability of the U.S. summer precipitation regime with emphasis on the southwestern monsoon. *J. Climate*, **11**, 2582-2606.
- Higgins, R., Y. Chen, and A. Douglas, 1999: Interannual variability of the North American warm season precipitation regime, *J. Climate*, **12**, 653-680.
- Hoffman, E.E., A.J. Busalacchi, and J.J. O'Brien, 1981: Wind generation of the Costa Rica Dome. *Science*, **214**, 552–554.
- Holton, J.R., 1992: An Introduction to Dynamic Meteorology, Third edition. Academic Press.
- Hong, Y., R. Adler, and G. Huffman, 2006: Evaluation of the potential of NASA multi-satellite precipitation analysis in global landslide hazard assessment. *Geophys. Res. Lett.*, **33**, L22402.
- Hong, Y., R. Adler, and G. Huffman, 2007: Use of satellite remote sensing data in mapping of global shallow landslide susceptibility. *J. Nat. Hazards*, **43** (2).
- Hong, Y., R. Adler, and G. Huffman, 2007: An experimental global prediction system for rainfall-triggered landslides using satellite remote sensing and geospatial datasets. *IEEE Trans. Geosci. Remote Sens.*, **45** (6), 1671-1680.
- Hurd W. E., 1929: Northers of the Gulf of Tehuantepec. *Mon. Wea. Rev.*, **57**, 192–194.
- Hurrell, J.W., Y. Kushnir, M. Visbeck, and G. Ottersen (Eds.), 2003: An Overview of the North Atlantic Oscillation. The North Atlantic Oscillation: Climate Significance and Environmental Impact. *Geophysical Monograph Series*, **134**, 1-35.
- IASCLIP: http://clivar.org/publications/wg_reports/vamos/pdf_files/IASCLIP.pdf
- Jin F.-F., 1997: An equatorial ocean recharge paradigm for ENSO. Part I: conceptual model. *J. Atmos. Sci.*, **54**, 811-829.
- Jochum, M., and R. Murtugudde, 2006: Temperature Advection by Tropical Instability Waves. *J. Phys. Oceanogr.*, **36**, 592-605.

- Johnson, G.C. and McPhaden, M.J., 1999: Interior pycnocline flow from the subtropical to the equatorial Pacific Ocean. *J. Phys. Oceanogr.*, **29**, 3073–3089.
- Johnson, G.C., 2001: The Pacific Ocean subtropical cell surface limb. *Geophys. Res. Lett.*, **28**, 1771-1774.
- Kalnay, E. and Coauthors, 1996: The NCEP/NCAR Reanalysis 40-year Project. *Bull. Amer. Meteor. Soc.*, **77**, 437-471.
- Karnauskas, K.B., and A.J. Busalacchi, 2006: Interannual variability in the east Pacific warm pool: high-resolution satellite observations. Proceedings of the 8th International Conference on Southern Hemisphere Meteorology and Oceanography, p.1289–1294. Foz do Iguacu, Brazil. April 24–28, 2006.
- Karnauskas, K.B., Ruiz–Barradas, A., Nigam, S., and A.J. Busalacchi: North American droughts in ERA–40 global and North American regional reanalyses: A Palmer Drought Severity Index perspective. *J. Climate* (accepted).
- Kessler, W.S., L.M. Rothstein and D. Chen (1998): The annual cycle of SST in the eastern tropical Pacific, as diagnosed in an ocean GCM. *J. Climate*, **11**, 777-799.
- Kessler, W.S., 2002: Is ENSO a cycle or a series of events? *Geophys. Res. Lett.*, **29** (23), 2125.
- Kessler, W.S., 2006: The circulation of the eastern tropical Pacific: A review. *Progr. Oceanogr.*, **69**, 181-217.
- Kiladis, G.N., and H.F. Diaz, 1989: Global climatic anomalies associated with extremes in the Southern Oscillation. *J. Climate*, **2**, 1069-1090.
- Knauss, J.A., 1997: Introduction to physical oceanography. 2nd. Ed. Prentice-Hall, London, 309pp.
- Koster, R.D., M.J. Suarez, and M. Heiser, 2000: Variance and predictability of precipitation at seasonal-to-interannual timescales, *J. Hydromet.*, **1**, 26-46.
- Koster, R.D., P.A. Dirmeyer, Z. Guo, G. Bonan, E. Chan, P. Cox, C.T. Gordon, S. Kanae, E. Kowalczyk, D. Lawrence, P. Liu, C.-H. Lu, S. Malyshev, B. McAvaney, K. Mitchell, D. Mocko, T. Oki, K. Oleson, A. Pitman, Y.C. Sud, et al., 2004: Regions of strong coupling between soil moisture and precipitation. *Science*, **305**(5687), 1138-1140.
- Kraus, E.B., and S.J. Turner, 1967: A one-dimensional model of the seasonal thermocline. Part II. *Tellus*, **19**, 98-105.
- Kug J.-S., I.-S. Kang, and S.-I. An 2003: Symmetric and anti-symmetric mass exchanges between the equatorial and off-equatorial Pacific associated with ENSO. *J. Geophys. Res.*, **108** (C8) 3284.
- Kummerow, C., J. Simpson, O. Thiele, W. Barnes, A. T. C. Chang, E. Stocker, R.F. Adler, A. Hou, R. Kakar, F. Wentz, P. Ashcroft, T. Kozu, Y. Hong, K. Okamoto, T. Iguchi, H. Kuroiwa, E. Im, Z. Haddad, G. Huffman, B. Ferrier, W. S. Olson, E. Zipser, E. A. Smith, T.T. Wilheit, G. North, T. Krishnamurti, K. Nakamura, 2000: The Status of the Tropical Rainfall Measuring Mission (TRMM) after Two Years in Orbit. *J. App. Meteor.*, **39**, 1965-1982.
- Lee, S.-K. and D.B. Enfield, C. Wang, 2005: Ocean general circulation model sensitivity experiments on the annual cycle of Western Hemisphere Warm Pool. *J. Geophys. Res.*, **110**, C09004.
- Lee, S.-K., D.B. Enfield, and C. Wang, 2007: What drives the seasonal onset and decay of the western hemisphere warm pool? *J. Climate*, **20**, 2133-2146.
- Levitus, S., and T. Boyer, 1994: Temperature. Vol. 4, World Ocean Atlas, NOAA Atlas NESDIS, 117 pp.
- Liebmann B. and C.A. Smith, 1996: Description of a Complete (Interpolated) Outgoing Longwave Radiation Dataset. *Bull. Amer. Meteor. Soc.*, **77**, 1275-1277.
- Lindzen, R.S., and S. Nigam, 1987: On the role of sea surface temperature gradients in forcing low level winds and convergence in the tropics. *J. Atmos. Sci.*, **44**, 2440-2458.
- Lu, P., and J. McCreary, 1995: Influence of the ITCZ on the flow of thermocline water from the subtropical to the equatorial Pacific Ocean, *J. Phys. Oceanogr.*, **25**, 3076-3088.

- Lukas, R., 1986: The termination of the equatorial undercurrent in the eastern Pacific. *Prog. Oceanogr.*, **16**, 63-90.
- Luo, J.-J., S. Masson, E. Roeckner, G. Madec and T. Yamagata. 2005: Reducing Climatology Bias in an Ocean–Atmosphere CGCM with Improved Coupling Physics. *J. Climate*, **18** (13), 2344–2360.
- Magaña, V., J.A. Amador, and S. Medina, 1999: The midsummer drought over Mexico and Central America. *J. Climate*, **12**, 1577-1588.
- Marzeion, B., A. Timmermann, R. Murtugudde and F.-F. Jin. 2005: Biophysical Feedbacks in the Tropical Pacific. *J. Climate*, **18** (1), 58–70.
- Matsuno, T., 1966: Quasi-geostrophic motions in the equatorial area. *J. Meteor. Soc. Japan*, **44**, 24–42.
- Mayer, D.A., R.L. Molinari, M.O. Baringer, and G.J. Goni, 2001: Transition regions and their role in the relationship between sea surface height and subsurface temperature structure in the Atlantic Ocean. *Geophys. Res. Lett.*, **28**, 20, 3943-3946.
- Mazeika, P.A., 1967: Thermal domes in the eastern Atlantic Ocean. *Limnology and Oceanogr.*, **12**, 537-539.
- McClain C.R., M.L. Cleave, G.C. Feldman, W.W. Gregg, S.B. Hooker, and N. Kuring, 1998: Science quality SeaWiFS data for global biosphere research. *Sea Technol.*, **39**, 10–16.
- McClain, C.R., G.C. Feldman, and S.B. Hooker, 2004: An overview of the SeaWiFS project and strategies for producing a climate research quality global ocean bio-optical time series. *Deep Sea Res. II*, **51**, 5-42.
- McCreary, J.P., 1983: A model of tropical ocean–atmosphere interaction. *Mon. Wea. Rev.*, **111**, 370–387.
- McCreary, J.P., H.S. Lee and D.B. Enfield, 1989: The response of the coastal ocean to strong offshore winds, with application to the Gulfs of Tehuantepec and Papagayo. *J. Mar. Res.*, **47**, 81-109.
- McCreary, J.P., and P. Lu, 1994: On the interaction between the subtropical and equatorial ocean circulation: the Subtropical Cell. *J. Phys. Oceanogr.*, **24**, 466–497.
- McPhaden, M.J., *et al.*, 1998: The Tropical Ocean Global Atmosphere (TOGA) observing system: A decade of progress. *J. Geophys. Res.*, **103**: 14,169-14,240.
- McPhaden, M.J., and D. Zhang, 2002: Slowdown of the meridional overturning circulation in the upper Pacific Ocean., *Nature*, **415**, 603-608.
- McPhaden, M.J., and D. Zhang, 2004: Pacific Ocean circulation rebounds, *Geophys. Res. Lett.*, **31**, L18301.
- Mechoso, C.R., A.W. Robertson, N. Barth, M.K. Davey, P. Delecluse, P.R. Gent, S. Ineson, B. Kirtman, M. Latif, H. Le Treut, T. Nagai, J.D. Neelin, S.G.H. Philander, J. Polcher, P.S. Schopf, T. Stockdale, M.J. Suarez, L. Terray, O. Thual and J.J. Tribia, 1995: The seasonal cycle over the tropical Pacific in coupled ocean-atmosphere general circulation models. *Mon. Weather Rev.*, **123** (9), 2825-2838.
- Meinen, C.S. and M.J. McPhaden, 2000: Observations of warm water volume changes in the equatorial Pacific and their relationship to El Niño and La Niña, *J. Climate*, **13**, 3551-3559.
- Meinen, C.S. and M.J. McPhaden, 2001: Interannual variability in warm water volume transports in the equatorial Pacific during 1993-1999, *J. Phys. Oceanogr.*, **31**, 1324-1345.
- Meinen, C.S., 2005: Meridional Extent and Interannual Variability of the Pacific Ocean Tropical-Subtropical Warm Water Exchange. *J. Phys. Oceanogr.*, **35**(3), 323-335.
- Mesinger F., and Coauthors, 2006: North American Regional Reanalysis. *Bull. Amer. Meteor. Soc.*, **87**, 343–360.
- Mitchell, T.P. and J.M. Wallace. 1992: The Annual Cycle in Equatorial Convection and Sea Surface Temperature. *J. Climate*, **5** (10), 1140–1156.

- Mitchell, D.L., and T.J. Brown, 1996: The role of the Eastern Pacific warm pool in the Mexican monsoon. Preprints, Eighth Conf. on Air-Sea Interaction and Conf. on the Global Ocean-Atmosphere-Land System (GOALS). AMS, Jan. 28 -Feb. 2, 1996, Atlanta, Georgia, 352-355.
- Mosiño, A.P. and E. García, 1966: Evaluacion de la sequia intraestival en la Republica Mexicana. *Proc. Conf. Reg. Latinoamerica Union Goegr. Int.*, **3**, 500-516.
- Murtugudde, R., R. Seager, and A. Busalacchi, 1996: Simulation of the Tropical Oceans with an Ocean GCM Coupled to an Atmospheric Mixed-Layer Model. *J. Climate*, **9**, 1795-1815.
- Murtugudde, R., J. Beauchamp, C.R. McClain, M. Lewis and A.J. Busalacchi. 2002: Effects of Penetrative Radiation on the Upper Tropical Ocean Circulation. *J. Climate*, **15** (5), 470-486.
- Nigam, S., 1997: The Annual Warm to Cold Phase Transition in the Eastern Equatorial Pacific: Diagnosis of the Role of Stratus Cloud-Top Cooling. *J. Climate*, **10**, 2447-2467.
- Nigam, S., and E. DeWeaver, 1998: Influence of orography on the extratropical response to El Niño events. *J. Climate.*, **11**, 716-734.
- Pacanowski, R.C. and A. Gnanadesikan, 1998: Transient response in a z-level ocean model that resolves topography with partial-cells. *Mon. Wea. Rev.*, **126** (12), 3248-3270.
- Pacanowski, R.C., and S.M. Griffies, 1998: MOM 3.0 Manual, NOAA/Geophysical Fluid Dynamics Laboratory, Princeton, USA 08542.
- PACS: <http://www.usclivar.org/Pubs/Pacs.new.pdf>
- Palacios D.M., S.J. Bograd, 2005: A census of Tehuantepec and Papagayo eddies in the northeastern tropical Pacific. *Geophys. Res. Lett.*, **32**, L23606.
- Pegion, P.J., M.A. Bourassa, D.M. Legler, and J.J. O'Brien, 2000: Objectively-derived daily "winds" from satellite scatterometer data. *Mon. Wea. Rev.*, **128**, 3150-3168.
- Peña, M., and M.W. Douglas, 2002: Characteristics of Wet and Dry Spells over the Pacific Side of Central America during the Rainy Season. *Mon. Wea. Rev.*, **130**, 3054-3073.
- Peres-Sierra, A.F., Inoue, M. and J.J. O'Brien, 1985: Estimates of Oceanic Horizontal Heat Transport in the Tropical Pacific Ocean. *J. Geophys. Res.*, **90**(C2), 3293-3303.
- Philander, S.G.H., W.J. Hurlin, and A. Seigel, 1987: A model of the seasonal cycle in the tropical Pacific Ocean. *J. Phys. Oceanogr.*, **17**, 1986-2002.
- Philander, S.G.H. and W.J. Hurlin, 1988: The Heat Budget of the Tropical Pacific Ocean in a Simulation of the 1982-1983 El Niño. *J. Phys. Oceanogr.*, **18**, 926-931.
- Philander, S.G., and A.V. Fedorov, 2003: Role of tropics in changing the response to Milankovich forcing some three million years ago. *Paleoceanography*, **18** (2), 1045.
- Picaut, J., Delcroix, T., 1995: Equatorial wave sequence associated with warm pool displacements during the 1986-1989 El Niño- La Niña. *J. Geophys. Res.*, **100**, 18393-18408.
- Picaut, J., F. Masia, Y. Du Penhoat, 1997: An advective-reflective conceptual model for the oscillatory nature of the ENSO. *Science*, **277**, 663-666.
- Pinker, R.T. and I. Laszlo, 1992. Modeling of surface solar irradiance for satellite applications on a global scale. *J. Appl. Meteor.*, **31**, 194-211.
- Price, J.F., R.A. Weller, and R. Pinkel, 1986: Diurnal cycling: Observations and models of the upper ocean response to diurnal heating, cooling, and wind mixing. *J. Geophys. Res.*, **91**, 8411-8427.
- Raymond, D.J., S.K. Esbensen, C. Paulson, M. Gregg, C.S. Bretherton, W.A. Petersen, R. Cifelli, L.K. Shay, C. Ohlmann and P. Zuidema, 2004: EPIC2001 and the Coupled Ocean-Atmosphere System of the Tropical East Pacific. *Bull. Amer. Meteor. Soc.*, **85** (9), 1341-1354.
- Reynolds, R.W. and T.M. Smith, 1994: Improved global sea surface temperature analyses using optimum interpolation. *J. Climate*, **7**, 929-948.
- Reynolds, R.W., N.A. Rayner, T.M. Smith, D.C. Stokes, and W. Wang, 2002: An improved in situ and satellite SST analysis for climate. *J. Climate.*, **15**, 1609-1625.
- Romero-Centeno, R., J. Zavala-Hidalgo, A. Gallegos and J.J. O'Brien, 2003: Isthmus of Tehuantepec wind climatology and ENSO signal. *J. Climate*, **16**, 2628-2639.

- Ropelewski, C.F., and M.S. Halpert, 1987: Global and regional scale precipitation patterns associated with the El Niño / Southern Oscillation. *Mon. Wea. Rev.*, **115**, 1606-1626.
- Ropelewski, C.F., and M.S. Halpert, 1989: Precipitation patterns associated with the high index phase of the Southern Oscillation. *J. Climate*, **2**, 268-284.
- Rossow, W.B., and R.A. Schiffer, 1991. ISCCP cloud data products. *Bull. Amer. Meteor. Soc.*, **72**, 2-20.
- Saha, S., S. Nadiga, C. Thiaw, J. Wang, W. Wang, Q. Zhang, H.M. van den Dool, H.-L. Pan, S. Moorthi, D. Behringer, D. Stokes, M. Pena, S. Lord, G. White, W. Ebisuzaki, P. Peng, P. Xie, 2006 : The NCEP Climate Forecast System. In press, *J. Climate*.
- Saravanan, R. and P. Chang, 2000. Interactions between the Pacific ENSO and tropical Atlantic climate variability. *J. Climate*, **13**, 2177-2194.
- Schneider, E.K. and Z. Zhu, 1998: Sensitivity of the simulated annual cycle of SST in the equatorial Pacific to sunlight penetration. *J. Climate*, **11**, 1932-1950.
- Schubert, S.D., M.J. Suarez, P.J. Pegion, R.D. Koster, and J.T. Bacmeister, 2004: Causes of Long-Term Drought in the U.S. Great Plains. *J. Climate*, **17**, 485-503.
- Schultz, D.M., W.E. Bracken, L.F. Bosart, G.J. Hakim, M.A. Bedrick, M.J. Dickinson, and K.R. Tyle, 1997: The 1993 superstorm cold surge: Frontal structure, gap flow, and tropical impact. *Mon. Wea. Rev.*, **125**, 5-39.
- Schultz D.M., W.E. Bracken, and L.F. Bosart, 1998: Planetary- and synoptic-scale signatures associated with Central American cold surges. *Mon. Wea. Rev.*, **126**, 5-27.
- Seager, R., Zebiak, S.E. and M.A. Cane, 1988: A Model of the Tropical Pacific Sea Surface Temperature Climatology. *J. Geophys. Res.*, **93**(C2), 1265-1280.
- Seager, R., M.B. Blumenthal, and Y. Kushnir, 1995: An Advective Atmospheric Mixed Layer Model for Ocean Modeling Purposes: Global Simulation of Surface Heat Fluxes. *J. Climate*, **8**, 1951-1964.
- Seager, R., D.S. Battisti, J. Yin, N. Gordon, N.H. Naik, A.C. Clement and M.A. Cane, 2002: Is the Gulf Stream responsible for Europe's mild winters? *Qtr. J. Roy. Meteor. Soc.*, **128**: 2563-2586.
- Seager, R., Y. Kushnir, C. Herweijer, N. Naik, and J. Velez, 2005: Modeling of Tropical Forcing of Persistent Droughts and Pluvials over Western North America: 1856-2000. *J. Climate*, **18**, 4065-4088.
- Shapiro, R., 1970: Smoothing, filtering and boundary effects. *Rev. Geophys. Space Phys.*, **8**, 359-387.
- Signorini, S.R., R. Murtugudde, C.R. McClain, J.R. Christian, J. Picaut, and A.J. Busalacchi, 1999: Biological and physical signatures in the tropical and subtropical Atlantic. *J. Geophys. Res.*, **104**, 18367-18382.
- Sloyan, B.M., G.C. Johnson, and W.S. Kessler, 2003: The Pacific Cold Tongue: A pathway for interhemispheric exchange. *J. Phys. Oceanogr.*, **33**, 1027-1043.
- Smith, T.M., and R.W. Reynolds, 2004: Improved Extended Reconstruction of SST (1854-1997). *J. Climate*, **17**, 2466-2477.
- Spencer, R.W., 1993: Global oceanic precipitation from the MUS during 1979-91 and comparisons to other climatologies. *J. Climate*, **6**, 1301-1326.
- Spillane, M., D. Enfield, and J. Allen, 1987: Intraseasonal Oscillations in Sea Level along the West Coast of the Americas. *J. Phys. Oceanogr.*, **17**, 313-325.
- Stevenson, M.R., and B.A. Taft. 1971. New evidence of Equatorial Undercurrent east of the Galápagos Islands. *J. Mar. Res.*, **29** (2), 103-115.
- Stockdale, T.N., A.J. Busalacchi, D.D. Harrison and R. Seager, 1998: Ocean Modeling for ENSO. *J. Geophys. Res.*, **103**: 14325-14356.
- Stumpf, H. G., 1975: Satellite detection of upwelling in the Gulf of Tehuantepec, Mexico. *J. Phys. Oceanogr.*, **5**, 383-388.

- Suarez, M.J., and P.S. Schopf, 1988: A delayed action oscillator for ENSO. *J. Atmos. Sci.*, **45**, 3283–3287.
- Sun, D., 2000: The heat sources and sinks of the 1986-1987 El Niño, *J. Climate*, **13**, 3533-3550.
- Sun, D.-Z., J. Fasullo, T. Zhang and A. Roubicek. 2003: On the Radiative and Dynamical Feedbacks over the Equatorial Pacific Cold Tongue. *J. Climate*, **16** (14), 2425–2432.
- Sun, D.-Z., T. Zhang, and S.-I. Shin, 2004: The effect of subtropical cooling on the amplitude of ENSO: a numerical study. *J. Climate*, **17**, 3786-3798.
- Sun, F., and J.-Y. Yu (2006), Impacts of Central America gap winds on the SST annual cycle in the eastern Pacific warm pool, *Geophys. Res. Lett.*, **33**, L06710.
- Swenson, M.S. and D.V. Hansen, Tropical Pacific ocean mixed layer heat budget: The Pacific cold tongue, *J. Phys. Oceanogr.*, **29**, 69-81, 1999.
- Takahashi, T., R.H. Wanninkhof, R.A. Feely, R.F. Weiss, D.W. Chipman, N. Bates, J. Olafson, C. Sabine and S.C. Sutherland, 1999: Net sea-air CO₂ flux over the global oceans: An improved estimate based on the sea-air pCO₂ difference. Proceedings of the 2nd International Symposium CO₂ in the Oceans, Center for Global Environmental Research, National Institute for Environmental Studies, Tsukuba, Japan, 9-15.
- Talley, L.D., and M.C. McCarthy, 1998: Potential vorticity in the Pacific and Indian Oceans. World Ocean Circulation Experiment (WOCE) Conference, Halifax Nova Scotia, Canada, 24-29 May 1998.
- Umatani, S. and T. Yamagata, 1991: Response of the eastern tropical Pacific to meridional migration of the ITCZ: The generation of the Costa Rica dome. *J. Phys. Oceanogr.*, **21**, 346-363.
- Vecchi, G., M. Harrison, A. Wittenberg, T. Rosati, 2005: Biases in Ocean and Coupled General Circulation Models. Workshop on the Application of EPIC2001 Data for Improving and Testing Coupled Atmosphere-Ocean Models, Seattle, WA., 11-13 May 2005.
- Vonder Haar, T.H., and A.H. Oort, 1973: New estimate of annual poleward energy transport by the northern hemisphere ocean. *J. Phys. Oceanogr.*, **3**, 169–172.
- Walker, G., T., and E.W. Bliss, 1937: World weather VI. Mem. Roy. Meteor. Soc., 4 (39), 119-139.
- Wang, C., and D.B. Enfield, 2001: The tropical Western Hemisphere warm pool. *Geophys. Res. Lett.*, **28**, 1635-1638.
- Wang, C., and D.B. Enfield, 2003: A Further Study of the Tropical Western Hemisphere Warm Pool, *J. Climate*, **16**: 1476-1493.
- Wang, C., D.B. Enfield, S.-K. Lee, and C.W. Landsea, 2006: Influences of the Atlantic warm pool on western hemisphere summer rainfall and Atlantic hurricanes. *J. Climate*, **19**, 3011-3028.
- Webster, P.J., V.O. Magaña, T.N. Palmer, J. Shukla, R.A. Tomas, M. Yanai and T. Yasunari, 1998: Monsoons: Processes, predictability, and the prospects for prediction. *J. Geophys. Res.*, **103**, 14451-14510.
- Webster, P.J., and R. Lukas, 1992: TOGA-COARE: The Coupled Ocean-Atmosphere Response Experiment. *Bull. Amer. Meteor. Soc.*, **73**, 1377-1416.
- White, W.B., 1973: An Oceanic Wake in the Equatorial Undercurrent Downstream from the Galápagos Archipelago. *J. Phys. Oceanogr.*, **3**, 156-161.
- Wijesekera, H.W., D.L. Rudnick, C.A. Paulson, S.D. Pierce, W.S. Pegau, J. Mickett, and M.C. Gregg, 2005: Upper ocean heat and freshwater budgets in the eastern Pacific warm pool, *J. Geophys. Res.*, **110**, C08004.
- Willmott, C.J. and K. Matsuura, 1995. Smart interpolation of annually averaged air temperature in the United States. *J. Appl. Meteor.*, **34** (12), 2577-2586.
- Wittenberg, A.T., A. Rosati, N.C. Lau, and J.J. Ploshay, 2006: GFDL's CM2 Global Coupled Climate Models. Part III: Tropical Pacific Climate and ENSO. *J. Climate*, **19**, 698–722.
- Woodruff, S.D., Slutz, R.J., Jenne, R.L., and Steurer, P.M., 1987: A comprehensive ocean-atmosphere data set, *Bull. Amer. Meteor. Soc.*, **68**, 1,239-1,250.
- Wyrtki, K., 1964a: Upwelling in the Costa Rica Dome. *Fish. Bull. US*, **63**, 355-372.

- Wyrski, K., 1964b: Surface currents of the eastern tropical Pacific Ocean. *Inter-Amer. Tropical Tuna Comm. Bull.*, **9** (5), 270-304.
- Wyrski, K., 1981: An Estimate of Equatorial Upwelling in the Pacific. *J. Phys. Oceanogr.*, **11**, 1205-1214.
- Xie, P.P., and P. Arkin, 1996: Analyses of Global Monthly Precipitation Using Gauge Observations, Satellite Estimates, and Numerical Model Predictions. *J. Climate*, **9**, 840-858.
- Xie, P.P., and P. Arkin, 1997: Global Precipitation: A 17-year monthly analysis based on gauge observations, satellite estimates, and numerical model outputs. *Bull. Amer. Meteor. Soc.*, **78**, 2539-2558.
- Xie, S.-P. and J.A. Carton, 2004: Tropical Atlantic variability: Patterns, mechanisms, and impacts. Earth's Climate: The Ocean-Atmosphere Interaction, C. Wang, S.-P. Xie and J.A. Carton (eds.), Geophysical Monograph, **147**, AGU, Washington D.C., 121-142.
- Xie, S.-P., H. Xu, W.S. Kessler, and M. Nonaka, 2005: Air-sea interaction over the eastern Pacific warm pool: Gap winds, thermocline dome, and atmospheric convection. *J. Climate*, **18**, 5-20.
- Xu, H., S.-P. Xie, Y. Wang, and J. Small, 2005: Effects of Central American mountains on the eastern Pacific winter ITCZ and moisture transport. *J. Climate*, **18**, 3856-3873.
- Yu, J.-Y., 2005: Enhancement of ENSO's persistence barrier by biennial variability in a coupled atmosphere-ocean general circulation model, *Geophys. Res. Lett.*, **32**, L13707.
- Yulaeva, E., and J.M. Wallace, 1994: The signature of ENSO in global temperature and precipitation fields derived from the Microwave Sounding Unit. *J. Climate*, **7**, 1719-1736.
- Zamudio, L., H.E. Hurlburt, E.J. Metzger, S.L. Morey, J.J. O'Brien, C.E. Tilburg, and J. Zavala-Hidalgo, 2006: Interannual variability of Tehuantepec eddies. *J. Geophys. Res.*, **111**, C05001.
- Zebiak, S.E., and M.A. Cane, 1987: A model El Niño-Southern Oscillation. *Mon. Weather Rev.*, **115**, 2262-2278.
- Zebiak, S.E., 1989: On the 30-60 day oscillation and the prediction of El Niño. *J. Climate*, **2**, 1381-1387.
- Zhang, C., 1993: Large-Scale Variability of Atmospheric Deep Convection in Relation to Sea Surface Temperature in the Tropics. *J. Climate*, **6**, 1898-1913.
- Zhang, Y., J.M. Wallace and D.S. Battisti 1997: ENSO-like Interdecadal Variability: 1900-93. *J. Climate*, **10**, 1004-1020.

Kristopher B. Karauskas

Curriculum Vitae

Campus Address:
Room 2223 CSS
University of Maryland
College Park, MD 20742
(301) 314-2624
kris@essic.umd.edu

Home Address:
1400 East-West Hwy. #1217
Silver Spring, MD 20910
(240) 350-0464
<http://essic.umd.edu/~kris>

Education

B.S., Honors in Major, Atmos. & Oceanic Sciences, University of Wisconsin-Madison, 2004.
Ph.D., (*expected 2007*), Atmos. & Oceanic Science, University of Maryland-College Park.
Thesis: Interannual variability of sea surface temperature in the eastern tropical Pacific Ocean and Central American rainfall
Advisor: Antonio J. Busalacchi, Earth System Science Interdisciplinary Center (ESSIC)

Honors and Awards

Lamont Postdoctoral Fellowship, Lamont-Doherty Earth Observatory, Columbia Univ., 1/08.
U.S. CLIVAR Drought In Coupled Models Project (DRICOMP) Grant (\$30K, NSF), 9/07.
AGU Student Travel Grant (\$1500, NSF), XXIV IUGG General Assembly, Perugia, Italy, 7/07.
First in theme, *Graduate Student Interaction Day 2007* (\$600), University of Maryland, 4/07.
NOAA Cooperative Institutes Exchange Program (OSU/CIOSS), 9/06.
Preparing for an Academic Career in the Geosciences (NSF), 7/05.
Citation for Scientific Outreach, University of Maryland, 2005.
Graduate Research Assistantship, University of Maryland, 2004-07.
Meteorological Satellite Applications Award (\$500), National Weather Association, 10/04.
Hilldale Undergraduate Research Fellowship (\$5K), University of Wisconsin, 2003-04.
Dean's List, University of Wisconsin, 2004.
NCAR Undergraduate Leadership Workshop, Boulder, CO, 6/03.

Employment, Service and Affiliations

Related Employment & Experience

Research Assistant III, UMD Earth System Science Interdisciplinary Center, 2005-07.
Visiting Scientist, NOAA R/V Ka'imimoana, 7/6-8/3, 2006.
Research Assistant I, UMD Earth System Science Interdisciplinary Center, 2004-05.
Undergraduate Research Asst., Coop. Inst. for Meteor. Satellite Studies (CIMSS), 2003-04.

Related Service

Reviewed for *J. Climate*, *J. Geophysical Research-Oceans*, and Dept. of Energy-Climate Panel
American Meteorological Society- Chapter Affairs Committee, 2006-08 term.
President, University of Wisconsin Chapter of the American Meteorological Society, 2003-04.
Mentor, Adult Role Models in Science, 2004.

Professional Affiliations

Member, Wash., D.C. Chapter of the American Meteorological Society, 2006 –
Member, National Weather Association, 2004 –
Member, American Geophysical Union, 2004 –
Member, American Meteorological Society, 2001 –

Teaching Experience

Academic Guest Lectures

Course: North American Hydroclimate (Prof. Sumant Nigam), University of Maryland–College Park, 2007 (1).

Course: Introduction to the Blue Ocean (Prof. Raghu Murtugudde), University of Maryland–College Park, 2006–07 (several).

Course: Weather Broadcasting (Mr. Greg Smith), American University–School of Comm., 2007.

Publications

Peer–Reviewed Literature

Karnauskas, K.B., and A.J. Busalacchi: Mechanisms for the interannual variability of SST in the east Pacific warm pool. (in preparation).

Karnauskas, K.B., and A.J. Busalacchi: The role of SST in the east Pacific warm pool in the interannual variability of Central American rainfall. (in preparation).

Karnauskas, K.B., and A.J. Busalacchi: The effect of the Central American gap winds on the interannual variability of SST in the east Pacific warm pool. (in preparation).

Karnauskas, K.B., Murtugudde, R., and A.J. Busalacchi: The effect of the Galápagos Islands on ENSO in forced and coupled ocean models. *J. Phys. Oceanogr.* (revisions).

Karnauskas, K.B., Busalacchi, A.J., and R. Murtugudde: Low–frequency variability and remote forcing of gap winds over the east Pacific warm pool. *J. Climate* (revisions).

Karnauskas, K.B., Ruiz–Barradas, A., Nigam, S., and A.J. Busalacchi: North American droughts in ERA–40 global and North American regional reanalyses: A Palmer Drought Severity Index perspective. *J. Climate* (accepted).

Karnauskas, K.B., Murtugudde, R., and A.J. Busalacchi, 2007: The effect of the Galápagos Islands on the equatorial Pacific cold tongue. *J. Phys. Oceanogr.*, **37** (5), 1266–1281.

>> *Featured in March 2007 BAMS ‘Papers of Note.’*

Karnauskas, K.B., 2006: The African meridional OLR contrast as a diagnostic for Atlantic tropical cyclone activity and implications for predictability. *Geophys. Res. Lett.*, **33**, L06809.

Other Papers and Presentations

- Murtugudde, R., Karnauskas, K.B., Wang, X., Christian, J.R., and A.J. Busalacchi: Incredible shrinking iguana: Gaia on Galápagos? Ocean Carbon & Biogeochemistry (OCB) Summer Workshop. Poster W20. Woods Hole, MA. July 23–26, 2007.
- Karnauskas, K.B., and A.J. Busalacchi, 2007: Interannual variability of SST in the east Pacific warm pool. IUGG XXIV General Assembly. Oral (JPS–001). Perugia, Italy. July 2–13, 2007.
- Karnauskas, K.B., Busalacchi, A.J., and R. Murtugudde, 2007: Low-frequency variability and remote forcing of gap winds in the eastern tropical Pacific. IUGG XXIV General Assembly. Oral (MS–011). Perugia, Italy. July 2–13, 2007.
- Karnauskas, K.B., Busalacchi, A.J., and R. Murtugudde, 2007: The effect of the Galápagos Islands on the Pacific cold tongue and ENSO. IUGG XXIV General Assembly. Oral (JMS–014). Perugia, Italy. July 2–13, 2007.
- Murtugudde, R., and K.B. Karnauskas, 2007: The incredible shrinking Iguana: Impact of Galápagos. AGU 2007 Joint Assembly. Oral (U32A). Acapulco, Mexico. May 22–25, 2007.
- Karnauskas, K.B., 2007: The effect of the Galápagos Islands on ocean and climate variability. Presentation at *Graduate Student Interaction Day 2007*. Theme: Our changing physical environment and beyond. April 12, 2007.
- Karnauskas, K.B., Murtugudde, R., and A.J. Busalacchi, 2007: Impact of the Galápagos Islands on the equatorial Pacific. Invited contribution, *Bull. Amer. Meteor. Soc.–Nowcast/Papers of Note*, **88** (3), 302–303.
- Karnauskas, K.B., 2007: The tropical Pacific: Interesting aspects of variability, and key questions with respect to long-term North American drought. Invited seminar, Lamont–Doherty Earth Observatory, Columbia University, Palisades, NY. February 8, 2007.
- Karnauskas, K.B., and A.J. Busalacchi, 2006: Mechanisms for interannual variability in the East Pacific Warm Pool. AGU Fall Meeting. Poster OS11A–1462. San Francisco, CA. Dec. 11–15, 2006.
- Karnauskas, K.B., 2006: Interannual variability of SST and Chlorophyll in the East Pacific Warm Pool: high-resolution satellite observations. Invited seminar, Cooperative Institute for Oceanographic Satellite Studies (CIOSS), Oregon State University, Corvallis, OR. September 25, 2006.
- Karnauskas, K.B., Busalacchi, A.J., and R. Murtugudde, 2006: Interannual variability of SST and Chlorophyll in the East Pacific Warm Pool: high-resolution satellite observations. 53rd Annual East Pacific Ocean Conference (EPOC). Poster. Mt. Hood, OR. September 28–30, 2006.
- Karnauskas, K.B., 2006: Improved modeling of SST in the Pacific Cold Tongue: implications for the NCEP GODAS and CFS. Invited contribution, *NOAA NWS S&TI Climate Bulletin*, July 2006.
- Karnauskas, K.B., Murtugudde, R., and A.J. Busalacchi, 2006: Improvements to the equatorial Pacific Cold Tongue region in an OGCM: possible implications for the NCEP GODAS/CFS.

Seminar, NOAA National Centers for Environmental Prediction (NCEP), Environmental Modeling Center (EMC), Camp Springs, MD. June 20, 2006.

Karnauskas, K.B., Ruiz-Barradas, A., and S. Nigam: A Palmer Drought Severity Index for the North American Regional Reanalysis and the ECMWF 40-year Reanalysis: comparative analysis and linkages to interannual and decadal climate variability. 2006 AGU Joint Assembly. Poster A33C-02. Baltimore, MD. May 23-26, 2006.

Karnauskas, K.B., and A.J. Busalacchi, 2006: Interannual variability in the East Pacific Warm Pool: high-resolution satellite observations. Proceedings of the 8th International Conference on Southern Hemisphere Meteorology and Oceanography, p.1289-1294. Foz do Iguacu, Brazil. April 24-28, 2006.

Karnauskas, K.B., Busalacchi, A.J., and R. Murtugudde, 2005: Seasonal and interannual variability of the East Pacific Warm Pool. Workshop on the Application of EPIC2001 Data for Improving and Testing Coupled Atmosphere-Ocean Models. Seattle, WA. May 11-13, 2005.

Schmit, T.J., Gurka, J., Menzel, W.P., Gunshor, M.M., and K.B. Karnauskas, 2005: Introducing the next generation geostationary imager- GOES-R's Advanced Baseline Imager (ABI). GOES-R/NPOESS Symposium, San Diego, CA, 8-13 January 2005. AMS, Boston, MA.

Karnauskas, K.B., 2004: Interannual variability of surface longwave radiation over the African continent as derived from AVHRR. 29th annual meeting of the National Weather Association. Poster P1.21. Portland, OR. October 16-21, 2004.

Karnauskas, K.B., 2004: Interannual variability of surface longwave radiation over the African continent as derived from AVHRR. NOAA 29th annual climate diagnostics and prediction workshop. Poster P2.29. Madison, WI. October 18-22, 2004.

Gurka, J.R., Dittberner, J.G., Schmit, T.J., Menzel, W.P., Gunshor, M.M., and K.B. Karnauskas, 2004: Plans for the GOES-R series and comparing the Advanced Baseline Imager to that on METEOSAT-8. Presentation at the EUMETSAT Conference, Prague, Czech Rep. June, 2004.

Schreiner, T., Schmit, T.J., Li, J., Ellrod, G., Gunshor, M., and K.B. Karnauskas, 2004: Using GOES-R to help monitor SO₂. 3rd NOAA GOES-R users conference, Boulder, CO. May, 2004.

Gunshor, M., Schmit, T.J., and K.B. Karnauskas, 2004: Simulation of the spectral bands on the Advanced Baseline Imager. 3rd NOAA GOES-R users conference, Boulder, CO. May 10, 2004.

Schmit, T.J., Menzel, W.P., Gurka, J., Li, J., Gunshor, M., Schmidt, C., Sieglaff, J., and K.B. Karnauskas, 2004: The next generation imager on GOES-R. Presentation at NOAA NESDIS, Washington, D.C. February 17, 2004.

Pryor, A., Ackerman, S.A., Mooney, M., Leary, J.P., De Rose, H., Holwerk, L., K.B. Karnauskas, Schmidt, C., and J. Yuenger, 2004: Wisconsin Weather Stories. Presentation at the Symposium on Education, Seattle, WA, January 11-15, 2004. Boston, MA, AMS, Paper P1.8. Reprint 3623.

